This electronic thesis or dissertation has been downloaded from Explore Bristol Research, http://research-information.bristol.ac.uk

Author:
Waite, Richard

Title:
Neutron Scattering Studies of Spin-Density Waves in Itinerant Systems

General rights
Access to the thesis is subject to the Creative Commons Attribution - NonCommercial-No Derivatives 4.0 International Public License. A copy of this may be found at https://creativecommons.org/licenses/by-nc-nd/4.0/legalcode This license sets out your rights and the restrictions that apply to your access to the thesis so it is important you read this before proceeding.

Take down policy
Some pages of this thesis may have been removed for copyright restrictions prior to having it been deposited in Explore Bristol Research. However, if you have discovered material within the thesis that you consider to be unlawful e.g. breaches of copyright (either yours or that of a third party) or any other law, including but not limited to those relating to patent, trademark, confidentiality, data protection, obscenity, defamation, libel, then please contact collections-metadata@bristol.ac.uk and include the following information in your message:

- Your contact details
- Bibliographic details for the item, including a URL
- An outline nature of the complaint

Your claim will be investigated and, where appropriate, the item in question will be removed from public view as soon as possible.

Neutron Scattering Studies of Spin-Density Waves in Itinerant Systems

Richard Waite

University of Bristol
September 2020

A thesis submitted to the University of Bristol in accordance with the requirements for
award of the degree of Doctor of Philosophy in the Faculty of Science,
School of Physics.

67,827 Words

Abstract

This thesis presents neutron scattering measurements of spin-density-waves (SDW) in $Sr_3Ru_2O_7$ and $CeAuSb_2$. Despite the microscopic differences, both compounds have recently been discovered to exhibit field induced SDW order associated with metamagnetism, and appear to host competing instabilities that can be tuned with symmetry breaking fields. In the case of $Sr_3Ru_2O_7$ the symmetry is broken by the orientation of a magnetic field with respect to different crystallographic axes, in $CeAuSb_2$ an orthorhombic distortion produced by compressive uniaixal stress.

Neutron diffraction can directly measure the SDW order parameter and is therefore an ideal tool for studying the symmetry and magnetic structure of the SDW phases. In addition, inelastic neutron scattering can be used to measure the spin fluctuations, which can have a profound effect on the physical properties of a system, particularly in the region of a quantum critical point (QCP).

The SDW phase diagram of $Sr_3Ru_2O_7$ for a magnetic field applied along the c-axis has been studied on the time-of-flight diffractometer WISH at ISIS, UK. In $Sr_3Ru_2O_7$ there are two adjacent SDW phases that mask the quantum critical end-point of a metamagnetic transition[1] . Recent thermodynamic measurements suggested the existence of an additional QCP. We find no evidence of SDW at the putative QCP but report on the field dependence of the SDW wavevector, which is compared to the behaviour of other systems that exhibit SDW near a ferromagnetic QCP (namely $FeNb_2$), and the temperature dependence of the high-field SDW-B for which thermodynamic probes only show weak anomalies. Our results indicate that the SDW order is driven by Fermi-surface nesting, with the nesting between different Fermi sheets in the two SDW phases. We find that the temperature dependence of the order parameter in both phases follows the same functional form. There is no indication that the SDW-B phase formation is different in nature to the SDW-A phase.

Neutron diffraction data for a magnetic field applied along the Ru-O bond in the plane of the bilayers (a-axis) of $Sr_3Ru_2O_7$ are presented, from several experiments on the triple axis spectrometers IN12 at the ILL, France and TASP at PSI, Switzerland. The symmetry breaking field was found to induce two C_2 symmetric SDW ordered phases. The two phases also coincide with metamagnetic transitions but the transport signatures of the two phases are different. The orientation of the axis of the order flips with respect to the field between the two phases which highlights the importance of spin-orbit effects in this material.

Additional inelastic measurements of the spin-fluctuations associated with the newly discovered SDW phases in $Sr_3Ru_2O_7$ for a magnetic field along the a-axis were performed on the triple-axis spectrometers IN12 and THALES at the ILL, France. The results demonstrate that low energy fluctuations in the quantum critical region over a wide field-range are well described by overdamped spin fluctuations that soften dramatically at a critical field associated with the high-field SDW phase boundary, with evidence of critical slowing down behaviour. Together this suggests the quantum critical fluctuations are well described by overdamped incommensurate spin-fluctuations.

Neutron diffraction measurements were undertaken on $CeAuSb_2$ with a novel device

(designed by C. Hicks of MPI, Dresden) to allow for in-situ uniaxial stress tuning. The experiment was performed on the WISH TOF diffractometer. Compressive uniaxial stress along the a-axis produces a monodomain of single-q SDW order that is believed to restore the continuous nature of the transition at T_{N} by reducing the point group symmetry of the fluctuations.

Acknowledgements

First and foremost I would like to thank my two supervisors Stephen Hayden and Russell Ewings. They have both been extremely patient and generous with their time and knowledge. I have benefited greatly from being a part of two institutions (Bristol University and ISIS) and to have been involved in many interesting and exciting projects.

I owe many thanks to Clifford Hicks, without whom the work on $CeAuSb_2$ would not have been possible. For his willingness to collaborate on the experiment and his generous help since I am most grateful. I had a great time when I visited the Max Planck Institut in Dresden to prepare for the experiment and I want to thank the hard-working and friendly people there who made me feel welcome. In particular, Dmitry Sokolov who helped me both in the Dresden lab and on WISH.

The experiments in this thesis were performed at external facilities and I am indebted to the many instrument scientists whose hard work has ensured the (mostly) smooth operation of the beamlines. Thanks to Paul Steffens on THALES and Greg Tucker on TASP (now at ISIS). A special thanks is reserved for the instrument scientists on WISH: Pascal Manuel, Dmitry Khalyavin and Fabio Orlandi. I am grateful not only for their incredible hard work on the beamline, but for their support throughout my PhD and beyond - in particular I thank Fabio for the collaboration on the various uniaxial stress experiments.

My thanks also to the scientists in the collective excitations group at ISIS who made me feel most welcome at ISIS and supported experiments on LET and MERLIN which unfortunately are not included in this thesis. In particular David Voneshen, Rob Bewley, Helen Walker, Toby Perring and of course Russell.

I am grateful to the science faculty workshop staff at Bristol, in particular Adrian Crimp, Patrick Alexander, Bartosz Dworzanski and Jake Rusby. They put up with many last-minute requests and always delivered.

My time in Bristol would not have been so enjoyable without the friendly bunch of students and academics in the CES group in Bristol. Thanks to Chris Bell, Sven Friedemann and Tony Carrington from whom I've learnt much (but by no means all that they tried to teach me). I want to thank all my fellow students, I will miss the coffee breaks together. In particular Emma Gilroy and Jake Ayres for their camaraderie. A special thanks to Lauren Cane and Maud Barthélemy with whom I had lot of fun sharing an office and performing experiments. I also want to thank Chris Lester, a former student and post doc in the CES group, who performed some of the experiments that contributed to this thesis.

I have written a large portion of this thesis while working as a software developer on the Mantid project at ISIS and I want to thank them for their patience, flexibility and understanding, in particular Lamar Moore, Danny Hindson and Nick Draper.

I want to thank my family for all their support over the years, they have helped push me to do the best that I can. Last, but not least, I must thank Alice. Without her I probably never would have started this, and I definitely would not have finished it.

Authors's declaration

I declare that the work in this thesis was carried out in accordance with the requirements of the University's Regulations and Code of Practice for Research Degree Programmes and that it has not been submitted for any other academic award. Except where indicated by specific reference in the text, the work is the candidate's own work. Work done in collaboration with, or with the assistance of, others, is indicated as such. Any views expressed in the thesis are those of the author.

SIGNED: .... DATE:..........................

Contents

Chapter 1

Introduction

This thesis presents neutron scattering measurements of spin-density-waves (SDW) in two strongly correlated itinerant systems: $Sr_3Ru_2O_7$ and $CeAuSb_2$.

Spin-density waves are a common phenomenon in condensed matter physics, observed in a variety of systems from ‘simple’ elemental chromium, to unconventional superconductors such as the high-T_c cuprates (see [2] and references therein) and iron pnictides (see [3] and references therein). They are symmetry breaking periodic modulations of the spin-density produced by the condensation of electron-hole pairs which opens a gap, Δ, at the Fermi-level between states separated by a wavevector, $\boldsymbol{q}$. In systems that exhibit large nested parallel portions of Fermi surface, it is possible for a single wavevector to gap out a significant fraction of carriers and significantly lower the energy of the system by reducing the density of states at the Fermi level. Such nesting occurs generically in 1D systems and therefore requires only a small interaction strength to stabilise order. In higher dimensions the enhancement tends to be less pronounced and the SDW instability depends on the detail of the electronic structure at the Fermi level.

The theoretical starting point for describing the electronic properties of metals at low temperature is Fermi liquid (FL) theory. Even though the Coulomb repulsion between electrons in metals is largely screened, it is still remarkable that in even the simplest metals (e.g. Na) many properties such as the temperature dependence of the electronic heat capacity follow the prediction of the free-electron model. The explanation is provided in Landau’s Fermi liquid theory [4] which considers the effect of adiabatically ‘switching on’ the interactions in an electron gas.

In this way it can be shown that the ground state and low energy excitations behave as a system non-interacting fermionic quasiparticles in a potential (i.e. half-integer spin quasiparticles that obey the Pauli exclusion principle and are governed by Fermi-Dirac statistics). These quaisparticles are actually due to a superposition of electron-hole excitations of the electron gas, but retain the charge and spin of bare electrons - in fact the adiabatic continuity ensures that there is a one-to-one correspondence between the quasiparticle states and the interacting electrons. The effect of the electronic interaction is then to renormalise the energy dispersion and various properties on a Fermi liquid such as the effective quasi-particle mass and the susceptibility. The quasiparticles are not exact eigenstates of the interacting system and have a finite lifetime, however near the Fermi level they are long-lived provided the decay rate is smaller than the excitation frequency (i.e. the quasiparticles do not decay before the interaction is fully switched 'on')[5].

FL theory is remarkably successful in describing the low temperature properties of metals where the conduction electrons are delocalised, but in many materials with strong correlations the conduction electrons maintain some of their atomic character. Typically, these strongly correlated materials have incomplete d or f-electron shells that are much more localised and produce narrow energy bands. The dichotomy between the itinerant and localised description of these materials is particularly evident in the magnetic properties. For example many heavy fermions exhibit Curie-Weiss behaviour in the susceptibility at high temperature, with a large effective moment corresponding to the local moment on the f electron ion, but at low temperature some order with much smaller moments indicative of itinerant magnetism. In these compounds the behaviour is tuned between the two extremes by the extent of the hybridisation of the more localised f electrons with the weakly interacting itinerant conduction electrons [1]. In general, strongly correlated materials exhibit a high a susceptibility to electronic orders and typically exhibit competing interactions with similar energy scales that can be tuned with external parameters such as pressure or magnetic field.

In some circumstances FL theory breaks down completely: one such instance is in the region of a quantum critical point [6]. For example, applying hydrostatic pressure to an itinerant ferromagnet (FM) will generically suppress the transition temperature by reducing the density of states at the Fermi level (promotes delocalization), at some critical pressure (and possibly magnetic field) the transition will approach zero temperature (for a review see [7]). At a quantum critical point (QCP) the continuous phase transition occurs at zero temperature. In clean itinerant ferromagnets the QCP is typically avoided by either a different ordered phase, typically antiferromagnetic (AFM), or the transition

---

[1] In the limit where the local moments are sufficiently screened by hybridisation with the conduction electrons, the f electrons are said to be incorporated into the Fermi sea. The cross-over regime is characterised by non-Fermi liquid behaviour, such as a resistivity that increases logarithmically as temperature decreases (due to spin-flip scattering of conduction electrons from the local moments).

becomes first-order[7]. In contrast to the AFM QCP, unconventional superconductivity in the region of a FM QCP is rare, only reported in a handful of urannium-based metals, such as UGe_2[8].

The majority of this thesis concerns the quasi-2D metal $Sr_3Ru_2O_7$ which is on the verge of a ferromagnetic instability, but instead exhibits multiple metamagnetic transitions (magnetic field induced first-order jump in the bulk magnetisation) at low temperature $T \lesssim 1$ K. This material has attracted much attention due the proximity to quantum criticality at ambient conditions: the critical point of one of the metamagnetic transitions could be suppressed to almost zero temperature for a magnetic field applied within $\lesssim 10°$ of the c-axis (perpendicular to the basal plane). Such a scenario would have been a rare example of a QCP that is not connected to a symmetry breaking ordered phase. However, it was found that the QCP was masked by an ordered phase that exhibited anomalously high resistivity and unusual signatures of rotational symmetry breaking (for a review see [9]). Recently neutron diffraction has shown that the QCP is masked by two adjacent SDW ordered phases [1], which has prompted renewed investigation into the phase diagram of $Sr_3Ru_2O_7$ and the thermodynamic signatures of the SDW order and metamagnetic quantum criticality. Less well studied is the metamagnetism for a magnetic field applied in the plane of the bilayers (ab-plane), which breaks the tetragonal symmetry of the lattice but also tunes the system away from the masked QCP (though quantum critical behaviour is still observed over a wide field range).

The other compound studied in this thesis is $CeAuSb_2$, a moderately heavy fermion compound. It is a quasi-2D material that hosts single-q incommensurate magnetic order, believed to be an itinerant nesting-driven SDW. A magnetic field can induce multi-q order that coincides with a metamagnetic transition. Signatures of magnetic field tuned quantum criticality have been reported [10], however the latest evidence suggests that the transition into the SDW phase is first-order [11]. The similarities between $CeAuSb_2$ and $Sr_3Ru_2O_7$ are striking: both exhibit metamagnetic transitions that bound field-induced SDW order associated with increased resistivity. The comparison with $Sr_3Ru_2O_7$ motivated the group of C. Hicks *et al.* in MPI, Dresden to measure the response of the SDW order to uniaxial strain in transport data - as such studies have previously played an important role in determining the symmetry of the SDW ordered phase in $Sr_3Ru_2O_7$[12]. The tetragonal system appears to host several competing instabilities that couple differently to uniaxial strain along certain directions - with a putative magnetic phase induced by a compressive strain along $\langle 100 \rangle$.

The features of the electronic structure which gives rise to the concomitant metamagnetism and SDW order in $Sr_3Ru_2O_7$ are quite generic to reduced dimensionality systems

- namely peaks in the density of states near the Fermi level and the presence of nested Fermi sheets. The physics of $Sr_3Ru_2O_7$ may apply to $CeAuSb_2$ and many other materials. For example, there are a range of heavy fermions with similar phase diagrams to the two compounds studied here: $CeNiGe_3$ [13], $CeRh_2Si_2$ [14] and $YbNiSi_3$ [15] all exhibit consecutive first-order metamagnetic transitions through an intermediate phase with higher resistivity, for which the phenomenology investigated here could be relevant.

In addition to the origin of SDW order, much of this thesis is concerned with the rotational symmetry breaking of SDW order and the coupling of that order to symmetry breaking fields. In the case of $Sr_3Ru_2O_7$ a magnetic field is applied in the basal plane in order to investigate the link between SDW order and the signatures of anisotropic transport and quantum criticality. In the case of $CeAuSb_2$, neutron diffraction is performed with the application of in-situ uniaxal stress in order to measure the symmetry of the putative induced phase and reveal competing instabilities.

The SDW order and dynamics in these materials were measured by neutron scattering - a powerful probe of magnetism [2]. Elastic magnetic scattering (diffraction) measures the spin-spin correlations of the time-averaged system. Static SDW order produces magnetic Bragg peaks offset from the structural Bragg peaks by the nesting wavevector, q. The intensity of the magnetic Bragg peaks is proportional to the square of the ordered moment, $|\boldsymbol{m_q}|^2$ and therefore directly probes the order parameter of the SDW [3]. Inelastic neutron scattering measures the SDW fluctuations through the components of the imaginary part of the spin-susceptibility, $\chi''(\boldsymbol{q}, \omega)$.

This thesis is organised as follows

Chapter 2 provides a theoretical background to itinerant magnetism and in particular the generalised spin-susceptibility and Stoner criterion for magnetic order. The SDW groundstate is discussed in the Hartree-Fock framework emphasising the phenomenological similarities between SDW theory and BCS superconductivity.

Chapter 3 provides a background to the theory of unpolarised neutron scattering and the instrumentation on which the data in this thesis were measured. Some practical considerations involved in the interpretation and analysis of neutron scattering data are reviewed - in particular the corrections to single-crystal diffraction intensities.

Chapter 4 has three sections. In the first section the family of layered perovskite strontium ruthenates are introduced and the trend between the dimensionality of the compounds and the nature of the magnetic correlations is compared to the generic phase

---

[2] Though it should be noted that the gapping of carriers by SDW order also produces signatures in transport measurements and is associated with a discontinuity in the entropy (which can be detected in a variety of quantities, such as heat capacity, thermal expansion and the magnetocaloric effect).

[3] In mean-field theory the ordered moment is proportional to the SDW gap, $|\boldsymbol{m_q}| \propto \Delta_{SDW}$.

diagram of an itinerant ferromagnet. A second section summarises the extensive thermodynamic measurements of the phase diagram of $Sr_3Ru_2O_7$ and the recent discovery of SDW order. In the last section the electronic structure of $Sr_3Ru_2O_7$ is calculated using a tight-binding model, and the features believed to be responsible for metamagnetism and SDW order in this compound are identified.

Chapter 5 presents systematic neutron diffraction measurements of the SDW phase diagram for a magnetic field applied perpendicular to the bilayer plane (parallel to the c-axis), motivated by evidence of an additional QCP associated with a metamagnetic transition at lower field. The measured phase diagram sheds new light on the thermodynamic properties of the recently discovered SDW phases and the link between SDW order and metamagnetic quantum criticality.

Chapter 6 presents the discovery of two new SDW ordered phases associated with different metamagnetic transitions for a magnetic field applied along the a-axis (in the bilayer plane). One of the SDW phases is connected to the metmagnetic transition with the avoided QCP for a field along the c-axis. The other to a region of anisotropic transport.

Chapter 7 is an extension of the previous chapter that uses inelastic neutron scattering to measure the evolution of the SDW-fluctuations with magnetic field over a region of the phase diagram that hosts quantum critical fluctuations.

Chapter 8 presents neutron diffraction measurements of the SDW order in $CeAuSb_2$ with the application of in-situ uniaxial stress using a novel device designed by the C. Hicks, to investigate the putative stress induced SDW order and reveal the symmetry of the competing instabilities.

A summary and overview of some future direction is given in Chapter 9.

Chapter 2

Itinerant Magnetism

2.1 Stoner ferromagnetism

Electrons in a metal interact principally via a screened Coulomb interaction. The motion of the itinerant electrons are correlated as a result of the collective behaviour to screen and decrease the Coulomb repulsion. The potential acting on an electron depends not only on the total electron density, but also the spin density due to exchange effects (a consequence of the Pauli exclusion principle prevents electrons with parallel spins occupying the same orbital leading to a reduction in the Coulomb repulsion) [1]. The net effect is that screened Coulomb potential, $V(r) \propto \exp(-r/r_{TF})/r$, decays with distance from the charge, r, much faster than in free-space, with an additional exponential decaying factor characterised by the Thomas-Fermi length, r_{TF} (which depends on the density of states at the Fermi level) [2].

The simplest model that includes these electron-electron interactions is the Hubbard model which assumes this potential to be sufficiently short-range so as to be modelled as a purely local repulsive interaction between electrons of opposite spin in each orbital of a lattice point. The Hubbard Hamiltonian for a single band in 1D can be written as,

$$\mathcal{H} = \sum_{k,\sigma} \epsilon_k c^{\dagger}_{k\sigma} c_{k\sigma} + U \sum_{i} n_{i\uparrow} n_{i\downarrow}, \tag{2.1}$$

where ϵ_k is the band dispersion, $c^{\dagger}_{k\sigma}/c_{k\sigma}$ are the creation/annihilation operators in the

---

[1] If the electrons were uncorrelated the probability of finding the pair of electrons at positions $\mathbf{r}$ and $\mathbf{r}'$ would be given by the product of the density at the respective point, $\rho(\mathbf{r})\rho(\mathbf{r}')$. Exchange and correlation effects reduce the probability of finding an electron in the vicinity of another - leading to a so-called exchange-correlation hole of depleted electron density (of total charge $+e$) which contributes to the effective mass of the electron.

[2] For a free-electron metal with the electron density of copper, $r_{TF} = 0.55$ Å.

Bloch basis for electrons with momentum k and spin state σ, $U > 0$ is the screened Coulomb potential and $n_{i\sigma}$ is the density of electrons of spin σ at the atomic site i [3].

For a half-filled band, a sufficiently large U will produce an antiferromagnetic (Mott) insulator, however away from half-filling the Coulomb interaction can favour the polarised ferromagnetic state in a metal. Spin polarisation costs kinetic energy, however this can be offset by the reduction in Coulomb repulsion in Eq.2.1. The interaction term is quartic in creation/annihilation operators therefore the Hamiltonian in Eq.2.1 cannot be readily diagonalised. In order to derive a condition for ferromagnetism we use mean-field theory, equivalent to the approach taken by Stoner[16]. The electron density of a given spin at the ith site can be written as $n_{i\sigma} = \langle n_\sigma \rangle + \delta n_{i\sigma}$, where $\delta n_{i\sigma}$ is a small deviation from the mean occupancy averaged over all sites, $\langle n_\sigma \rangle$. Ignoring terms that are quadratic in $\delta n_{i\sigma}$, the interaction term becomes,

$$n_{i\uparrow} n_{i\downarrow} = n_{i\uparrow} \langle n_\downarrow \rangle + n_{i\downarrow} \langle n_\uparrow \rangle - \langle n_\uparrow \rangle \langle n_\downarrow \rangle. \tag{2.2}$$

Substituting Eq.2.2 into Eq.2.1 and using the identity $\sum_i n_{i,\sigma} = \sum_k c^\dagger_{k,\sigma} c_{k,\sigma}$ gives the Stoner Hamiltonian,

$$\mathcal{H} = \sum_{k,\sigma} (\epsilon_k + U\langle n_{-\sigma} \rangle) c^\dagger_{k\sigma} c_{k\sigma} - NU \langle n_\uparrow \rangle \langle n_\downarrow \rangle. \tag{2.3}$$

where N is the number of lattice sites. The two-particle Coulomb interaction has been approximated by an effective single-particle term which produces a rigid band shift between the two spin species. The interpretation of Eq.2.4 is that the electrons of each spin interact with the average field due to the electrons of the opposite spin.

To find a ferromagnetic solution it is helpful to re-write the expectation values in Eq.2.4 as $\langle n_\sigma \rangle = n/2 + \sigma m$, where $\sigma = \pm 1$ for the up and down spin states respectively, $n = \langle n_\uparrow \rangle + \langle n_\downarrow \rangle$ and $m = \frac{1}{2}(\langle n_\uparrow \rangle - \langle n_\downarrow \rangle)$ are the average electron and spin density. The Hamiltonian is then,

$$\mathcal{H} = \sum_{k,\sigma} (\epsilon_k - \sigma U m) c^\dagger_{k\sigma} c_{k\sigma} + NUm^2, \tag{2.4}$$

where terms relating to the total density, n, have been incorporated into the chemical potential of the band dispersion, ϵ_k. The important result is that the exchange splitting

---

[3] The number density operator $n_{i\sigma} = c^\dagger_{i\sigma} c_{i\sigma}$ is the product of the creation and annihilation operators for electrons on site i (related to the Bloch operators by Fourier transform, e.g. $c_i = \frac{1}{\sqrt{N}} \sum_k c_k \exp(ikr_i)$, where N is the total number of unit cells).

of the two spin bands is proportional to the ferromagnetic spin-moment,

$$\Delta = 2Um, \tag{2.5}$$

which is an analogous result to the Weiss molecular field, though in this case the origin of the effective field is not an exchange interaction between local moments, but a consequence of a Coulomb interaction and the Pauli exclusion principle in an itinerant system (i.e. the difference in the exchange-correlation potentials seen by opposite spins). A schematic of the splitting is shown in Fig.2.1.

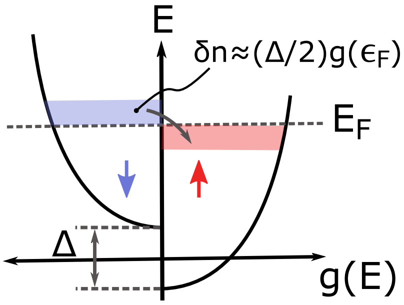

Figure 2.1: Schematic of the density of states of a spin split free electron system showing that the number of electrons increase/decrease in the majority/minority spin bands by an amount that depends on the splitting and the density of states at the Fermi level. The energy of the split bands is given by $E_{k,\sigma} = \epsilon_k + \sigma m U$. If the splitting is sufficiently small, we can assume the density of states does not change appreciably near the Fermi level such that $g(E_F) \approx g(\epsilon_F)$, where ϵ_F is the Fermi level of the paramagnetic bands.

The Stoner criterion for a ferromagnetic ground state can be found by minimising energy given by the Hamiltonian in Eq.2.4 with respect to m [4]. The change in potential energy per unit volume due to spontaneous spin polarisation is given by,

$$\Delta E_{ex} = -Um^2. \tag{2.6}$$

For small splitting the density of states can be assumed to be constant for both spin bands and therefore the kinetic energy gain per unit volume is approximately,

$$\Delta E_K \approx g(\epsilon_F)\left(\frac{\Delta}{2}\right)^2. \tag{2.7}$$

where $g(\epsilon_F)$ is the density of states per spin at the Fermi level for the unpolarised bands (assumed to be constant over the splitting) Substituting Eq.2.5 into Eq.2.7, it can be

---

[4] This is best done by converting the sum over k to an energy integral using the density of states, $g(\epsilon)$, which results in an energy per unit volume given by $E = \sum_\sigma \left[\int_0^{\epsilon_F} d\epsilon(\epsilon - \sigma mU)g(\epsilon)\right] + Um^2$.

seen that the total energy is reduced when

$$g(\epsilon_F)U \geq 1. \tag{2.8}$$

which is referred to as the Stoner condition. Therefore systems with a larger density of states at the Fermi-level will be more susceptible to ferromagnetic order.

2.2 Itinerant metamagnetism

In a system which does not fulfil the Stoner criterion in Eq.2.8 but has a peak in the density of states near the Fermi level, a magnetic field can produce a first-order jump in the bulk magnetisation known as a metamagnetic transition [5]. This corresponds to the rapid spin polarisation of the Fermi-surface as a peak in the density of states of one spin-species passes through the Fermi level, resulting in a large change of the moment due to the jump in the chemical potential of the opposite spin species to conserve the overall charge.

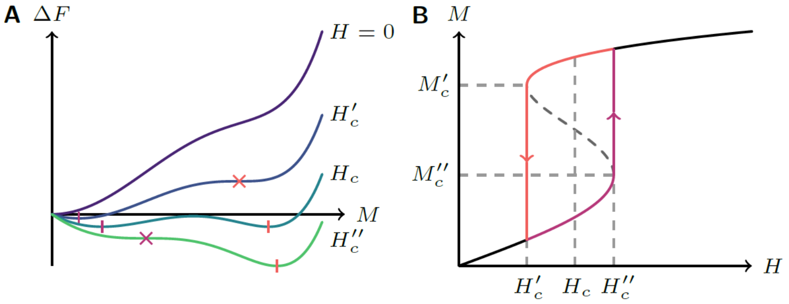

Figure 2.2: (A) Schematic of the evolution of the free energy for a system that exhibits a first-order hysteretic transition. Vertical bars and crosses indicate minima and inflection points respectively. (B) The resulting moments as a function of magnetic field strength, $H \approx B/\mu_0$. Figures taken from [17].

The value of the magnetisation at a given field, B, can be determined by minimising the following free energy density, F, subject to the constraint of charge conservation $n = n_\uparrow + n_\downarrow$, which at zero temperature is given by [18, 19],

$$F[m] = \int_0^{\mu_\uparrow} \epsilon g(\epsilon) d\epsilon + \int_0^{\mu_\downarrow} \epsilon g(\epsilon) d\epsilon + U\left(\frac{n^2}{4} + m^2\right) - g\mu_B m B, \tag{2.9}$$

---

[5] Metamagnetic transitions also occur in local moment antiferromagnets when a field applied transverse to the axis of the moment directions produces a re-orientation of the moments.

where $g \approx 2$ for the spin moment of electrons, and μ_σ is defined via the integral for, n_σ,

$$n = \int_0^{\mu_\sigma} g(\epsilon) d\epsilon, \tag{2.10}$$

and therefore the spin moment $m = \frac{1}{2}(n_\uparrow - n_\downarrow)$ is

$$m = \frac{1}{2} \int_{\mu_\downarrow}^{\mu_\uparrow} g(\epsilon) d\epsilon. \tag{2.11}$$

It should be noted that μ_σ are not the chemical potential of the spin bands, The chemical potential is the same for both spin bands with the exchange split dispersion $E_{k,\sigma} = \epsilon_k + \sigma m U$ (see Fig.2.1). Fig.2.2 shows the evolution of a generic free energy with magnetic field and the resulting hysteretic jump in the moment that is produced at fields when the local maximum of the free energy at zero field becomes an inflection point. It can be seen that the free energy must include terms that produce two local minima in order to produce the inflection point required for the metamagnetic jump in the moment.

2.3 Interpreting a magnetic instability via susceptibility

Here we only consider the spin contribution to the susceptibility that typically dominates the contribution from the orbital angular momentum which is largely quenched in transition metals in a crystal field.

The Coulomb term in Eq.2.1 produces an enhancement in the paramagnetic susceptibility, defined as $\chi = M/H$, where the magnetisation density is given by $M = 2\mu_B m$ (taking $g \approx 2$) and the magnetic field strength, $H \approx B/\mu_0$. The exchange splitting in a magnetic field is given by,

$$\begin{aligned} \Delta &= 2mU + 2\mu_B B, & (2.12) \\ &= \frac{2m}{g(\epsilon_F)} & (2.13) \end{aligned}$$

where the last line evaluates the integral in Eq.2.11 for a constant density of states over the energy range $\Delta = \mu_\uparrow - \mu_\downarrow$. Equating the self-consistent equations in Eq.2.13 it can be shown that the paramagnetic susceptibility is given by,

$$\chi = \frac{2\mu_0 \mu_B^2 g(\epsilon_F)}{1 - U g(\epsilon_F)}. \tag{2.14}$$

The well-known Pauli paramagnetic susceptibility of a non-interacting electron gas, $\chi_P = 2\mu_0\mu_B^2 g(\epsilon_F)$ can be recovered from Eq.2.14 by setting $U = 0$. A finite positive U corresponds to an enhancement of the susceptibility relative to the non-interacting electron gas. It can be seen that Eq.2.14 diverges at the value of U that satisfies the Stoner criterion in Eq.2.8, which corresponds to a ferromagnetic instability.

2.4 Generalised susceptibility

So far we have considered the response of a system to a uniform magnetic field, H, which produced a uniform magnetisation, however, in general a perturbing field will vary time and space. An oscillating magnetic field can be considered to be the superposition of different Fourier components of the form $\boldsymbol{H} = \boldsymbol{H_0} \exp^{-i(\boldsymbol{Q}\cdot\boldsymbol{r}-\omega t)}$, with wavevector $\boldsymbol{Q}$ and angular frequency ω. The linear response of the magnetisation to this single Fourier component is then given by the generalised (wavevector and frequency dependent) susceptibility,

$$m(\boldsymbol{Q},\omega) = \sum_{\beta} \chi_{\alpha\beta}(\boldsymbol{Q},\omega) H_{\alpha}(\boldsymbol{Q},\omega), \tag{2.15}$$

where the summation represents a matrix multiplication over the Cartesian indices $\alpha, \beta \in [x, y, z]$. Due to the translational symmetry of the crystal the magnetisation and therefore the susceptibility tensor $\boldsymbol{\chi}$ are periodic in reciprocal space such that we consider only the response as a function of the reduced wavevector, $\boldsymbol{q}$, in the first Brillouin zone,

$$\boldsymbol{\chi}(\boldsymbol{Q},\omega) = |f(Q)|^2 \boldsymbol{\chi}(\boldsymbol{q},\omega) \tag{2.16}$$

where $f(Q)$ is the magnetic form-factor (discussed in more detail in Section 3.4.1) [6] and $\boldsymbol{Q} = \boldsymbol{q} + \boldsymbol{G}$ where $\boldsymbol{G}$ is a reciprocal lattice vector.

Before considering how electron-electron interactions renormalise the generalised susceptibility, we first consider the so-called ‘bare’ susceptibility, $\boldsymbol{\chi}_0$, in the absence of electron correlations (i.e. $U = 0$). In a magnetic system it is helpful to consider the longitudinal/transverse components of the response relative to the axis of quantisation of the spin (conventionally taken to be z), which couples states of the same/opposite spin respectively. The diagonal components of the susceptibility tensor for a single band system

---

[6] The magnetic form-factor decays as a function of Q due to the spatial extent of the magnetic moment on each atom. In itinerant systems the conduction electrons are to some extent delocalised and the appropriate magnetic form-factor may vary from the ionic one.

are given by[20],

$$\chi_0^{xx} + \chi_0^{yy} = \frac{1}{2}(\chi_0^{\uparrow\downarrow} + \chi_0^{\downarrow\uparrow}) \tag{2.17}$$

$$\chi_0^{zz} = \chi_0^{\uparrow\uparrow} + \chi_0^{\downarrow\downarrow} \tag{2.18}$$

where for a single-band metal the susceptibility $\chi^{\sigma'\sigma}$ is given by the Lindhard function,

$$\chi_0^{\sigma'\sigma}(\boldsymbol{q}, \omega) = \mu_0 \frac{(2\mu_B)^2}{N} \lim_{\eta \to 0^+} \sum_{\boldsymbol{k}} \frac{f_{\boldsymbol{k}+\boldsymbol{q}}^{\sigma'} - f_{\boldsymbol{k}}^{\sigma}}{E_{\boldsymbol{k}+\boldsymbol{q}}^{\sigma'} - E_{\boldsymbol{k}}^{\sigma} - \hbar\omega + i\eta} \tag{2.19}$$

where $E_{\boldsymbol{k}}^{\sigma}$ and $f_{\boldsymbol{k}}^{\sigma}$ are the energy and Fermi occupancy of the band state with wavevector $\boldsymbol{k}$ and spin σ respectively. It is important to note that the susceptibility is a complex quantity - the response of the system has components in and out of phase with the perturbing field. The real and imaginary parts of the susceptibility are related by the Kramers-Kronig relations. Of particular interest is the imaginary part of the susceptibility which is the quantity measured by neutron scattering,

$$\chi_0^{\sigma'\sigma\,\prime\prime}(\boldsymbol{q}, \omega) = \pi\mu_0 \frac{(2\mu_B)^2}{N} \sum_{\boldsymbol{k}} (f_{\boldsymbol{k}+\boldsymbol{q}}^{\sigma'} - f_{\boldsymbol{k}}^{\sigma}) \delta(E_{\boldsymbol{k}+\boldsymbol{q}}^{\sigma'} - E_{\boldsymbol{k}}^{\sigma} - \hbar\omega), \tag{2.20}$$

which essentially counts the possible excitations of electron with initial state $|\boldsymbol{k}, \sigma\rangle$ to an empty state $|\boldsymbol{k} + \boldsymbol{q}, \sigma'\rangle$ with energy $\hbar\omega$. It can be seen that the transverse susceptibility involves spin-flip excitations ($\sigma \neq \sigma'$) and the longitudinal susceptibility involves non spin-flip excitations ($\sigma = \sigma'$) - full expressions for both in terms of Eq.2.19 can be found in [21, 22]. In this thesis we are only concerned with scattering from an unpolarised neutron beam where the measured intensity is an average of the spin-flip and non-spin-flip scattering, for a paramagnet this corresponds to an average susceptibility $\chi_0 = \frac{1}{3}(\chi_0^{zz} + 2\chi_0^{\uparrow\downarrow})$.

We are concerned with the instability of the paramagnetic state to magnetic order. For simplicity we consider an isotropic paramagnet in the absence of a magnetic field for which the spin-bands are degenerate. We can therefore omit the spin-indices and consider only a single susceptibility denoted by $\chi_0 = \chi_0^{\uparrow\downarrow} = 2\chi_0^{zz}$ (due to rotational invariance).

A time-dependent generalisation of the mean-field approach employed in Section 2.1, known as the Random Phase Approximation (RPA) [7] leads to a similar renormalisation

---

[7] RPA neglects cross-terms arising from spin-density oscillations with different phases (wavevectors) [23].

of the susceptibility by the Coulomb term, U, given by[21]

$$\chi(\boldsymbol{q},\omega) = \frac{\chi_0(\boldsymbol{q},\omega)}{1 - \frac{U}{(2\mu_B)^2}\chi_0(\boldsymbol{q},\omega)}. \tag{2.21}$$

In general, one can include higher order terms by having a q-dependent U, though in practice this is often neglected (for example [24]). From Eq.2.21, it can be shown that the real-part of the susceptibility at zero energy, $\chi_0'(\boldsymbol{q},0)$, diverges under the following condition [8],

$$\frac{U}{(2\mu_B)^2}\chi_0'(\boldsymbol{q},0) \geq 1, \tag{2.22}$$

a result known as the generalised Stoner criterion for a magnetically ordered groundstate with reduced wavevector $\boldsymbol{q}$. For $q = 0$ this is equivalent to the Stoner criterion for ferromagnetism.

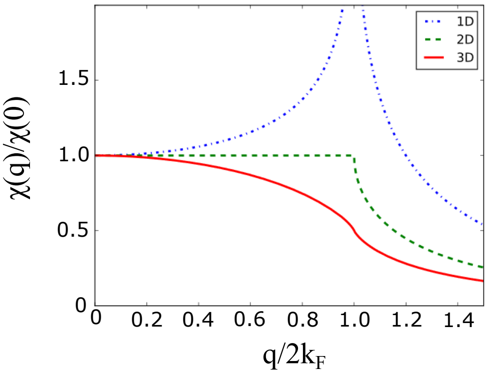

Figure 2.3: The non-interacting susceptibility of a free electron gas in one to three dimensions. The divergence is most pronounced in lower dimensionality systems. Figure taken from [25]

It can be seen that the criterion will met for a sufficiently large U and $\chi_0'(\boldsymbol{q},0)$ - the latter depends on the electronic structure at the Fermi-level. In low-dimensional systems it is common to find large portions of the Fermi-surface that can be nested by a single-wavevector, $\boldsymbol{q}$. Formally this condition is often written as $\epsilon_{\boldsymbol{k}} = -\epsilon_{\boldsymbol{k}+\boldsymbol{q}}$. In this case the denominator of $\chi_0'(\boldsymbol{q},0)$ in Eq.2.19 will diverge for many pairs of states in the Brillouin zone summation. Such nesting occurs generically in 1D systems and produces a logarithmic divergence in $\chi'(\boldsymbol{q},\omega=0)$[26]. In higher dimensions the enhancement tends to be less pronounced (see Fig.2.3). However, spin (and charge) density wave order is still very prevalent in 2D systems. Another important factor in stabilising incommensurate

---

[8] To prove this requires the knowledge that the imaginary component of the susceptibility is an odd-function of energy that is well behaved as $\omega \rightarrow 0$ and therefore $\chi''(\boldsymbol{q},0)) = 0$.

order is the presence of saddle-points in the dispersion of electronic bands producing a divergent density of states (often referred to as van Hove singularities, VHS) at the Fermi-level. We have seen that a large density of states at the Fermi level naturally increases the susceptibility to ferromagnetic order, however it has also been shown that $\chi_0'(\boldsymbol{q}, 0)$ will diverge for wavevectors that connect the VHS (shown specifically for 2D systems in [27]) [9].

Before considering the incommensurate state that is stabilised when the generalised Stoner criterion is fulfilled it should be noted that mean-field treatment of the sort detailed here have proven successful in predicting the ground state of various materials at low temperature (when the moment is saturated), however they are less accurate at larger temperatures. Typically they considerably overestimate the transition temperature (predicted to be the temperature at which the there is equality in Eq.2.22), for example in the weak ferromagnet $ZrZn_2$[28]. This is because at finite temperature it is necessary to account for the effect of spin fluctuations on the equilibrium state, in particular near the critical region. This is possible within Self-Consistent Renormalization (SCR) Theory, which adds an additional term to the denominator that is itself a function of the renormalised susceptibility, for details see [29, 22].

2.5 Spin-density waves

2.5.1 Mean-field Hamiltonian

The material in this section follows the approach and notation of the textbook by Sólyom [30], but is also influenced by [31, 32].

If the generalised Stoner criterion is met in Eq.2.22, then the groundstate will be a spin-density wave (SDW) - a periodic modulation of the spin-density with wavelength $\lambda = 2\pi/q$. The SDW ground-state can be considered in a mean-field weak-coupling framework in a similar manner to conventional BCS superconductivity. Though as expected the pairing interaction for the SDW state comes from the electron-electron interactions. To see this we return to a single-band Hubbard Hamiltonian in which the electron densities

---

[9] Counter-intuitively the authors of [27] predict that the gapping of the states at the saddle-points which have very small Fermi-velocities might actually increase the conductivity. Generically the gapping of carriers would be expected to decrease the conductivity.

are written in terms of Fourier components,

$$n_{q,\sigma} = \sum_j c_j^\dagger c_j e^{iqr_j} \tag{2.23}$$

$$= \sum_k c_{k+q,\sigma}^\dagger c_{k\sigma}. \tag{2.24}$$

where the last line used the definition of the Wannier operators and a delta function. The physical interpretation of $n_{q,\sigma}$ is the production of a singlet electron-hole pair for states separated by wavevector q on the Fermi surface [10]. We consider the case of a SDW modulation with a single q that maintains a uniform charge density such that $n_{q,\sigma} = -n_{q,\sigma'}$, where $\sigma' = -\sigma$.

The single band Hubbard Hamiltonian can be written as,

$$\mathcal{H} = \sum_{k,\sigma} \epsilon_k c_{k,\sigma}^\dagger c_{k,\sigma} + U \sum_{k,k',\sigma} c_{k+q,\sigma}^\dagger c_{k,\sigma} c_{k'-q,\sigma'}^\dagger c_{k',\sigma'}. \tag{2.25}$$

The interaction term describes the scattering of states k and k' into states $k+q$ and $k'-q$ respectively. In order to consider only the Fourier components corresponding to $+q$ we can perform a change of variables $k' \to k'+q$. We choose a similar mean-field decomposition that will produce a modulated spin-density along the z axis,

$$c_{k+q,\sigma}^\dagger c_{k,\sigma} c_{k'-q,\sigma'}^\dagger c_{k',\sigma'} \approx \langle c_{k+q,\sigma}^\dagger c_{k,\sigma} \rangle c_{k',\sigma'}^\dagger c_{k'+q,\sigma'} + c_{k+q,\sigma}^\dagger c_{k,\sigma} \langle c_{k',\sigma'}^\dagger c_{k'+q,\sigma'} \rangle - \langle c_{k+q,\sigma}^\dagger c_{k,\sigma} \rangle \langle c_{k',\sigma'}^\dagger c_{k'+q,\sigma'} \rangle. \tag{2.26}$$

From the definition of n_q and the requirement of a uniform charge distribution we can write the mean-field Hamiltonian as

$$\mathcal{H} = \sum_{k,\sigma}{}' \left(c_{k,\sigma}^\dagger, c_{k+q,\sigma}^\dagger \right) \begin{pmatrix} \epsilon_k & \sigma\Delta \\ \sigma\Delta^* & \epsilon_{k+q} \end{pmatrix} \begin{pmatrix} c_{k,\sigma} \\ c_{k+q,\sigma} \end{pmatrix} - \Delta^2, \tag{2.27}$$

where the summation is over the reduced Brillouin zone [11] and the SDW order parameter

---

[10] Recall that annihilating an electron of spin, σ is equivalent to creating a hole with spin $-\sigma$

[11] Though we will keep the labels k and $k+q$ referring to wavevectors in the extended Brillouin zone so as not to introduce too many operators. For simplicity the modulation is assumed to be commensurate, the treatment would still be valid for an incommensurate wavevector but the sum would be infinite.

is given by,

$$\Delta = U \sum_{k'} \langle c^\dagger_{k+q,\downarrow} c_{k,\downarrow} \rangle \tag{2.28}$$

$$= -\frac{U}{2} \sum_{k',\sigma} \langle S^z_q \rangle \tag{2.29}$$

where the last line assumes a uniform charge density and $S^z_q = \sum_{k',\sigma} \langle c^\dagger_{k+q,\sigma} \sigma c_{k,\sigma} \rangle$. The order parameter is therefore proportional to the amplitude of a periodic modulation of the spin-density along z,

$$\langle m^z(r) \rangle = \frac{1}{N} \sum_k \left[\langle S^z_q \rangle e^{iq\cdot r} + \langle S^z_q \rangle e^{-iq\cdot r} \right], \tag{2.30}$$

$$= \frac{2}{N} |\langle S^z_q \rangle| \cos(qr + \phi), \tag{2.31}$$

where and ϕ is the phase of the complex order parameter (contained within S^z_q) [12].

So far we have considered only the z-component of the spin moment, however the spin operator is a vector with Cartesian components,

$$S^\alpha_q = \sum_{ss'} c^\dagger_{k,s} \sigma^\alpha_{ss'} c_{k+q,s}. \tag{2.32}$$

where σ^α is the Pauli spin matrix for the Cartesian component $\alpha = [x, y, z]$ (previously we have used the notation $\sigma = \pm 1$ which are the eigenvalues of σ^z). However, the Hamiltonian must be invariant to spin-rotation. This can be made explicit by the application of Wick's theorem to decouple the interaction term into all possible creation-annihilation pairs, including those that couple operators with opposite spin (for example see [31]). The formalism remains the same, for instance one can choose and order parameter of the form $\Delta = U \sum_k \langle c^\dagger_{k+q,\uparrow} c_{k,\downarrow} \rangle$ which describes a spiral modulation in the xy plane - related to the expectation of S^+_q, where $S^\pm = S^x \pm iS^y$. The order parameter is proportional to the Fourier component of the spin-moment, which we shall see in the weak-coupling limit is governed by the BCS form self-consistent gap equation.

---

[12] Sometimes an SDW polarized along z is referred to as a superposition of charge-density waves (CDW) where the electron densities for the opposite spins oscillate out of phase.

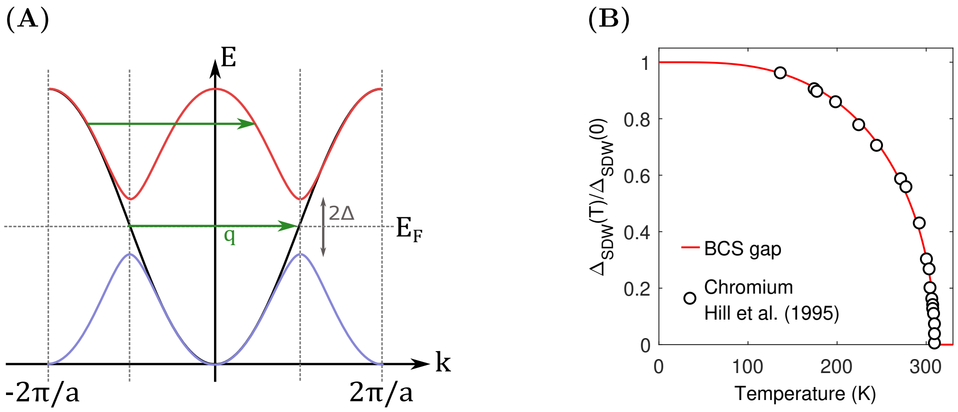

Figure 2.4: (A) Schematic of commensurate nesting of a single-band at $q = 2k_F$ producing a gap between the new quasiparticle bands (red/blue) at the new Brillouin zone boundary. The original dispersion is shown in black. (B) SDW order parameter in elemental chromium taken from [33] fitted with the interpolation formula for the temperature dependence of the BCS gap in Eq.2.40.

2.5.2 SDW order parameter

As in the BCS theory of superconductivity, the mean-field Hamiltonian can be diagonalised with a unitary (Bogoliubov) transformation to a new quasiparticle basis,

$$\begin{pmatrix} \alpha_{k,\sigma} \\ \beta_{k,\sigma} \end{pmatrix} = \begin{pmatrix} u_k & \sigma v_k \\ -\sigma v_k^* & u_k^* \end{pmatrix} \begin{pmatrix} c_{k,\sigma} \\ c_{k+q,\sigma} \end{pmatrix}, \tag{2.33}$$

where $|u_k|^2 + |v_k|^2 = 1$ [13]. The transformation produces two quasi-particle bands with dispersions,

$$E_k^{\alpha\beta} = \epsilon_k^+ \pm \sqrt{(\epsilon_k^-)^2 + \Delta^2}, \tag{2.34}$$

where $\epsilon_k^\pm = \frac{1}{2}(\epsilon_k \pm \epsilon_{k+q})$ [14]. Furthermore, the diagonalisation requires that,

$$|u_k|^2 = \frac{1}{2}\left(1 + \frac{\epsilon^-}{\sqrt{(\epsilon_k^-)^2 + \Delta^2}}\right), \tag{2.35}$$

$$|v_k|^2 = \frac{1}{2}\left(1 - \frac{\epsilon^-}{\sqrt{(\epsilon_k^-)^2 + \Delta^2}}\right). \tag{2.36}$$

The groundstate is then a product sum of the occupied quasiparticle states (in the

---

[13] From the definition of a unitary matrix.

[14] The chemical potential is omitted for clarity - in general it will need to be determined self-consistently post reconstruction of the Fermi surface.

lower band),

$$\Psi_{SDW} = \prod_{k<k_F\sigma} \alpha_k^\dagger |0\rangle \tag{2.37}$$

$$= \prod_{k<k_F\sigma} \left(u_k c_{k,\sigma}^\dagger + \sigma v_k c_{k+q,\sigma}^\dagger\right) |0\rangle \tag{2.38}$$

where k_F is the Fermi wavevector (in the reduced/extended Brillouin zone in the top/bottom line) and $|0\rangle$ is the vacuum state. The new quasiparticle bands, $E_k^{\alpha\beta}$, are gapped by an amount $2|\Delta|$ (as illustrated in Fig.2.4A). Evaluating the order parameter with the SDW groundstate gives a self-consistent equation,

$$|\Delta| = \frac{U}{2} \sum_k \frac{|\Delta|}{\sqrt{(\epsilon_k^-)^2 + \Delta^2}} \left[f(E_k^\alpha, T) - f(E_k^\beta, T)\right] \tag{2.39}$$

where the temperature dependence comes from the Fermi function $f(E,T)$ occupancy.

In the weak coupling limit ($Ug(\epsilon_F) << 1$), the SDW gap equation follow the same BCS form as an s-wave superconductor. This has been experimentally verified in many well-nested SDW ordered metals, most notably in chromium[34, 35]. Fig.2.4B shows the magnitude of the SDW order parameter $|\Delta(T)|$ (proportional to the staggered moment) fitted with an interpolation formula for the temperature dependence of the BCS order parameter [36],

$$|\Delta(T)| = |\Delta(0)| \tanh\left(1.7365\sqrt{\frac{T_\mathrm{N}}{T} - 1}\right) \tag{2.40}$$

where T_N is the transition temperature.

Chapter 3

Neutron Scattering

This chapter provides a brief introduction to the theory and practicalities of unpolarised neutron scattering, with a particular emphasis on the coherent scattering cross-sections in the Born approximation. The chapter concludes with an overview of the instrumentation during the various experiments that contributed to this thesis and the various corrections to the diffraction data that may be relevant to the analysis. The approach taken in this chapter is based on two particular textbooks [20, 37], but there exist many other resources on the topic (e.g. [38, 39, 40]).

3.1 Neutrons as a probe of condensed matter

Neutron scattering provides a unique means of studying the static and dynamic properties of condensed matter systems. Neutrons can be produced with wavelengths comparable to interatomic spacing and kinetic energy comparable to excitations such as phonons and magnons that are of interest. Neutrons have no charge and can interact with the atomic nuclei via the strong force. As the neutron has a magnetic dipole moment (it is a spin-1/2 particle) it can also probe the magnetism of a system - interacting with the local magnetic flux density due to the nuclear spin and the orbital and spin momentum of unpaired elections in the sample. Both these interactions are fairly weak compared to other scattering probes (e.g x-rays or electrons), and as a result neutrons are highly penetrating. This provides two advantages: firstly the neutrons scatter from the bulk of the sample and are not sensitive to surface effects, secondly we can treat the scattering in the Born-approximation which greatly simplifies the quantitative analysis of the neutron scattering cross-section. The disadvantage is that neutron scattering (particularly inelastic neutron scattering) requires larger samples, and often long counting times relative to other probes.

3.2 Scattering formalism

3.2.1 Scattering basics

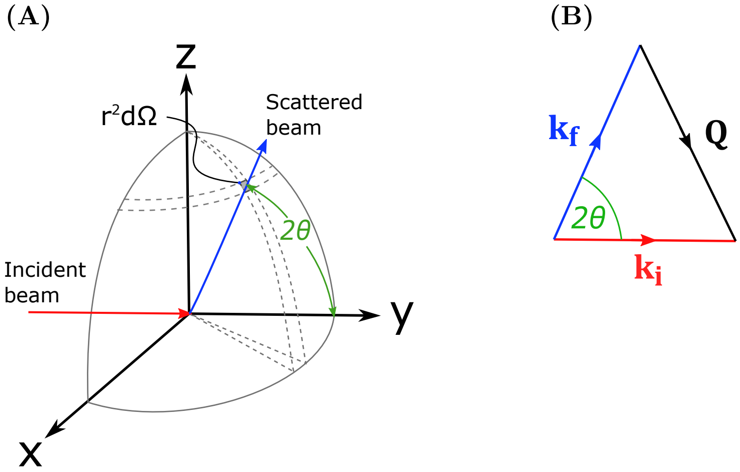

Figure 3.1: (A)Geometry of a scattering experiment. Neutrons incident on a sample (wavevector $\boldsymbol{k_i}$) are scattered into a solid angle $\boldsymbol{d\Omega}$ along the direction $\boldsymbol{k_f}$. (B) Schematic of the scattering triangle to illustrate the momentum transfer $\boldsymbol{Q} = \boldsymbol{k_i} - \boldsymbol{k_f}$.

We consider a particle incident on a sample with initial momentum $\boldsymbol{k_i}$ and energy E_i that is scattered with final momentum $\boldsymbol{k_f}$ and energy E_f. The momentum and energy transfer during the scattering process are defined as,

$$\boldsymbol{Q} = \boldsymbol{k_i} - \boldsymbol{k_f}, \tag{3.1}$$

$$\hbar\omega = E_i - E_f, \tag{3.2}$$

such that $\omega > 0$ corresponds to the neutron losing energy to the sample, producing an excitation such as a phonon. The angle between the initial and final neutron momentum is referred to as 2θ (see Fig.3.1). Any scattering event must conserve energy, momentum and spin.

The momentum transfer $\boldsymbol{Q}$, is a vector in reciprocal space and can be written in the basis of the reciprocal lattice basis vectors $\boldsymbol{a}^*$,$\boldsymbol{b}^*$ and $\boldsymbol{c}^*$,

$$\boldsymbol{Q} = h\boldsymbol{a}^* + k\boldsymbol{b}^* + l\boldsymbol{c}^*. \tag{3.3}$$

The indices h, k, and l are often referred to as the Miller indices, which correspond to the inverse of the fractional intercept of the scattering planes along the three real-space lattice vectors of the unit cell ($\boldsymbol{a}$,$\boldsymbol{b}$ and $\boldsymbol{c}$). The reciprocal lattice points at integer h, k, l are denoted by $\boldsymbol{G}$, which is a vector oriented normal to the scattering planes with a magnitude $|\boldsymbol{G}| = 2\pi/d$, where d is the separation between the planes in direct-space [1].

3.2.2 Definition of the cross-section

The sample attenuates the incident particle beam by two processes: absorption and scattering. Here we only consider the number of scattering events per second, J, which is proportional to the incident flux, Φ (number of particles per unit time and area),

$$J = \sigma\Phi, \tag{3.4}$$

where σ is the total cross-section which has units of area. In a scattering experiment a detector measures the count rate of scattered particles into a small solid angle $d\Omega$, in the direction given by two angles θ and ϕ. If the final energy of the particle can be discriminated, then the experimentally measured quantity is actually the partial differential cross-section,

$$\frac{\mathrm{d}^2\sigma}{\mathrm{d}\Omega \mathrm{d}E_f} = \frac{\begin{pmatrix}\text{number of neutrons scattered per second in solid angle } \mathrm{d}\Omega \\ \text{in the direction } (\theta,\, \phi) \text{ with final energy between } E_f \text{ and } E + \mathrm{d}E_f\end{pmatrix}}{\mathrm{d}\Omega \mathrm{d}E_f}. \tag{3.5}$$

Which incorporates all the angular and energy dependence of the scattering from the sample. The total cross-section is then,

$$\sigma = \int_0^\infty \int_0^{4\pi} \frac{\mathrm{d}^2\sigma}{\mathrm{d}\Omega \mathrm{d}E_f} d\Omega dE_f \tag{3.6}$$

3.2.3 The master formula for the scattering cross-section

If we assume that the interaction between the sample and neutron is only a small perturbation to the whole system, then an expression for the partial differential cross-section can be derived using the golden rule of first-order perturbation theory - which is equivalent to the Born approximation. This approximation neglects multiple scattering and allows for the incident and scattered neutron far from the scattering site to be described by plane waves.

---

[1] The reciprocal lattice is the Fourier transform of the direct lattice. The direct-space lattice points, $\boldsymbol{l} = l_1\boldsymbol{a} + l_2\boldsymbol{b} + l_3\boldsymbol{c}$ and reciprocal lattice points, $\boldsymbol{G}$ obey the relation $\exp(i\boldsymbol{G} \cdot \boldsymbol{l}) = 1$.

Without the interaction (i.e. before scattering) the system (sample and neutron) is in the eigenstate $|\boldsymbol{k_i}, \sigma_i, n_i\rangle$, where the neutron has an initial wavevector $\boldsymbol{k_i}$ and spin, σ, and the sample is in a state labelled n_i. As we do not measure the initial or final state of the sample, we are interested in the probability per second for the neutron to scatter from initial state $|\boldsymbol{k_i}, \sigma_i\rangle$ to final state $|\boldsymbol{k_f}, \sigma_f\rangle$ which is given by,

$$W_{k_i,\sigma_i \to k_f,\sigma_f} = \frac{2\pi}{\hbar} \sum_{n_i,\sigma_i} p(n_i) p(\sigma_i) \sum_{n_f} |\langle \boldsymbol{k_f}, \sigma_f, n_f | V | \boldsymbol{k_i}, \sigma_i, n_i \rangle|^2 \, \delta\left(E_f - E_i - \hbar\omega\right), \tag{3.7}$$

where V is the neutron-sample interaction potential, $p(\sigma_i)$ is the probability that the incident neutron has initial spin σ_i (for unpolarised neutrons $\sigma_i = 1/2$) and $p(n_i)$ is the probability that the sample is in the initial state labelled n_i, given by the Boltzman distribution,

$$p(n_i) = e^{-E_{n_i}/k_B T} / \sum_{n_i} e^{-E_{n_i}/k_B T}. \tag{3.8}$$

and the δ function ensures the conservation of energy.

The number of neutrons scattered per second in the direction of $\boldsymbol{k_f}$ with final wavevector between k_f and $k_f + dk_f$ into a solid angle $d\Omega$, depends on the number of final states available and is given by

$$J = W_{k_i,\sigma_i \to k_f,\sigma_f} \frac{V_0}{(2\pi)^3} k_f^2 \mathrm{d}k_f \mathrm{d}\Omega, \tag{3.9}$$

where V_0 is the sample volume. Writing the incident flux of the neutrons in terms of the initial wavevector,

$$\Phi = \frac{\hbar k_0}{V_0 m_n}, \tag{3.10}$$

where m_n is the mass of the neutron, and using Eq.3.4 the expression for the partial differential cross-section becomes,

$$\frac{\mathrm{d}^2\sigma}{\mathrm{d}\Omega \mathrm{d}E_f} = \left(\frac{m}{2\pi\hbar^2}\right)^2 \frac{k_f}{k_i} \sum_{n_i,\sigma_i} p(n_i) p(\sigma_i) \sum_{n_f} |\langle \boldsymbol{k_f}, \sigma_f, n_f | V(\boldsymbol{r}) | \boldsymbol{k_i}, \sigma_i, n_i \rangle|^2 \, \delta\left(E_f - E_i - \hbar\omega\right). \tag{3.11}$$

In the Born approximation we can treat the incoming and outgoing states as plane waves, $|\boldsymbol{k}, \sigma\rangle = e^{i\boldsymbol{k}\cdot\boldsymbol{r}} |\sigma\rangle$ [2]. Performing the integration over the neutron position, $\boldsymbol{r}$, it can be shown that the matrix elements in Eq.3.11 are related to the Fourier transform of the

---

[2] Technically the scattered wave is spherical, however far from the scatterer the curvature of the wavefront is negligible.

scattering potential, $V(\boldsymbol{Q})$,

$$\langle \boldsymbol{k_f}, \sigma_f, n_f | V(\boldsymbol{r}) | \boldsymbol{k_i}, \sigma_i, n_i \rangle = \langle \sigma_f, n_f | V(\boldsymbol{Q}) | \sigma_i, n_i \rangle \,, \tag{3.12}$$

where $V(\boldsymbol{Q})$ is given by,

$$V(\boldsymbol{Q}) = \int V(\boldsymbol{r}) e^{i\boldsymbol{Q}\cdot(\boldsymbol{r})} d\boldsymbol{r}. \tag{3.13}$$

Combining these results produces the ‘master’ equation for the partial differential cross-section,

$$\frac{\mathrm{d}^2\sigma}{\mathrm{d}\Omega \mathrm{d}E_f} = \left(\frac{m}{2\pi\hbar^2}\right)^2 \frac{k_f}{k_i} \sum_{n_i,\sigma_i} p(n_i)p(\sigma_i) \sum_{n_f} |\langle \sigma_f, n_f | V(\boldsymbol{Q}) | \sigma_i, n_i \rangle|^2 \, \delta\left(E_f - E_i - \hbar\omega\right). \tag{3.14}$$

It is often convenient to write the cross-section as so,

$$\frac{\mathrm{d}^2\sigma}{\mathrm{d}\Omega \mathrm{d}E_f} = \frac{k_f}{k_i} S(\boldsymbol{Q}, \omega), \tag{3.15}$$

where $S(\boldsymbol{Q}, \omega)$ is the *scattering function* that relates only to the neutron-sample interaction and the pre-factor relates only to the experimental setup.

A scattered neutron can lose or gain energy and momentum and the relative likelihood of those two scenarios is governed by the probability of the system being in an initially excited state. At a given temperature, the probability of state of energy $\hbar\omega$ being initially excited will be lower by a factor $e^{-\hbar\omega/k_B T}$ (due to Boltzman statistics). The scattering function for unpolarised neutrons then follows the relation,

$$S(-\boldsymbol{Q}, -\omega)_{\sigma_f \to \sigma_i} = e^{-\hbar\omega/k_B T} S(\boldsymbol{Q}, \omega)_{\sigma_i \to \sigma_f}, \tag{3.16}$$

known as the *principle of detailed balance* [3]. At zero temperature no quasiparticles are excited and a neutron can only scatter inelastically by losing energy to the sample (creating an excitation). For the majority of systems, the symmetry of the crystal also dictates that $S(\boldsymbol{Q}, \omega) = S(-\boldsymbol{Q}, \omega)$.

3.2.4 Scattering function and correlations

Before describing the scattering potential, $V(\boldsymbol{Q})$ for nuclear and magnetic scattering, we first consider the physical meaning of the scattering function, $S(\boldsymbol{Q}, \omega)$ and how this

---

[3] Eq.3.16 relates the scattering of inverse processes - for polarised neutrons this also includes the initial and final spin state of the neutron if the potential is spin-dependent.

is related to observables of the system. As the potential is Hermitian, the term in the summation of Eq.3.14 can be written as,

$$|\langle\sigma_f, n_f|V(\boldsymbol{Q})|\sigma_i, n_i\rangle|^2\,\delta(E_f - E_i - \hbar\omega) = \\ \frac{1}{2\pi\hbar}\int_{-\infty}^{\infty}\langle i|V^\dagger|f\rangle\,\langle f|V|i\rangle\exp[i(E_f - E_i)t/\hbar]\exp(-i\omega t)dt, \quad (3.17)$$

where $\langle f|V|i\rangle = \langle\sigma_f, n_f|V(\boldsymbol{Q})|\sigma_i, n_i\rangle$ and the δ-function representing energy conservation has been written in integral form. The term $\exp[i(E_f - E_i)t\hbar]$ can be incorporated into the time-dependence of the potential operator [4]. The final states $|f\rangle$ form a complete basis set and via the closure relationship the sum over final states in Eq.3.14 simplifies to give,

$$S(\boldsymbol{Q}, \omega) = \frac{1}{2\pi\hbar}\left(\frac{m}{2\pi\hbar^2}\right)^2\int_{-\infty}^{\infty}\langle V^\dagger(0)V(t)\rangle\exp(-i\omega t)dt, \quad (3.18)$$

where the angle brackets $\langle ...\rangle$ denote the average over the initial states given by,

$$\langle V^\dagger(0)V(t)\rangle = \sum_{n_i}\sum_{\sigma_i}p(n_i)p(\sigma_i)\,\langle\sigma_f, n_f|V^\dagger(\boldsymbol{Q},\boldsymbol{0})V(\boldsymbol{Q},\boldsymbol{t})|\sigma_i, n_i\rangle\,. \quad (3.19)$$

The scattering function is then related to the time Fourier transform of the correlation function $\langle V^\dagger(0)V(t)\rangle$ (so called because it measures the correlation between the observable at time t and $t = 0$). The principle of detailed balance can be derived from the properties of correlation functions (see [20]).

From Eq.3.18 and the definition of a δ-function, the energy integrated structure factor follows the sum rule,

$$S(\boldsymbol{Q}) = \int_{-\infty}^{\infty}S(\boldsymbol{Q})d\omega = \left(\frac{m}{2\pi\hbar^2}\right)^2\langle|V(0)|^2\rangle, \quad (3.20)$$

where $\langle|V(0)|^2\rangle$ is referred to as the instantaneous correlation function - the correlations at a snapshot in time (which for a system in thermal equilibrium is also constant in time) [5].

Due to dissipation, time-dependent (dynamic) correlations will tend to zero as $t \to \infty$ such that $\langle V(\infty)\rangle = \langle V(0)\rangle$. The remaining static correlations (of the average structure) is then of the form,

$$\langle\langle V(0)^\dagger\rangle\langle V(\infty)\rangle\rangle = |\langle V(0)\rangle|^2. \quad (3.21)$$

---

[4] In the Heisenberg picture of quantum mechanics an operator corresponding to a physical observable has a time-dependence given by $A(t) = \exp(i\mathcal{H}t/\hbar)A(0)\exp(-i\mathcal{H}t/\hbar)$ where $\mathcal{H}$ is the Hamiltonian of the system. The energies are eigenvalues of the Hamiltonian such that $\mathcal{H}\,|i\rangle = E_i\,|i\rangle$

[5] For a system in thermal equilibrium $\langle|V(0)|^2\rangle = \langle|V(t)|^2\rangle$

It is the static correlations that are measured by elastic scattering. The dynamic correlations are measured by inelastic response, $\tilde{S}(\boldsymbol{Q},\omega)$, which is given by the difference between Eq.3.18 and Eq.3.21,

$$\tilde{S}(\boldsymbol{Q},\omega) = S(\boldsymbol{Q},\omega) - \left(\frac{m}{2\pi\hbar^2}\right)^2 |\langle V(0)\rangle|^2 \delta(\hbar\omega). \tag{3.22}$$

The dynamic response, $\tilde{S}(\boldsymbol{Q},\omega)$, is related to the imaginary part of the generalized susceptibility, $\chi''(\boldsymbol{Q},\omega)$ (charge and magnetic) by the fluctuation-dissipation theorem,

$$\tilde{S}(\boldsymbol{Q},\omega) = [1 + n(\omega)]\frac{1}{\pi}\chi''(\boldsymbol{Q},\omega), \tag{3.23}$$

where the Bose factor, $n(\omega)$, describes the thermal population of the excitations, and is given by,

$$n(\omega) = \frac{1}{\exp(\hbar\omega/k_B T) - 1}. \tag{3.24}$$

which provides an equivalent formulation that is particularly illustrative when considering inelastic magnetic scattering. From the Kramers-Kronig relation between the real and imaginary part of the susceptibility it is possible to write the so-called bulk or uniform susceptibility (that for magnetic scattering would correspond to the quantity measured in a SQUID) to the integrated dynamic response,

$$\chi'(0,0) = \frac{1}{\pi}\int_{-\infty}^{\infty} \frac{\tilde{S}(0,\omega)}{\omega}\left[1 - \exp(\hbar\omega/k_B T)\right] d\omega. \tag{3.25}$$

3.3 Nuclear scattering

The interaction between the nucleus and the neutron due to the strong force is very short-range (about 10^{-5} smaller than the wavelength of thermal neutrons), and can be approximated by the Fermi pseudopotential which takes the form,

$$V_N(\boldsymbol{r}) = \frac{2\pi\hbar^2}{m}\sum_j b_j \delta(\boldsymbol{r} - \boldsymbol{r}_j) \tag{3.26}$$

where $\boldsymbol{r}_j$ and b_j are the position and scattering length of the nucleus at site j. For a single nucleus this corresponds to isotropic scattering with cross-section, $\sigma = 4\pi b^2$. The Fourier transform of Eq.3.26 is

$$V_N(\boldsymbol{Q}) = \frac{2\pi\hbar^2}{m}\sum_j b_j e^{i\boldsymbol{Q}\cdot\boldsymbol{r}_j} \tag{3.27}$$

It should be emphasised that the scattering length is then an experimentally determined quantity such that the observed isotropic scattering far from a single fixed nucleus of a given isotope is recovered in the Born approximation. The scattering length depends on the nuclear isotope, and the component of the nuclear spin along the axis of the neutron spin. It can be considered to be a complex number, with the imaginary part related to the absorption cross-section - however for simplicity we will assume it is real and consider absorption separately.

As the force between any two nuclei is independent of the scattering length the correlations in the scattering length and nuclei positions can be considered independently. Substituting Eq.3.27 into Eq.3.18 for the scattering function in terms of the correlation function gives,

$$S(\boldsymbol{Q},\omega) = \frac{1}{2\pi\hbar}\sum_{n_i} p(n_i) \sum_{jk} \langle b_j b_k \rangle \int_{-\infty}^{\infty} \langle \exp(-i\boldsymbol{Q}\cdot\boldsymbol{r_j}(0)) \exp(i\boldsymbol{Q}\cdot\boldsymbol{r_k}(t)) \rangle \exp(-i\omega t) dt. \tag{3.28}$$

Because the scattering lengths are uncorrelated $\langle b_j b_k \rangle = \langle b \rangle^2$ for $i \neq j$ and $\langle b^2 \rangle$ for $j = k$. Note that $\langle b_k \rangle$ implicitly performs a weighted average over the isotopes of the atom at site k and all possible combinations of nuclear and neutron spin states. The sum over the pairs of atoms can be separated into two terms, a coherent term that involves scattering from all pairs of nuclei with an average scattering length with cross-section,

$$S(\boldsymbol{Q},\omega)_{coh} = \frac{1}{2\pi\hbar}\sum_{jk} \langle b_j \rangle \langle b_k \rangle \int_{-\infty}^{\infty} \langle \exp(-i\boldsymbol{Q}\cdot\boldsymbol{r_j}(0)) \exp(i\boldsymbol{Q}\cdot\boldsymbol{r_k}(t)) \rangle \exp(-i\omega t) dt, \tag{3.29}$$

and an incoherent term due to the variance in scattering lengths with cross-section, $\sigma_{inc} = 4\pi(\langle b^2 \rangle - \langle b \rangle^2)$ (which essentially corrects for the double counting of the nuclei with itself in the sum in Eq.3.29),

$$S(\boldsymbol{Q},\omega)_{inc} = \frac{1}{2\pi\hbar}\frac{\sigma_{inc}}{4\pi}\sum_{j} \int_{-\infty}^{\infty} \langle \exp(-i\boldsymbol{Q}\cdot\boldsymbol{r_j}(0)) \exp(i\boldsymbol{Q}\cdot\boldsymbol{r_j}(t)) \rangle \exp(-i\omega t) dt. \tag{3.30}$$

The incoherent scattering measures the self-correlation of the same nuclei at different times (e.g. diffusion) which produces an isotropic, $\boldsymbol{Q}$ independent background. The coherent scattering depends on correlations between different nuclei at different times which through interference effects yields information about the relative atomic positions and therefore the structure and collective dynamics. Hereafter the focus is on coherent scattering.

The position of the nucleus at a given time in a crystalline material can be written as,

$$\boldsymbol{r}(t) = \boldsymbol{l} + \boldsymbol{d} + \boldsymbol{u}_{ld}(t) \tag{3.31}$$

where $\boldsymbol{l}$ is the position of a lattice point, $\boldsymbol{d}$ is the position of the nucleus within the unit-cell and $\boldsymbol{u}_{ld}$ is the displacement from the average position within the unit-cell, which is the sum over a set of quantised normal modes, s, of the form,

$$\boldsymbol{u}_{\boldsymbol{ld}}(t) = \frac{1}{\sqrt{Nm_d}} \sum_s \boldsymbol{e}_{ds} \exp(i\boldsymbol{q} \cdot \boldsymbol{l}) \left[a_s^\dagger \exp(i\omega_s t)) + a_s \exp(-i\omega_s t))\right] \tag{3.32}$$

where m_d is the mass of the nucleus at (average) position $\boldsymbol{d}$ in the unit-cell, $\boldsymbol{e_{ds}}$ is the eigenvector/polarisation of the displacement of mode s, $a_s^\dagger$ is the creation operator and ω_s is the energy of the excitation (phonon). The wavevector of the phonon is a vector in the first Brillouin zone, $\boldsymbol{q} = \boldsymbol{Q} - \boldsymbol{G}$, a consequence of the fact that the normal mode is periodic in reciprocal space.

The sum over all atom pairs in Eq.3.29 decomposes into a sum over all pairs of lattice points (which is equivalent to N sums over the lattice points, where N is the number of lattice points) and all pairs of atoms in the unit cell. Substituting Eq.3.31 into Eq.3.29 then gives,

$$\begin{aligned} S(\boldsymbol{Q}, \omega)_{coh} = \frac{N}{2\pi\hbar} \sum_{\boldsymbol{l}} \exp(i\boldsymbol{Q} \cdot \boldsymbol{l}) \sum_{\boldsymbol{d},\boldsymbol{d'}} \langle b_d \rangle \langle b_{d'} \rangle \exp(i\boldsymbol{Q} \cdot \boldsymbol{(d - d')}) \\ \int_{-\infty}^{\infty} \langle \exp(P) \exp(D) \rangle \exp(-i\omega t) dt, \end{aligned} \tag{3.33}$$

where,

$$U = -i\boldsymbol{Q} \cdot \boldsymbol{u}_{\boldsymbol{ld'}}(0), \tag{3.34}$$

$$P = i\boldsymbol{Q} \cdot \boldsymbol{u}_{\boldsymbol{ld}}(t). \tag{3.35}$$

For a harmonic potential, the normal modes produce a displacement with a Gaussian probability distribution, hence it can be shown that,

$$\langle \exp(U) \exp(P) \rangle = \exp(U^2) \exp(\langle UP \rangle). \tag{3.36}$$

The last term can be expanded in the power series

$$\exp\langle UP \rangle = 1 + \langle UP \rangle + \frac{1}{2!} \langle UP \rangle^2 + ... + \frac{1}{n!} \langle UP \rangle^n \tag{3.37}$$

where the n^{th} term corresponds to scattering from a n-phonon process. Here we consider only the elastic scattering $\exp\langle UP\rangle = 1$.

3.3.1 Coherent elastic nuclear scattering

Elastic scattering corresponds to setting $\exp(\langle UP\rangle) = 1$ in Eq.3.33 (the $n = 0$ term of the expansion in Eq.3.37). The energy integral becomes a δ-function at $\omega = 0$ (and hence $k_i = k_f$). The sum over the lattice points can also be re-written as a δ-function,

$$\sum_{\boldsymbol{l}} \exp(i\boldsymbol{Q}\cdot\boldsymbol{l}) = \frac{(2\pi)^3}{v_0}\sum_{\boldsymbol{G}}\delta(\boldsymbol{Q}-\boldsymbol{G}), \tag{3.38}$$

where v_0 is the volume of the unit cell and $\boldsymbol{G}$ is a reciprocal lattice vector - oriented normal to the diffracting planes with magnitude $|\boldsymbol{G}| = 2\pi/d$, where d is the separation between the planes.

Together the final scattering function for the coherent elastic scattering is

$$S(\boldsymbol{Q},\omega=0) = N\frac{(2\pi)^3}{v_0}\sum_{\boldsymbol{G}}|F_N(\boldsymbol{Q})|^2\,\delta(\boldsymbol{Q}-\boldsymbol{G}), \tag{3.39}$$

where $F_N(\boldsymbol{Q})$ is the nuclear structure factor given by,

$$F_N(\boldsymbol{Q}) = \sum_{\boldsymbol{d}}\langle b_d\rangle\exp(i\boldsymbol{Q}\cdot\boldsymbol{r}_d)\exp(-W_d(\boldsymbol{Q})). \tag{3.40}$$

with the Debye-Waller factor, $W_d(\boldsymbol{Q})$, given by,

$$W_d(\boldsymbol{Q}) = \frac{1}{2}\langle(\boldsymbol{Q}\cdot\boldsymbol{u}_{ld})^2\rangle. \tag{3.41}$$

The important results are that coherent elastic scattering (as Bragg peaks) occur when

$$\boldsymbol{k_i} - \boldsymbol{k_f} = \boldsymbol{G}, \tag{3.42}$$

which is an equivalent condition to the familiar Bragg's Law for diffraction,

$$\lambda = 2d\sin(\theta). \tag{3.43}$$

The nuclear structure factor, F_N, depends on the sum of the phases from the average position of every atom in the unit-cell, weighted by the average scattering length of the species. The effect of thermal motion is to reduce the intensity of the Bragg peak by a factor that depends on the mean-squared displacement parallel to $\boldsymbol{Q}$.

The mean-squared displacement can be described by a matrix that defines a three-dimensional Gaussian distribution - a constant probability surface of this distribution is in general an ellipsoid. The elements of this matrix are referred to as the anisotropic displacement parameters (ADP), which can be refined from diffraction data with a sufficient number of reflections. For data at low temperature and a limited number of reflections it is common to constrain the displacement to be isotropic (a sphere) defined by a matrix with diagonal elements, $U_{iso} = \frac{1}{3}\langle \boldsymbol{u}_{ld}^2 \rangle$.

3.4 Magnetic scattering

The neutron has a magnetic moment given by,

$$\boldsymbol{\mu}_N = -2\gamma\mu_N \boldsymbol{s}_N, \tag{3.44}$$

where μ_N is the nuclear magneton, γ is the gyromagnetic ratio (≈ 1.91) and the spin operator $\boldsymbol{s} = \pm\frac{1}{2}$ for spin up/down respectively. The neutron spin interacts with the magnetic dipole field in the sample due to the spin and orbital momentum of unpaired electrons. The strength of this interaction is weaker than that of the strong nuclear force. It also acts over a larger range and therefore it is not possible to use a pseudo-potential of the form of Eq.3.26.

The interaction potential is direct-space is given by,

$$V_M(\boldsymbol{r}) = -\boldsymbol{\mu}_N \cdot \boldsymbol{B}(\boldsymbol{r}), \tag{3.45}$$

where the magnetic flux density, $\boldsymbol{B}(\boldsymbol{r})$, at position $\mathbf{r}$ from an electron is given by,

$$\mathbf{B}(\mathbf{r}) = -\frac{2\mu_0\mu_B}{4\pi}\left\{\nabla \times \left(\frac{\mathbf{s}\times\mathbf{r}}{r^3}\right) + \frac{1}{\hbar}\left(\frac{\mathbf{p}\times\mathbf{r}}{r^3}\right)\right\}.,\tag{3.46}$$

where $\mathbf{s}$ and $\mathbf{p}$ are the spin and momentum of an electron. It can be shown that the Fourier transform of the interaction potential is related to the sample magnetisation,

$$V_M(\mathbf{Q}) = \left(\frac{2\pi\hbar^2}{m_\mathrm{n}}\right)\left(\frac{\gamma r_\mathrm{e}}{g\mu_\mathrm{B}}\right)\boldsymbol{s}_N \cdot \left\{\hat{\mathbf{Q}} \times \left(\mathbf{M}(\mathbf{Q}) \times \hat{\mathbf{Q}}\right)\right\}, \tag{3.47}$$

where $r_\mathrm{e} = \mu_0 e^2/4\pi m_e$ is the classical radius of the electron and $g \approx 2$ is the Landé g-factor.

The term $\mathbf{M}(\mathbf{Q})$ is the Fourier transform of the real space magnetisation, $\mathbf{M}(\mathbf{r})$, defined as

$$\mathbf{M}(\mathbf{Q}) = \int \mathbf{M}(\mathbf{r}) \exp(i\mathbf{Q} \cdot \mathbf{r}) \mathrm{d}\mathbf{r}. \tag{3.48}$$

From Eq.3.47 it can be seen that the interaction potential depends only on the component of $\mathbf{M}(\mathbf{Q})$ perpendicular to the scattering vector,

$$\mathbf{M}_{\perp}(\mathbf{Q}) = \hat{\mathbf{Q}} \times \left(\mathbf{M}(\mathbf{Q}) \times \hat{\mathbf{Q}}\right) \tag{3.49}$$

$$= \mathbf{M}(\mathbf{Q}) - \mathbf{M}(\mathbf{Q}) \cdot \hat{\mathbf{Q}}. \tag{3.50}$$

The magnitude of which can be written as

$$|\mathbf{M}_{\perp}(\mathbf{Q})|^2 = \sum_{\alpha\beta} (\delta_{\alpha\beta} - \hat{Q}_{\alpha}\hat{Q}_{\beta}) M_{\alpha}^{\dagger} M_{\beta}, \tag{3.51}$$

where α, β denote the Cartesian axes x, y, z.

The neutron spin-operator acts only on the spin part of the wavefunction and therefore the matrix elements can be written as,

$$\langle \sigma_f, n_f | \boldsymbol{s}_N \cdot \boldsymbol{M}_{\perp}(\boldsymbol{Q}) | \sigma_i, n_i \rangle = \langle \sigma_f | \boldsymbol{s}_N | \sigma_i \rangle \cdot \langle n_f | \boldsymbol{M}_{\perp}(\boldsymbol{Q}) | n_i \rangle . \tag{3.52}$$

For unpolarised neutron scattering the spin matrix elements are averaged over all possible incident and final spin states, and the scattering function is then,

$$S(\boldsymbol{Q}, \omega) = \left(\frac{\gamma r_{\mathrm{e}}}{g\mu_{\mathrm{B}}}\right)^2 \frac{1}{2\pi\hbar} \langle \boldsymbol{M}_{\perp}^{\dagger}(\boldsymbol{Q}, \boldsymbol{0}) \boldsymbol{M}_{\perp}(\boldsymbol{Q}, \boldsymbol{t}) \rangle \exp(-i\omega t) dt. \tag{3.53}$$

3.4.1 Coherent elastic magnetic scattering

The elastic scattering measures the static correlations and therefore from Eq.3.21 we can write,

$$S(\boldsymbol{Q}, \omega = 0) = \left(\frac{\gamma r_{\mathrm{e}}}{g\mu_{\mathrm{B}}}\right)^2 \frac{1}{2\pi\hbar} \left|\langle \boldsymbol{M}_{\perp}(\boldsymbol{Q}) \rangle\right|^2 . \tag{3.54}$$

This makes it clear that the magnetic Bragg peak intensity is proportional to the average of the Fourier component of the moment $M_{\perp}(\boldsymbol{Q})$ squared. To evaluate Eq.3.54 we assume that the magnetisation is sufficiently localised to be associated with specific ions in the unit cell to be written in the form,

$$\boldsymbol{M}(\boldsymbol{r}) = \sum_{j} \boldsymbol{M}_j(\boldsymbol{r} - \boldsymbol{r}_j). \tag{3.55}$$

Therefore the Fourier transform of the magnetisation is given by,

$$\boldsymbol{M(Q)} = \sum_{j} \boldsymbol{M_j(Q)} \exp(i\boldsymbol{Q} \cdot \boldsymbol{r_j}). \tag{3.56}$$

In the dipole approximation, the magnetisation of a single ion $\boldsymbol{M_j(Q)}$ is dominated by the dipole moment. For $3/4d$ electrons the orbital momentum is typically quenched in the crystal electric field so the dipole moment is equal to the total spin moment. The magnetisation is then of the form,

$$\boldsymbol{M_j(Q)} \approx f(\boldsymbol{Q})\boldsymbol{\mu_j}, \tag{3.57}$$

where the magnitude of the dipole moment of the ion $|\boldsymbol{\mu_j}| = -g\mu_B S$, where S is the total spin moment ($g \approx 2$ for a spin-only moment). $f(\boldsymbol{Q})$ is the form-factor which is the Fourier transform of the spin density (typically the square of the radial wavefunction of the orbital in which the unpaired electron resides) [6]. It is a decaying function of Q (which for a spin-only moment is typically assumed to be isotropic, $f(Q)$) that arises due to the long-range nature of the magnetic interaction. The form-factor has been approximated with an analytical expression with tabulated coefficients that can be found in [41].

From Eq.3.56 it can be seen that the scattering function will involve a sum over pairs of ions. As in the treatment of nuclear scattering in Section 3.3, this can be decomposed into a summation of the lattice vectors and a sum over the relative phase differences between ions in the magnetic unit cell (which can be different from the nuclear). The scattering function can then be written as,

$$S(\boldsymbol{Q}, \omega = 0) = (\gamma r_{\mathrm{e}})^2 N \frac{(2\pi)^3}{v_0} \sum_{\boldsymbol{G}_M} |\boldsymbol{F_{M_\perp}(Q)}|^2 \, \delta(\boldsymbol{Q} - \boldsymbol{G}_M), \tag{3.58}$$

where $\boldsymbol{G_M}$ is a reciprocal lattice vector of the magnetic unit cell, $f(Q)$ is the magnetic form-factor (which accounts for the spatial extent of the moment on an ion - discussed in more detail later) and $\boldsymbol{F_{M_\perp}(Q)}$ is given by,

$$\boldsymbol{F_{M_\perp}(Q)} = \hat{\mathrm{Q}} \times \left(\boldsymbol{F_M(Q)} \times \hat{\mathrm{Q}}\right) \tag{3.59}$$

---

[6] A general expression for $\boldsymbol{M_j(Q)}$ and $f(Q)$ can be found in [20] for systems in which the orbital momentum is not quenched and/or there is non-negligible spin-orbit coupling.

where $\boldsymbol{F_M(Q)}$ is the magnetic structure factor. In the dipole approximation,

$$F_M(\boldsymbol{Q}) = \sum_d f(Q)\langle\boldsymbol{\mu}_d\rangle \exp(i\boldsymbol{Q}\cdot\boldsymbol{d})\exp(-W_d(\boldsymbol{Q})), \tag{3.60}$$

where $\langle\boldsymbol{\mu}_d\rangle$ is the average magnetic dipole moment of the ion at $\boldsymbol{d}$. In contrast to nuclear scattering, the intensity of the magnetic scattering decreases with Q as $|f(Q)|^2$.

In general a magnetic structure can be decomposed into individual Fourier components corresponding to a propagation wavevector, $\boldsymbol{q}$, such that the magnetic moment of the ion at position d is given by,

$$\boldsymbol{\mu_{ld}} = \sum_{\boldsymbol{q}} \boldsymbol{m_{q,d}} \exp(-i\boldsymbol{q}\cdot\boldsymbol{l}), \tag{3.61}$$

where $\boldsymbol{q}$ is a wavector in the first Brillouin zone and the complex Fourier components, $\boldsymbol{m_{q,d}}$, describe the amplitude and phase of the modulation.

Consider a modulation with single wavevector $\mathbf{q} = (\delta, 0, 0)$. The modulation is commensurate when the wavelength is equal to an integer number of lattice units (i.e. δ is a rational fraction of a reciprocal lattice unit $2\pi/a$), in which case it is possible to define a new (larger) unit-cell that describes the combined nuclear and magnetic structure. In this case Bragg peaks will occur at reciprocal lattice vectors of the magnetic cell with intensity calculated in Eq.3.62. In general, one might want to index the magnetic Bragg peaks using the unmodulated (structural) unit-cell, indeed if the modulation is incommensurate (δ is an irrational fraction of reciprocal lattice units) then the translational symmetry of the crystal is broken and it is not possible to define new combined unit-cell. Because the moment, μ_{ld}, is a real observable, the summation in Eq.3.61 must include $-\boldsymbol{q}$ as well as $+\boldsymbol{q}$, and the Fourier components that must be related by $\boldsymbol{m^{\dagger}_{q,d}} = \boldsymbol{m_{-q,d}}$. Substituting Eq.3.61 into Eq.3.54 and performing the summation over lattice points as in Eq.3.38, gives the following,

$$S(\boldsymbol{Q}, \omega = 0) = (\gamma r_{\mathrm{e}})^2 N \frac{(2\pi)^3}{v_0} \sum_{\boldsymbol{G}_M} |\boldsymbol{F_{M_\perp}(Q)}|^2 \, \delta(\boldsymbol{Q} - \boldsymbol{G_M} \pm \boldsymbol{q}_{\mathrm{SDW}}), \tag{3.62}$$

where the structure factor is given by,

$$F_M(\boldsymbol{Q}) = \sum_d f(Q)\langle\boldsymbol{m_{q,d}}\rangle \exp(i\boldsymbol{Q}\cdot\boldsymbol{d})\exp(-W_d(\boldsymbol{Q})). \tag{3.63}$$

which is the same as in Eq.3.63 with the replacement of $\boldsymbol{\mu}_d$ with $\boldsymbol{m_{q,d}}$. The result is that magnetic Bragg peaks occur at points $\boldsymbol{G} \pm \boldsymbol{q}_{\mathrm{SDW}}$ due to the additional Fourier component of the SDW modulation.

Representation Analysis

The Fourier components $\boldsymbol{m_{q,d}}$ are constrained by the symmetry of the crystal and the propagation vector, $\boldsymbol{q}$. In representation theory, they can be described as a linear combination of modulations that are transformed by the irreducible representations (irreps) associated with the wavevector q - where the irreducible representations describe how a modulation transforms under the symmetry operations belonging to the structural spacegroup of the crystal. The details of representation analysis of modulated structures is beyond the scope of this thesis, a comprehensive introduction can be found in reference[42]. An important result is that a continuous phase transition involves distortions transformed by a single irrep [7]. This constraint greatly reduces the number of degrees of freedom when refining a magnetic structure. Common tools such as ISODISTORT[44] can identify the irreps of a spacegroup compatible with a given propagation vector, and this functionality is often included in refinement software such as Jana2006[45].

3.4.2 Inelastic magnetic scattering and the generalised susceptibility

There are various forms of magnetic excitation, for example it is possible to derive n-magnon cross-sections in a similar way to the n-phonon cross-section. This thesis is concerned with itinerant systems and the single-particle excitations related to the electronic structure near the Fermi-surface. In this case it is preferable to consider the spin-correlations in terms of the generalised susceptibility and the Lindhard functions discussed in Section 2.4.

Using the fluctuation-dissipation relation in Eq.3.23, the dynamic response is given by,

$$\tilde{S}(\boldsymbol{Q},\omega) = \sum_{\alpha\beta}(\delta_{\alpha\beta} - \hat{Q}_\alpha\hat{Q}_\beta)\left[1+n(\omega)\right]\frac{1}{\pi}\chi''_{\alpha\beta}(\boldsymbol{Q},\omega), \tag{3.64}$$

where $\chi''_{\alpha\beta}(\boldsymbol{Q},\omega)$ are components of the generalised susceptibility tensor as defined in Eq.2.15, that dictate the response of the system along α due to a perturbation by a small field along β.

---

[7] In Landau theory the term in the free energy which leads to the continuous transition must remain invariant during the symmetry-breaking transition. It can be shown that terms that couple more than one irrep are not invariant[43].

3.5 Resolution

A neutron scattering experiment will aim to measure the response of the system at a given point, $S(\boldsymbol{Q_0}, \omega_0)$. Due to the finite resolution of the instrument, the measured intensity at that point, $I(\boldsymbol{Q_0}, \omega_0)$, is actually the integral over some volume in $(\boldsymbol{Q}, \omega)$ space due to the detection of neutrons that have a distribution of $\boldsymbol{k_i}$ and $\boldsymbol{k_f}$ round the nominal values,

$$I(\boldsymbol{Q_0}, \omega_0) \propto \int\int R(\boldsymbol{Q} - \boldsymbol{Q_0}, \omega - \omega_0) S(\boldsymbol{Q}, \omega) d^3\boldsymbol{Q} d\omega. \tag{3.65}$$

The resolution function, $R(\boldsymbol{Q} - \boldsymbol{Q_0}, \omega - \omega_0)$, is peaked at $(\boldsymbol{Q_0}, \omega_0)$. R is the inverse of the covariance matrix that describes a four-dimensional Gaussian distribution in $\boldsymbol{Q} - E$ space of the form[20],

$$R(\boldsymbol{Q} - \boldsymbol{Q_0}, \omega - \omega_0) = \frac{|C|^{1/2}}{(2\pi)^2} \exp(-\frac{1}{2}\boldsymbol{X}^T C \boldsymbol{X}), \tag{3.66}$$

where $\boldsymbol{X}$ is a column vector with elements $(\boldsymbol{Q} - \boldsymbol{Q_0}, \omega - \omega_0)$ and C is the resolution matrix and the integral of R is normalised to unity. In general C is not diagonal - i.e. the eigenvectors are not oriented along the axes of the $(\boldsymbol{Q}, \omega)$ coordinate system.

3.6 Neutron sources and instrumentation

There are two methods of neutron production in high-flux neutron sources: spallation and nuclear fission. Reactor sources, such as the Institut Laue-Langevin (ILL) in Grenoble, France, operate by neutron induced fission of uranium enriched with the isotope ^{235}U which decays with the following products,

$$n +^{235} U \rightarrow 2.5n + 200 \text{ MeV} + nuclei. \tag{3.67}$$

The neutrons released in a fission event have typical energies of $\sim$ 2 MeV [46]. In order to trigger subsequent events and hence achieve a chain-reaction it is necessary to slow the neutrons down in a moderator (typically D_2O or graphite) [8]. Through subsequent collisions with the moderator nuclei, the neutrons reach thermal equilibrium with a Maxwellian distribution of wavelengths, with the average wavelength determined by the temperature of the moderator. Research reactors are designed so that an excess

---

[8] Lighter nuclides such as H and D are the most efficient moderators - for example a neutron will on average lose 1/2 of the initial kinetic energy per collision with a proton (approximately the same mass as a neutron).

of neutrons can escape the moderator and are transported to the beamlines by guides. Different beamlines are optimised for particular applications and are fed by guides from moderators at a suitable temperature - such that the distribution of neutron wavelength (energy) is comparable to the length-scale and excitations of interest (typically $1-10$ Å). The guides are designed to be curved and oriented so as to avoid a line-of-sight to the reactor core/source so as to reduce the transmission of high energy neutrons that have not been moderated (and other fission decay products such as high-energy γ radiation). [9].

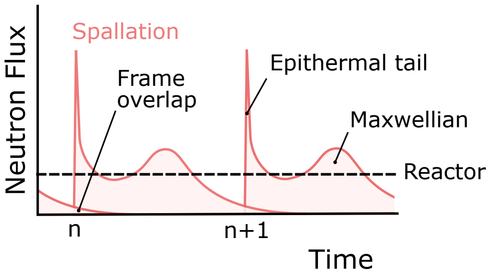

Figure 3.2: Schematic of the neutron flux incident on the sample as a function of time for a typical pulsed spallation source (index n refers to the n^{th} pulse) and a steady-state reactor.

Spallation is a process by which lighter nucleons (mostly neutrons) are ejected from a heavy nuclei after a collision with a high-energy proton. The energy is not dissipated in a single decay but rather triggers an intra-nuclear nuclear cascade that produces of the order of 20 neutrons per incident proton with a typical energy of $20-30$ MeV[20]. The ISIS spallation source at the Rutherford Appleton Laboratory in Harwell, UK, produces the high-energy protons in two stages: H^- ions are accelerated up to an energy of ≈ 70 MeV in a linear accelerator, stripped of the electrons when passing through an aluminium oxide foil before entering a synchrotron accelerator, which accelerates bunches of protons to ≈ 800 MeV. The high-energy protons are then diverted at a fixed frequency towards the heavy metal target (in this case tantalum). As in the reactor source, it is then necessary to slow the neutrons in a moderator or before being guided to the beamlines. However in addition to the Maxwellian distribution of wavelengths exiting the moderator, there remains a tail of very high-energy (epithermal) neutrons which are not thermalized in the moderator (shown in Fig.3.2).

---

[9] Neutron guides operate by total internal reflection of the beam. Total internal reflection occurs below a critical angle when the component of the neutron's kinetic energy normal to the surface of the guide is insufficient to penetrate the potential barrier (for a homogeneous medium the potential is proportional to the scattering length density)[47]. The critical angle can be increased by the addition of supermirror coatings to the walls (stacks of interfaces with ever increasing separation) to provide specular reflection for a large range of wavelengths at larger angles.

In contrast to reactors which produce a constant flux of neutrons, spallation sources are inherently pulsed (see Fig.3.2). The operating frequency of the spallation source and the moderator temperature (i.e. the wavelength distribution of the flux) determines the extent of frame overlap, where fast neutrons from a pulse overtake slower neutrons from previous pulses. This thesis contains data from the SINQ, spallation source at the Paul-Scherrer Institut in Villigen, Switzerland, which operates at a sufficiently fast frequency that adjacent pulses overlap completely to produce a time-independent flux.

3.6.1 Triple-axis spectrometers

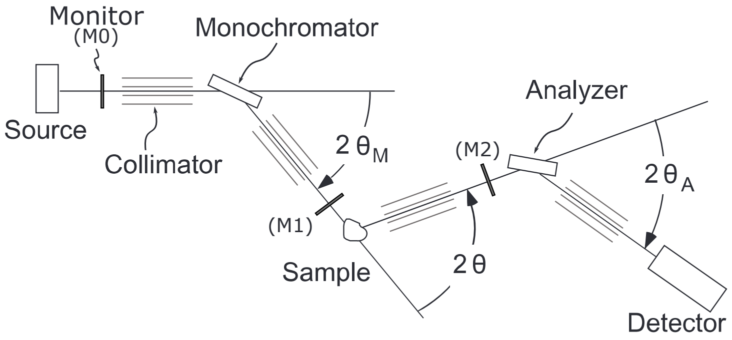

Figure 3.3: Schematic of a triple-axis neutron spectrometer adapted from [46]. Monitors (low-efficiency detectors) are often placed between the monochromator and sample and between the sample and analyser.

Fig.3.3 shows a schematic of a triple-axis neutron spectrometer (TAS), commonly found at continuous sources. The neutrons leave the moderator with a Maxwellian distribution of wavelength determined by the moderator temperature. The incident and final neutron energy are selected by adjusting the scattering angles $2\theta_M$ and $2\theta_A$ of the monochromator and analyser respectively, which are related to the wavelength by Bragg's Law in Eq.3.43. By adjusting the three angles $(2\theta_M, 2\theta, 2\theta_A)$ where 2θ is the scattering angle from the sample it is possible to measure a point in $(\boldsymbol{Q}, \omega)$-space of the horizontal scattering plane.

An experiment consists of step-wise scans along trajectories in $(\boldsymbol{Q}, \omega)$ space. Typically, the spectrometer is operated by varying up to two of the angles: with either a fixed k_i $(2\theta_M)$ or a fixed k_f $(2\theta_A)$. For several reasons it is normally advisable to choose a fixed k_f. If k_f is fixed, the detector counts normalised to the counts from the monitor between the monochromator and the sample (M1) is then proportional to scattering function $S(\boldsymbol{Q}, \omega)$ which is the quantity of interest - this is because the monitor efficiency is inversely proportional to k which then accounts for k_i in the pre-factor k_f/k_i in Eq.3.18.

Additionally the reflectivity of the analyser will vary with $2\theta_A$ which cannot be measured in-situ (whereas for a fixed k_f the reflectivity of the monochromator is not of concern because the counts at M1 can be used as a measure of the incident flux).

The monochromator and analyser are actually co-aligned arrays of single-crystals, which can be bent horizontally and vertically to focus the beam onto a smaller cross-sectional area at the sample position. The focussing increases the divergence of the beam - angular deviations from the mean direction. The beam divergence can reduced with collimation. The beam paths of a TAS are typically collimated with Soller collimators - parallel plates coated in neutron absorbing material (such as gadolinium) as demonstrated in Fig.3.3. The plate separation and length along the beam defines the range of angles transmitted and also the transmission. Even with focussing, the cross-section of the neutron beam is often larger than the sample, such that a significant portion of the beam is scattered from the sample environment contributing to the background. Collimation can reduce this background to some extent, but it is more effective to use horizontal and vertical slits/jaws constructed from neutron absorbing material to reduce the beam cross-section to better match the sample size. Sets of slits/jaws along the beam path can also be used as a form of collimation.

For neutron energies $E \lesssim 40$ meV the standard choices of monochromator/analyser are the (002) reflection of pyrolytic graphite (PG) and the (111) reflection of silicon. PG(002) has a much higher reflectivity than Si(111), however in some circumstances Si(111) might be preferable due to the lack of second-order contamination (transmission of $\lambda/2$) due to the systematic absence (zero structure factor) of the (222) reflection. Though Si(111) can still transmit λ/n for odd n. Higher order contamination can give rise to spurious peaks. On the elastic line higher-order contamination can produce peaks at wavevectors that are a rational fraction of a reciprocal lattice vector. It can be much harder to predict the location of spurious inelastic signal.

Filters can be placed before or after the sample in order to remove the higher-order contamination. Such filters work on the principle that in a polycrystalline material neutrons will not be attenuated by Bragg scattering if the wavelength $\lambda > 2d_{max}$, where d_{max} is the longest interplanar separation in the crystal (see Eq.3.43). For materials with a large coherent cross-section (and ideally small incoherent and absorption cross-sections), this leads to a steep decline in transmission for $\lambda < 2d_{max}$. A common filter for cold neutrons is polycrystalline Be which transmits neutrons with wavevectors below $k \leq 1.55$ Å^{-1} ($\lambda \gtrsim 4$ Å). The Be filter is cooled with liquid nitrogen so as to reduce the probability of a neutron exciting a phonon and losing sufficient energy to pass through the filter.

In some experiments it is crucial to account for the broadening due to the instrument resolution. For example when measuring the lifetimes of excitations, where the broadening depends sensitively on the orientation of the resolution ellipsoid with respect to the dispersion. Such measurements were not undertaken in this thesis and therefore the resolution is only discussed briefly. The resolution of a TAS is principally determined by two factors: the beam divergence which depends on factors such as the collimation, as well as the monochromator/analyser mosaic and focussing; and the monochromator/analyser $\Delta d/d$ resolution which depends on the focussed mosaic and the scattering angle. The orientation of the resolution ellipsoid depends on the scattering sense of the spectrometer axes and their orientation for a given $(\boldsymbol{Q}, E)$. This means that the resolution can change significantly across the trajectory of scans [10].

There are two commonly used techniques for calculating the TAS resolution: the Cooper and Nathans method [48] is the simplest method in which the beam divergence is a function only of the effective collimation and the homogeneous mosaic of the monochromator/analyser; and the Popivici method [49] that can account for other aspects of the TAS configuration such as geometrical focussing of the monochromator/analyser and the effect of the neutron source size and shape. Both require detailed knowledge of the TAS configuration. In practice some of the quantities to which the resolution is very sensitive, such as the effective mosaic of the monochromator/analyser, are not well known (especially if vertical as well as horizontal focussing is employed). Therefore it is common to infer the resolution from quantities that can be measured. For example, if the scattering of interest is diffuse and broad relative to the resolution, the observed energy broadening (at low energy transfer) can be estimated from the width of the elastic incoherent scattering near the wavevector of interest - note that in general this will overestimate the resolution broadening of a sharp Bragg peak.

3.6.2 Time-of-flight diffractometer

Here we consider a time-of-flight (TOF) diffractometer operating on a pulsed spallation source where the wavelength of the scattered neutrons can be determined from the time-of-flight, T (the difference between the time of detection and the pulse start). It is also possible to use a chopper on a continuous source to create pulses, however this is not commonly done as it uses only a small fraction of the available time-averaged flux.

Fig.3.4 shows a schematic of the WISH beamline at ISIS, UK[50]. Neutrons from

---

[10] In some circumstances the gain in flux might be might be worth the loss of resolution. For example when measuring weak diffuse fluctuations that are broader than the resolution in $(\boldsymbol{Q}, E)$ (as in the case of the inelastic measurements in this thesis). If the resolution out of the scattering plane is less crucial, one might also consider only applying vertical focussing of the monochromator and analyser.

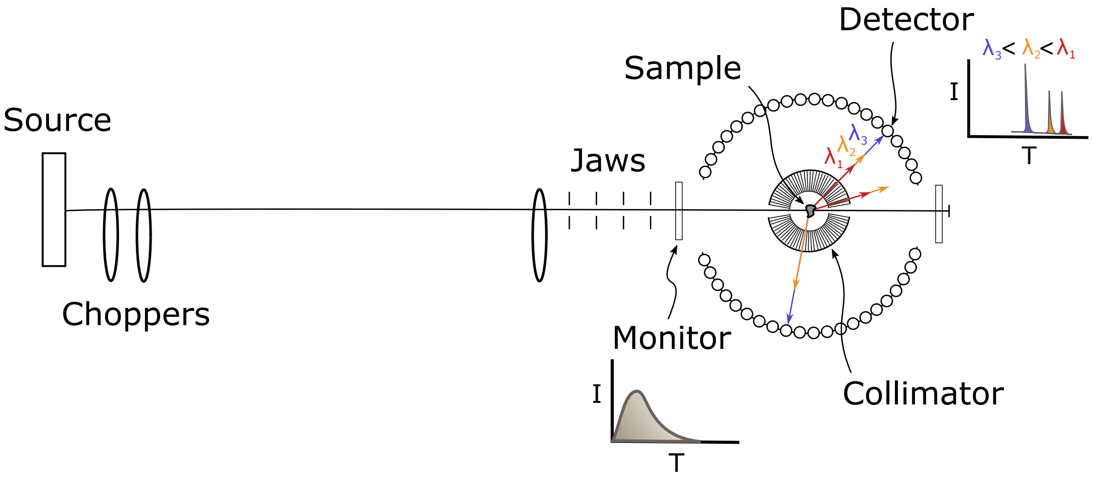

Figure 3.4: Schematic of the WISH TOF diffractometer. A pulsed white-beam is incident on the sample and the wavelength of the scattered neutron is determined from the TOF.

each pulse exit the moderator with a broad distribution of wavelengths and scatter from the sample into an array of position sensitive detectors that cover a large range of 2θ. Each detector pixel measures the counts as a function of time (typically binned into a histogram). The wavelength of the scattered neutrons is determined from the total distance travelled (source-detector), L, and the time-of-flight, T,

$$\lambda = \frac{hT}{m_n L}. \tag{3.68}$$

Substituting Eq.3.68 into Bragg's law in Eq.3.43, it can be seen that d is proportional to T,

$$d = \frac{hT}{2m_n L \sin(\theta)}. \tag{3.69}$$

An oscillating radial collimator can be placed around the sample to reduce the divergence and background [11]. The bandwidth of wavelengths incident on the sample can be set by the speed and phase (with respect to the pulse frequency) of the disk choppers (rotating disks with a transmitting window). There are two set of choppers, de-phasing the second set allows the instrument to run at half the frequency - i.e. use alternate frames to increase the accessible Q-range.

TOF diffractometer can efficiently measure a large range of $\boldsymbol{Q}$ with detector coverage over a large solid angle. In an experiment the sample can be rotated with respect to the spectrometer to map out large volumes of reciprocal space, and measure equivalent reflections at different scattering angles, 2θ (and therefore λ). Another advantage of

---

[11] The collimator oscillates so as not to preferentially shadow a subset of detectors

TOF diffractometers is that the resolution, $\Delta d/d$, is to first order constant for a given scattering angle - i.e. the narrowest peaks are at low d-spacing where it is more likely to have many reflections with similar d-spacing (particularly in powder samples). From Eq.3.69 the resolution can be written as,

$$\left(\frac{\Delta d}{d}\right)^2 = \left(\frac{\Delta T}{T}\right)^2 + \left(\frac{\Delta L}{L}\right)^2 + (\cot(\theta)\Delta\theta)^2 \tag{3.70}$$

where the uncertainty in TOF, ΔT, is dominated by the initial width of the pulse in time from the moderator [12], and the uncertainty in path length, ΔL is small governed by sample placment and detector calibration (typically small deviations of the order of 1 cm relative to a total flight path of e.g. ≈ 42 m for WISH). Both these contributions are set by the instrument/source and are constant. The uncertainty on the scattering angle, $\Delta\theta$, has several contributions,

$$(\Delta\theta)^2 = (\Delta\theta_{det})^2 + (\Delta\theta_{div})^2 + (\Delta\theta_{sample})^2 \tag{3.71}$$

where $\Delta\theta_{det}$ is due to the angular resolution of the detector, $\Delta\theta_{div}$ is due to the divergence of the beam and $\Delta\theta_{sample}$ is due to the finite size of the sample. The angular term in Eq.3.70 comes from the first derivative of Bragg's Law with respect to θ and is minimised when $\theta = 90°$ (referred to as back-scattering). The terms $\Delta\theta$ can be reduced by increasing the secondary flight path (sample-detector), however this will reduce the solid angle coverage of the detector.

There are several disadvantages to a TOF diffractometer over a conventional constant wavelength instrument. Reflections are measured over large range of wavelengths which means it is important to correct for absorption and extinction effects which can have a dramatic effect on the integrated intensities (outlined in Section 3.6.3). Secondly, the moderator pulse shape as a function of time, $N(T)$, is very asymmetric with a steep onset and more slowly decaying tail. The Bragg peak lineshape (as a function of TOF or d-spacing) is then the convolution of the pulse function and some peak, typically a Gaussian or pseudo-Voigt. As a consequence the maximum of the peak does not coincide with the d-spacing of the reflection in Eq.3.69 (though the asymmetry is less severe at larger λ).

---

[12] The moderator can be optimised to produce a narrow pulse width (at the cost of flux) by poisoning or decoupling, which involves the addition of neutron absorbing material (e.g. cadmium) to soak up slow neutrons that have a long lifetime in the moderator.

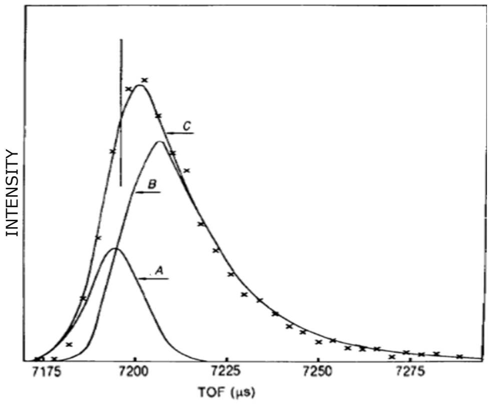

Figure 3.5: The (222) Bragg peak of a nickel sample measured on a TOF diffractometer fitted with a back-to-back exponential convoluted with a Gaussian peak, labelled as curve C. Curves labelled A and B correspond to the terms in Eq.3.73 that arise from the rising exponential (coefficient α) and decaying exponential (coefficient $-\beta$) respectively. The solid vertical line marks the position of the center of the peak (which does not coincide with the maximum). Figure taken from [51].

The simplest approximation for the pulse shape is a back-to-back exponential[51],

$$N(T) = \begin{cases} \frac{\alpha\beta}{2(\alpha+\beta)} \exp(\alpha T), & T < 0 \\ \frac{\alpha\beta}{2(\alpha+\beta)} \exp(-\beta T), & T \geq 0, \end{cases} \tag{3.72}$$

where α and β are positive [13]. There is an analytical form for a back-to-back exponential convoluted with a Gaussian peak at time T_0 with standard deviation σ[51],

$$I(T) = \frac{\alpha\beta}{2(\alpha+\beta)} \left[\exp(u)\mathrm{erfc}(y) + \exp(v)\mathrm{erfc}(z)\right], \tag{3.73}$$

where erfc is the complimentary error function,

$$u = \frac{1}{2}\alpha(\alpha\sigma^2 + 2[T - T_0]), \tag{3.74}$$

$$v = \frac{1}{2}\beta(\beta\sigma^2 - 2[T - T_0]), \tag{3.75}$$

$$y = \frac{\alpha\sigma^2 + [T - T_0]}{(2\sigma^2)^{1/2}}, \tag{3.76}$$

---

[13] There is a more complicated form for $P(T)$ proposed by Ikeda and Carpenter [52] that better captures the steep onset of the pulse, however it has more adjustable parameters and therefore the back-to-back exponential is typically preferred unless the parameters that relate to the beamline and moderator are well characterised by refinements of standard sample data.

$$z = \frac{\beta\sigma^2 - [T - T_0]}{(2\sigma^2)^{1/2}}. \tag{3.77}$$

Fig.3.5 shows an example of a Bragg peak fitted with Eq.3.73 and the TOF of the peak centre corresponding to the d-spacing of the reflection. Unfortunately the parameters α, β (and therefore the peak shape) depend on the wavelength and scattering angle as well as the details of the moderator. There are empirical forms for the d-spacing dependence of these parameters that seem to be valid for spectra with coefficients that are refined for powder spectra from a single bank of detectors (e.g. spanning a range of $2\theta \sim 20 - 30°$). In single-crystals there are other factors that influence the peak shape, such that the refinements are not as straightforward.

3.6.3 Corrections for diffracted intensities

Absorption

The neutron beam is attenuated by two processes: absorption and scattering. The transmission is then given by the Beer-Lambert law,

$$\frac{I(z)}{I(z=0)} = \exp(-\mu t), \tag{3.78}$$

where μ is the linear coefficient of attenuation which depends on the cross-section of the sample,

$$\mu = n(\sigma_s + \sigma_a) \tag{3.79}$$

where n is the number density of the formula unit, and σ_s and σ_a are the total scattering (coherent and incoherent) and absorption cross-section of a formula unit. The absorption cross-section varies between different elements and isotopes and depends on the neutron energy/wavelength. Typically the absorption cross-section is less than the scattering cross-section and is inversely proportional to the neutron speed $\sigma_a \propto 1/v$ (i.e. the absorption increases linearly with the time the neutron is in the vicinity of a nucleus). However, there are certain energies which correspond to resonant excitations of a nucleus: for example a neutron can be captured by the nucleus if the energy is close to that of the bound state. In the majority of elements these resonances do not coincide with the typical neutron energy range used in neutron scattering experiments, with the notable exception of some ‘special’ isotopes ^{10}B and ^{113}Cd and ^{157}Gd which have a very large absorption cross-section for thermal neutrons and can be used in shielding or to poison moderators. To correct properly for absorption requires knowledge of the average path length through the sample (for inelastic scattering one would also need to account for the difference in the wavelength dependence of the absorption cross-section). In principle this can be done by Monte-Carlo simulation, but typically one approximates the sample to be high symmetry shapes (sphere, cylinder or infinite slab) for which there are analytical forms for the transmission as a function of scattering angle.

Extinction

Extinction refers to the loss of intensity due to diffraction processes within a crystal - both before and after the scattering event (inelastic scattering has a negligible contribution to the extinction of Bragg peaks). There are two types of extinction process. Primary extinction is due to coherent multiple Bragg scattering within a perfect crystallite as illustrated in Fig.3.6. As intensity is reduced at each scattering event multiple scattering therefore leads to a lower than expected Bragg intensity. Typical samples are comprised of a ‘mosaic’ of many crystallites with a random distribution of orientations around some mean value - typically with a width of the order of $\sim 1°$. In this case the diffracted beam can be diffracted again by a separate crystallite with a sufficiently similar orientation - a process known as secondary extinction.

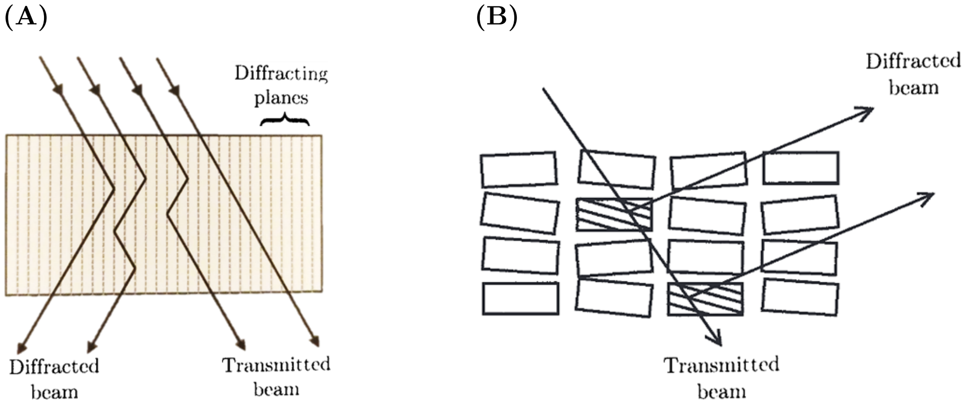

Figure 3.6: (A) Schematic of primary extinction process taken from [20] (B) Schematic of secondary extinction taken from [53].

The most common method for extinction correction was proposed by Becker and Coppens[54] where the two extinction processes are assumed to be independent such that the measured Bragg intensity,

$$I \propto y_p y_s \frac{d\sigma}{d\Omega} \tag{3.80}$$

where y_s and y_p are coefficients for the primary and secondary extinction respectively. In the case of a spherical crystal of spherical crystallites both coefficients take the form,

$$y_i = \left[1 + 2x_i + \frac{A_i(\theta)x_i^2}{1 + B_i(\theta)x_i}\right]^{-1/2}, \tag{3.81}$$

where $i \rightarrow [s, p]$ and analytical forms for A_i and B_i and x_i can be found in reference [20]. Both x_p and x_s are proportional to the squared structure factor $|F(\boldsymbol{G})|^2$ and have a strong wavelength dependence. The secondary extinction parameter x_s also requires an assumed distribution for the mosaic spread in angles - typically Gaussian or Lorentzian as it is difficult to measure this distribution in the bulk of the sample directly. Extinction is corrected for in the refinement as parameters in the least square fit as it depends on the structure factor (in contrast to absorption for which the integrated intensities can be corrected before the refinement).

The attenuation due to extinction is greater for larger samples and is most severe for Bragg reflections with large structure factors. Ideally one would then use a small, spherically shaped sample in diffraction measurements. In practice the sample size and shape is often decided by other factors, such as the growth and the strength of the signal to be measured [14]. It is also desirable to refine reflections measured at multiple wavelengths due to the wavelength dependence of the extinction parameters, x_i.

Lorentz Correction

As can be seen in Eq.3.40 the translational symmetry of the crystal lattice gives rise to infinitely sharp Bragg peaks in reciprocal space when the momentum transfer is equal to a reciprocal lattice vector (when a reciprocal lattice vector intersects the Ewald sphere). In reality, due to the mosaic of the sample, Bragg peaks are not δ-functions but have a finite width, and the instrumental resolution means the diffraction condition is fulfilled for a range of nominal momentum transfers such that the integrated intensity,

$$I \propto L\frac{d\sigma}{d\Omega} \tag{3.82}$$

where L is the Lorentz factor which corrects for the duration the Bragg condition was fulfilled in a scan [15]. L depends on the direction of the scan with respect to the reciprocal lattice vector - for example a scan direction tangential to the Ewald sphere will measure a larger Bragg peak intensity than a radial scan.

---

[14] If the sample contains very strongly absorbing isotopes it may also be necessary to consider optimising the sample size to reduce the absorption.

[15] i.e. the measured should be divided by L to correct for this effect.

In a white-beam TOF Laue the orientation of the sample with respect to $\boldsymbol{k_i}$ is fixed and therefore single-crystal Bragg peaks occur at a fixed scattering angle 2θ and it is effectively measured as a function of λ - which corresponds to a radial scan. In this case the Lorentz factor is given by [55],

$$L_{TOF} = \frac{\sin^2(\theta)}{\lambda_{hkl}^4}, \tag{3.83}$$

where λ_{hkl} is the wavelength that satisfies the Bragg condition. A TOF measures reflections across a large range of λ and hence this correction is critical when comparing integrated intensities.

On a TAS there are different possible trajectories through the Bragg peak - general expressions for L can be found in [56]. The relevant scans in this thesis were made by rotating the detector at twice the rate of the sample axis (perpendicular to the scattering plane), sometimes referred to as a $\theta - 2\theta$ scan, which is a longitudinal trajectory through a Bragg peak ($\boldsymbol{Q}$ parallel to $\boldsymbol{G}$). In this case, L is a function only of the scattering angle 2θ [16],

$$L_{\theta-2\theta} = \frac{1}{\sin(2\theta)}. \tag{3.84}$$

---

[16] The Lorentz factor in Eq.3.84 also holds for so-called θ scans where the sample is rotated but the detector position 2θ is kept constant.

Chapter 4

Background to $Sr_3Ru_2O_7$

The partially filled d-bands in transition metal oxides (TMOs) typically give rise to heavy quasiparticles bands which can produce varied and interesting phenomena if near the Fermi level. Hybridisation between the d orbitals and the oxygen $2p$ orbitals can produce systems which are tuned close to the boundary of metallic and insulating behaviour and typically susceptible to exotic forms of electronic order. For example, the cuprate family of $3d$ TMOs are charge-transfer insulators, but doping induces high-T_c superconductivity and itinerant charge and spin density wave order [57, 58].

The $d-p$ hybridisation in $4d$ TMOs, such as the ruthenates, is in general greater than their $3d$ analogs due to the larger spatial extent of the $4d$ orbitals. As a consequence, the on-site Coulomb repulsion would be expected to be weaker thus promoting more itinerant behaviour. In addition the heavier $4d$ elements also exhibit stronger spin-orbit coupling, which as well as lifting degeneracies, introduces momentum dependent mixing of the d orbital character of quasiparticle states. The existence of competing overlapping energy scales that arise from the interplay of orbital, spin, and structural degrees of freedom in such compounds produces diverse and novel behaviour.

4.1 Ruddlesden-Popper series of strontium ruthenates

The Ruddlesden-Popper (RP) series of layered perovskite strontium ruthenates $Sr_{n+1}Ru_nO_{3n+1}$ have attracted much attention due the profound and systematic dependence of their physical properties on the number of layers of RuO_6 octahedra stacked along the c-axis, n. There is an overall trend towards ferromagnetism with increasing n, which appears to tune the system through the generic phase diagram of an itinerant ferromagnet[7] shown in Fig.4.1.

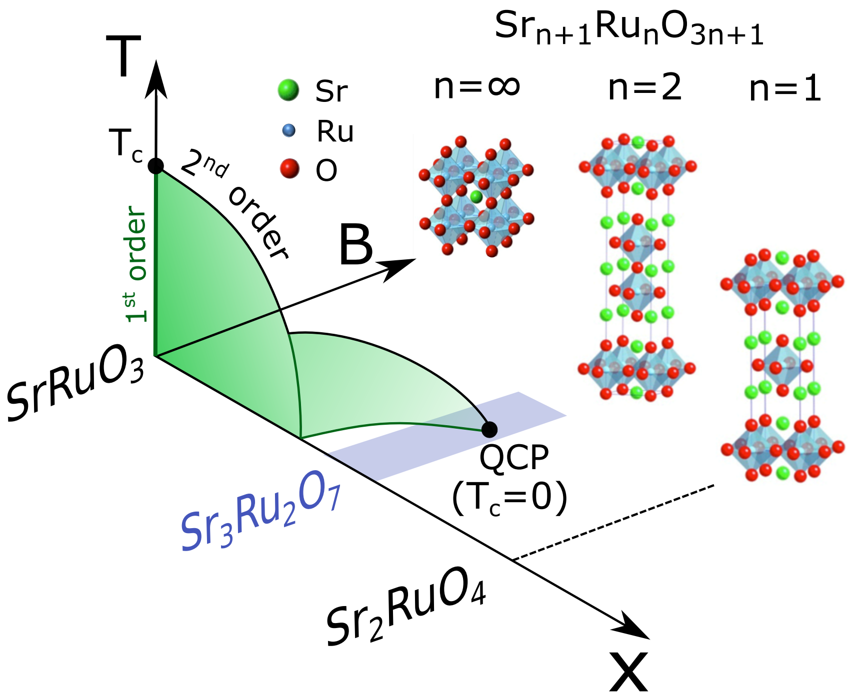

Figure 4.1: The crystal structure of the Ruddlesden-Popper (RP) series of layered perovskite strontium ruthenates $Sr_{n+1}Ru_nO_{3n+1}$, and their position in the generic phase diagram of an itinerant ferromagnet where the critical temperature, T_c, is suppressed to a quantum critical point (QCP) at zero temperature by some non-thermal tuning parameter (in this case number of layers, n).

The most three-dimensional member (n=∞) $SrRuO_3$ is an itinerant ferromagnet [59]. In contrast, the single-layered (n=1) compound Sr_2RuO_4 is an unconventional superconductor[60] with strong incommensurate antiferromagnetic (AFM) spin fluctuations due to nesting between quasi-1D bands at the Fermi level[61, 62]. The superconductivity in Sr_2RuO_4 is thought to be spin mediated, however no gap is observed in the incommensurate fluctuations in the superconducting state[63]. Instead, it has been proposed that the pairing is provided by ferromagnetic (FM) spin fluctuations as in superfluid ^{3}He (for a comprehensive review see[64, 65]), though inelastic neutron scattering only provides tentative evidence of their existence[66] which appear to be inconsistent with the calculated spin susceptibility[67, 68, 69, 70].

The bilayer member $Sr_3Ru_2O_7$ (n=2) has intermediate dimensionality. It is on the verge of a ferromagnetic instability[71], which is naturally tuned very close to quantum criticality. A magnetic field drives the end-point of the transition shown in Fig.4.1 towards zero temperature, however, the quantum critical point (QCP) is masked by spin-density-wave order[1]. Indeed the dominant spin-fluctuations are antiferromagnetic at low-temperature for all fields [72, 73]

The coexistence and competition between ferromagnetic and antiferromagnetic correlations arises from the electronic structure near the Fermi-level. The layered structure of Sr_2RuO_4 and $Sr_3Ru_2O_7$ gives rise to quasi-2D and quasi-1D bands that couple to the ferromagnetism and SDW fluctuations respectively. The competition can also be tuned with chemical substitution, for example the isovalent substitution of Sr with Ca eventually stabilises antiferromagnetic order in the single-layer compound[74, 75]. However, the superconductivity in Sr_2RuO_4 and the SDW order in $Sr_3Ru_2O_7$ are very sensitive to disorder.

The rest of this chapter provides a overview of the current experimental and theoretical understanding of $Sr_3Ru_2O_7$, then proceeds to discuss the electronic structure using an illustrative tight-binding model.

4.2 $Sr_3Ru_2O_7$

$Sr_3Ru_2O_7$ is a quasi-2D metal that is a strongly-enhanced paramagnet with a Wilson's ratio ∼10 that indicates a large $q = 0$ susceptibility at low temperature[76]. Indeed, a modest uniaxial pressure of 0.1 GPa along the c-axis (perpendicular to the bilayers) induces a ferromagnetic transition at 80 K [77]. $Sr_3Ru_2O_7$ is remarkable because the system is tuned very close to the quantum critical point of the ferromagnetic instability which can be approached with magnetic field at ambient pressure.

4.2.1 Quantum criticality

Before discussing the signatures of quantum criticality in $Sr_3Ru_2O_7$ is worth providing a brief explanation of the phenomenon.

The critical temperature of a continuous transition, T_c, marks the point at which the correlation length and time-scale of the fluctuations diverge. Below T_c there exists static long-range order and the thermodynamic average of the order parameter (e.g. the bulk magnetisation in a ferromagnet) increases continuously as temperature decreases. As T_c is approached from high-temperature, short-range order develops and in the critical region ξ and τ scale as a power law,

$$\xi = t^{-\nu} \tag{4.1}$$

$$\tau = \xi^z = t^{-z\nu}, \tag{4.2}$$

where $t = |T - T_c|/T_c$ and ν, z are critical exponents (additional exponents exist for the critical scaling of other quantities including the order parameter, susceptibility and heat capacity). At T_c the characteristic frequency of the fluctuations $\omega \to 0$ so for $T_c > 0$ the critical fluctuations are in the classical limit, $k_B T > \hbar\omega$, in which case only the spatial correlations are relevant. The divergence of the correlation length produces scale-invariance and the critical exponents must depend only on the dimensionality and symmetry of the order parameter rather than the microscopic interactions [1].

A quantum critical point (QCP) occurs when T_c is suppressed to zero temperature - via some non-thermal tuning parameter, p, such as hydrostatic pressure or magnetic field. In a thermal phase transition, as T_c is reduced, the width of the classical critical region decreases. In contrast the effects of quantum criticality can be felt over a large temperature range. At zero temperature it is quantum fluctuations arising from from Heisenberg's uncertainty principle that melt the order at some critical tuning parameter, p_c - producing a quantum phase transition. In a quantum mechanical system the temporal and spatial fluctuations cannot be decoupled. The time scale of quantum critical fluctuations scales as $\tau \sim (|p - p_c|/p_c)^{-z\nu}$[6], therefore at finite temperature the quantum fluctuations can still exhibit critical behaviour. The cross-over between classical and quantum behaviour of the fluctuations occurs when $k_B T \sim \hbar\omega$. The quantum critical region becomes progressively broader in p with increasing temperature. In this region the physical properties are governed by the excitation spectrum of the quantum fluctuations, which scatter the quasiparticles to the extent that the adiabatic continuity of the Fermi-liquid (FL) breaks down (the decay-rate of the quasiparticles exceeds the excitation frequency of interacting system) [2]. This gives rise to non-FL behaviour, typically a linear-T dependence of the resistivity and a logarithmic divergence of the linear coefficient of temperature dependence of the electronic heat capacity (a well known example of such behaviour is at the QCP of the anitferromagnetic transition in Au-doped $CeCu_6$[79]).

QCP are often realised experimentally at the boundary of a symmetry breaking low temperature ordered phase. This is not the case in $Sr_3Ru_2O_7$ where the continuous transition is the end-point of a first-order metamagnetic transition in which the symmetry is unchanged.

---

[1] Systems which exhibit the same set of critical exponents belong to the same universality class in renormalisation group theory (for a review see [78]).

[2] It should be noted that non Fermi liquid behaviour is also exhibited in a thermal phase transition, however long-range order develops below T_c and at low temperature FL behaviour will be restored[6].

4.2.2 Metamagnetic QCP

The proximity of the layered ruthenates to a ferromagnetic instability is attributed to peaks in the density of states(DOS) near the Fermi-level (discussed in more detail in the next section), which are a generic feature of many low dimensionality systems (e.g. in bilayer graphene[80]). In $Sr_3Ru_2O_7$, the DOS at zero field is not sufficient to fulfil the Stoner criterion for ferromagnetic order. The application of a magnetic field splits the spin bands producing a metamagnetic transition (first-order jumps in the magnetisation) due to the rapid spin-polarisation of the Fermi-surface as a peak in the density of states for one spin species is driven through the Fermi level[81] (see Section 2.2). This situation is illustrated in Fig.4.2 with a simple 2D nearest neighbour tight-binding dispersion, which has saddle-points at $k = (\pi, 0)$ and $(0, \pi)$ which produces a logarithmically divergent peak in the DOS (van Hove singularity) at half-filling. The relevance of this dispersion to the electronic structure of the ruthenates will be made clear in Section 4.3.

The metamagnetic transition is analogous to the liquid-gas transition as a function of pressure, it involves as sudden increase in the order-parameter density which is necessarily first order below a critical temperature T_c. There is no change in symmetry across the transition. $Sr_3Ru_2O_7$ exhibits a series of metamagnetic transitions with a T_c that depends on the orientation of the applied field with respect to the bilayers (decreasing as the field is tilted out of the basal plane). Early AC susceptibility measurements indicated that T_c of one of the metamagnetic transitions could be tuned almost to zero temperature by a field of ≈ 7.8 T applied within 10° of the c-axis (see Fig.4.3)[82, 83].

It had proven hard to experimentally realise this situation in other itinerant ferromagnets (for example suppressing T_c by hydrostatic pressure). Indeed, there is a general tendency for ferromagnetic quantum critical points in clean metallic systems to be avoided by either antiferromagnetic order (e.g. PrPtAl [85]) or the transition becomes first-order at low temperature (e.g. ZrZn2 [86]). For a comprehensive review see [7].

However, quantum criticality can be extremely sensitive to disorder and in samples with an order of magnitude smaller residual resistivity extrapolated to zero temperature ($\rho_{res} \lesssim 0.5$ $\mu\Omega$cm relative to the previous studies with $\rho_{res} \lesssim 5$ $\mu\Omega$cm) it was found that the QCP was avoided by an electronically ordered phase characterised by enhanced resistivity[87, 88] and bounded by first-order metamagnetic transitions (shown in Fig.4.3). The enhanced resistivity shows large anisotropy for a field tilted away from c-axis, with the the resistivity parallel to the component of the field in the ab-plane larger than perpendicular ($\rho_{//} > \rho_\perp$) as shown in Fig.4.4 (there is also a region of anisotropic transport is observed for an in-plane field)[88, 89, 12]. This anisotropy is also observed in other

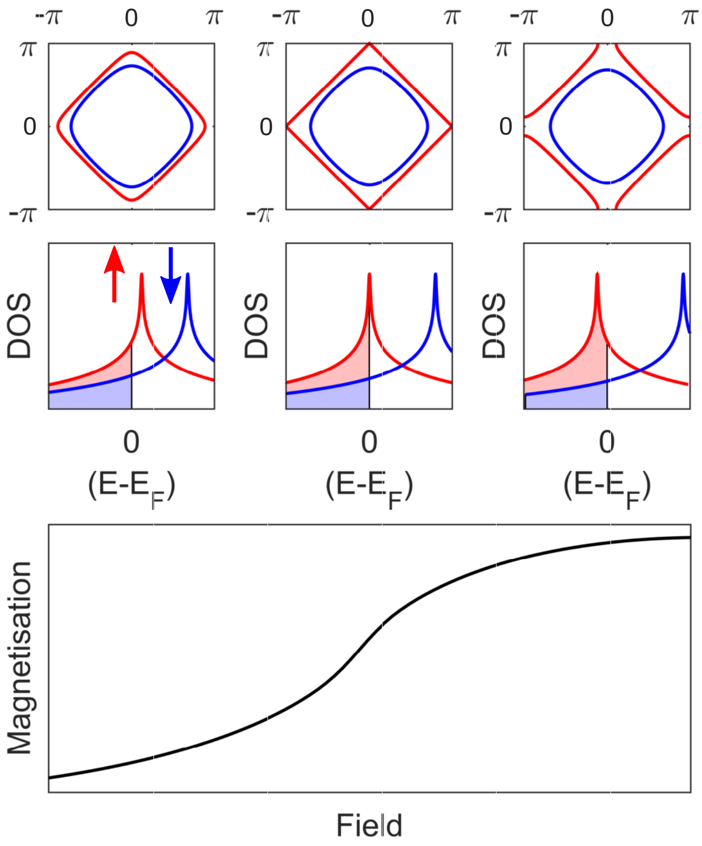

Figure 4.2: Schematic of metamagnetic transition in 2D nearest neighbour tight binding with rigid band Zeeman splitting. Fermi surfaces (Top) and density of states (middle) of the spin up (red) and spin down (blue) bands. (Bottom) Magnetisation (difference between number of up and down electrons below the Fermi energy E_F) as a function of field.

thermodynamic properties such as the magnetostriction and thermal expansion[90, 91].

4.2.3 Discovery of SDW order

It was speculated that the origin of the transport anisotropy was due to domains of C_2 distorted Fermi surfaces[92, 9], possibly due to orbital ordering[91] or by a Pomeranchuk instability[93, 94]. Hence the regions are often said to host 'nematic' transport due to the broken rotational symmetry.

In a breakthrough discovery, neutron diffraction measurements by Lester *et al.* found two abutting incommensurate spin-density-wave (SDW) ordered phases A & B in the regions of anisotropic transport observed for a field close the c-axis (a schematic phase diagram is shown in Fig.4.5). Both phases have a wavevector along the Ru-O bond in the ab-plane, $\boldsymbol{q}_{\mathrm{SDW}} = (\delta, 0, 0)$ and $(0, \delta, 0)$, with $\delta = 0.233$ and $\delta = 0.218$ for the A and B

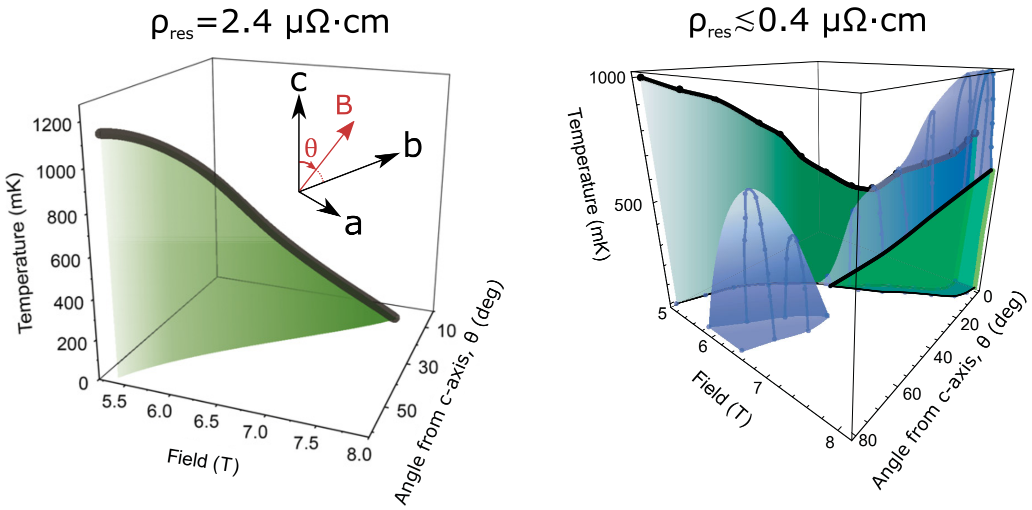

Figure 4.3: AC susceptibility measurements as a function of magnetic field and angle of the field from the c-axis (perpendicular to the bilayer planes) for samples with different residual resistivity. T_c is indicated by a solid black line. (Left) Figure taken from [83]. (Right) Figure taken from [84] with regions of enhanced resistivity shaded in blue.

phase respectively, with the ordered moment transverse to $\boldsymbol{q}_{\mathrm{SDW}}$ along the orthogonal Ru-O bond in the ab-plane[1] (see Fig.4.4) [3]. A schematic phase diagram is shown in Fig.4.5. The gapping of the Fermi surface by the SDW order provides a natural explanation for the enhanced resistivity. In Fig.4.4 it can be seen that for a field along the c-axis, the magnetic order exhibits apparent fourfold symmetry with two pairs of Bragg peaks. When the field is tilted by ≈ 10° away from the c-axis, only the component of the SDW parallel to the in-plane field is observed, corresponding to the direction of the enhanced resistivity. Such anisotropic transport is seen in other SDW systems. For example, when chromium is field-cooled through T_N it hosts a single-q SDW domain with a wavevector parallel to the field, the resistivity is higher parallel to SDW wavevector than perpendicular[95].

Despite the observed anisotropy for fields that break the tetragonal symmetry of the system, for a magnetic field along the c-axis ($\theta = 0°$) the SDW does not microscopically break four-fold symmetry. When the field is tilted from the c-axis the suppression of one SDW component is not accompanied by the enhancement of the other component [1], and no hysteresis is observed in transport when varying the component of the field in the bilayer plane[12]. The anisotropy observed for C_2 fields is then not due to a changing volume fraction of C_2 domains of single-q order, but due to the independent evolution of

---

[3] The incommensurate nature of the SDW phases (i.e. wavevector that is not a rational fraction of the reciprocal lattice vectors) means that the order breaks translational symmetry hence the term 'nematic' is not valid.

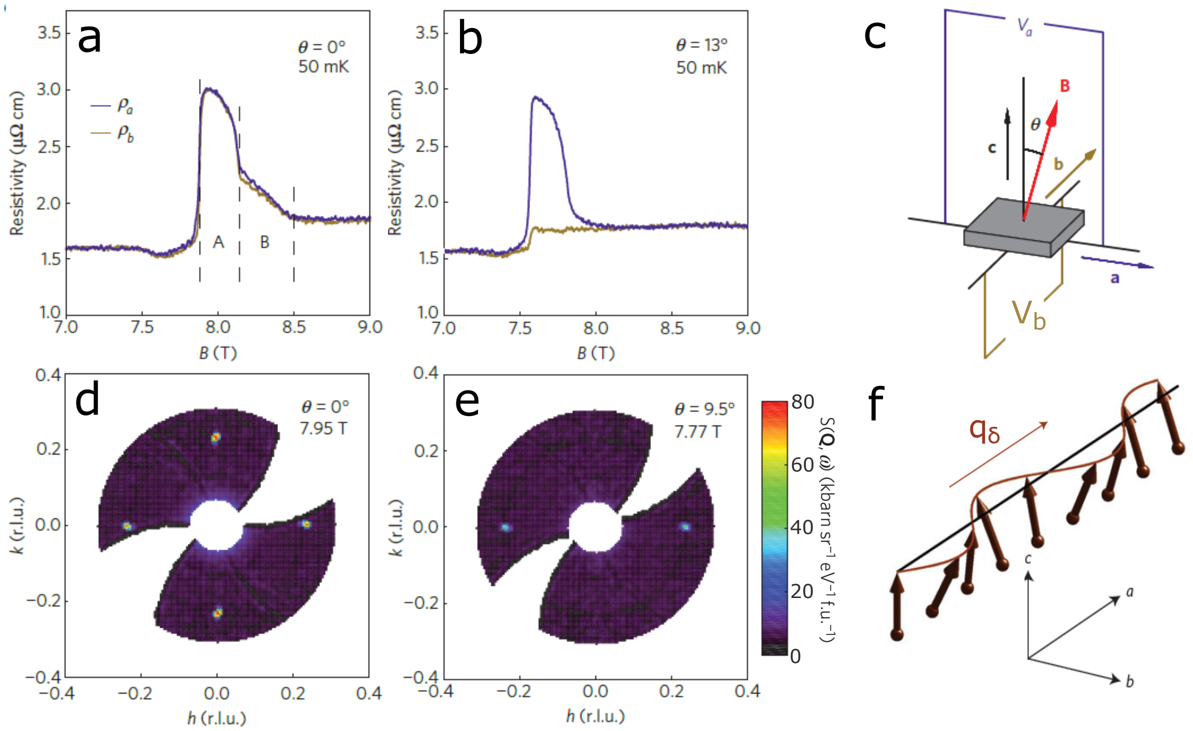

Figure 4.4: Figure taken from Lester *et al.*[1] (a-b) resistivity from Borzi *et al.* [88] showing the tilted field (in-plane component along the a-axis) causes a marked reduction in ρ_b (i.e. perpendicular to the field). (c) Schematic showing the potentials V_a and V_b along the a- and b-axes and a magnetic field rotated in the ac-plane. (d-e) Elastic scattering on the neutron spectrometer LET (ISIS,UK) that shows tilting the field towards the a-axis suppresses the SDW component along b. (f) schematic of the magnetic structure of the linear SDW order with wavevector and ordered moment along orthogonal in-plane Ru-O bonds (a and b).

the two components of $2q$-order[4]. In general, whether single-q or multi-q order is stabilised depends on cross-terms in the free energy that couple the components[96, 97, 98]. The cross-terms compete with other terms that couple SDW moment to the field (either directly or indirectly) which produces the anisotropy.

4.3 Electronic structure

The nominal valence of the ruthenium ion in this series is Ru^{4+}, which has the electronic configuration $4d^4$. The $4d$ states are split into the t_{2g} and e_g manifolds by the octahedral crystal field of the perovskite structure. The d_{xy}, d_{xz}, and d_{yz} orbitals that comprise the

---

[4] Note that rotational symmetry breaking is not necessary to produce a second-order phase transition at T_N as the incommensurate SDW breaks translational symmetry.

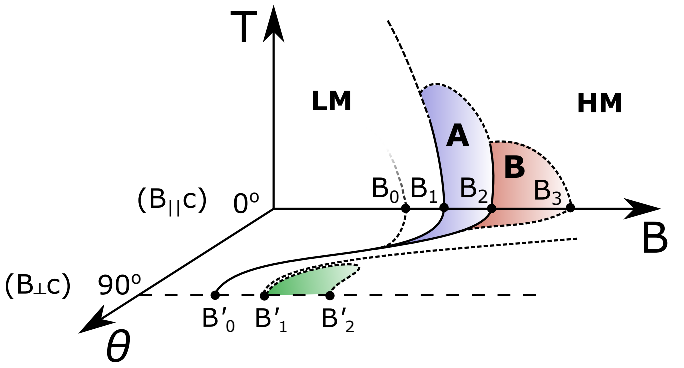

Figure 4.5: Schematic phase diagram of $Sr_3Ru_2O_7$ as a function of magnetic field, temperature and angle of the magnetic field from the c-axis θ. First-order transitions which exhibit a peak in the imaginary part of the AC susceptibility are shown as solid black lines, Dashed lines represent second-order transitions/crossovers that produce a peak in only the real part of the AC susceptibility. The low-moment paramagnetic (LM), high-moment paramagnetic (HM) and the SDW phases (A& B) are labelled. Shaded regions exhibit enhanced resistivity for a current applied along at least one of the in-plane tetragonal axes [9]. The observed metamagnetic transitions are numbered B_i and B'_i for a field applied along the c-axis and a-axis respectively.

t_{2g} manifold are lower in energy than the e_g orbitals which have lobes that point towards the oxygen atoms at the octahedral vertices.

A review of the electronic structure of the perovskite ruthenates can be found in [99]. Here we build a toy model for $Sr_3Ru_2O_7$ by starting with the simple bandstructure of the single-layered compound Sr_2RuO_4 in the manner done by Puetter *et al.*[100].

4.3.1 Sr_2RuO_4

The single-layer Sr_2RuO_4 has the simplest electronic structure, that forms the basis of understanding the physics of all the layered ruthenates. The large separation of the RuO_2 layers results in sheets of Fermi-surface that exhibit only weak dispersion along the c-axis in angle-resolved quantum oscillations measurements[101]. The Fermi surface measured by ARPES[102] exhibits three sheets shown in Fig.4.6A. The α and β sheets are due to the hybridisation of the quasi-1D bands derived from the Ru d_{xz} and d_{yz} orbitals. The d_{xy} orbitals produce the quasi-2D band at the zone centre, labelled γ.

Though LDA calculations predict that the contribution of the hybridised oxygen $2p$ orbital to the density of states at the Fermi energy is not negligible[99], the electronic structure near the Fermi-level is well described by the following 2D tight binding Hamiltonian

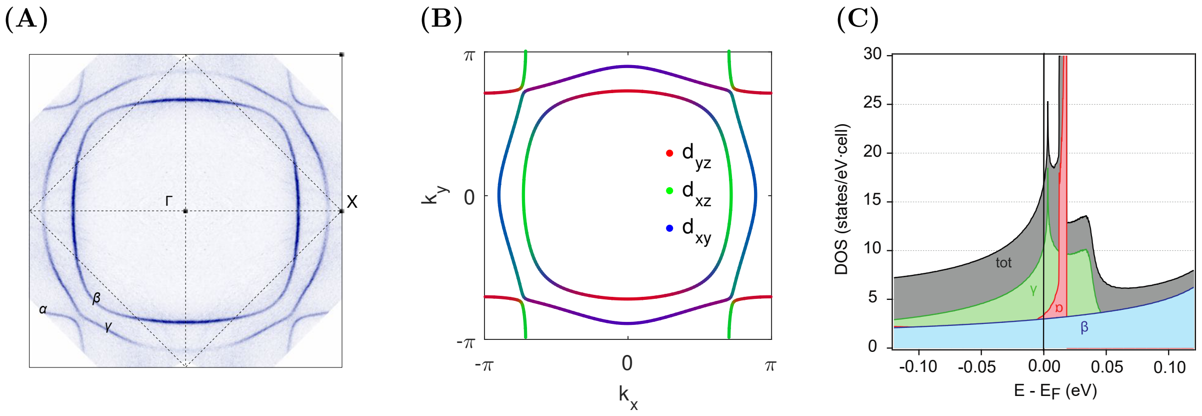

Figure 4.6: (A) Fermi surface measured by ARPES taken from [102]. (B) Fermi surface with orbital character form tight-binding model in [103]. (C) Density of states for the tight-binding bandstructure, taken from [103].

for a square lattice of Ru atoms (ignoring the body-centring of the lattice) [67, 68, 103, 69],

$$H_{214} = \sum_{k,\sigma} \Psi^{\dagger}_{k,\sigma} A_k \Psi_{k,\sigma} \tag{4.3}$$

where $\Psi^{\dagger}_{k,\sigma} = (c^{yz\dagger}_{k,\sigma}, c^{xz\dagger}_{k,\sigma}, c^{xy\dagger}_{k,-\sigma})$ are the creation operators for electrons in the t_{2g} orbitals with spin σ (spin-orbit coupling mixes the spin states of the orbitals in the basis vector). The diagonal elements of the matrix A_k are the tight-binding dispersion of the different bands,

$$\begin{aligned}
A_{11} &= -2t_1 \cos(k_y) - 2t_2 \cos(k_x) - \mu \\
A_{22} &= -2t_1 \cos(k_x) - 2t_2 \cos(k_y) - \mu \\
A_{33} &= -2t_3(\cos(k_x) + \cos(k_y)) - 4t_4 \cos(k_x)\cos(k_y) - 2t_5(\cos(2k_x) + \cos(2k_y)) - \mu
\end{aligned}$$

where the hopping strengths, t_i, are shown in Fig.4.7. The off-diagonal terms include a small hopping between the quasi-1D orbitals, and terms due to spin-orbit coupling of the form $\lambda \boldsymbol{S} \cdot \boldsymbol{L}$, where $\boldsymbol{S}$ and $\boldsymbol{L}$ are the spin and orbital angular momentum operators respectively. In the basis of the t_{2g} manifold this coupling gives rise to the terms[69],

$$\begin{aligned}
A_{12} &= -4t_6 \sin(k_x)\sin(k_y) + i\sigma\lambda \\
A_{21} &= -4t_6 \sin(k_x)\sin(k_y) - i\sigma\lambda \\
A_{13} &= A_{31} = -\sigma\lambda \\
A_{23} &= -A_{32} = i\lambda/2
\end{aligned}$$

where the spin state governs the sign of the interaction, $\sigma = \pm 1$. As the spin-orbit interaction couples opposite spins on the $d_{xz/yx}$ and d_{xy} orbitals, the spin is not strictly a good quantum number and is replaced by a pseudospin in the band basis.

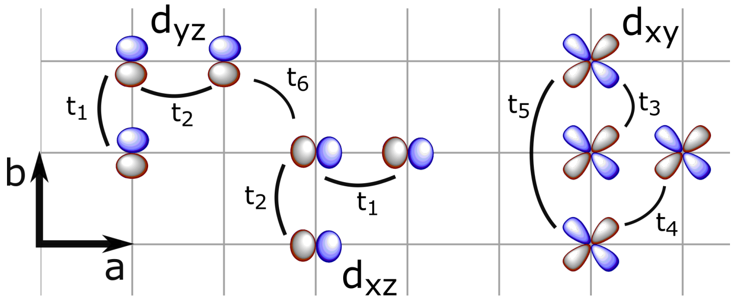

Figure 4.7: Hopping integrals between Ru d-orbitals in the ab-plane as defined in [103].

The bandstructure determined from diagonalising the above tight-binding model using parameters determined from fits to the renormalised band measured by ARPES[103] are shown in Fig.4.6B. It can be seen that the orbital character of the quasiparticle states is strongly angular dependent. Hopping between the $d_{xz/yx}$ and d_{xy} orbitals is forbidden by symmetry[24], however, the spin-orbit coupling results in strong mixing between all d orbitals, particularly along the $\langle 110 \rangle$ where the dispersions in the orbital basis are nearly degenerate at the Fermi-level. A saddle-point in the dispersion of the quasi-2D γ band at the X-point of the Brillouin zone produces a VHS in the density of states (as in the simple 2D dispersion shown in Fig.4.2) very near to the Fermi level.

The presence of a VHS near the Fermi level has a profound effect on the thermodynamic stability of various ordered phases[80]. In Sr_2RuO_4 it is strongly correlated with the superconductivity. Recent transport and magnetisation measurements show uniaxial strain can be used to induce a Lifshitz transition (topological change in the Fermi surface) as the VHS passes through the Fermi-level[104]. This coincides with a peak of the superconducting critical temperature T_c and an enhancement of the upper critical field[105, 106, 107].

As has been discussed in Section 2.4, in the context of the generalised Stoner criterion, an enhancement of the density of states at the Fermi level can drive other forms of order such as charge and spin density waves (C/SDW). Recent theoretical work that only considers the γ band has predicted that before the Lifshitz transition is reached under uniaxial strain, the system becomes SDW ordered due to the nesting at low Q[108]. Fluctuations associated with that nesting are then expected to be intimately related to the superconductivity, yet neutron scattering measurements have so far failed to unambiguously detect them.

	μ	t_1	t_2	t_3	t_4	t_5	t_6	λ	g
Sr_2RuO_4	0.62	0.5	0.05	0.45	0.23	0.03	0	0.142	N/A
$Sr_3Ru_2O_7$	0.575	0.5	0.05	0.5	0.1	-0.03	0.05	0.1375	0.1

Table 4.1: Tight-binding parameters for Sr_2RuO_4 taken from [103] and $Sr_3Ru_2O_7$ taken from [100] (written in units of $2t_1$). The staggered lattice potential (see main text) is only relevant for $Sr_3Ru_2O_7$.

4.3.2 $Sr_3Ru_2O_7$

Due to the different ionic sizes of Ru^4+ and Sr^2+, the layers of RuO_6 octahedra are under strain, which for the $n > 2$ layered compounds induces an octahedral rotation (such rotations are a common feature of perovskites). In $Sr_3Ru_2O_7$ the octahedra rotate about the c-axis by $\approx 7°$, with apical sharing octahedra in each layer of the bilayer structure rotating in the opposite sense lowering the symmetry to the orthorhombic spacegroup *Bbcb* structure that doubles the unit cell, with the new a and b axis at 45° to the Ru-O bond[109] (shown in Fig.4.8A). Neutron diffraction cannot resolve any difference in the Ru-O bond distance in the ab-plane, and no difference is resolved in the electronic transport at zero field[110].

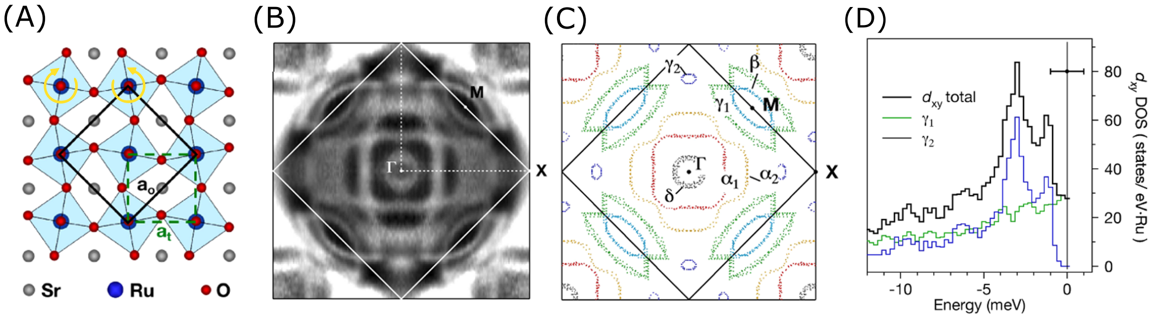

Figure 4.8: (A) Orthorhombic unit cell of a RuO_2 layer (black) and tetragonal unit cell (green). (B) Fermi surface measured by ARPES. (C) Extracted Fermi surface contours and band labels. (D) Density of states obtained from the band contours shown in (C). The horizontal error bar indicates a ±1 meV uncertainty in absolute energy values. Figures taken from [111].

The bilayer splitting and the back-folding of the bands due to the $\sqrt{2}\times\sqrt{2}$ reconstruction of the cell results in a fragmented Fermi surface with six bands (α_1, α_2, β, γ_1, γ_2, δ) shown in Fig.4.8. The nesting along the $\langle 110 \rangle$ direction observed in Sr_2RuO_4 is removed by the reconstruction. As in Sr_2RuO_4, the Fermi level is close to a VHS in the density of states due to a saddle point in the dispersion of the γ_2 near the X-point of the tetragonal Brillouin zone associated with quasi-2D states of predominantly d_{xy} character. Due to the resolution of the photoemission experiments, there is some uncertainty as to whether this band actually crosses the Fermi-level at zero field and dHvA measurements cannot resolve such small orbits[112]. However, the energy of the VHS on the γ_2 is roughly consistent with Zeeman energy for the fields at which the metamagnetic transitions are observed[111].

Puetter *et al.* [100] have shown that the main features of the electronic structure can be reproduced with the tight-binding model for the single-layer Sr_2RuO_4 and a staggered potential, $G = g\mathbb{I}$ with a modulation of $Q = (\pi, \pi)$ to account for the octahedral rotation

$$H_{327} = \sum_{k,\sigma} \Psi^{\dagger}_{k,\sigma} \begin{pmatrix} A_k & G \\ G^{\star} & A_{k+Q} \end{pmatrix} \Psi_{k,\sigma} \tag{4.4}$$

where $\Psi^{\dagger}_{k,\sigma} = (c^{yz\dagger}_{k,\sigma}, c^{xz\dagger}_{k,\sigma}, c^{xy\dagger}_{k,-\sigma}, c^{yz\dagger}_{k+Q,\sigma}, c^{xz\dagger}_{k+Q,\sigma}, c^{xy\dagger}_{k+Q,-\sigma})$, A_k has the same definition as in Eq.4.3. The staggered lattice potential which couples states with momenta k and $k+(\pi,\pi)$ seems to reproduce most bands adequately, though the addition of staggered inter-layer hopping is necessary to recover the α_2 band (for the purposes of this discussion such complexity is not required). The δ band is due to $d_{x^2-y^2}$ orbital states from the e_g manifold which are not included in the model, however, this band has a very small Fermi-velocity and is not expected to influence the physical properties a great deal[113].

The parameters of the model published in [100] are summarised in Table.4.1. The chemical potential has been determined by the requirement that the bands be occupied by a total of 4 electrons per Ru ion. The resulting Fermi surface along with the orbital character (determined from the eigenvectors of the Hamiltonian) is shown in Fig.4.9C, which agree well with the ARPES data. It can be seen that the α_1 and β bands are due to hybridisation of the bilayer split quasi-1D sheets derived from the $d_{xz/yz}$ orbitals. The $\gamma_{1/2}$ bands are due to hybridisation of the quasi-2D d_{xy} and the bilayer split 1D bands, which give rise to two VHS above/below the Fermi-level respectively with majority d_{xy} character (see Fig.4.9). The peaks in the density of states are associated with saddle-points in the dispersion that occur near the X-point of the tetragonal BZ. Fig.4.9C shows the constant energy surfaces at the filling of the saddle-points. It can be seen that if a magnetic field were to drive the chemical potential to coincide with the VHS, the Fermi surface would undergo a topological Lifshitz transition[80].

The SDW order coincides with the metamagnetic transition in $Sr_3Ru_2O_7$. But from Fig.4.9C & 4.9D it can be seen that the parallel sections derived from the quasi-1D states ($d_{xz/yz}$ character), that would naively provide the nesting along the direction SDW order is observed, do not change drastically as the VHS on the γ_2 band approaches the Fermi-level, at least in the rigid-band picture. To understand the coincidence of SDW order and metamagnetism it is necessary to properly account for the effect of the magnetic field on the electronic structure and in particular the role of spin-orbit coupling, which hybridizes the quasi-1D bands and 2D bands with opposite spins.

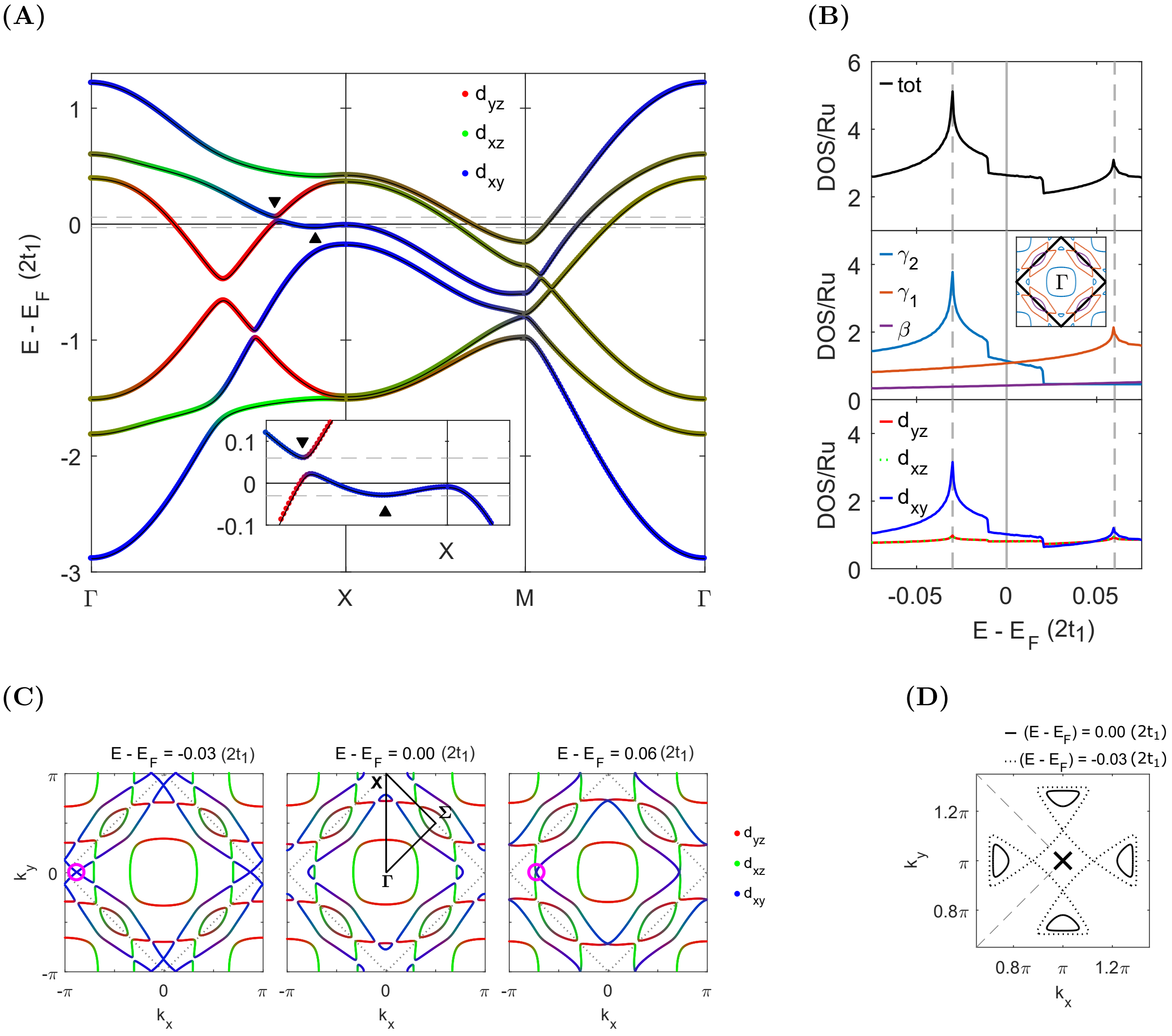

Figure 4.9: Tight-binding electronic structure of $Sr_3Ru_2O_7$ using the model published in [100]. (A) Dispersion of the bands along high-symmetry directions. The black arrows correspond to the location of the saddle points which give rise to the VHS (B) The total density of states (top) and the partial density of states in the band (middle) and orbital (bottom) basis. (C) The Fermi surface (middle) and the constant energy contours at different fillings corresponding to the position of the energy of the VHS at $E - E_F = -0.03$ and 0.06 $(2t_1)$, marked by pink circles (left and right respectively). The dotted lines mark the 2D orthorhombic Brillouin zone edge. (D) The contour of the γ_2 band at the Fermi level and at $E - E_F = -0.03$ $(2t_1)$ which shows the flat 1D section is relatively insensitive to the VHS. The cross marks the location of the X-point and the dashed lines mark the 2D orthorhombic Brillouin zone edge.

Chapter 5

Spin density wave order in $Sr_3Ru_2O_7$ for a magnetic field along the c-axis

---

Motivated by recent low-temperature measurements of the heat capacity, the SDW phase diagram is determined from systematic neutron diffraction measurements. The phase boundaries are found to be consistent with the published phase diagram from a combination of thermodynamic probes. No SDW order is observed in the vicinity of the putative low-field QCP at 7.5 T. In addition the field-dependence of the SDW wavevector is reported which exhibits qualitatively different behaviour to that observed at the ferromagnetic QCP in $NbFe_2$. This result places constraints on any candidate nesting vectors. The adjacent SDW-A & B phases are consistent with nesting on different sheets and exhibit the same functional form for the temperature dependence of the order parameter. There is no evidence that the SDW-B phase formation should exhibit qualitatively different thermodynamic signatures than the SDW-A phase, as has been suggested.

5.1 Progress since the discovery of spin density wave order

The discovery of spin-density wave order in the quantum critical region of the metamagnetic transition in $Sr_3Ru_2O_7$ solved the long-standing puzzle of the enhanced resistivity and observed anisotropy in transport[88, 89, 12] (and other properties [114]) for a field within $\lesssim 10°$ of the c-axis (perpendicular to the bilayer planes). It also prompted a renewed interest in the thermodynamic phase diagram of $Sr_3Ru_2O_7$ and in particular the boundary of the SDW-B phase and the signatures of quantum criticality.

For a magnetic field applied along the c-axis of $Sr_3Ru_2O_7$ (perpendicular to the bilayer plane), there are three peaks in the real part of the AC susceptibility at low temperature ($T \lesssim 0.5$ K)[92]: what was previously assumed to be a crossover at $B_0 \approx 7.5$ T [115, 92] and two first-order transitions at low temperature $B_1 \approx 7.85$ T and $B_2 \approx 8.07$ T, which Lester *et al.* discovered bounded a spin-density wave phase (SDW-A), with an abutting phase (SDW-B) terminating at $B_3 \approx 8.4$ T where AC susceptibility measurements do not detect a peak[1]. In retrospect, the most obvious signature of the SDW-B phase in thermodynamic probes is the coincidence of the transition temperature ($T_N \sim 0.5$ K at 8.15 T, the only field for which the temperature-dependence of the SDW-B Bragg scattering was measured by Lester *et al.*[1]) with the temperature at which the transition at B_2 becomes first-order (as seen in AC susceptibility data[92]).

The transition at B_1 roughly coincides with the extrapolated position of the metamagnetic quantum critical point[92, 116]. Indeed thermodynamic measurements observe a large accumulation of entropy [115] at this field which is not removed by the SDW order: both phases having larger entropy than the low and high-field paramagnetic phases at the same temperature. This is unexpected and has drawn analogies with the Pomeranchuk effect in ^{3}He[117].

A similar accumulation of entropy at low temperature is seen in the vicinity of the metamagnetic feature at B_0, which was previously believed to be a broad crossover rather than a continuous transition. Two recent studies by Sun *et al.*[117] and Tokiwa *et al.*[118], which have extended heat capacity and magnetocaloric measurements to lower temperatures than previously possible (< 0.2 K), have suggested that the field dependence of the specific heat coefficient, C/T, and the magnetic Grüneisen parameter, $\Gamma_H = (dM/dT)/C$, are actually consistent with an additional field-tuned QCP at B_0[118, 117]. Fig.5.1A shows the magnetic Grüneisen parameter goes from negative to positive with increasing field, indicating an increase in entropy either at the border of an ordered phase (as at B_1) or a QCP. The low-field data show the critical scaling expected for a 2D metamagnetic quantum critical point (additional scaling of the temperature dependence at different fields was also reported)[118].

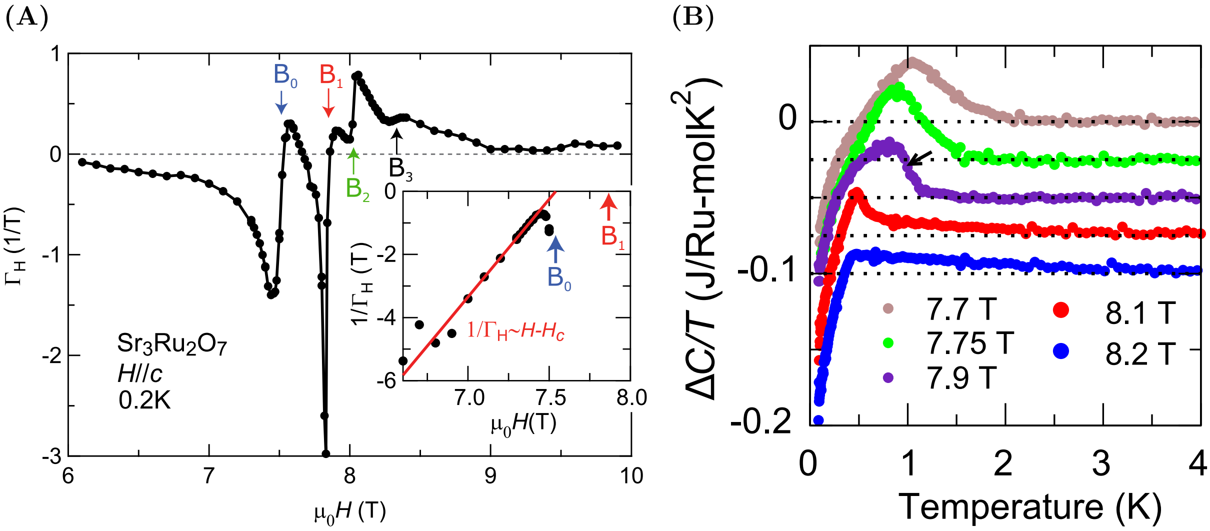

Figure 5.1: (A) Magnetic Grüneisen parameter taken from [118], labels have been altered to match the schematic phase diagram in Fig.4.5. Inset shows the scaling expected for a field-induced QCP at B_0. (B) Specific heat capacity coefficient at select fields after subtraction of the logarithmically diverging background at 7.9 T extrapolated to low temperatures, taken from [117]. The black arrow indicates the transition temperature at 7.9 T. Offset vertically for clarity.

Prior to the discovery of the SDW-B phase there was no evidence of a high-field phase boundary for $B > B_2$ in other thermodynamic properties such as heat capacity [115, 116]. The latest heat capacity and magnetocaloric data shows only weak anomalies in heat capacity and magnetocaloric measurements associated with the SDW-B phase, that in isolation are not characteristic of an equilibrium phase transition[118, 117]. In particular, the weak and broad nature of the anomaly in the heat capacity when entering the SDW-B phase from high-temperature (shown in Fig.5.1B) has led to speculation the SDW-B phase could be more sensitive to disorder and possibly even host glassy rather than long-range order[117].

5.2 Motivation

Motivated by the new thermodynamic data, a systematic investigation of the field-temperature phase diagram by neutron diffraction was performed with the following aims.

Firstly to confirm that the weak anomalies in the latest heat capacity and magnetocaloric data coincide with the onset of magnetic Bragg scattering and in particular to measure the temperature dependence of the SDW order parameter in both phases so as to establish whether there is any evidence that the phase formation differs from that observed in the SDW-A phase.

Secondly, to investigate the possibility of SDW order between the location of the putative additional metamagnetic quantum critical point at B_0 and the low-field SDW-A phase boundary at B_1. There appears to be a correlation between metamagnetic quantum criticality and SDW order in $Sr_3Ru_2O_7$ and an additional abutting SDW phase at low field would explain several unusual aspects of the phase diagram. It would provide a natural explanation for the temperature at which the transition at B_1 becomes first-order (by analogy with the behaviour of the boundary between the SDW-A & B phases at B_2) and the increase in entropy upon entering the SDW-A phase from low-field.

Thirdly, to investigate the possibility that the SDW order is driven by an intrinsic instability to long-wavelength magnetic order at a ferromagnetic QCP. It has been predicted that soft quantum critical fluctuations give rise to nonanalytic terms in the free energy which drive the transition first-order and produce a singular q-dependence in the susceptibility of the form $\chi_q^{-1} \sim q^2 \ln(q)$[119, 120, 121, 122]. Such a scenario is thought to be the origin of the SDW order masking a FM quantum critical point in the band magnet $Nb_{1-y}Fe_{2+y}$[123], which displays a characteristic dependence of the SDW wavevector decreasing towards the ferromagnetic transition as a function of temperature and doping. In $Sr_3Ru_2O_7$ the situation might be somewhat different as the SDW fluctuations dominate at low temperature at all fields well away from quantum criticality. They are believed to be related to nesting between Fermi sheets[72, 73], in which case the field-dependence of the SDW wavevector will be related to evolution of Fermi-surface which changes rapidly as function of field near the metamagnetic transitions.

5.3 Experimental Details

5.3.1 Overview of the contributing experiments

Neutron diffraction measurements were performed on the WISH diffractometer [50], a white-beam time-of flight (TOF) instrument at the ISIS spallation source, UK. This chapter contains data from three separate experiments.

The first experiment in February 2014 (#1) was performed by C. Lester and S. Hayden and led to the first discovery of SDW order (as published in Lester *et al.* [1]). These data have been re-analysed by fitting the peaks with a more conventional peak shape (back-to-back exponential convoluted with a Gaussian [1]) from which the magnetic field dependence of the SDW wavevector has been extracted.

Subsequent experiments (#2 and #3) were performed by the author and S.M. Hayden in September and November 2016 with two principal aims: (1) to look for SDW order near the putative metamagnetic QCP at $B_{c0} \approx 7.5$ T; (2) to investigate the high temperature phase boundary of the SDW-B phase, to confirm that the weak anomalies in recent thermodynamic measurements are associated with the onset of the magnetic Bragg scattering and to establish whether there is any evidence that the phase formation differs from that observed in the SDW-A phase by comparing the temperature dependence of the SDW intensity.

5.3.2 Experimental Procedure

A single crystal of $Sr_3Ru_2O_7$ of mass 0.1 g (previously used in Lester *et al.* [1]) was grown by the travelling solvent floating zone technique in an image furnace (by C. Lester and R. Perry at ISIS, UK). Resistivity and magnetization measurements performed by C. Lester and T. Croft confirmed the high sample quality. The sample has a residual resistivity $\rho_{res} < 1$ $\mu\Omega$cm which is comparable with samples used in other studies [87, 88, 89] and SQUID magnetometery found no evidence of ferromagnetic minority phases for $T \geq 2$ K. More details about the sample characterization can be found in the supplementary information of Lester *et al.* [1].

The sample was mounted on an aluminium post with 50 μm diameter aluminium wire, aligned with backscattering x-ray Laue diffraction, then coated in CYTOP fluorinated glue to provide additional rigidity and better thermal contact with the post.

All experiments followed the same procedure, the sample was mounted in a dilution refrigerator with a cryomagnet and measurements were made in the temperature range (0.05-1.2 K). The data presented here concern scattering with momentum transfer along one direction, $\boldsymbol{a}^*$, which scattered at an angle of $2\theta = 17°$ - corresponding to a wavelength of $\lambda = 4.93$ Å and 5.27 Å for the SDW-A and SDW-B Bragg peaks at positions $\boldsymbol{Q} = (0.233, 0, 0)$ and $(0.218, 0, 0)$ respectively. Reciprocal space has been indexed using the aristotype tetragonal unit-cell for $Sr_3Ru_2O_7$ with the a and b axes are parallel to the Ru-O bond in the bilayer plane ($a = b = 3.89$ Å). As previously discussed, there is a small orthorhombic distortion and $\sqrt{2} \times \sqrt{2}$ reconstruction due to a rotation of the RuO_6 ochathedra, but it is conventional to use the tetragonal unit cell [72, 124, 73] as the Ru-O

---

[1] A typical profile for a Bragg peak on a white-beam time-of-flight diffractometer that accounts for the asymmetry introduced by the pulse shape from the moderator.

bonds are equal within experimental uncertainty [109] .

It should be noted that a different cryomagnet was used in 2014 (experiment #1) and 2016 (experiments #2 & #3) which produced different backgrounds and transmission that can be seen in the raw data.

5.3.3 Data processing

Data from exp #1 were re-analysed in the same manner as the subsequent experiments. The counts were normalised by the proton charge accumulated at the ISIS target station (as a measure of integrated neutron flux at the sample) and to the wavelength spectrum of the closest monitor upstream of the sample. The data were then corrected for the Lorentz factor.

A cut along the [1,0,0] direction was made by combining d-spacing spectra of pixels in the solid angle subtended by the magnetic Bragg peak on the position sensitive detector bank using the 'DiffractionFocussing' algorithm in the Mantid software[125].

For each experiment a background was subtracted by fitting a cubic polynomial to a combination of high-temperature and high/low-field runs that did not exhibit SDW order. The integrated intensity of the SDW-A and SDW-B Bragg peaks were found by summing the counts over a d-spacing range of 16.05-17.30 Å and 17.45-18.70 Å respectively. This was necessary because there were a significant number of runs in exp #2 & #3 which were counted for less than 20μAh of proton charge and did not have sufficient statistics to fit the weak magnetic Bragg peaks reliably. The summation is a valid method of determining the integrated intensity because of the negligible overlap of the SDW-A and SDW-B peaks. The sum of the counts was in excellent agreement with the integrated intensity extracted from fits to the data with sufficient statistics using the analytical expression for a Gaussian peak convoluted with a back-to-back exponential in Eq.3.73.

5.4 Results

5.4.1 Consistency of different experiments

To allow for quantitative comparison, the data in experiments #2 and #3 were scaled to the data published in [1] where the size of the ordered moment at 7.95 T in the SDW-A phase was established to be 0.10 ± 0.02 μ_B/Ru [1].

Fig.5.2 shows the integrated intensity of the SDW peaks as a function of field at base temperature (0.05 K) in the three experiments before and after the scaling. The marker indicates the sweep direction of the field (up, field-cooled, down) and it can be seen that the SDW intensity does not exhibit any resolvable hysteresis. Aside from a scale factor, there are two notable discrepancies between the data from experiment #1 and the subsequent experiments #2 and #3. Firstly, the ratio of the maximum SDW-A/SDW-B intensity in experiment #2 is roughly 60% smaller than in experiment #1. This discrepancy could be due to a combination of extinction and absorption effects in the sample, and transmission of the different magnets. The latter probably dominates as a rough calculation of the transmission for path-length through the short/long axis of the sample produces an order of magnitude smaller effect. Secondly, it can be seen that the SDW-A peak intensity disappears at a slightly higher field near $B_2 \approx 8.1\ T$ in experiment #1 [2], presumably due to the calibration of the different magnets that were used.

The data from experiment #1 were interpolated in the shaded regions indicated in Fig.5.2 and then scaled to each of the subsequent experiments with the ratio of the scale factors for the SDW-A and SDW-B phases constrained to be the same for both experiments. The inverse of this scaling was applied to the intensities in experiments #2 and #3 such that the intensities were consistent with those in exp #1. In addition, a field shift (the same for both experiments and SDW phases) was also included in the fit to account for the difference in magnet calibration. The optimal field-shift was found to be +0.025(1) T.

The axial displacement of the sample from the magnet center can also produce a slightly lower field than expected - in this case the field-shift would not be expected to be the same for the two experiments and would be a fraction of the field applied, rather than a constant. The field homogeneity of the magnet used in experiment #2 and #3 has been measured by a Hall probe (not by the author). An axial displacement of $\sim$ 2 mm would give a shift of $\sim$ 0.025 T at 8 T. This displacement is reasonable as the sample positioning did account for the thermal contraction of the sample rod, however there were insufficient reflections measured at different orientations to constrain the sample position to that precision.

5.4.2 Field dependence of SDW intensity

Fig.5.3 shows the magnetic field dependence of the SDW intensity at base temperature (0.05 K) from experiment #1 and published resistivity [88] and the AC susceptibility

---

[2] From inspection the discrepancy is of the order of $\approx$ 0.025 T between experiment #1 and subsequent experiments (the smallest field spacing used in experiment #1) which is consistent with the fitted field offset (see main text)

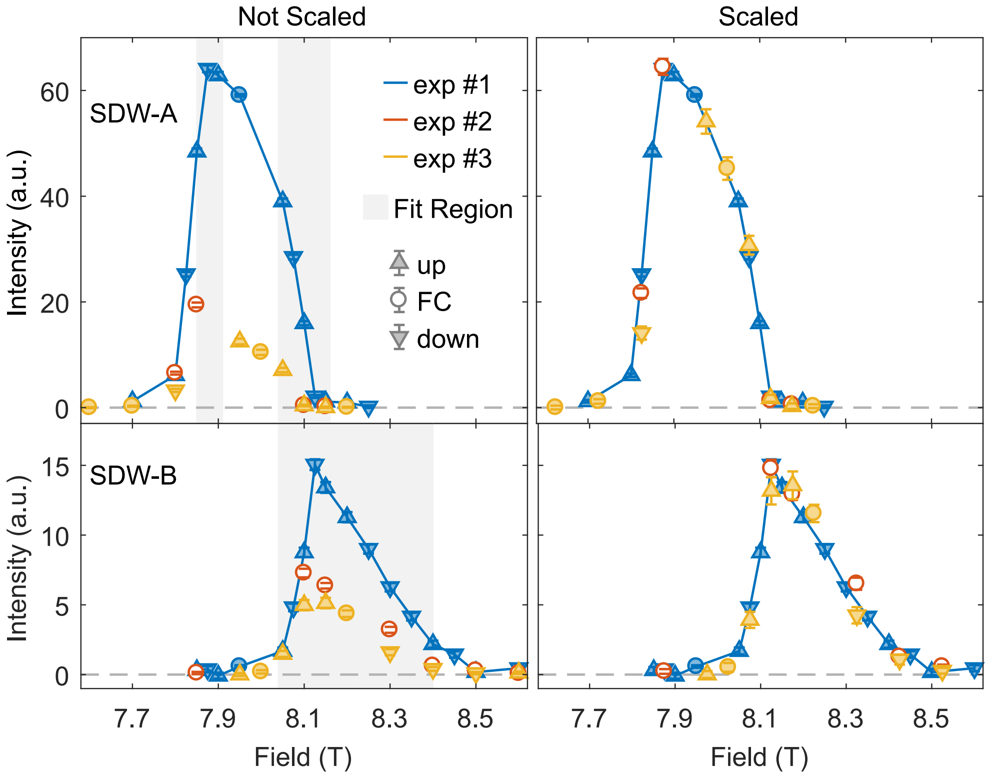

Figure 5.2: The intensity of the magnetic Bragg peaks associated with the SDW-A (Top) and SDW-B (Bottom) phase for the three experiments before scaling (left) and after scaling (right) as a function of magnetic field at the lowest temperature measured 50 mK. The scaling involved interpolating the intensity of experiment #1 in the shaded regions indicated (see main text for details). The marker denotes the direction of the field sweep (see legend). Lines are guides to the eye.

data [92]. In the absence of SDW order (e.g. when the field is tilted sufficiently far from the c-axis) the metamagnetic transition at B_1 produces a step-like jump in the resistivity[88] (denoted by ρ_{mm} in Fig.5.3) that is seen in other metamagnetic materials such as $CeRu_2Si_2$ [126]. The ratio of the increased resistivity inside the SDW-A and SDW-B phase agrees well with the ratio of the maximum magnetic Bragg peak intensity in the two phases (proportional to the square of the SDW order parameter). Though it is important to note there are other factors that could influence the resistivity in the SDW ordered phase: the reduction in carrier density (due to the SDW gap) may be partially cancelled out by factors such as a decreased scattering rate arising from a reduction in the density of final states available to electron scattering processes (as has been proposed to occur in the charge density wave state of the rare-earth tritellurides[127]).

The low-field onset of the SDW-A and SDW-B intensity are linear in magnetic field, in both cases going from the background to the maximum intensity over a narrow field range of ≈ 70 mT. This is comparable to the width of the peak in the AC susceptibility data [92] shown in Fig.5.3 (and in other probes such as heat capacity [115]). The maximum of the SDW-B phase intensity coincides with the field at which the A-phase intensity disappears. The phase boundary B_1 and B_2 have been taken to be the field which corresponds to half the maximum intensity of the low-field onset of the SDW-A and SDW-B phase respectively (extracted through linear fits), which agree well with the peaks in the AC susceptibility. The high-field phase boundary of the SDW-B phase (B_3) has been found by the extrapolation of a linear fit to the SDW-B intensity in the field-range $8.125 - 8.35$ T. As previously stated, there is no peak in the AC susceptibility at B_3. The weak anomalies in the magnetic Grüneisen parameter in Fig.5.1A are at a slightly lower field of 8.35 T. This discrepancy might be due to the the presence of critical scattering in the vicinity of B_3.

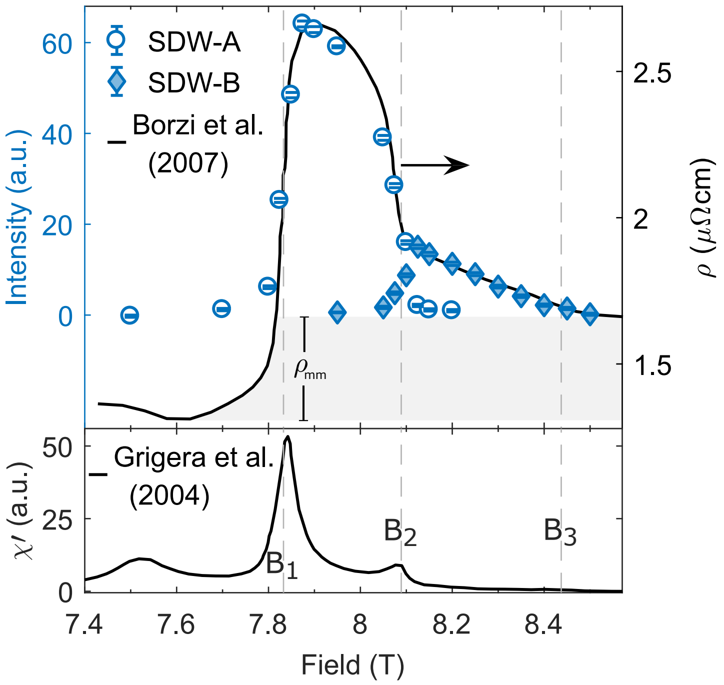

Figure 5.3: (Top) The intensity of the two SDW Bragg peaks as a function of field at 50 mK from experiment #1. The black line is the magnetoresistivity along an in-plane tetragonal axis taken from [88]. The jump in resistivity due to the metamagnetism ρ_{mm} is shaded. (Bottom) The AC susceptibility measured at a frequency of 17 Hz taken from [92]. The dashed vertical lines represent the transition fields B_{1-3}

5.4.3 No evidence of SDW order near B_0

In Fig.5.3, there is a peak in the AC susceptibility at $B_0 = 7.53$ T that is thought to correspond to a metamagnetic cross-over that has recently been proposed to be a QCP (due to the end-point of another metamagnetic transition)[118, 117]. Fig.5.4 shows the scattering along [1,0,0] direction (parallel to wavevector of the SDW-A and B phases) at select magnetic fields in the vicinity of B_0 and at 7.7 T which corresponds to the low-field onset of SDW-A Bragg peak intensity. Within the statistics there is no evidence of SDW order along that direction.

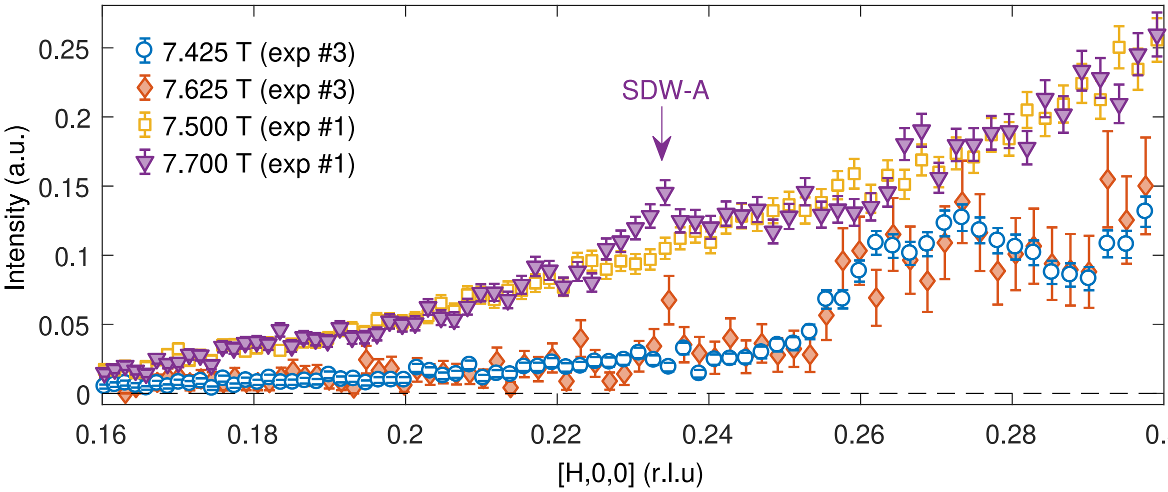

Figure 5.4: Data from two experiments of the scattering parallel to $\boldsymbol{q_{SDW}}$ of the SDW-A & B phases at fields near the putative QCP at $B_0 = 7.5$ T. The arrow indicates the location of the SDW-A Bragg peak which onsets at 7.7 T.

5.4.4 Field-dependence of the SDW wavevector

Fig.5.5A shows data from experiment #1 having swept the field (up) at base temperature (0.05 K). The Bragg peaks due to both phases are well resolved at 8.1 T, and the peak centre is observed to shift with magnetic field. The Bragg peaks were fitted with a back-to-back exponential convoluted with a Gaussian as a function of d-spacing and transformed to $\boldsymbol{Q}$ for display in Fig.5.5A using the observed lattice parameter $a = 3.89$Å. The rising and decaying exponential parameters were refined globally (i.e. the same parameters for both SDW-A and SDW-B peaks at all fields).

Fig.5.5B shows the fitted peak centre as a function of magnetic field for all the data taken at base temperature in experiment #1. It can be seen that the wavevector of the SDW-A/SDW-B phases increase/decrease linearly with the field - a trend that is present in all experiments. There may be some effect of hysteresis on the wavevector of the SDW-A phase due to the first-order nature of the phase boundaries at B_1 and B_2. The field-cooled data point at 7.95 T agrees well with the fitted line that represents the average of the up/down sweeps.

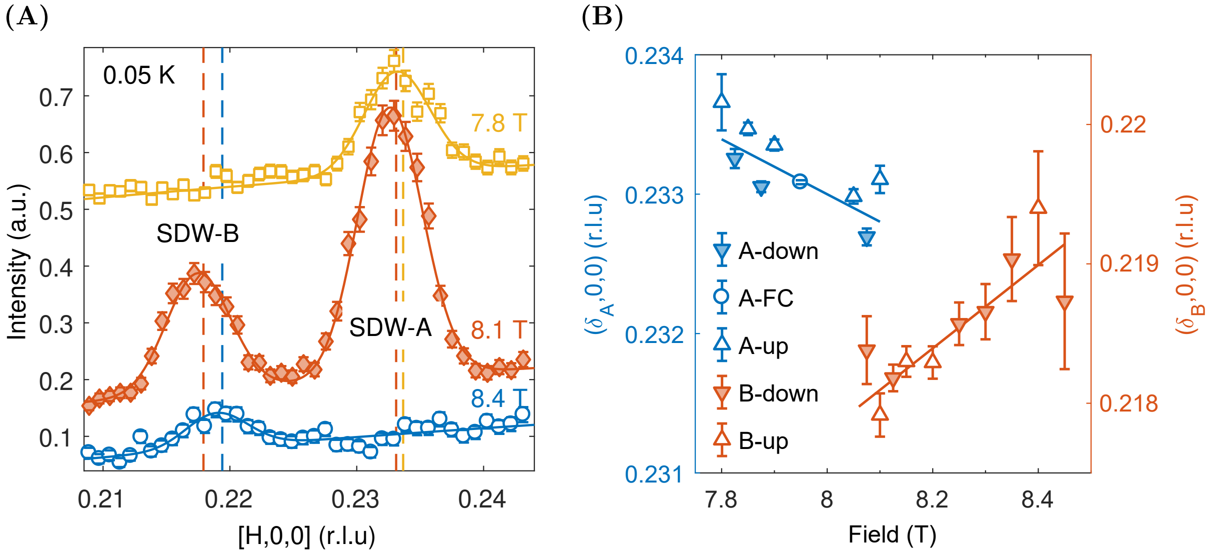

Figure 5.5: (A) Raw data from experiment #1 at 0.05 K for scattering parallel to $\boldsymbol{q}_{\mathrm{SDW}}$ at select magnetic fields (offset for clarity). Dashed lines indicate the peak centre. (B) The magnetic field dependence of the SDW wavevector for the two phases, the marker indicates the direction of the magnetic field sweep. Lines are fits to the combined data (up, down and field-cooled).

Comparison of the temperature dependence of the SDW phases

It can seen in Fig.5.6 that the temperature dependence of the integrated intensity of the SDW Bragg peaks does not exhibit a sharp transition at T_{N}, rather the transition is rounded and broad (relative to T_{N}).

The energy-integrated intensities from a white-beam TOF diffractometer such as WISH will measure a portion of critical scattering in the vicinity of T_{N} which could contribute to the broadness of the transition. Additionally, though the sample used here is of excellent quality, the SDW phases are extremely sensitive to disorder which can also produce such a broad transition. This is seen in the doped Fe-based superconductors, where it is common to extract critical exponents by assuming a Gaussian distribution of T_{N} with a standard deviation of σ_{N} [128, 129, 130]. Such an analysis relies on the assumption that the order parameter still obeys a single power law outside of the region ($T < T_{\mathrm{N}} - \sigma_{\mathrm{N}}$). Due to the width of the transition relative to the low T_{N}, it is not clear such an assumption is valid in $Sr_3Ru_2O_7$. Thus it is preferable to model SDW intensity over the entirety of the temperature range $0.05 \leq T \leq T_N$.

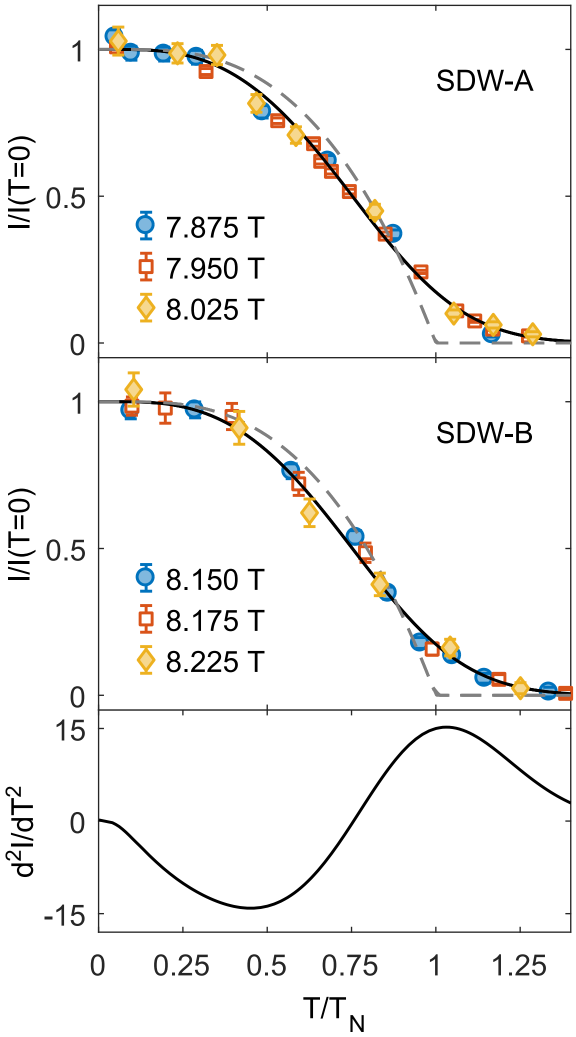

Figure 5.6: The intensity SDW Bragg peaks for the two phases A (Top) and B (Middle) at select magnetic fields (from all experiments) fitted to the BCS order parameter with a Gaussian distribution of T_N (same fraction of T_N for the both phases) shown by the solid black line. The BCS order parameter for the average T_N is shown by the grey dashed line. Data are normalised by the zero temperature intensity and plotted as a function of T/T_N such that the intensity for two SDW phases at all fields fall onto the same line. (Bottom) The second derivative of the BCS order parameter with a Gaussian distribution of T_N fit is shown to have a maximum within 3% of the average T_N of the fit.

Fig.5.6 shows data from all three experiments fitted with the square of the BCS order parameter in Eq.2.40 (recall that the magnitude of the ordered moment, m_q, is proportional to the SDW order-parameter, Δ, in the mean-field framework of Section

2.5.2) with a Gaussian distribution of T_{N} such that,

$$I(T) = \int_{-\infty}^{\infty} dt_{\mathrm{N}} \frac{1}{\sigma_{\mathrm{N}}\sqrt{2\pi}} e^{-\frac{1}{2}\left(\frac{t_{\mathrm{N}}-T_{\mathrm{N}}}{\sigma_{\mathrm{N}}}\right)^2} m_q(T)^2 \tag{5.1}$$

where σ_{N} was constrained to be the same fraction of the average T_{N} for all fields in both SDW phases (such that the normalised data for each phase falls onto the same curve as shown in Fig.5.6). The convolution was performed numerically for $|t_{\mathrm{N}}| < 6\sigma_{\mathrm{N}}$. The optimal σ_{N} is a significant fraction of T_{N} (approximately 20%), hence the convoluted fit deviates significantly from the square of Eq.2.40 above the temperature at which the moment saturates. Nevertheless, the model agrees well with the data within the statistical uncertainty at all fields in both SDW phases. The temperature dependence of the order parameter in the two phases appears to follow the same functional form. The temperature-dependence of the resistivity exhibits a similarly broad transition, with T_{N} taken to be the maxima of the second-derivative of the resistivity [92]. Fig.5.6) shows that the second-derivative of the fit to Eq.5.1 has a maxima within 3% of the average T_{N}.

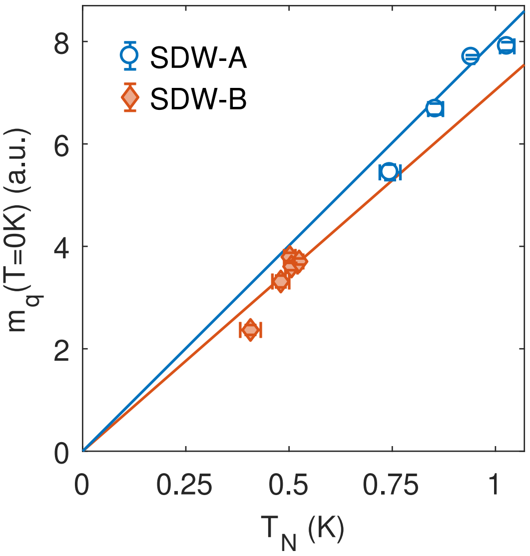

Figure 5.7: The fitted zero temperature SDW order parameter against the average T_{N}. The lines are guides to the eye with a gradient equal to the average ratio of $m_q(0)/T_{\mathrm{N}}$ for each phase, passing through the origin as expected for the BCS model.

The validity of the extracted T_{N} is supported by the observation that T_{N} is proportional to $m_q(0)$ as shown in Fig.5.7 (as expected in the BCS mean-field phenomenology) - though small systematic differences in the intensity between experiments may persist post-scaling. The ratio $m_q(0)/T_{\mathrm{N}}$ (the gradient in Fig.5.7) for the different fields in each phase are consistent, however the SDW-B phase ratio is about 12% smaller than the

SDW-A phase (a statistically significant difference). This discrepancy is much larger than the differential absorption predicted from the wavelength dependence of the absorption cross-section ($\lesssim 1\%$), but much smaller the systematic difference between the ratio of the SDW-A/SDW-A intensities between experiments #1 and more recent experiments #2 & #3.

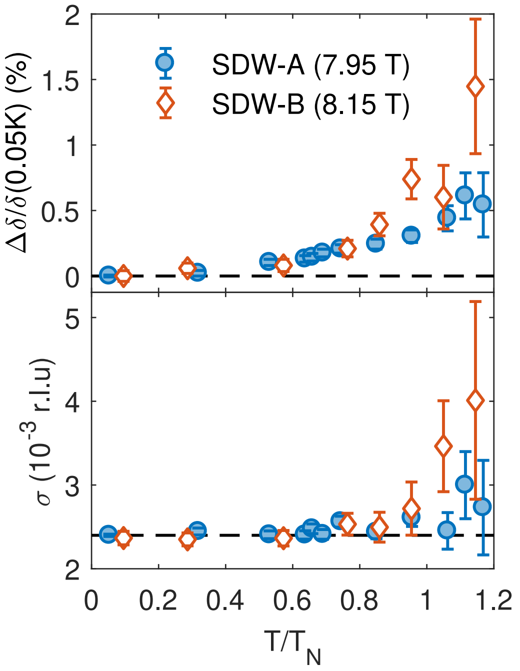

Figure 5.8: (Top) Fractional change in the SDW wavevector $\boldsymbol{q}_{\mathrm{SDW}} = (\delta, 0, 0)$ (Bottom) Gaussian standard deviation from fits of the a back-to-back exponential convoluted Gaussian to the data at two fields which exhibit each of the SDW phases in experiment #1. Data are plotted as a function of T/T_{N} from the BCS order parameter fits. The black dashed line represent the base temperature value for the SDW-A phase.

Fig.5.8 shows the temperature dependence of the fractional change in the SDW wavevector $\boldsymbol{q}_{\mathrm{SDW}} = (\delta, 0, 0)$ and the change in Gaussian standard deviation, σ (a parameter of the back-to-back exponential convoluted with a Gaussian profile using the same rising/decaying exponential parameters determined from the field-dependent fits) for data from experiment #1 at two magnetic fields which were counted for the largest proton charge. The wavevector of both the SDW-A and B phases increases with temperature which is typical for density waves in itinerant systems[131]. At T_{N} the wavevector is approximately 0.5% larger than at base temperature for both phases - which is comparable to the magnitude of the change with field over the extent of the phases.

At base temperature the Gaussian component of the SDW-A and SDW-B Bragg peaks have a standard deviation of approximately $\sigma = 0.0024$ r.l.u. which is consistent with the width of a longitudinal cut of the SDW-A Bragg peak at 7.95 T observed on LET (0.0026 r.l.u.)[1]. This indicates that the back-to-back exponential adequately captures the broadening due to the pulse-width, which is the dominant contribution to the resolution. However, before extracting a correlation length $\xi = 1/\sigma$ it is important to quantify the broadening from the other contributions to the resolution. The resolution $\Delta d/d$ is expected to be constant at fixed 2θ (see Section 3.6.2) and can be estimated from a nuclear Bragg peak at a similar 2θ which can be assumed to be close to resolution limited. A nuclear Bragg peak at $2\theta = 19°$ was fitted with a back-to-back exponential convoluted with a Gaussian. The standard deviation of the Gaussian component was approximately $\approx$ 0.5% of the d-spacing (d = 2.4Å). Under the assumption that the peak and resolution widths add in quadrature (i.e. the final variance is the sum of the variances of the individual contributions) the intrinsic (resolution de-convoluted) width of the SDW-A peak is approximately σ = 0.0021 r.l.u. - i.e. the SDW Bragg peak is not resolution limited [3]. The estimated correlation length of the SDW order is then $\xi \approx 300$ Å (roughly 77 lattice parameters, a). Above T_{N} the width of the SDW Bragg peaks (in particular for the SDW-B phase) increases as would be expected with the onset of critical scattering.

5.4.5 Phase Diagram

The temperature dependence of the integrated Bragg intensity at select magnetic fields is shown in Fig.5.9. It can be seen that the SDW-A phase is suppressed at low temperatures for fields 7.825 T and 8.125 T. The latter is associated with the onset of the SDW-B phase and is shown more clearly in the raw data (post-background subtraction) shown in Fig.5.10. Due to the width of the first-order transition at B_2 the Bragg scattering due to SDW-A and SDW-B order coexists in a narrow field-range.

The low-temperature suppression of the SDW-A phase agrees well with the curvature of the phase boundary as measured by AC susceptibility [92]. No suppression of the SDW-B phase was observed at low temperature near B_2 or B_3. The curvature of the first-order phase boundary is governed by the sign of the change of entropy and ferromagnetic moment by the Clausius-Clapeyron relation[4]. The suppression of SDW-A at low

---

[3] In actuality the same intrinsic width can be recovered from consideration of the FWHM of the entire back-to-back convoluted Gaussian curves rather than just the Gaussian component. However the quadrature summation is only strictly valid for convoluted Gaussian distributions and the TOF broadening/back-to-back exponential is asymmetric

[4] Clausius-Clapeyron relation dictates that the curvature of the magnetic field-temperature phase boundary is given by $\mu_0 dH_c/dT_c = \Delta S/\Delta M$, where ΔS is the change in entropy and ΔM the bulk magnetisation. This can be derived from the Gibbs free energy, $dG = -SdT - \mu_0 MdH$, which at a first

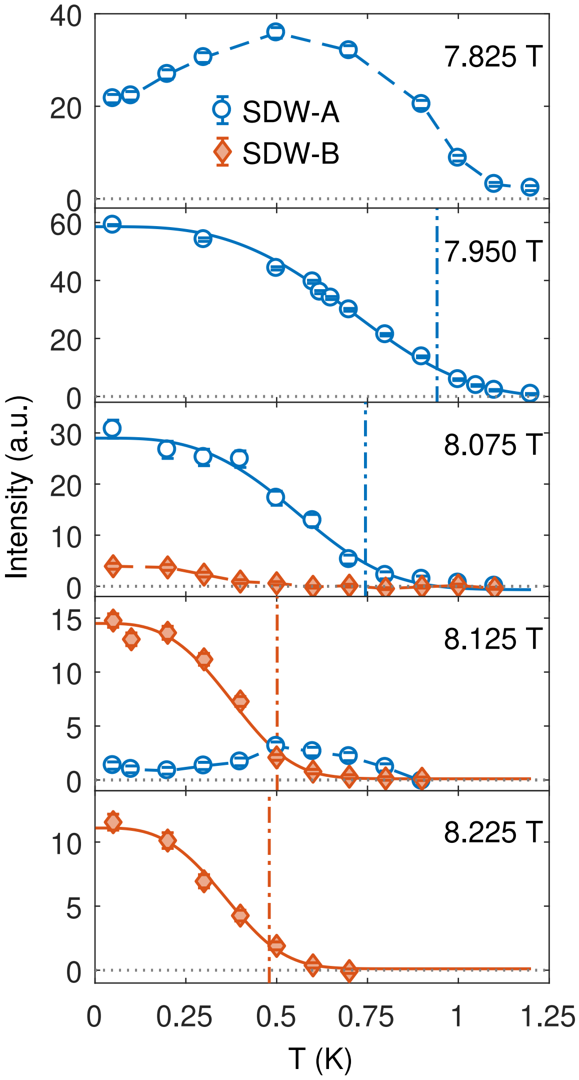

Figure 5.9: Temperature dependence of the SDW intensity at selected fields. Solid lines are BCS fits, dashed lines are guides to the eye and dashed-dot lines indicate the average T_N from the BCS fit.

temperatures indicates the A-phase has a higher entropy than the adjacent low-moment paramagnetic phase and the SDW-B phase, in agreement with magnetisation and heat capacity measurements [133].

Fig.5.11 shows the phase diagram as measured by a combination of thermodynamic probes (for a review see [9]) with the boundary extracted from the neutron data presented here (including the field-dependent points at base temperature, 0.05 K). The extracted T_N agree well with the published phase boundary. The largest discrepancy is at the

---

order phase boundary is the same for both phases. For a detailed derivation the reader is referred to the textbook[132].

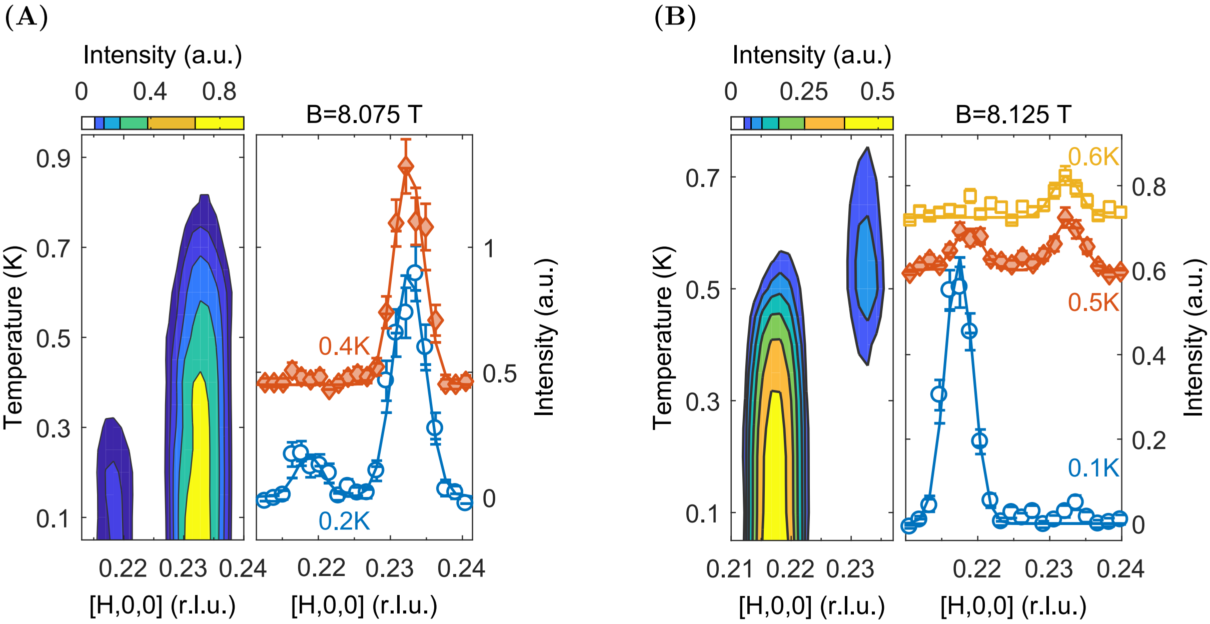

Figure 5.10: Contours of the (smoothed) scattering intensity parallel to $\boldsymbol{q}_{SDW}$ and temperature (post subtraction of a temperature independent background) alongside the raw data at select temperatures (offset for clarity and to match the temperature on the contour plot). Data are shown for two fields: at 8.075 T measured in experiment #3 (A) at 8.125 T measured in experiment #2 (B) that demonstrate the low temperature suppression of the SDW-A intensity and curvature of the phase boundary at B_2.

high-field SDW-B phase boundary determined from the linear extrapolation of the base-temperature data (0.05 K) from experiment #1.

5.5 Discussion

5.5.1 Static long-range SDW order

The SDW Bragg peaks seen on WISH are consistent with long-range order with a correlation length of $\xi \approx 300$ Å (77 unit cells) - estimated under the assumption that a nuclear Bragg peak at a similar scattering angle was resolution limited and the TOF broadening due to the moderator pulse width could be modelled with a back to back exponential. This is comparable to other density wave systems, for example $BaFe_2As_2$ has a minimum $\xi > 385$ Å which corresponds to ~ 70 unit cells [134] [5]. Better estimates for the correlation length of density wave systems can be obtained with x-ray diffraction, which has an intrinsically better momentum resolution than neutron diffraction. The charge-density

---

[5] The magnetic Bragg peak was resolution limited.

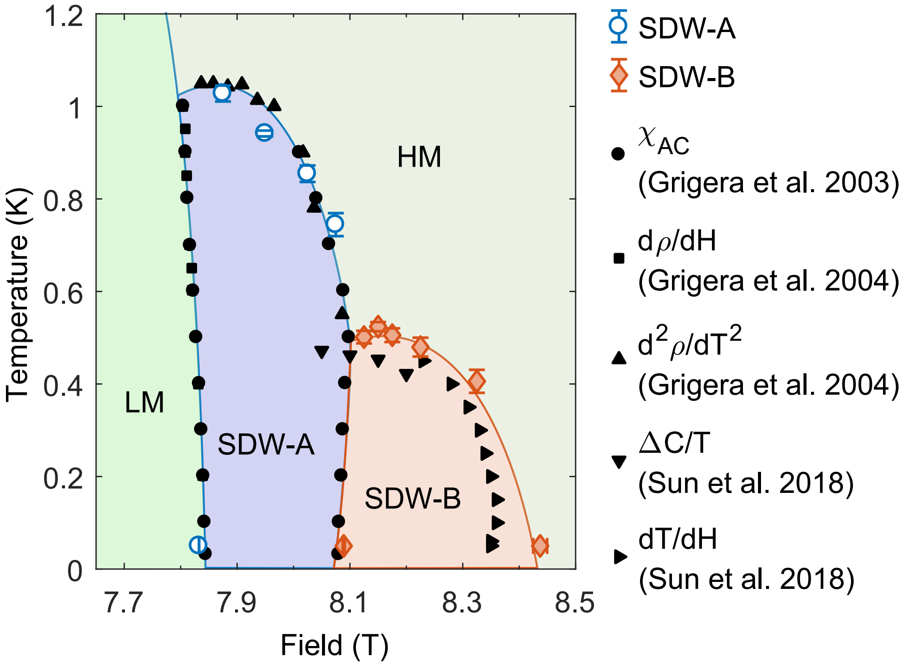

Figure 5.11: Phase diagram from thermodynamic measurements as indicated in the legend: AC susceptibility and resistivity from [92] and weak anomalies in heat capacity and magnetocaloric measurements from [117] that have been associated with the SDW-B phase. Phase diagram points taken from the neutron diffraction data are plotted and are broadly consistent.

wave (CDW) in $NbSe_2$ was determined to have $\xi \approx 600$ Å [131]. In Cr the SDW order has been measured directly by magnetic x-ray diffraction, which observed an atypically large correlation length of $\xi \approx 3000$ Å (comparable to the nuclear Bragg peak) [33] - an order of magnitude larger than observed in $Sr_3Ru_2O_7$.

Lester *et al.* established that the order is static on the timescale of neutron diffraction with a resolution of approximately 4 μeV [1] (roughly 1 GHz). NMR measurements with orders of magnitude better energy resolution (excitation frequencies in the range of 20-80 MHz) detect substantial AFM fluctuations in the field range $B_1 < B < B_3$ but no divergence in the relaxation rate is observed at T_N that would indicate static order[135]. There are two explanations for this disparity. It is possible that the previous NMR measurements suffer from similar sample heating effects [6] which prevented the observation of the drop in the ^{17}O Knight-shift in the superconducting state of Sr_2RuO_4[136], which has only recently been confirmed[137, 138].

Another possibility is that the spin fluctuations are gradually slowing as the temper-

---

[6] Due to the instantaneous destruction of superconductivity by eddy currents induced by the radio frequency pulses.

ature decreases such that order is observed at the temperature when the timescale of the spin fluctuations becomes greater than that of the probe. This is the case for the SDW order near the 1/8 anomaly in the lanthanum-based cuprates, where the transition is very broad as a function of temperature and the T_{N} is found to be probe dependent [139]. This could in principle be confirmed by measuring the temperature dependence of the magnetic Bragg intensity over a large range of wavelengths (and therefore energy resolution), however this may prove challenging due to the small $\boldsymbol{Q}$ of the SDW Bragg peak which necessitates the use of relatively long wavelengths at low scattering angles where there is a larger background.

5.5.2 Fermi surface nesting and the field-dependence of the SDW wavevector

The magnitude of the change in the SDW wavevector is roughly 0.5% over the field range of the two phases. This is two orders of magnitude larger than the magnetostrictive response of the lattice parameter a, which increases by $10^{-3}\%$ between 7.5-8.5 T[114]. It is also much smaller than the change in the SDW wavevector observed in $\mathrm{Nb}_{1-y}\mathrm{Fe}_{2+y}$ which decreases by $\approx 30\%$ as the FM QCP is approached as a function of doping[123]. Indeed, the SDW-A phase wavevector shows the opposite trend, decreasing as the field shifts the system further from the avoided QCP near B_1.

Together with the characteristic temperature dependence, the data indicate that the change in the SDW wavevector is due to the changing electronic structure at the Fermi energy. The states involved in the nesting of a linear SDW reside on bands of opposite spins[35]. In the case of $\mathrm{Sr_3Ru_2O_7}$ the field drives a VHS on the γ_2 band of one spin-species through the Fermi-level which produces a rapid spin-polarisation (due to conservation of charge) that might be expected to alter the nesting wavevector.

The response of the Fermi-surface with magnetic field in the SDW ordered phases has been measured by de Haas-van Alphen oscillations[112]. The frequency due to the small γ_2 pocket that occurs in the narrow field-range where metamagnetism and SDW order occur could not be resolved, however the frequency attributed to the α_1 band has been measured as a function of magnetic field. The data are consistent with the charge transfer to the γ_2 band at the metamagnetic transition producing a non-linear increase in the cross-sectional area of α_1 band for one spin-species and a slowdown in the field-dependence of the area of the other spin-species.

A quantitative comparison of the field dependence of the quantum oscillations and SDW wavevector is difficult as the instantaneous frequency of the quantum oscillations at a particular field is actually given by $F(B) \propto A(B) - B(dA/dB)$ [140, 141, 112]. The insensitivity to the linear field-dependence of the area means it is not possible to reconstruct the splitting and infer the change in any nesting wavevectors directly without accurate electronic structure calculations.

Nevertheless it is possible to conclude that the SDW-A & B phases are not due to nesting between the same Fermi sheets at different k_z, as the field dependence would have the same sign. The data here provide strong constraints on any microscopic theory for the SDW formation in $Sr_3Ru_2O_7$. In combination with the dHvA data[112] and electronic structure calculations it may now be possible to infer the states involved in the SDW nesting.

5.5.3 Lack of SDW at 7.5 T

The sign-change (negative to positive) in the magnetic Grüneisen parameter, Γ, seen at the metamagnetic feature at $B_0 \approx 7.5$ T implies a build-up of entropy that is consistent with two scenarios: a QCP [142] or a transition to an ordered phase (indeed there is also a zero-crossing of Γ at the boundary of the SDW-A phase, B_1). There is no evidence of SDW order with $\boldsymbol{q}_{SDW} = (\delta, 0, 0)$ and no other high-symmetry directions were measured at the low scattering angles required to measure magnetic Bragg peaks at small Q (it should be noted that inelastic neutron scattering only observes incommensurate fluctuations along $\langle 100 \rangle$).

The SDW phases in $Sr_3Ru_2O_7$ are very sensitive to disorder, it could be possible even in the excellent quality samples studied here, that the level of disorder is sufficient to suppress magnetic order at B_0, therefore it would be interesting to examine whether there is any change in the energy scale or wavevector of the incommensurate fluctuations at that field.

The search for an abutting ordered phase for $B < B_1$ was motivated by the observed increase in entropy and first-order nature of the transition at B_1 and the low temperature suppression of the SDW-A intensity (which is unexpected for the boundary with a disordered phase) and analogous to the observed behaviour at the boundary between the SDW-A & B phase at B_2. It has been suggested that there could be $q = 0$ order for fields $B_0 < B < B_1$ [117], which may be more consistent with the lack of anisotropic transport observed for $B < B_0$ when the field is tilted from the c-axis. Such a scenario is more suited to investigation with polarised neutrons.

5.5.4 Mean-field behaviour of the SDW temperature dependence

Due to the relatively small number of data points at $T < T_{\mathrm{N}}$ measured at each magnetic field and the assumptions made in modelling the broadness of the transition, these data are only suggestive of a mean-field BCS temperature dependence of the SDW order parameter. However, the theory of the spin pairing for SDW formation parallels that of particle/hole paring in superconductors, hence the expressions for the order parameter are the same[35, 26], which has been experimentally verified in many systems, including the similarly quasi-2D cuprate $\mathrm{La_2CuO_{4+y}}$.

An important result is that the temperature dependence of the order parameter for the two SDW phases exhibits the same functional form with a characteristic broadening of the transition that is the same fraction of T_{N} for the two phases. On the basis of these data there is no reason to suspect that the SDW-B phase formation is more strongly affected by disorder, or that the thermodynamic signatures associated with the SDW-B phase boundary should be different from the SDW-A boundary, as has been suggested[117].

A broad transition at T_{N} is also seen in heat capacity measurements [115] and was thought to be a consequence of the width of the first-order transitions at B_1 and B_2 as a function of magnetic field seen in AC susceptibility[92, 88] and in the diffraction data presented here. A careful study of the AC susceptibility with different sample shapes concluded that the width is not due to demagnetising fields but due to intrinsic factors such as unquenched disorder in the samples [88]. The intrinsic field width (and similarly any demagnetising fields) could broaden the transition as a function of temperature due to the curvature of the phase boundary, however this scenario cannot be the dominant cause of the broadening as the diffraction data are consistent with the transition width σ_N being proportional to T_{N} (regardless of magnetic field). For instance the transition into the SDW-A phase at 8.075 T where the curvature of the phase boundary is the largest has a lower $T_{\mathrm{N}} \approx 0.75$ K (and therefore smaller temperature width, σ_{N}) than the transition at 7.95 T where $T_{\mathrm{N}} \approx 1$ K and the phase boundary is independent of field over of 50 mT.

The broadening of the transition as a function of temperature could then be due to a distribution of T_{N} as in Eq.5.1 which is consistent with the data, but it could also be a result of particularly strong critical scattering. To distinguish between the two possibilities would require the critical scattering to be directly measured on a spectrometer. We note that such prominent scattering above T_{N} is not unique to $\mathrm{Sr_3Ru_2O_7}$ but also seen in many rare-earth alloys that exhibit low temperature (<10 K) magnetic phases. Of particular note is the well-studied local-moment ferromagnetic superconductor $ErRh_4B_4$ which has a very similar transition temperature $T_c \approx 1$ K to the SDW-A phase and similarly exhibits scattering up to 1.2 K [143].

5.6 Comparison with other materials

The saddle-point in the dispersion of the γ_2 band produces a peak in the density of states near the Fermi level that is responsible for the metamagnetism in $Sr_3Ru_2O_7$ [111, 112]. This is a generic feature of other systems on the verge of ferromagnetism. For example $NbFe_2$ also exhibits a similar saddle-point in the electronic dispersion which is believed to produce the itinerant ferromagnetism. It has been suggested that the SDW order at the FM QCP could coincide with a Lifshitz transition at a critical doping [144].

The coincidence of SDW order and metamagnetism is seen in many systems, most notably heavy fermion compounds which are located near the border between itinerant and local moment behaviour (typically a commensurate AFM ordered phase). A so-called 'pseudogap' in the density of states is a common feature of such compounds due the hybridisation of the localised f electrons and the conduction band which gives rise to peaks in the density of states near the Fermi level. For example, UPt_3 exhibits a metamagnetic transition between SDW order and a polarised paramagnetic state [145, 146, 147] which recent quantum oscillation data and a rigid band analysis of the electronic structure indicate is due to a Lifshitz transition as a VHS is driven through the Fermi level by the applied field [148] - a scenario that appears to be very similar to the metamagnetism in $Sr_3Ru_2O_7$. The heavy fermion compound URu_2Si_2[7] exhibits incommensurate SDW order over a narrow field range at low temperature bounded by metamagnetic transitions at the field-induced QCP associated with the hidden-order phase [150, 151]. Inside the hidden-order phase there are also several field-induced Lifshitz transitions [152], however the situation is likely to be more complicated than the band metamagnetism in UPt_3, as the magnetic field is also associated with the breakdown of the Kondo screening and the localisation of the f-electrons [153].

In $Sr_3Ru_2O_7$ the link between metamagnetic quantum criticality and SDW formation is not clear. There is no evidence of SDW order at the putative QCP at $B_0 = 7.5$ T and the field-dependence of the SDW wavevector does not shift towards low-q as the QCP at B_1 is approached (as exemplified in $NbFe_2$). Indeed the coincidence of SDW order and metamagnetism is seen in systems which do not exhibit obvious signatures of quantum

---

[7] URu_2Si_2 is a well-studied compound but much about the phase diagram and physics remains unresolved, a recent review can be found in reference[149].

criticality. A notable example is $CeAuSb_2$ which exhibits incommensurate SDW order at zero field, with a first-order metamagnetic transition into a second SDW phase at higher field, which is similarly characterised by a higher resistivity and a higher entropy than the high-field paramagnetic state [11, 154].

Despite the microscopic differences between heavy-fermion compounds and $Sr_3Ru_2O_7$, it is evident that metamagnetism and SDW order coincide in many compounds and that a divergent density of states near the Fermi-level governs the physics in a broad range of materials. However, a complete microscopic understanding of the field induced SDW order in $Sr_3Ru_2O_7$ is still lacking.

5.7 Conclusion

The neutron diffraction data presented here show that the two magnetic field induced SDW phases A & B have a correlation length of approximately $\xi = 300$ Å. The temperature dependence of the SDW order parameter of both phases is consistent with the weak-coupling BCS superconducting order parameter (as is seen in other systems such as Cr) and the SDW-B phase boundary agrees well with weak anomalies in recent heat capacity magnetic Grüneisen parameter data [118, 117].

The magnetic field-dependence of the SDW wavevector does not appear to be consistent with the prediction of the singular q-dependence of the susceptibility predicted to arise from soft quantum critical fluctuations in the vicinity of the QCP[119, 120, 121, 122] and is qualitatively different than the behaviour of $NbFe_2$[123]. Instead, it is likely to be due to the evolution of the Fermi-surface as a VHS in the density of states is driven through the Fermi level by the field splitting. From the sign of the field-dependence, it can be concluded that the SDW-A & B phases are not produced by nesting between the same pair of Fermi-sheets. These data may provide the missing link, which in combination with existing dHvA data and electronic structure calculations could allow for the states involved in the SDW nesting to be determined.

The link between metamagnetism, quantum criticality and SDW order is further explored in the next chapter where the magnetic field is applied in the plane of the bilayers breaking the lattice symmetry and taking the system away from quantum criticality.

Chapter 6

Discovery of new field-induced SDW ordered phase in $Sr_3Ru_2O_7$

The phase diagram of SDW order at the metamagnetic transitions in $Sr_3Ru_2O_7$ has been well investigated for a magnetic field applied perpendicular to the bilayers (along the c-axis). Less well studied is the phase diagram for a field applied in the ab-plane, which induces a region of nematic transport bounded by metamagnetic transitions[88], characteristic of SDW order breaking rotational symmetry (as observed for a field tilted slightly from the c-axis [1]). Here we present the discovery of two new SDW ordered phases for a magnetic field applied along the Ru-O bond in the ab-plane. The anisotropic transport is indeed associated with SDW order, but there exists an additional SDW phase at lower field that coincides with a metamagnetic transition associated with the previously observed SDW phase for the field along the c-axis. This was unexpected and the direction of the ordered moment in the new SDW phases hints at the important role of spin-orbit effects in coupling the SDW order to the field. These results shed new light on the link between metamagnetic quantum criticality and SDW order in this compound.

6.1 Motivation

As mentioned in Section 4, the SDW ordered phases that exist for a magnetic field applied along the c-axis (out of the bilayer plane) are highly sensitive to in-plane fields that lift the pseudo tetragonal symmetry of the lattice. Lester *et al.* showed that in the absence of an in-plane field component the SDW order exhibits two Fourier components producing two pairs of magnetic Bragg peaks of equal intensity with $\boldsymbol{q}_{\mathrm{SDW}} = (\pm\delta, 0, 0)$ and $(0, \pm\delta, 0)$. When the field is tilted by small angle, $\theta \lesssim 10°$, towards one of the in-plane tetragonal axes (parallel to the Ru-O bond), the component propagating perpendicular to the in-plane component of the field is rapidly suppressed resulting in a large anisotropy in the resistivity for currents parallel and perpendicular to the field direction ($\rho_{||} > \rho_{\perp}$) [88, 89]. This anisotropy is also seen in magnetostriction and thermal expansion measurements[90]).

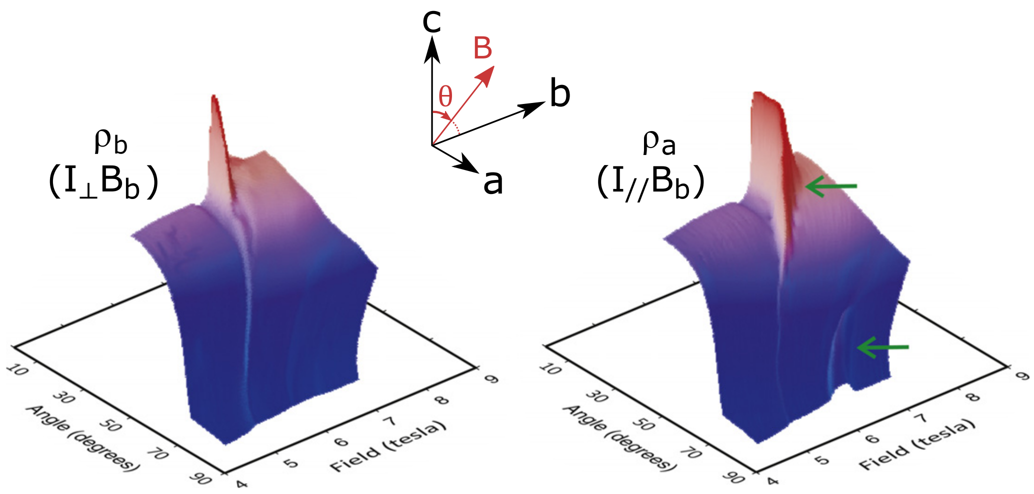

Figure 6.1: Magnetoresistance as a function of the angle of the field from the c-axis for two current orientations: perpendicular to the in-plane component of the field (left) and parallel to the in-plane component of the field. Green arrows mark regions of anisotropic transport. Colorscale (blue-red) is proportional to the resistivity (no colorbar was published). Figure taken from [88].

Borzi *et al.* [88] made an extensive study of the magnetoresistivity for a magnetic field tilted between the c-axis and an in-plane tetragonal axis. Fig.6.1 shows the resistivity for a current perpendicular and parallel to the in-plane component of the field as a function of the angle of the field from the c-axis, θ. Recall the enhanced resistivity is observed for a current parallel to the SDW wavevector. It can be seen that tilting the field away from the c-axis weakens the SDW order: the magnitude of the resistive anomaly decreases, as does the extent of the phase in field. The SDW component with wavevector perpendicular to the in-plane field is suppressed by $\theta \approx 10°$, but the SDW component with wavevector parallel to the in-plane field persists until $\theta_c \approx 40°$. At θ_c AC susceptibility measurements[155, 92] show the two transitions that bound the SDW-A phase merge, for $\theta > \theta_c$ there is a single metamagnetic transition marked by a ridge in the resistivity seen in both current orientations, that terminates at $B_0' \approx 5$ T for $\theta = 90°$.

For a field within $\sim 30°$ degrees of the a/b-axes, there is a second region of enhanced resistivity that is present only in the channel with the current parallel to the in-plane field. Differential susceptibility measurements (dM/dB) show that this second-region is bounded by 'two-step' metamagnetic transitions: at $B_1' \approx 5.8$ T, which has been shown to be weakly first-order[156], and second-order transition at $B_2' \approx 6.3$ T (shown in Fig.6.2).

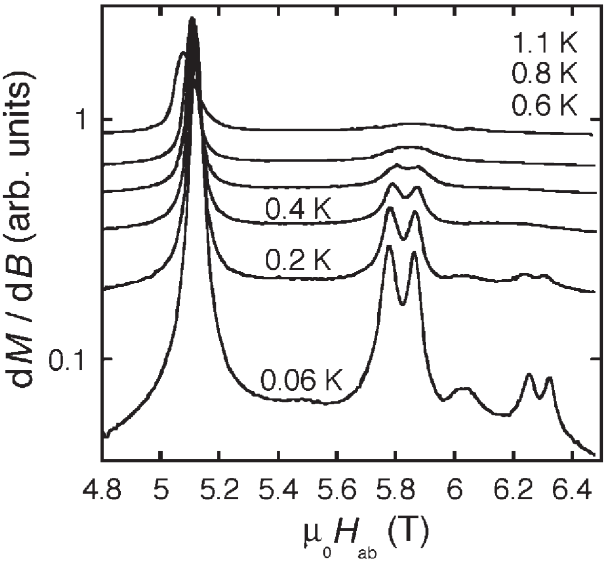

Figure 6.2: Differential bulk susceptibility measured using a capacitative Faraday force magnetometer at select temperatures (offset for clarity) . Figure taken from [157].

The region of anisotropic transport induced by a field in the ab-plane shares many common features with the behaviour of the SDW phases for a field tilted slightly away from the c-axis, indeed heat capacity measurements also show a similar build-up of entropy at low-temperature in this field region[157]. Motivated by this possibility, neutron diffraction measurements were performed with a magnetic field applied along the Ru-O bond in the ab-plane with the aim of searching for SDW order in this region. The enhanced resistivity is observed for a current parallel to the in-plane field, which would indicated the putative SDW order has a wavevector parallel to the field (requiring the field to be applied in the scattering plane). Measurements were also performed with the field perpendicular to the scattering plane, which would be sensitive to the preferred SDW component at small field-tilts from the c-axis, to determine whether the SDW order associated with the metamagnetic quantum critical transition could persist for an in-plane field at B_0'.

6.2 Experiment

Two neutron diffraction experiments were performed with a magnetic field applied along an in-plane tetragonal axis (Ru-O bond in the bilayer plane) on different triple-axis spectrometers . In 2014 C. Lester and S.M. Hayden used IN12 at the ILL[158] with a vertical magnet to measure the scattering along the direction of the in-plane axis perpendicular to the magnetic field (subsequent data analysis was performed by the author). In 2018, the author and S.M. Hayden performed an experiment on TASP at the PSI[159] with a horizontal magnet (MA07) which enabled the scattering along the in-plane tetragonal axes parallel and perpendicular to the direction of the magnetic field to be measured.

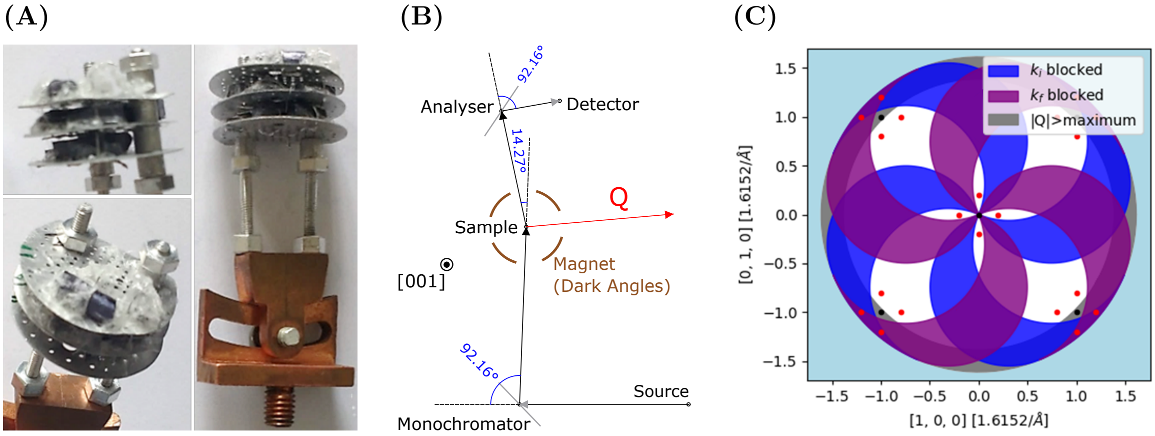

Figure 6.3: (A) Sample array before mounting on TASP (B) Components of the TASP instrument with the MA07 magnet measuring elastic scattering with $\boldsymbol{Q} = (0.2, 0.0)$ using $\boldsymbol{k_f} = 1.3\text{Å}^{-1}$) . (C) Accessible $\boldsymbol{Q}$ in the scattering plane due to magnet dead angles when $\boldsymbol{k_f} = 1.3\text{Å}^{-1}$ (using julia code written by Gregory Tucker the local contact on TASP).

The IN12 experiment used a co-aligned array of single-crystals (grown by C.Lester and R. Perry by the same method published in [1]) with a total mass of 5.5 g mounted on thin aluminium plates with the [001] direction surface normal using 50 μm Al wire and CYTOP fluorinated glue for rigidity and good thermal contact. The plates were separated by aluminium washers and attached to a copper goniometer by two aluminium screws. The TASP experiment used a subset of the same crystals (a crystal of mass 0.7 g fell off in transit) which are shown in Fig.6.3A. The copper goniometer was shielded with cadmium before being mounted in a dilution refrigerator with a cryomagnet (the

Instrument	Year	Sample mass (g)	k$_f$ (Å^{-1})	Mono/Analyser	Scattering Plane	Be filter	Velocity Selector	Cryomag.
IN12	2014	5.5	1.05	PG(002)/PG(002)	[001]∧[100]	k_f	Yes	Vert.(10T)
TASP	2018	4.8	1.30	PG(002)/PG(002)	[100]∧[010]	k_f	No	Horiz.(7T)

Table 6.1: Table of experiments and the configuration used. Scans were made with a fixed final wavevector, k_f as shown above unless otherwise stated in the main text.

IN12 experiment used a vertical magnet so the array was mounted at 90 degrees to the orientation shown in Fig.6.3A). A rocking curve over the magnetic Bragg peak at 5 T on TASP had a FWHM of 1.4° (which includes the contribution of the resolution) [1].

The experimental configurations used in the two experiments are summarised in Table.7.1. Both experiments used a flat monochromator and analyser (not focussed). IN12 had $60'$ collimation on k_i and TASP had $40'$ collimation on k_i and k_f.

Of particular importance to the experiment on TASP was the alignment of the magnetic field with respect to the sample. A schematic of the instrument configuration and the horizontal magnet used on TASP is shown in Fig.6.3B and the regions of reciprocal space rendered inaccessible by the magnet dark angles are shown in Fig.6.3C. The sample was aligned on a peak at (0.5,0.5,0) due to scattering from the (1,1,0) Bragg peak by neutrons with $\lambda/2$ (no Be filter was used). The magnet dark angles were found by rotating the magnet with respect to the sample until the peak intensity at (0.5,0.5,0) was halved.

The scattering with momentum transfer parallel and perpendicular to the field direction was measured by rotating the sample by 90° about the vertical axis inside the magnet (using a motor at the top of the sample stick) then rotating the magnet (and sample) together by the 90° in the opposite sense (which is the A3 angle that was moved during the scans, sometimes referred to as theta). The net effect was that the field direction was rotated with respect to the sample, but the direction of the momentum transfer $\hat{\boldsymbol{Q}}$ did not change with respect to the sample frame. This was done to keep the same path length of the incident and scattered beam through the sample.

Rotation of the sample at base temperature inside the magnet at field caused considerable heating: for example the sample temperature increased from 0.07 K to ~ 0.16 K when the sample was rotated 90° at a stick motor speed of 4000 (arbitrary units) at a field of 5 T. Therefore rotations were performed with a stick motor speed of 100 (arbitrary units) at ~ 0.8 K (above the SDW phase boundary) which produced no observable heating. Data were taken post field-cooling (unless otherwise specified), with the temperature

---

[1] The mosaic was not measured on IN12 in 2014. The TASP measurement provides an upper bound on the mosaic of the single crystal sample used in Chapter 5 for which the mosaic has not been measured.

dependence measured on warming.

Data are normalised by a given number of counts on the monitor between the monochromator and sample (M1) as specified in the y-axis label of the plots.

6.3 Results

Hereafter the direction of the scattering perpendicular to the magnetic field has been labelled as being along the tetragonal $\boldsymbol{a}^*$ and scattering parallel to the field to be along the tetragonal $\boldsymbol{b}^*$. In this notation the magnetic field is along the tetragonal b-axis for both orientations. The scans presented here are referred to as longitudinal, the step in $\boldsymbol{Q}$ was parallel to $\boldsymbol{Q}$. It is important to stress that $\hat{\boldsymbol{Q}}$ was the same for longitudinal scans in both field orientations.

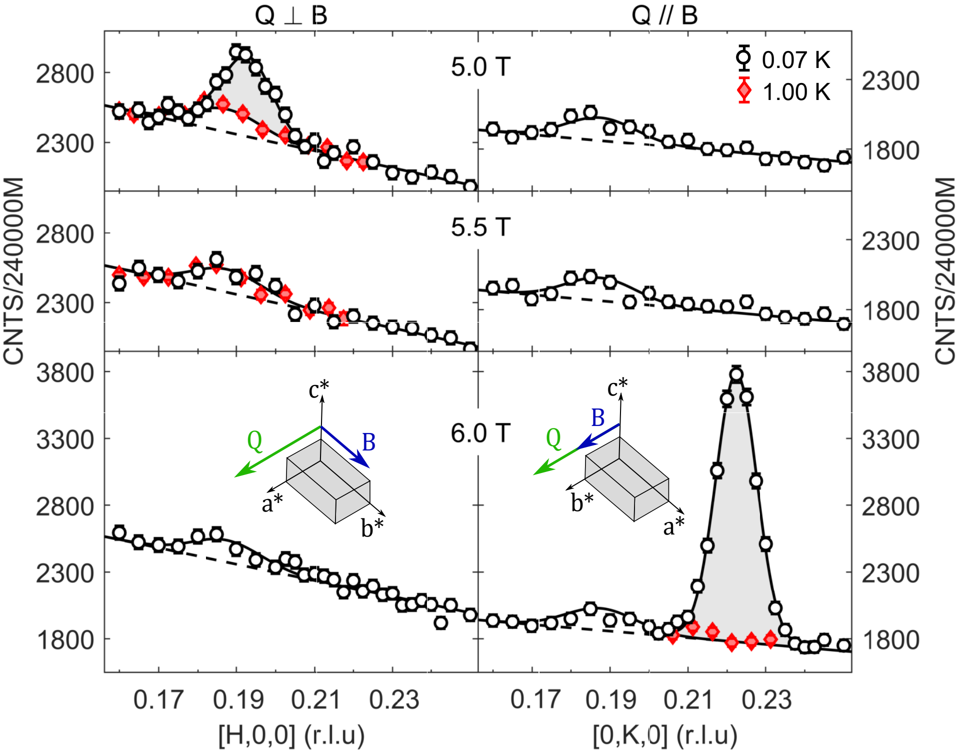

Figure 6.4: Longitudinal scans at 3 fields (5 T, 5.5 T and 6 T) show magnetic Bragg peaks (shaded) at 5 T and 6 T for Q perpendicular and parallel to the field respectively (data taken on TASP). Note that the direction of Q with respect to the crystal was the same for both field orientations (as shown in the schematic insets), the axes $\boldsymbol{a}^*$ is defined to be parallel to the field and $\boldsymbol{b}^*$ to be perpendicular. Note a weak temperature and magnetic field independent peak at 0.185.

Fig.6.4 shows longitudinal scans taken on TASP at three magnetic fields in both orientations (indicated by the schematic). There is a magnetic peak at 5 T with a wavevector perpendicular to the field direction (a phase which will be referred to as SDW-A′). Another magnetic peak at 6 T is observed with a wavevector parallel to the magnetic field (SDW-C phase). In each phase the orthogonal field orientation does not exhibit any magnetic scattering. As neutrons only scatter from components of the magnetisation perpendicular to the scattering wavevector we can conclude that the ordered moment in both SDW phases is transverse to $\boldsymbol{q}_{SDW}$ and oriented along the in-plane tetragonal axis parallel and perpendicular to the field direction for the SDW-A′ and SDW-C phases respectively.

It can be seen in Fig.6.4 that there is a temperature and magnetic field independent peak at Q $= 0.185$ $(2\pi/a)$, that has the same intensity in both field orientations which was assumed to be due to an aluminium powder line (the Q is consistent with the (200) peak for neutrons of wavelength $\lambda/9$, assuming the scattering occurred at the sample position). Though the orientation of $\hat{\boldsymbol{Q}}$ is the same for both field orientations, it can also be seen that the background of the scattering parallel to the field is lower than the background perpendicular to field. The backgrounds in the two orientations are not related by either of a multiplicative factor or constant offset. Any difference in background is then likely to be due to the magnet which is rotated with respect to the beam in the two field orientations.

The windows of the MA07 magnet are not perfectly four-fold symmetry: the vertical angle subtended by the magnet window parallel and perpendicular to the field is $\pm 22.5°$ and $\pm 6.7°$ respectively. The vertical extent of the window perpendicular to the field is comparable to the vertical beam size (40 mm) and could contribute to a difference in background due to reduced transmission. Indeed, the lowest background is detected with a magnetic field applied parallel to $\boldsymbol{Q}$, when the incident and scattered beam travel through the window perpendicular to the field direction. However, the flux incident on the sample is not necessarily very different in the two orientations as the sample array was smaller than the beam in the vertical direction. Indeed, the non-magnetic peak at $Q = 0.185(2\pi/a)$ has the same intensity for both field orientations, which indicates that no correction to the magnetic intensity is required (assuming the non-magnetic peak is due to scattering at the sample position).

Fig.6.5 shows longitudinal scans of the magnetic Bragg peaks in the two field orientations on TASP, measured for a magnetic field swept in different directions (and having field-cooled from $T \gtrsim 0.7$ K at the field indicated in the title). It can be seen that the intensity of the SDW-C Bragg peak exhibits strong hysteresis, whereas no hysteresis is observed for the SDW-A′ Bragg peak, despite the fact the metamagnetic transition at 5 T is strongly first-order (with a critical temperature of $T_c \approx 1.2$ K[92]). Although there were no data taken on the down-sweep for this field orientation.

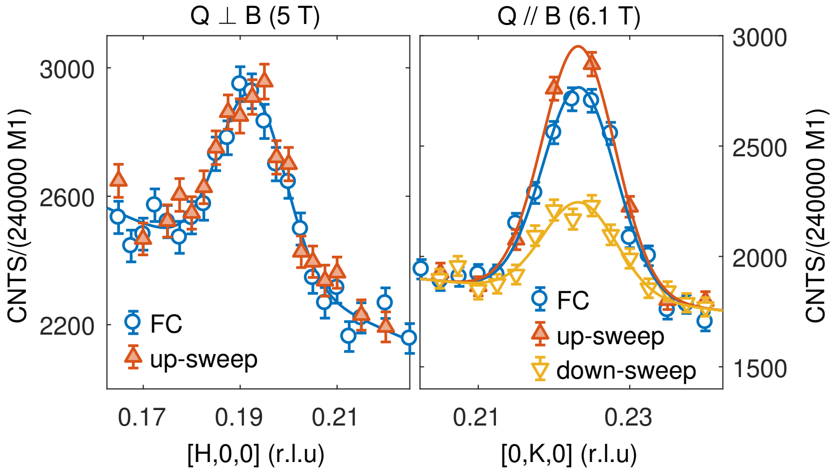

Figure 6.5: Hysteresis observed in TASP data at 0.07 K when field is swept up/down into the SDW phase at 6 T ($\boldsymbol{Q}$ parallel to $\boldsymbol{B}$), but no observable hysteresis is associated with the SDW phase at 5 T in the up-sweep ($\boldsymbol{Q}$ perpendicular to $\boldsymbol{B}$). Lines are fits of Gaussian peaks with linear background.

Fig.6.6 shows longitudinal scans through the position of the SDW Bragg peaks for a series of magnetic fields measured on IN12 (field perpendicular to $\boldsymbol{Q}$) and TASP (field parallel to $\boldsymbol{Q}$) at base temperature (~ 0.07 K for both experiments). IN12 data were taken having swept the field up from 4.6 T, the TASP data were taken having field-cooled at each field. Peaks were fitted with a Gaussian function with a field-independent width and field-independent background on each instrument. The IN12 data show no evidence of the non-magnetic peak at $Q = 0.185(2\pi/a)$ seen on TASP (it would be most evident at 4.8 T where the SDW peak is at larger Q), which supports the notion that it is due to higher-order contamination (a Be filter was used on IN12).

Fig.6.7 shows the peak centre and intensity as a function of magnetic field extracted from the fits in Fig.6.6. The peak centre of the two phases, or equivalently the incommensurability, δ, has the opposite field dependence. The trend is less convincing for the IN12 data due to small number of points on the SDW-A′ peak, however the shift of the peak centre to lower Q as the field is increased from 5 T to 5.1 T can clearly be seen in the raw data in Fig.6.6A. The δ of the low-field SDW-A′ phase has a similar in magnitude to the connected SDW-A phase for an out-of-plane field, and decreases with increasing field in both phases. Perhaps more surprising is that the δ in the high-field phases for both an out-of plane (SDW-B) and in-plane field (SDW-C) also have similar magnitude and

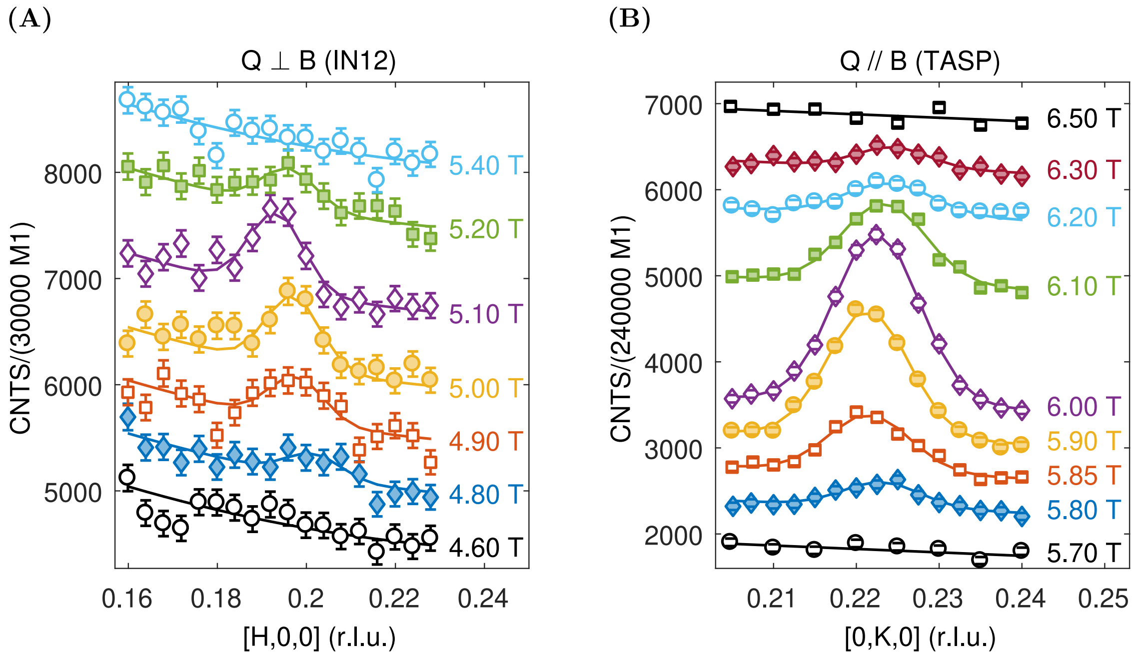

Figure 6.6: Longitudinal scans through the position of magnetic Bragg peaks offset vertically for clarity. (A) IN12 data with $\boldsymbol{Q}$ perpendicular to $\boldsymbol{B}$, taken having swept the field up from 4.6 T. Fitted with Gaussian peaks on a field independent cubic background. (B) TASP data with $\boldsymbol{Q}$ parallel to $\boldsymbol{B}$ having field-cooled at each field. Fitted with Gaussian peaks on a field independent linear background.

both increase with increasing field. The SDW-B and SDW-C phase are not connected by a contiguous line of metamagnetic transitions, however these observations would suggest the two phases may be related.

The SDW intensities in Fig.6.7 have been normalised to the ratio of the intensities at 5 T and 6 T observed on TASP. Fig.6.7 also shows the real part of the bulk differential susceptibility (field derivative of the DC magnetisation) and the resistivity measured with a current parallel to the field direction, taken from [157]. It can be seen that the SDW-A' phase is only associated with a single peak in the susceptibility which coincides with the field at which the Bragg intensity is maximum. In contrast the SDW-C phase is bounded by two pairs of peaks, with perhaps a small feature at ~ 6 T where the Bragg scattering is most intense. There is a kink in the resistivity at the metamagnetic transition at 5 T, but a pronounced enhancement in the SDW-C phase where the SDW wavevector, $\boldsymbol{q}_{SDW}$, is parallel to the current.

Fig.6.8 shows the temperature dependence of the counts at the Bragg peak centre for both field orientations at select fields, taken warming up having field-cooled at each field from above 0.7 K on TASP. In Section 5.4.4, the temperature dependence of the

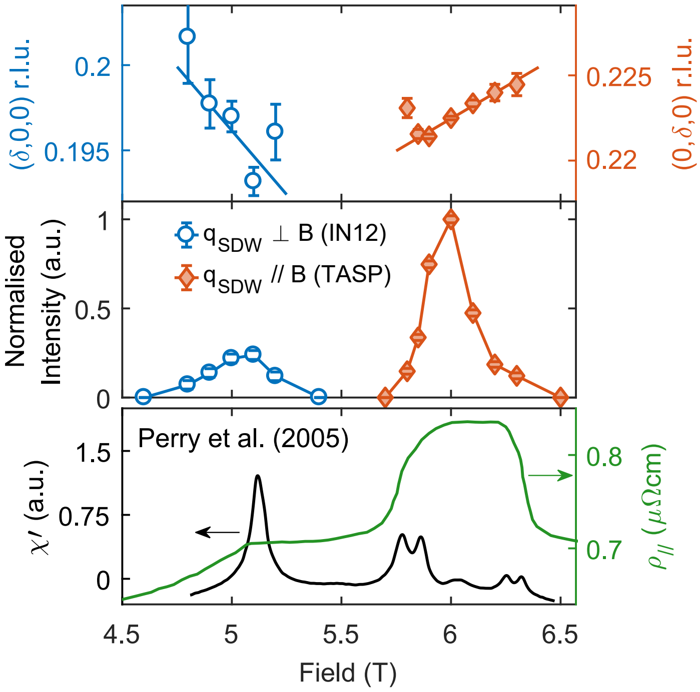

Figure 6.7: Field-dependence of the SDW wavevector (top) and intensity normalised by the intensity of the SDW peak at 6 T measured on TASP (middle). Note that the IN12 data has been normalised such that the intensity at 5 T agrees with the ratio of the peak intensities in the two phases (at 5 T and 6 T) as measured on TASP (see main text for details). (Bottom) A comparison of AC susceptibility and resistivity over the same field range (at 0.06 K and 0.1 K respectively) taken from [157].

SDW Bragg peak intensity was fitted with the square of the BCS order parameter with a Gaussian distribution of T_N of standard deviation σ_N (Eq.5.1). The same procedure was applied here to data at 5.9 T and 6 T for a magnetic field parallel to $\boldsymbol{Q}$. Data at both fields were constrained to have the same $m_q(0)/T_\mathrm{N}$ and $\sigma_\mathrm{N}/T_\mathrm{N}$. The high-temperature background was fixed at the value of the background extracted from the constant energy scans shown in Fig.6.6. It can be seen that the data at 5.9 T and 6 T are consistent with the above constraints. The data at 5 T were then fitted using the same values for $\sigma_\mathrm{N}/T_\mathrm{N}$ and $m_q(0)/T_\mathrm{N}$ after correcting for the ratio of the Lorentz factor in Eq.3.84. Despite the lack of data at 5 T, there was only one adjustable parameter (T_N) in the fit and the ratio of the intensities at base temperature and 0.3 K are in good agreement. The consistency of $m_q(0)/T_\mathrm{N}$ for both field orientations indicates that the magnetic intensities are not affected by the different backgrounds seen in Fig.6.4.

The fitted T_N at 5 T is also consistent with data taken on IN12 shown in Fig.6.9. The sample was cooled from high temperature with an average ramp rate of ∼1.2 mK/min

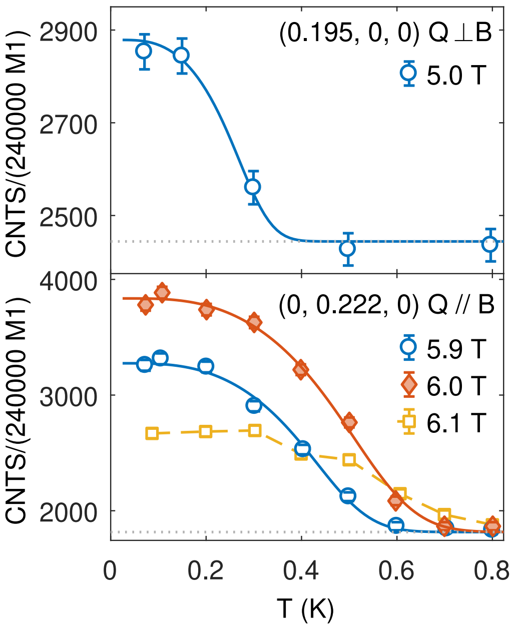

Figure 6.8: Temperature dependence of the SDW Bragg peak intensity measured on TASP for a magnetic field perpendicular (top) and parallel (bottom) to $\boldsymbol{Q}$. Solid lines are fits to the square of the BCS order parameter (see main text), dashed line is a guide to the eye.

(data have been rebinned for clarity), and displays a step-like increase in the Bragg intensity at the T_N from the fit to the TASP data in Fig.6.8. However, not all fields for which the temperature dependence was measured on TASP are consistent with the BCS scaling. Fig.6.8 also shows data for a field of 6.1 T applied parallel to $\boldsymbol{Q}$, which has a similar transition temperature to the data at 6 T but half the intensity at base temperature. The origin of this discrepancy is not clear.

In the BCS formalism T_N is proportional to the ordered moment. A rough estimate of the ordered moment for the new SDW phases can be obtained from the ratio of T_N relative to the SDW-A phase, for which measurements were published in absolute units by Lester *et al.*[1]. The authors of [1] calculated the SDW-A ordered moment on the assumption that each pair of peaks corresponded to a C_2 domain that occupied 50% of the sample volume. It is now believed the SDW preserves the four-fold symmetry and both components microscopically coexist through the entirety of the sample (i.e. no C_2 domains). Both structures give the same estimate for the ordered moment. Table 6.2 shows the T_N for the SDW phases and the estimated ordered moment .

	Field direction	B (T)	$\boldsymbol{q_{SDW}}$	δ $(2\pi/a)$	T_N (K)	Moment direction	m_q (μ_B/Ru)
SDW-A	(0,0,B)	7.95	$(\delta, 0, 0)$ $(0, \delta, 0)$	0.218(2)	0.942(6)	$(m_q, 0, 0)$ $(0, m_q, 0)$	0.10(2)*
SDW-B	(0,0,B)	8.15	$(\delta, 0, 0)$ $(0, \delta, 0)$	0.233(2)	0.52(1)	$(m_q, 0, 0)$ $(0, m_q, 0)$	0.06(1)
SDW-A′	(0,B,0)	5.00	$(\delta, 0, 0)$	0.197(1)	0.327(3)	$(0, m_q, 0)$	0.034(7)
SDW-C	(0,B,0)	6.00	$(0, \delta, 0)$	0.2225(1)	0.619(6)	$(m_q, 0, 0)$	0.07(1)

* Ordered moment measured on LET published in [1]

Table 6.2: Summary of the SDW phases in $Sr_3Ru_2O_7$ for different field orientations and the transition temperature, T_N, from which an estimate of the ordered moment is made from the measured value of the SDW-A phase at 7.95 T published by Lester *et al.* [1]. The error on T_N may seem small given the broadness of the transition, however it also is constrained in the fit by the square-root of the intensity at base temperature. Nevertheless, due to the lack of data at 5 T, the fit was performed for a fixed ratio of $m_q(0)/T_N$ and σ_N/T_N determined from the data in the orthogonal field direction (see main text) - this assumption reduced the degrees of freedom in the fit quite considerably and as such the error on T_N is likely to be an underestimate.

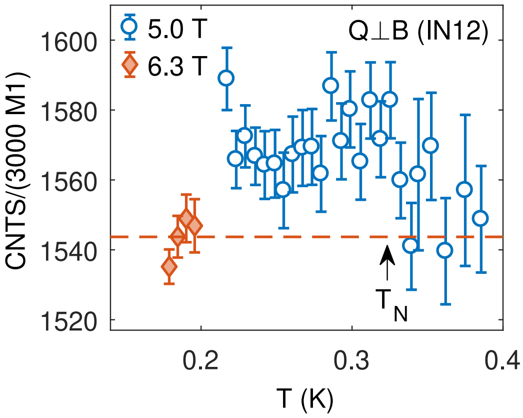

Figure 6.9: Temperature dependence of the SDW Bragg peak intensity for a magnetic field perpendicular to $\boldsymbol{Q}$ measured on IN12 with $k_f = 1.55$ Å^{-1} . Data were taken cooling at a rate of ≈ 0.0012 K/minute with each point counted for 1.2 minutes (and subsequently re-binned for presentation). The T_N extracted from the BCS fit in Fig.6.8 is shown by a black arrow.

6.4 Discussion

The discovery of the C_2 symmetric SDW-C ordered phase for a field of 6 T along the a-axis explains the so-called ‘nematic’ transport observed [88]. The resistivity anomaly is observed for a current oriented parallel to the SDW wavevector, $\boldsymbol{q_{SDW}}$ - as is the case for the SDW-A & B phases when the pseudo-tetragonal symmetry is broken by a field tilted slightly ($\lesssim 10°$) away from the c-axis towards the b-axis. Our data provide direct evidence that the enhanced resistivity is an intrinsic property of the SDW order and not due to domain boundaries (as there is only one domain for an in-plane field). Previously this could only inferred from a lack of resolvable hysteresis in transport data when the component of the field in the ab-plane was varied - which indicates a lack of C_2 domains[12]. The authors of [12] point out that in a mono-domain sample of $Sr_3Ru_2O_7$ produced with uniaxial strain, the jump in the resistivity below T_N for a current parallel to $\boldsymbol{q}_{SDW}$ is much larger ($\rho_{||I}/\rho_{\perp I} \approx 2.4$) than in other SDW metals such as chromium ($\rho_{||}/\rho_{\perp} \approx 1.08$[95]). It does seem unlikely that such anisotropy could be solely due to the gapping out of carriers by a single wavevector (especially considering the highly fragmented Fermi-surface).

The bulk differential susceptibility is highly structured in the vicinity of the SDW-C phase. The onset of the SDW scattering coincides with double peak features and there is a broader hump at 6 T where the Bragg intensity is largest. It has been speculated that the double peaks could be due to the in-plane field breaking the four-fold symmetry of the electronic structure (via spin-orbit coupling effects such as magnetostriction) lowering the degeneracy of the pairs of Van Hove singularities (that occur near the X-point of the tetragonal Brillouin zone), producing a small splitting in energy [160]. It is unclear why such splitting does not occur at the transition at 5 T. Nevertheless, the fact that no signature of this splitting is evident in the neutron diffraction measurements, which would seem to confirm this picture, as the SDW is itself C_2 symmetric and would only couple to one pair of the Van Hove singularities. However it should be noted that measurements were made on quite a coarse set of fields comparable to the splitting (~ 0.1 T), and such features may be blurred given the field will vary slightly over the extent of the sample in the magnet [2].

On the timescales probed by neutron diffraction, both SDW phases appear to be statically ordered. (see Chapter 7 for the energy width of the SDW Bragg peaks). As the SDW-A′ is incommensurate and breaks the translational symmetry of the lattice (the field has broken the rotational symmetry), one would expect the phase to be bounded by two second-order transition - whereas only a single first-order transition is observed[92, 157].

---

[2] The extent of this variation depends on the field homogeneity of the magnet over the extent of the sample volume at the sample position, which to the author's knowledge has not been measured. From unpublished data taken on IN12 by C. Lester and S. Hayden (not included in this thesis) the variation could be of the order 0.05 T, estimated from the additional broadening of the SDW-A phase boundary at B_1 as a function of magnetic field applied along the c-axis compared to the WISH data presented in Chapter 5 (which used a much smaller sample).

In the SDW-A phase for a field along the c-axis the low-field phase boundary is first-order. It is possible previous measurements could not resolve a second weak transition associated with the SDW-A′ at a nearby field. It should be noted that the SDW-A′ phase has a smaller ordered moment than the SDW-B phase for which only very recent low temperature measurements have detected a thermodynamic signature at the high-field phase boundary[117, 118]. Similarly, transport measurements have not detected any anisotropic transport associated with the SDW-A′ phase, just a cusp-like feature at the metamagnetic transition that is observed for a current applied both parallel and perpendicular to $\boldsymbol{q}_{SDW}$ [88]. This may be due to the fact that the expected anisotropy is much smaller than the SDW-A phase. Previous measurements have either used different samples [160] or different electrical contacts on the same sample [88], thus requiring some rescaling which might make the identification of a small anisotropy difficult. Additionally the response would be also be sensitive to the field and current orientation in the ab-plane.

The same field dependence and similar magnitude of the SDW-A & A′ phase wavevectors would suggest that the two phases, which are connected by a contiguous line of metamagnetic transitions as the field is tilted from the c-axis, involve nested states on the same Fermi-sheets. However, there is one notable difference: the direction of the SDW-A′ wavevector is perpendicular to the field, which corresponds to the Fourier component of the SDW-A phase that is suppressed for small field tilts from the c-axis[1].

At the field tilt for which the metamagnetic transition bifurcates to produce the two separate transitions that bound the SDW-A phase, there is a peak in the imaginary part of the AC susceptibility which would be consistent with the wavevector and ordered moment) flipping. Phenomenologically the direction of the SDW ordered moment, $\boldsymbol{m_q}$, relative to the magnetic field is governed by a term in the free energy that arises due to spin-orbit coupling, $L(\boldsymbol{M_0} \cdot \boldsymbol{m_q})^2$, where $\boldsymbol{M_0}$ is the bulk magnetisation[97, 96, 161]. The flip in the spin orientation as the field is tilted and between the two phases for an field along the a-axis (SDW-A′ & C) will then be induced by other competing terms in the free energy. For instance the presence of spin-orbit interaction means the underlying electronic structure will change with the field direction[100] and additionally provides a term that couples the moment to the lattice [3].

A similar phenomenon is observed in chromium, which exhibits a first-order spin-flip transition below T_{N} from a transverse to longitudinal SDW [162]. It is believed that the transition is driven by terms which couple the strain field to the magnetic field of the SDW itself via magnetostrictive effects (which ultimately arise through spin-orbit

---

[3] The situation is further complicated by the fact that, in general, spin-orbit coupling will also produce an anisotropic g tensor, such that the polarizability in the basal plane will be different to the c-axis [94].

coupling)[163]. The term was found to be sensitive to the magnitude of the SDW wavevector, which varies continuously through the transition[164]. Such a mechanism might be relevant to the SDW order in $Sr_3Ru_2O_7$ as transport and magnetostriction measurements have been shown the SDW order to be sensitive to orthorhombic distortions[114, 12] which could occur due to the coupling between the lattice and the applied field or the C_2 symmetric SDW order at tilted field.

The relation of the two new SDW phases to the metamagnetic quantum criticality also appears to be very different to the SDW-A & B phases. The SDW order in $Sr_3Ru_2O_7$ is strongest in the metamagnetic quantum critical region at B_1 for a field oriented along the c-axis (SDW-A phase). These results have established that the SDW order at that transition persists for field in the ab-plane, albeit with a reduced moment and a smaller energy scale than the metamagnetism ($T_\mathrm{N} \approx 0.3$ K compared to $T_\mathrm{c} \approx 1.2$ K). In contrast, the SDW-C phase does not appear to be associated with metamagnetic quantum criticality. The magnitude of the peaks in the AC susceptibility at the SDW-C boundary, and the anisotropic resistivity associated with the order have been shown to be remarkably insensitive to hydrostatic pressure, even at pressures sufficient to suppress the end-point of the transition at $B_0' \approx 5$ T to zero temperature[156, 160]. Hydrostatic pressure weakens the metamagnetism as it suppresses the VHS in the density of states - if the SDW order was correlated with the metamagnetism it would be expected to respond (T_N would either increase or decrease). In fact, the enhancement in the resistivity associated with the SDW-A & B phases is quickly suppressed with hydrostatic pressure[165]. The authors of [160] found the weakly first-order boundary of the SDW-C phase at B_1' becomes second-order for small hydrostatic pressures, raising the previously unexplored possibility of proximate antiferromagnetic quantum criticality (explored in more detail in Chapter 7).

6.5 Conclusion

Two new SDW ordered phases have been discovered for a magnetic field applied along the a-axis of $Sr_3Ru_2O_7$. The low field phase (SDW-A$'$) is associated with the metamagnetic transition for which the SDW-A and SDW-B phases mask the quantum critical end-point for a field long the c-axis. The high-field phase (SDW-C) is associated with another metamagnetic transition and a region of anisotropic transport properties. Clearly there is a deep link between metamagnetism and SDW order in this compound.

The magnetic field breaks the tetragonal symmetry of the system and produces C_2 symmetric single-q SDW order. For this reason, the SDW-A$'$ phase would also be expected to produce anisotropic transport, however the ordered moment is $\sim 1/2$ that of the SDW-C phase and therefore the effect will be much smaller and perhaps difficult to resolve.

The ordered moment is along the Ru-O bond in the ab-plane, parallel and perpendicular to the field direction for the SDW-A′ & C phases respectively. The moment direction of the SDW-A′ phase is particularly interesting as it corresponds to the SDW component that is suppressed for small field-tilts from the c-axis[1]. This indicates the existence of a spin flip transition with analogies to the behaviour of the SDW order in chromium. Overall the coupling of the field direction to the SDW wavevector implies a complex interplay of spin, orbital and lattice degrees of freedom due to spin-orbit coupling effects. In chromium the spin-flip transition is believed to be due magnetostrictive coupling of the SDW moment to the lattice strain. It is plausible such a mechanism is responsible for the observed behaviour in $Sr_3Ru_2O_7$.

Chapter 7

Low energy spin fluctuations in $Sr_3Ru_2O_7$ for magnetic field along the a-axis

---

This chapter presents inelastic neutron scattering measurements of the low energy incommensurate spin fluctuations associated with the two magnetic field induced spin-density-wave (SDW) phases discovered for a magnetic field oriented parallel to the Ru-O bonds in the plane of the bilayers of $Sr_3Ru_2O_7$. The fluctuations associated with the SDW-A′ phase (ordered moment parallel to the field direction) have been confirmed to be 2D in nature, with the two planes that comprise the bilayer fluctuating in-phase but with no correlation between bilayers. As the magnetic field approaches the low-field boundary of each SDW phase the fluctuations soften and susceptibility diverges. In particular the timescale of the fluctuations associated with the SDW-C phase exhibit classic critical slowing-down behaviour expected for a second order phase transition.

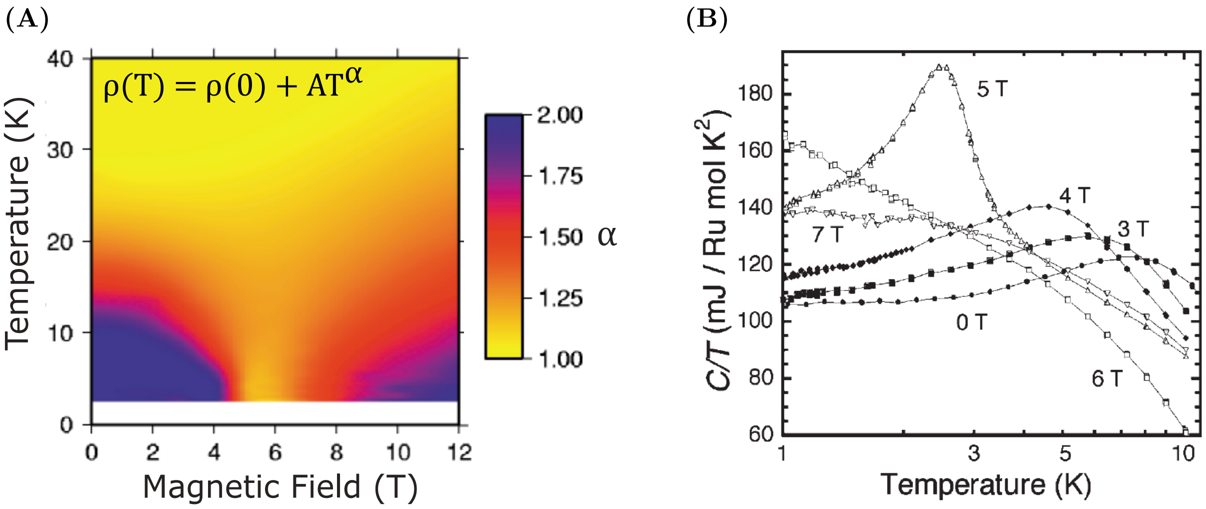

Figure 7.1: (A) The magnetic field and temperature dependence of α for resistivity of the form T^{α} for a current parallel to the magnetic field applied in the bilayer plane (for a sample of insufficient quality to display the SDW ordered phases) taken from[82] (B) The specific heat capacity divided by temperature as a function of temperature and magnetic field applied along an in-plane Ru-O bond (in the bilayer plane) post subtraction of phonon contribution. Figure taken from [157].

7.1 Motivation

The newly discovered SDW phases for a magnetic field applied along the Ru-O bond in the bilayer planes (a-axis) of $Sr_3Ru_2O_7$ exist over a relatively small field range. However, transport measurements show a non-Fermi-liquid temperature dependence of the resistivity that is indicative of strong quantum critical fluctuations over a much larger field range ($4.5 \lesssim B \lesssim 7$ T) [82] (see Fig.7.1A). The specific heat capacity measurement for a coarse set of fields (see Fig.7.1B), exhibits an enhancement at low temperature in the region of strong quantum critical fluctuations, indicating a build-up of entropy. At a field of 6 T the linear coefficient of the specific heat capacity, $\gamma = C/T$, increases nearly-logarithmically down to the lowest temperature measured (1 K), which is highly suggestive of a quantum critical point in the vicinity.

The scenario at $B \sim 6$ T may then be analogous to the formation of the SDW-A phase for a magnetic field along the c-axis. Recent (unpublished) measurements by C. Lester and S.M. Hayden[166] have shown that in the quantum critical region with a magnetic field applied along the c-axis, the low energy fluctuations are overdamped spin fluctuations (see section 7.3.3) with a characteristic frequency, Γ, which can be tuned with the field, softening (moving to lower energy) dramatically at some critical field inside the SDW-A ordered phase (see Fig.7.2). The enhancement of the low-energy spin

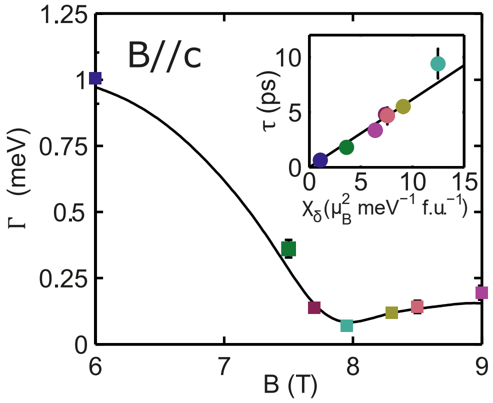

Figure 7.2: Characteristic frequency of the spin fluctuations as a function of magnetic field applied parallel to the c-axis, from fits of an overdamped harmonic oscillator response (see Section 7.3.3). Inset shows the relaxation rate, $\tau = 1/\Gamma_0$, varies linearly with the static susceptibility, χ_δ, indicating critical slowing down of the fluctuations (solid line is a linear fit constrained to pass through the origin). Figure taken from [166].

fluctuations is associated with a build-up of entropy in the quantum critical region and the estimated contribution of the spin-fluctuations to the low temperature γ agreed well with the measured heat capacity [133] .

The following experiments were motivated by two aims. Firstly, to determine whether an in-plane magnetic field could (similarly to the fluctuations for an out-of-plane field) be used to tune the relaxation rate of the spin-fluctuations and whether the softening of the fluctuations could explain the build-up of entropy at low temperature observed in heat capacity measurements, particularly at 6 T. Secondly, to determine whether the spin-fluctuations with moments parallel and perpendicular to the magnetic field exhibit qualitatively different behaviour given the former order at a field which coincides with a strongly first-order metamagnetic transition (with a critical temperature $T_c >> T_N$).

7.2 Experimental Details

The fluctuations at the incommensurate wavevector were measured in two magnetic field orientations (parallel to the Ru-O bond) in two separate experiments. The fluctuations with a magnetic field applied perpendicular to the wavevector (moment fluctuating parallel to the field direction) were measured by C. Lester and S.M. Hayden on the triple-axis spectrometer IN12[158] with a vertical magnet in 2014 (subsequent data analysis performed by the author). The fluctuations with a magnetic field applied parallel to the wavevector (moment fluctuating perpendicular to the field direction) were measured with a horizontal magnet on THALES[159] by the author in 2019.

Instrument	Year	Sample mass (g)	k_f (Å^{-1})	Mono/Analyser	Scattering Plane	Be filter	Velocity Selector	Cryomag.
IN12	2014	5.5	1.15	PG(002)/PG(002)	[001]$\wedge$[100]	k_f	Yes	Vert.(10T)
THALES	2019	6.3	1.15	Si(111)/PG(002)	[100]$\wedge$[010]	k_f	Yes*	Horiz.(6T)

*The velocity selector broke (see Section 7.3.1)

Table 7.1: Table of experiments and the configuration used. The value of k_f in the table refers to the k_f at which the magnetic scattering was measured (unless otherwise stated in the main text). Scans were made with fixed final wavevector, k_f.

The IN12 experiment used a co-aligned array of single-crystals with a total mass of 5.5 g (same as in Chapter 6). Two more single crystals with a combined mass of 0.8 g were added before the THALES experiment, such that the co-aligned array had a total mass of 6.3 g and a mosaic of $\sim 1.5°$ measured on the (200) peak on ALF (ISIS,UK). The samples were mounted in a dilution refrigerator with a cryomagnet. The experimental configuration used in the two experiments is summarised in Table.7.1. Measurements were made with a fixed final wavevector, k_f. As the inelastic magnetic response is not sharp in $\boldsymbol{Q} - E$ space some resolution was sacrificed to increase the intensity by focussing the monochromator and analyser. Open collimation was used on THALES and IN12 had $60'$ collimation on k_i. An important difference in the configuration used on THALES was the choice of a Si(111) monochromator which has an intrinsically superior mosaic to pyrolytic graphite (PG) which reduces the background at low energy transfers (at the expense of a large reduction in flux) [1]. Geometrical constraints placed by the horizontal magnet constrained the measurement of the magnetic signal to lower energy transfers than were accessed on IN12 ($E < 0.45$ meV).

7.3 Data Analysis

7.3.1 Scaling THALES data by the transmission of the velocity selector

The initial configuration of the THALES instrument had a velocity selector before the monochromator. The velocity selector broke after run 24188 and subsequent runs were taken without the velocity selector. The removal of the velocity selector increases the flux of neutrons with the desired wavelength (due to the imperfect transmission) but the

---

[1] The mosaic of the PG(002) monochromator on THALES has a FWHM of 0.5°[159] whereas the intrinsic mosaic of the Si(111) monochromator is typically two orders of magnitude less, however the Si(111) monochromator is bent and the effective mosaic will depend on the extent of the focussing[167].

monitor count rate will have an additional contribution due to contamination of the beam post-monochromator with higher order harmonics which should have been removed by a Be filter before the analyser (though neutrons with $\lambda/2$ are not reflected from the Si (111) monochromator). To distinguish between the two effects, the signal was normalised by time, rather than the monitor count, such that the fractional increase in the magnetic signal is due only to the transmission of the velocity selector.

Fig.7.3 shows constant energy scans taken in both configurations. The SDW Bragg peaks were measured after field cooling at 5.9 T from above T_{N} (0.8 K and 0.7 K with and without the velocity selector respectively). It can be seen that intensity of the SDW Bragg peak is greater with the velocity selector than without, which cannot be explained by the transmission of the velocity selector and must be intrinsic to the sample. Though the data were taken having field cooled to avoid hysteric effects, there was a magnet quench between the measurement of the SDW Bragg peaks in the two configurations. Additionally small changes in sample alignment (or orientations with respect to the field) post-quench would also be expected to have a much greater effect on the measured Bragg peak intensity than the inelastic signal. Fortunately, the inelastic signal appears to scale consistently with the non-magnetic background and the discrepancy in the SDW Bragg intensities does not impact the subsequent analysis.

The data in each constant energy scan were fitted with a linear background that differed between the two configurations only by an additional multiplicative scale factor applied to the data with the selector (the same scale factor for data at both energies). The magnetic signal was modelled with a Gaussian peak with a centre constrained to be the same for both configurations. The optimal scale-factor from the background fit was found to be 1.28(1), which also agrees well with the ratio of the inelastic peak heights. Constant Q scans shown in Fig.7.9 are also consistent with this scaling, therefore it can be concluded that the velocity selector does not increase the signal-to-background ratio and the difference in the count-rate is due solely to the transmission of the velocity selector (which from the inverse of the scale factor is approximately 0.8). The validity of this scaling is confirmed in the analysis of constant Q scans at 4 T and 5.9 T shown in Fig.7.9.

7.3.2 Estimated energy resolution

In order to determine if the fluctuations soften at the metamagnetic transition it is important to consider the impact of the resolution on two factors: the contamination of the low-energy fluctuations by the tail of the magnetic Bragg peak (when present)

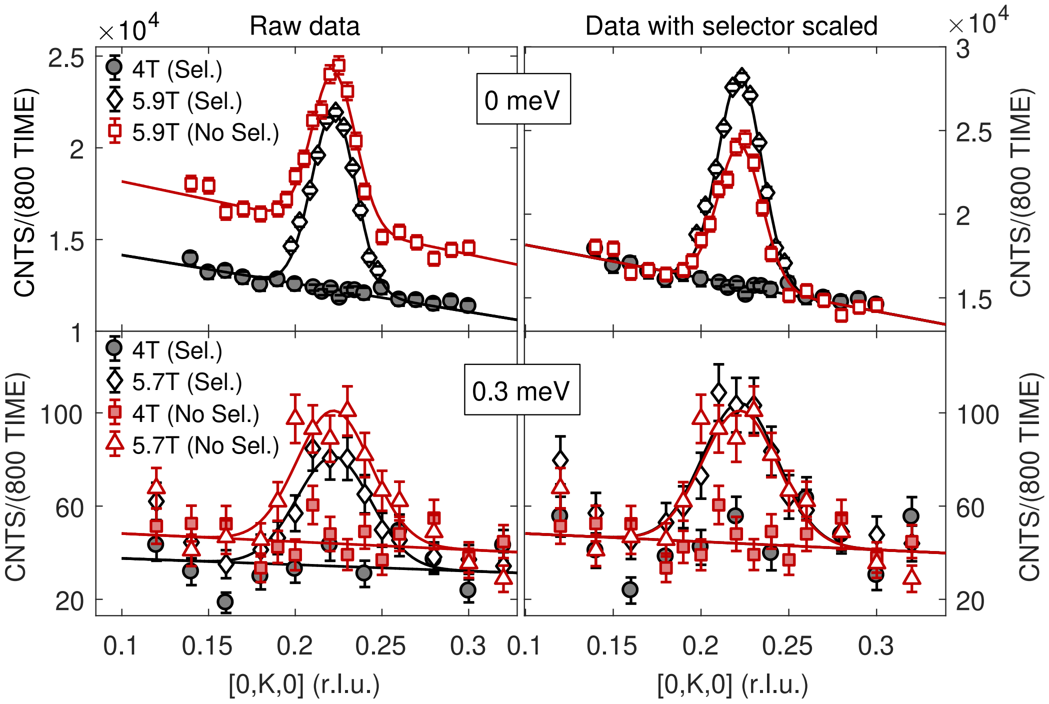

Figure 7.3: Constant energy transfer scans at 0 meV (top) and 0.3 meV (bottom) taken on THALES in two instrument configurations (with/without a velocity selector). The plots in the right column have the data with the velocity selector scaled such that the background and inelastic scattering match the data taken without the velocity selector. Solid lines are fits to Gaussian peak and linear background.

captured by the resolution ellipsoid at finite energy transfer, and the broadening of the inelastic response by the resolution. Typically a Bragg peak is much sharper than the resolution and the observed width then depends on the width of the resolution function in the scattering plane. At the other extreme, if the features in $S(\boldsymbol{Q}, E)$ are much broader than the resolution then the width of the energy resolution at small energy transfers can be estimated from incoherent elastic scattering at the relevant wavevector. The incoherent scattering has no wavevector dependence and therefore the observed energy width is essentially a projection of the resolution ellipsoid volume onto the scan direction. The inelastic magnetic scattering is much broader than the Bragg scattering and therefore will be somewhere between the two limits.

Fig.7.4 shows the constant Q scans at two wavevectors/fields for each orientation: a scan that exhibits a Bragg peak due to static SDW order, and another for which the elastic scattering is from the incoherent background. The spectral weight at higher energy transfer is due to the low-energy of the spin fluctuations (with a background Lorentzian tail due to the effective mosaic of the focussed monochromator). The FWHM of the Gaussian peak fitted to the incoherent elastic scattering are 0.08 meV and 0.04 meV for the IN12 and THALES data respectively - though the latter is an upper bound as there are no data between $0 \text{ meV} < E < 0.05 \text{ meV}$ (in addition the centre of the Gaussian was fixed at 0 meV for the THALES data).

There are a sufficient number of points in the constant Q scan shown in Fig.7.4A to estimate the width of the SDW Bragg peak on IN12. Fig.7.5 compares the width of the incoherent elastic and Bragg scattering for the same data in Fig.7.4A. The SDW peak was modelled as an additional Gaussian peak on top of the incoherent elastic peak. Note that that the fluctuations produce a tail at positive energy transfer which is not included in the fit (greyed out in Fig.7.5). This tail is not seen at negative energy transfer (neutron energy gain) due to the Bose population factor at the temperature measured ($T = 0.1$ K). The resulting FWHM of the Bragg peak is 0.065 meV - as expected it is sharper in energy than the incoherent elastic scattering. It can be seen that the fluctuations measured on IN12 will not be contaminated by magnetic Bragg scattering for energy transfers $E \gtrsim 0.15$ meV. As there are insufficient data to establish the energy width of the SDW Bragg peak on THALES we will proceed with the conservative upper bound as estimated from the incoherent elastic scattering in Fig.7.4B, which is negligible for energy transfers $E \gtrsim 0.07$ meV.

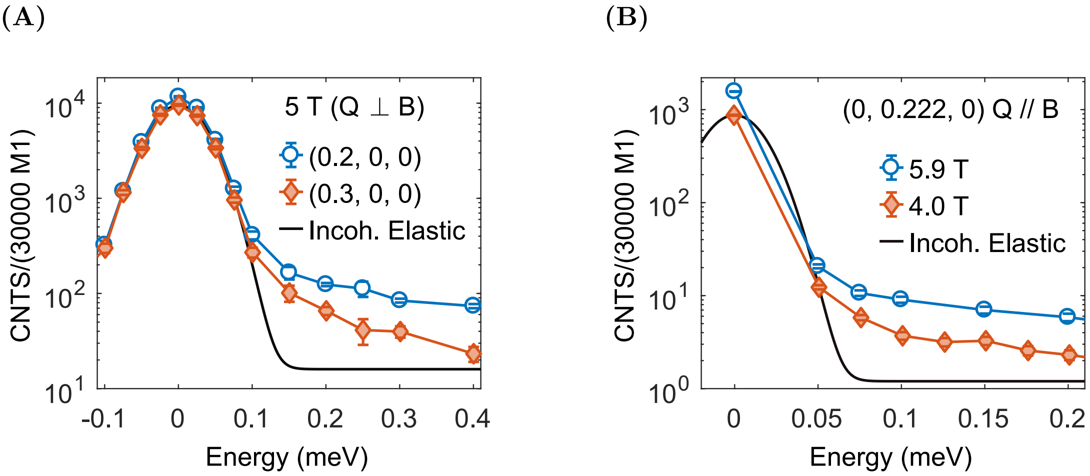

Figure 7.4: Constant Q scans with the y-axis plotted on a log scale. (A) Scan at the SDW Bragg peak wavevector and at a nearby position in reciprocal space where there is no Bragg peak which exhibits a peak at zero energy due to incoherent elastic scattering, the black line is a Gaussian fit to the incoherent elastic peak with a constant background (extracted from high-energy transfer at which the scattering intensity saturates). Data were taken on IN12 for a field of 5 T perpendicular to $\boldsymbol{Q}$. (B) Scan at the SDW Bragg peak wavevector at two fields (4 T and 5.9 T) applied parallel to $\boldsymbol{Q}$ outside and inside the ordered phase respectively. An estimate for the incoherent elastic scattering was made by fitting two low energy points of the 4 T data with a Gaussian peak with the centre constrained to be at zero energy (black line). A constant background was extracted from high energy transfer.

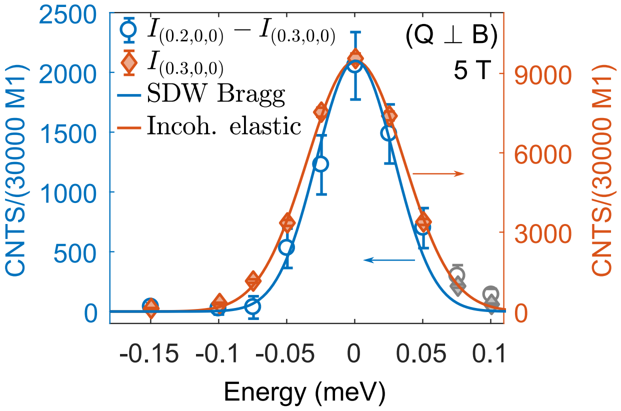

Figure 7.5: Figure shows the same data in Fig.7.4A, taken on IN12. The data at (0.3,0,0) has been subtracted from (0.2,0,0). The solid lines show the Gaussian contributions of the incoherent elastic scattering and Bragg scattering. Note that the data were fit simultaneously, i.e. the Bragg scattering was not fitted to the subtracted data, but to the raw data at (0.2,0,0) - with the incoherent elastic scattering fitted simultaneously to the (0.3,0,0) data. Greyed out markers were excluded form the fit (due to the presence of fluctuations)

.

7.3.3 Modelling the fluctuations

The data are analysed with the general response for a nearly antiferromagnetic metal which takes the form of an overdamped harmonic oscillator, which is often used to describe the spin-fluctuations in systems with an instability to SDW order, notably in the ruthenates (e.g. [61, 168, 169, 66]) and the cuprates (e.g. [170, 171]). The expression can be derived from the RPA form of the susceptibility in Eq.2.21, with a non-interacting susceptibility peaked at the wavevector of the instability, q_δ, using a power series expansion of the inverse of the Lindhard function of a single isotropic band in terms of $q - q_\delta$ and ω.[172, 22] [2].

The resulting response function is given by,

$$\chi''(\boldsymbol{q},\omega) = \frac{\omega\chi_{\boldsymbol{q}}\Gamma_{\boldsymbol{q}}}{\Gamma_{\boldsymbol{q}}^2+\omega^2} \tag{7.1}$$

where $\boldsymbol{q} = \boldsymbol{Q} - \boldsymbol{q_\delta}$ is the difference between the scattering wavevector and the wavevector

---

[2] Recall that Eq.2.21 can be re-written as $\chi(\boldsymbol{q},\omega)^{-1} = \chi(\boldsymbol{q},\omega)_0^{-1} + U$ (often referred to as the Dyson equation).

of the instability [3]. The characteristic frequency is given by,

$$\Gamma_{\boldsymbol{q}} = \Gamma_{\boldsymbol{\delta}}(1 + \xi^2 \boldsymbol{q}^2) \tag{7.2}$$

and the static susceptibility by

$$\chi_{\boldsymbol{q}}^{-1} = \chi_{\boldsymbol{\delta}}^{-1}(1 + \xi^2 \boldsymbol{q}^2) \tag{7.3}$$

where the ξ is the correlation length which determines the width of the peak in constant energy scans [4]. From Eq.7.1 it can be seen that at a given $\boldsymbol{q}$ the response has the form of an over-damped harmonic oscillator with correlations decaying exponentially in time with relaxation rate Γ,

$$\chi''(\omega) = \chi'(0)\frac{\omega\Gamma}{\omega^2 + \Gamma^2} \tag{7.4}$$

The measured intensity is proportional to the differential cross-section which is related to the imaginary part of the susceptibility as detailed in Chapter 3. These data were taken at low temperature ($T \lesssim 0.1$ K) such that the Bose population factor $[n(\omega, T) + 1] \approx 1$ for the energy transfer range included in the fit. The magnetic form-factor was included in the fitting function, using the tabulated parametrisation for the Ru^+ ion [41] [5].These data were not fitted with resolution convolution - it will be shown that the estimated resolution from the energy width of the incoherent elastic scattering is much sharper than the energy dependence of overdamped spin-fluctuations.

7.4 Results

The static SDW order is three-dimensional as evidenced by the sharpness of the peak along the L direction in reciprocal space, as discussed in Chapter 6. Fig.7.6B shows a constant energy scan for a field of 5 T applied perpendicular to the scattering plane on IN12. The broad L-dependence indicates there is no correlation between spins in different bilayers (i.e. the fluctuations are two-dimensional). The interaction between spins in the

---

[3] In a 2D material the spins are not correlated along $\boldsymbol{c}^*$ so the L-component can be ignored, however in this case all measurements were at $L = 0$.

[4] For the non-isotropic case the correlation length can be different for components of $\boldsymbol{q}$ parallel and perpendicular to the wavevector of the instability $\boldsymbol{q_\delta}$.

[5] The Ru ions in $Sr_3Ru_2O_7$ are not Ru^+ but are nominally Ru^{4+} for which there is no published form-factor, Nevertheless, the Ru^+ has been empirically shown to provide a reasonable approximation for the form-factor of many itinerant ruthenate compounds[173].

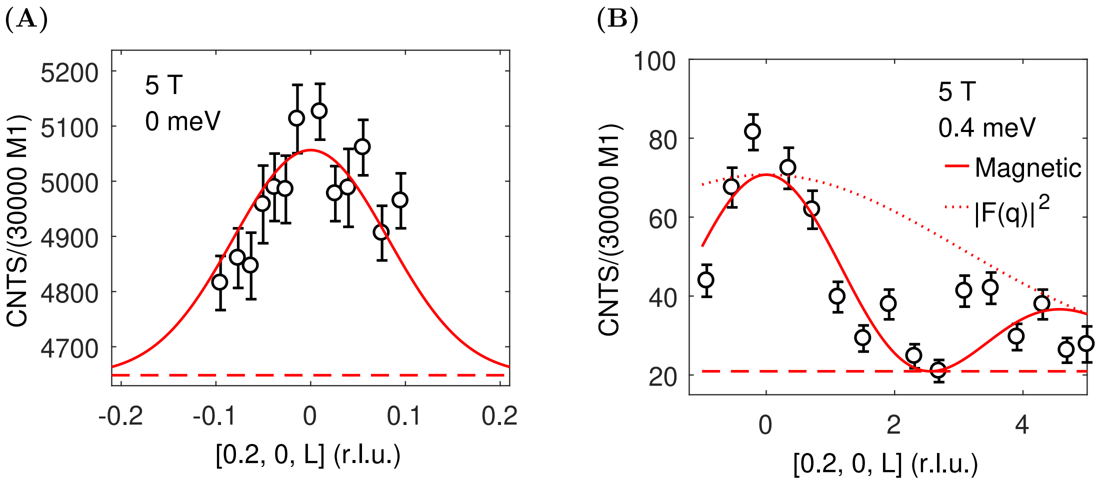

Figure 7.6: Constant energy scan along the L direction with a field of 5 T applied perpendicular to Q at 0 meV (A) and at 0.4 meV (B) measured on IN12. The SDW Bragg peak in (A) has been fitted with a Gaussian function with a constant background taken as the value of background at (0.2,0,0) taken from fits to the longitudinal scans in Fig.7.7. The fluctuations in (B) are fitted with a model where the spin fluctuations in each bilayer are in-phase (solid red line) as detailed in the main text. The square of the magnetic form-factor for the spin-only Ru^0 ion is also plotted for reference (dashed red line). The background is assumed to be constant, fixed at a value of the background at 0.4 meV from constant Q scans at (0.2,0,0).

two planes of a bilayer do however give rise to an oscillating response given by,

$$\chi''(h,k,l,E) = \chi''_{odd}(h,k,E)\sin^2\left(\frac{\pi d}{c}l\right) + \chi''_{even}(h,k,E)\cos^2\left(\frac{\pi d}{c}l\right) \qquad (7.5)$$

where d is the separation between the $\mathrm{RuO_2}$ planes that comprise the bilayer and the labels odd/even correspond to the ferromagnetic/antiferromagnetic coupling of the spins in the bilayer planes respectively. The data in Fig.7.6B are consistent with only ferromagnetic coupling of the bilayers (indicated by the solid red-line), which is also observed in the fluctuations at zero field [124] and for a magnetic field applied along the c-axis[72]. The scattering geometry of the THALES experiment did not allow for the L-dependence of the fluctuations for a magnetic field applied parallel to the incommensurate wavevector to be measured.

Fig.7.7 shows longitudinal scans through the incommensurate fluctuations at two energy transfers (0.3 meV and 1 meV) at select magnetic fields applied perpendicular to Q measured on IN12. As the fluctuations are two-dimensional they are also observed at the position $(1-\delta,0,0)$ (as is seen in the 1 meV data) because $(1,0,\pm1)$ are reciprocal lattice

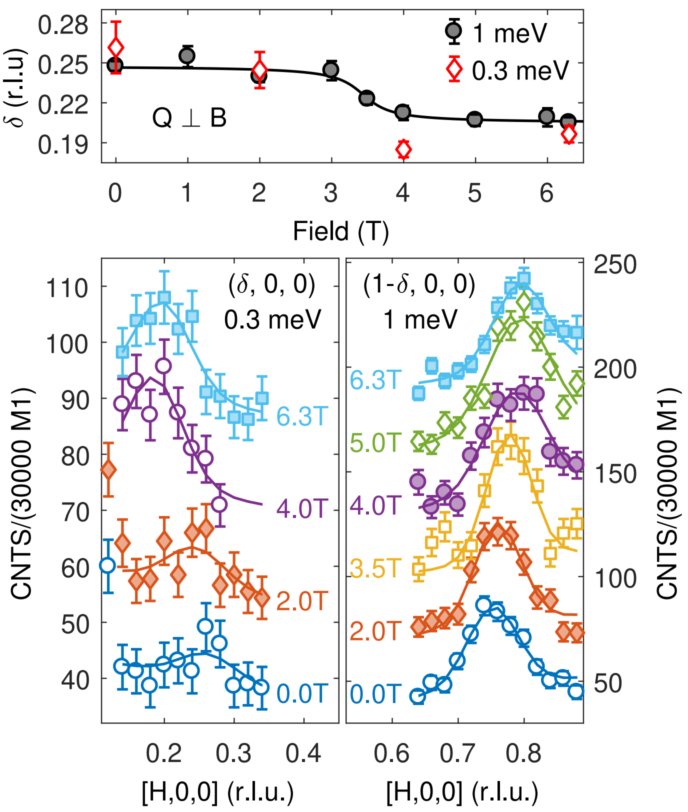

Figure 7.7: Longitudinal scan at constant energy through the incommensurate magnetic scattering at two energy transfers: 0.3 meV with k_f=1.15 Å^{-1} (left) and 1 meV with k_f=1.55 Å^{-1} (right) at select magnetic fields applied perpendicular to Q measured on IN12. Data are offset for clarity and were fitted with a Gaussian peak and a field independent linear background. (Top) The incommensurability of the peak as a function of magnetic field.

points of the body-centred lattice (even though $(1, 0, 0)$ is not). The spectral weight of the fluctuations at low energy is most-sensitive to the magnetic field: the fluctuations at 0.3 meV are weak at low magnetic field (the peak is only just resolvable within the statistic at zero field) and increases with the field for $B < 5$ T. The wavevector of the fluctuations measured at both energy transfers are consistent, with an almost commensurate value at low-field $\delta \approx 0.25$ decreasing sharply at ~ 3.5 T to value $\delta \approx 0.2$ which is comparable to the wavevector of the SDW order at 5 T.

Fig.7.8 shows longitudinal scans through the incommensurate fluctuations at two energy transfers (0.1 meV and 0.3 meV) at select magnetic fields applied parallel to Q measured on THALES. The weak peak at 0.3 meV in the zero-field IN12 data cannot be identified within the statistics on THALES (the use of a Si monochromator severely reduced the incident flux). The wavevector of the fluctuations are consistent with the

SDW ordering wavevector $\delta \approx 0.222$, with no resolvable change between 0.1-0.3 meV in the field range measured ($4\ \mathrm{T} \geq B \leq 6\ \mathrm{T}$).

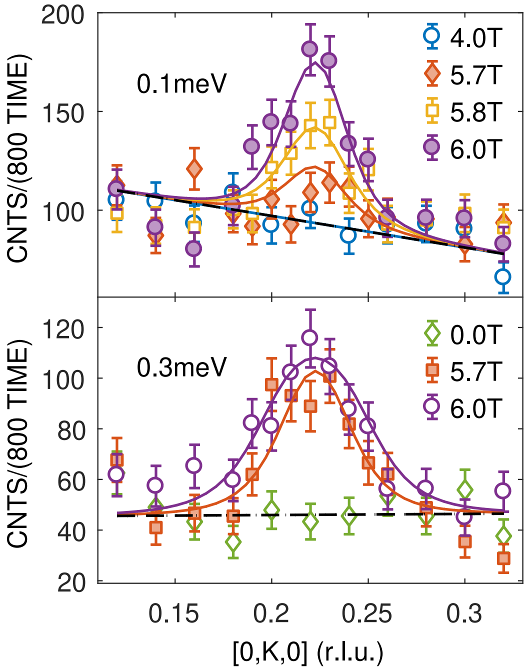

Figure 7.8: Longitudinal scan at constant energy through the incommensurate magnetic scattering at two energy transfers: 0.1 meV (top) and 0.3 meV (bottom) at select magnetic fields applied parallel to Q, measured on THALES without the velocity selector. These data and constant Q scans were fitted simultaneously with a DHO function (see main-text).

Fig.7.9 shows constant Q scans at the position of the incommensurate fluctuations at select magnetic fields applied parallel to Q measured on THALES. The FWHM of the resolution as estimated from the elastic incoherent scattering (horizontal black bar in Fig.7.9) is much smaller than the broad response of the spin-fluctuations. The data in Fig.7.8 and Fig.7.9 at each magnetic field were fitted with the phenomenological model in Eq.7.1 with the wavevector of the instability constrained to be the same for all fields. The fit model included the pre-factor $\mathrm{k}_f/\mathrm{k}_i$ in Eq.3.15 as the data were not normalised by time rather than a monitor before the sample. ξ was included in the model for the subset of fields at which a constant Q scan was measured - which provides a lower bound on the actual correlation length due to resolution broadening. Data in both velocity selector configurations at the same field were fitted with a common Γ_δ but independent $\chi'(\boldsymbol{q}, 0)$ (post-scaling). The magnetic response was fitted over the energy transfer range $E \geq 0.075$ meV to ensure there was no contamination from the SDW Bragg peak. The non-magnetic background was assumed to be field-independent. The background of constant Q scans was modelled as the sum of a Gaussian peak for the incoherent elastic scattering and a Lorentzian tail for the monochromator mosaic and fitted to the 4 T data. Constant energy scans were fitted with a linear background that matched the background of the constant Q scans at (0,0.222,0) at that energy. It can be seen that for $B \leq 5$ T there is negligible magnetic scattering in the energy range measured. The incommensurate fluctuations soften (spectral weight moves to lower energy) as the magnetic field is increased and approaches the boundary of the SDW ordered phase.

Fig.7.10 shows constant Q scans for a series of magnetic fields applied perpendicular to Q at three different positions in reciprocal space measured on IN12: the incommensurate wavevector (0.2,0,0) as determined from constant energy scans for $B > 4$ T (see Fig.7.7) and at two nearby positions (0.25,00) and (0.3,0,0). The FWHM of the resolution as estimated from the elastic incoherent scattering (horizontal black bar in Fig.7.10) is much smaller than the broad response of the spin-fluctuations. The data at (0.2,0,0) and (0.25,0,0) were fitted independently Eq.7.4 for energy transfers $E \geq 0.2$ meV. No attempt was made to fit the wavevector dependent response in Eq.7.1 as there are insufficient points to constrain the width in the constant energy scans shown in Fig.7.7. There was no need to multiply the model by the pre-factor $\mathrm{k}_f/\mathrm{k}_i$ as the data were normalised to the monitor between the monochromator and sample. The non-magnetic background was assumed to be field-independent, with an energy dependence modelled with a Lorentzian tail fitted to the data at position (0.3,0,0) over the same energy range for fields above the SDW ordered phase, $B \geq 5.7\ T$ (including data at 7 T not shown in Fig.7.10). Similar to the SDW fluctuations measured on THALES, the fluctuations soften at the field at which the SDW order is detected (5 T). In this experiment it was possible to measure larger magnetic fields, above the SDW ordered phase, it can be seen that for $B \geq 5.7$ T the fluctuations are hardening (spectral weight moving to higher energy).

The parameters from the fits to the THALES and IN12 data are shown in Fig.7.11, for magnetic fields at which the characteristic frequency, Γ_δ is comparable to the energy transfers included in the fit. The fits to the THALES data with a magnetic field parallel to the scattering wavevector show a convincing sharp softening of the characteristic energy, Γ_δ, at the phase boundary $B \approx 5.8$ T reaching a minimum at 5.9 T - which is comparable to the lowest energy transfer included in the fit, 0.075 meV. This is effectively an upper bound on the actual Γ_δ as the fit is not well constrained for such low energy scales as Γ_δ becomes highly correlated with the static susceptibility. The static susceptibility $\chi'(\boldsymbol{q}, 0)$ and correlation length ξ peak at 5.9 T which coincides with the minimum in Γ_δ. The behaviour for the IN12 data in the other field-orientation (perpendicular to the wavevector) is similar, though there are only three fields at which reliable fits could be

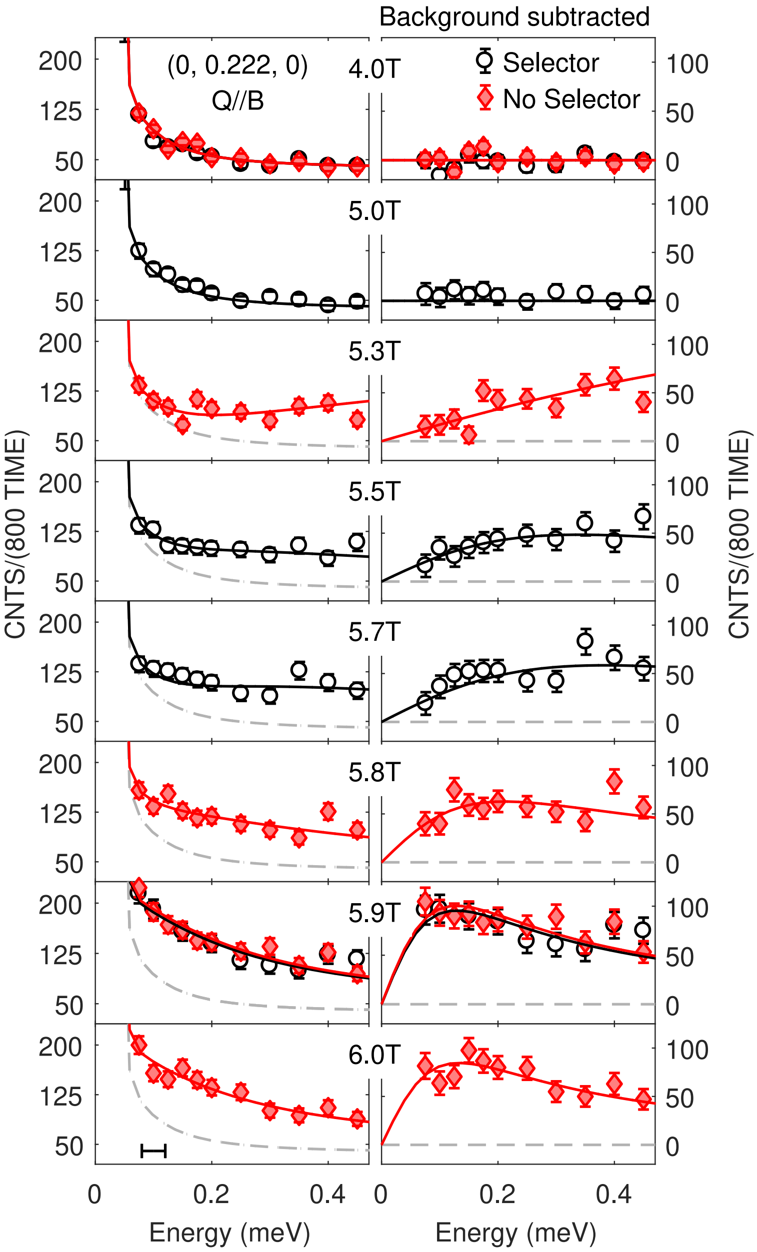

Figure 7.9: Constant Q scans at the incommensurate peak of the magnetic scattering (0, 0.222,0) a series of magnetic fields applied parallel to Q. Data were taken on THALES in two configurations with and without a velocity selector as indicated by the legend, the former have been scaled to account for the transmission of the velocity selector (see main text). The background (dashed grey line) is a Lorentzian peak on the elastic line to model the tail due to the mosaic of the monochromator, fitted at 4 T. Data post background subtraction are shown in the second column. These data and constant energy scans (a subset of which are shown in Fig.7.8) were fitted simultaneously with the model in Eq.7.1 (see main-text for full details). The FWHM of the resolution as estimated from the elastic incoherent scattering is indicated by the horizontal black bar in the bottom-left plot.

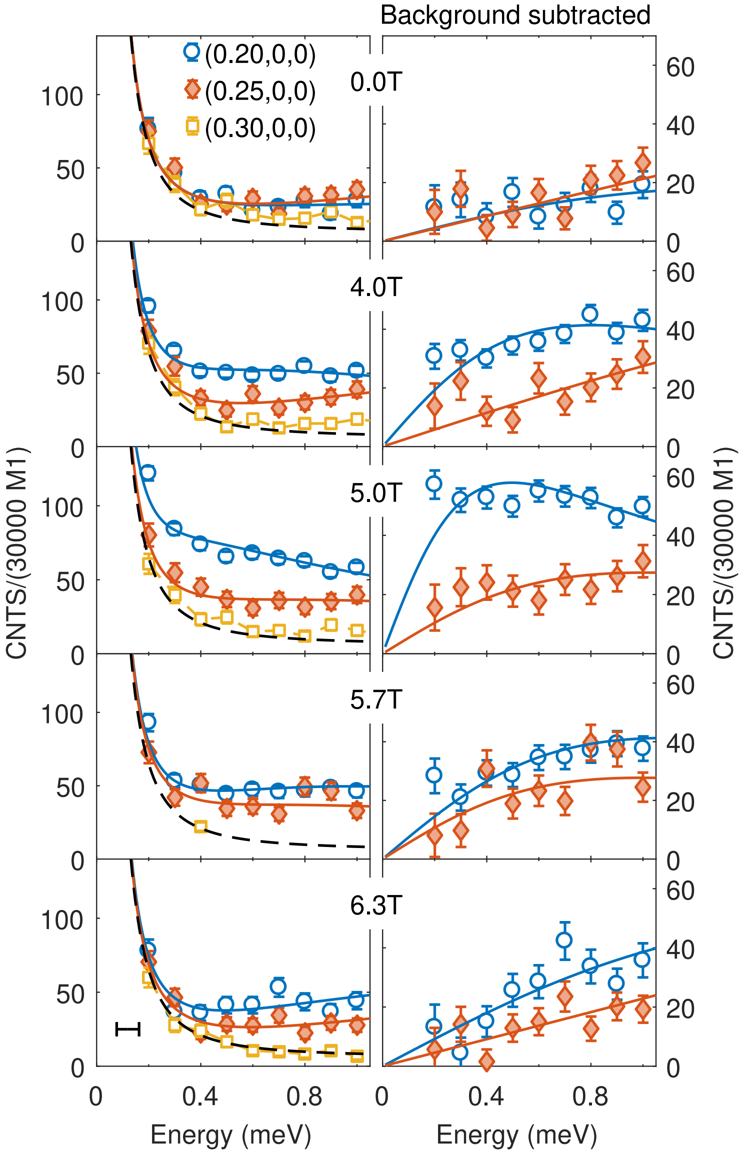

Figure 7.10: Constant Q scans for a series of magnetic fields applied perpendicular to Q at three different wavevectors: the approximate position of the SDW Bragg peak (0.2,0,0), and (0.25,0,0) & (0.3,0,0) that are progressively further from the incommensurate peak position. Data were taken on IN12. The background (dashed grey line) is a Lorentzian peak on the elastic line to model the tail due to the mosaic of the monochromator, fitted to data for $B \geq 5.7\ T$ at position (0.3,0,0). Data at positions (0.2,0,0) and (0.25,0,0) post background subtraction are shown in the second column. These data were fitted with a DHO function without any Q-dependence. The FWHM of the resolution as estimated from the elastic incoherent scattering is indicated by the horizontal black bar in the bottom-left plot.

made. Γ_δ is a minimum at the magnetic field which exhibits SDW order (5 T), which is accompanied by an increase in $\chi'(\boldsymbol{q}, 0)$ (the model did not include ξ).

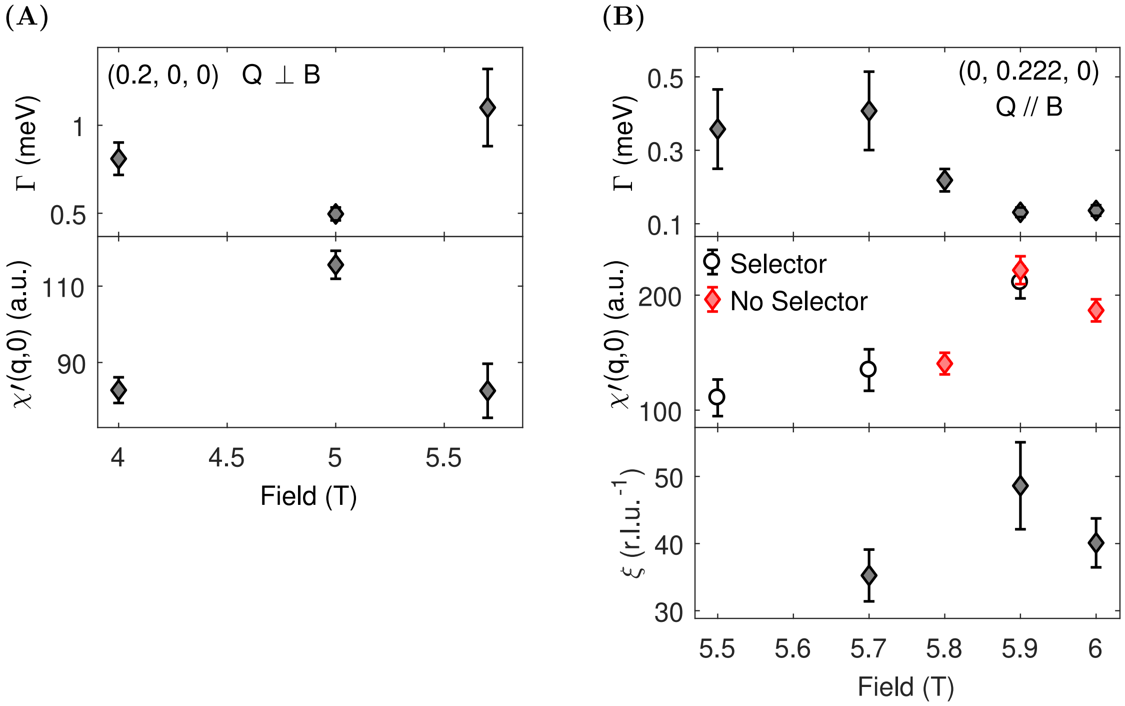

Figure 7.11: Parameters of the DHO model as a function of magnetic field from fits to IN12 data (A) and THALES data (B) for a field applied perpendicular and parallel to Q respectively. Note that the IN12 data does not include the correlation length, ξ, as there are insufficient data at constant energy (scans taken at only one energy transfer that is shown in Fig.7.7, with poor statistics).

Fig.7.12 shows a plot of the characteristic timescale of the fluctuations ($1/\Gamma_\delta$) against $\chi'(\boldsymbol{q}, 0)$ for the fits to data in the different field orientations from both experiments. The data have been fit with a line that passes through the origin that represents the classic critical slowing-down behaviour of a second order phase transition (typically observed as a function of temperature). The agreement for the THALES data (field applied parallel to the wavevector) shown in Fig.7.12B is quite convincing. The behaviour of the IN12 data (field applied perpendicular to the wavevector) shown in Fig.7.12A is suggestive of such behaviour (from the ratio of points at 4 T and 5 T), though it is difficult to draw firm conclusions based on only three data points.

7.5 Discussion

The results presented here show the existence of strong incommensurate fluctuations with an energy scale that can be tuned with the magnetic field in the same range at which thermodynamic probes observe non Fermi-liquid behaviour. Inside the ordered phase

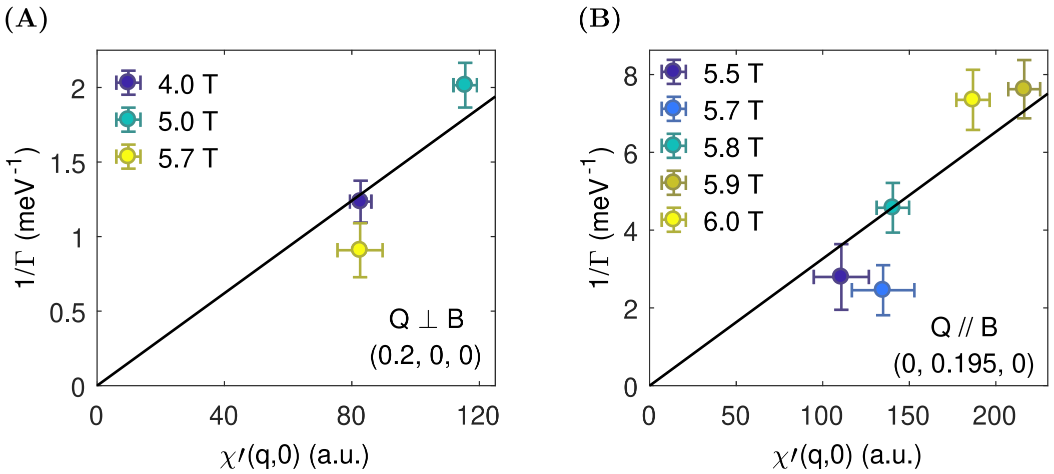

Figure 7.12: Plots of the characteristic timescale of the fluctuations $(1/\Gamma)$ against $\chi'(q,0)$ from ODHO fits to data from IN12 (A) and THALES (B) for select fields applied perpendicular and parallel to Q respectively.

there should exist gapped excitations associated with the order parameter, though the ordered moment is small ($\sim 0.05\ \mu_B$/Ru) and the response appears to be dominated by a background of strong quantum critical fluctuations.

There are two overlapping (but independent) regions of enhanced low-energy spin fluctuations: a low field region ($B \geq 4$ T) associated with the SDW-A′ phase at ~ 5 T with magnetisation parallel to the field direction (measured with a magnetic field perpendicular to the wavevector on IN12); and a high-field region ($B \geq 5$ T) associated with the SDW-C phase at $\sim$ 6 T with magnetisation perpendicular to the field direction (measured with a magnetic field parallel to the wavevector on THALES). In contrast to the C_4 symmetric low-energy fluctuations at small-field tilts from the c-axis, an in-plane field produces fluctuations with the same C_2 symmetry as the SDW order, indicating that the field has fundamentally changed the symmetry of the electronic structure, most likely via spin-orbit effects which clearly need to be included in any theoretical description of the physics in $Sr_3Ru_2O_7$ (a point also made in [100]). Of interest is the kink at $\sim$ 3.5 T in the wavevector of the magnetic fluctuations with a moment parallel to the magnetic field (seen in the IN12 data), which is suggestive of a sudden change in the Fermi-surface, at a much lower field than the boundary of the SDW ordered phase at $\sim$ 5 T.

The fluctuations associated with both phases show qualitatively similar behaviour: the characteristic frequency of the fluctuations, Γ_δ, softens in the vicinity of the SDW ordered phase and the amplitude of the fluctuations quantified by the static susceptibility $\chi'(\boldsymbol{q},0)$ increases. In particular, the THALES data (with the magnetic field parallel to the wavevector) are consistent with the critical slowing down of the fluctuations ($1/\Gamma_\delta \propto \chi'(\boldsymbol{q}, 0)$) in the vicinity of a field-tuned critical point near 5.9 T. The correlation length, ξ of the fluctuations also increases in the vicinity of the critical field, indicating the resolution is sharper than the momentum dependence of the magnetic scattering. Though due to the resolution broadening the value of ξ is a lower bound and the measurements are not sensitive to a divergence.

This behaviour is qualitatively consistent with the observed enhancement of the low-temperature electronic heat capacity in this field region[157] as the contribution of the spin-fluctuations to the specific heat coefficient, $\gamma = C/T$, is proportional to the Brillouin zone average of $1/\Gamma_{\boldsymbol{q}}$ [174]. The associated increase in entropy could lead to an entropy-driven phase transition into the magnetically-ordered phases seen at low temperature.

At 6 T, γ increases nearly logarithmically down to the lowest temperature measured, 1 K (no measurements were made at 5.9 T), which raises the possibility of a proximate QCP that is avoided by static SDW order (the same scenario that is realised for a magnetic field along the c-axis). The possibility of a QCP for an in-plane field has been investigated with AC susceptibility [156] and transport measurements [160] under hydrostatic pressure (which reduces the peak in the density of states and should weaken the metamagnetism). The low-field phase boundary at $B_1' \approx 5.7$ T is weakly first-order at ambient pressure with a small peak in χ'' that is quickly suppressed with pressure [156]. However, the peak in χ' and the anisotropic transport associated with what we now identify as the SDW-C phase shifts to higher fields with increasing pressure, but with a magnitude that is insensitive to pressure [156, 160].This indicates the SDW-C order is decoupled from the mechanism of itinerant metamagnetism and, together with the results presented in this chapter, the evidence suggests that the spin-fluctuations may be responsible for the signatures of quantum criticality observed in this field region.

The evidence of critical slowing down of the fluctuations associated with the SDW-A′ phase at $B_0' \approx 5$ T is less conclusive. However, the observation of such low-energy spin fluctuations coinciding with a first-order transition is striking and raises the possibility that quantum fluctuations are responsible for driving the transition first-order. AC susceptibility measurements under hydrostatic pressure with an in-plane field show that the temperature-dependence of χ' at B_0' exhibits a maximum that is suppressed (both in magnitude and temperature) with increasing pressure well below the pressure at which the critical end-point of the transition is suppressed to zero temperature[156]. The authors of that study conclude that fluctuations of the uniform magnetisation are suppressed as the quantum critical endpoint is approached. On the basis of the data presented in this chapter, it is natural to conclude that the dominant fluctuations are likely to be antiferromagnetic in nature.

In order to confirm the link between the observed spin-fluctuations and the signatures of quantum criticality, further experiments are required to measure the temperature dependence of the fluctuations: for example critical-slowing down of spin fluctuations and a diverging $\chi'(T)$ as $T \rightarrow 0$ K have been observed at a field-tuned QCP of an SDW phase in the heavy fermion compound $CeCu_2Ge_2$ [175].

Near a quantum critical point, the energy scale of the fluctuations should be governed by the temperature T, which produces E/T scaling of the form,

$$\chi''(E,T) = T^{-\alpha} g(E/T) \tag{7.6}$$

that has been observed in the high-T_c cuprate $La_{2-x}Sr_xCuO_{4+y}$[176], and many heavy-fermion materials, notably $CeCu_{6-x}Au_x$ [177] [6]. Though the power, α, and precise functional form of $g(E/T)$ depends on the theory and microscopic details (e.g. itinerant or local-moment magnetism).

In addition, these results should prompt more detailed measurements of the heat capacity and the magnetocaloric effect for magnetic fields in the ab-plane (as have been done for the field along the c-axis), to investigate the signatures of quantum criticality and map out the entropy landscape in the region of the SDW phases, particularly at the critical field identified in this study, 5.9 T.

7.6 Conclusion

The results in this chapter show that a magnetic-field applied along the Ru-O bond in the RuO_2 planes of the bilayers in $Sr_3Ru_2O_7$ can be used to tune the relaxation rate of strong quantum-critical magnetic fluctuations which soften at fields inside the SDW ordered phases. In particular, the fluctuations with a moment perpendicular to the field (measured on THALES with a magnetic field parallel to the incommensurate wavevector) exhibit critical slowing down behaviour ($1/\Gamma_\delta \propto \chi'(\boldsymbol{q}, 0)$) consistent with a field-tuned critical point near 5.9 T, that is avoided by static order. The data agree qualitatively with thermodynamic measurements such as the enhancement of the low-temperature heat capacity for $B > 4\ T$. The logarithmic divergence of the heat capacity coefficient is observed at the same critical field identified by these data[157]. It is clear that low-energy spin-fluctuations are relevant to the physics and thermodynamic properties of $Sr_3Ru_2O_7$, and the role of metamagnetic quantum criticality may need to be re-examined.

---

[6] And also in $CeCu_2Ge_2$.

In particular, further experimental work is required to confirm that the fluctuations exhibit the E/T scaling expected at a quantum critical point.

Chapter 8

Uniaxial stress tuned spin-density-wave order in $CeAuSb_2$

Recently transport measurements indicate that $CeAuSb_2$ hosts competing instabilities that couple differently to uniaixial stress along certain high-symmetry directions[178]. This chapter presents neutron diffraction measurements with a novel device (designed by C. Hicks of MPI, Dresden) to allow for in-situ uniaxial stress tuning. Compressive uniaxial stress along the a-axis produces a monodomain of single-q SDW order that is believed to restore the continuous nature of the transition at T_{N} by reducing the point group symmetry of the fluctuations. Sufficient data were taken to allow for a refinement of the magnetic structure, from which it can be inferred that the order is consistent with an itinerant SDW modulation.

8.1 Magnetism in heavy fermion compounds

Here we provide a brief introduction to the phenomenology and the magnetism of heavy-fermion materials, which will be necessary to interpret the results of this chapter. There are many reviews of heavy fermion physics for example [179, 180, 181] (the latter focusses explicitly on quantum criticality).

Heavy fermion materials are a class of intermetallic compounds containing elements with incomplete f-electron shells (such as Ce, U and Yb) that exhibit large quasiparticle effective masses [1]due to the antiferromagnetic (Kondo) interaction between the localised f-electron moments and conduction electrons.

At high temperatures, the f electron spins are localized. As the temperature decreases below some characteristic energy scale referred to as the Kondo temperature, T_{K}, the local moments are progressively screened by the hybridisation of the f electrons with the conduction electrons, forming singlet-state quasiparticles that contribute to the Fermi-surface volume and eventually Fermi liquid behaviour is restored. The hybridization results in a pseudo-gap in the density of states at the Fermi level and flat bands above and below the Fermi level associated with peaks in the density of states which can produce itinerant metamagnetism.

As a function of temperature there is a continuous crossover from a small Fermi surface with localised spins to a large Fermi surface in which the moments are screened. The extent to which the moments are screened depends on the competition between the Kondo effect and the Ruderman-Kittel-Kasuya-Yosida (RKKY) interaction - an indirect exchange interaction between the local moments that oscillates with distance from the f moments. Physically, the RKKY interaction arises from an f spin coupling to the induced spin-density oscillation due to the non-local susceptibility of the conduction electrons which are perturbed by the field of another f spin (similar to a SDW with a decaying amplitude).

If the RKKY interaction dominates then the system will exhibit local moment order (typically AFM) at low temperature. Otherwise the Kondo effect produces a paramagnetic Fermi liquid that can host other instabilities such as spin density wave (SDW) order, the susceptibility to which can be strongly influenced by the structure in the density of states near the Fermi level produced by the hybridisation.

The Kondo temperature and RKKY exchange scale differently with the strength of the Kondo interaction and the density of states of the conduction electrons at the Fermi

---

[1] For example the heavy-fermion compound $CeAl_3$ has a Sommerfeld coefficient (linear coefficient of the temperature dependent electronic heat capacity - proportional to the effective mass) of 1620 mJ $\mathrm{mol}^{-1}\mathrm{K}^{-2}$, compared to a value of 1 mJ $\mathrm{mol}^{-1}\mathrm{K}^{-2}$ for copper[182].

level - which can be tuned with non thermal parameters such as doping, magnetic field and hydrostatic pressure. The two regimes can be separated by a quantum critical point (QCP) of long-range antiferromagnetic order (local moment or SDW), for example in $\mathrm{YbRh_2Si_2}$, where Hall effect measurements also indicate that the QCP coincides with the reconstruction of the Fermi-surface and the localisation of the $4f$ spins[183].

8.2 Background to $\mathrm{CeAuSb_2}$

$\mathrm{CeAuSb_2}$ is a moderately heavy fermion system, with a Sommerfeld coefficient of 236 mJ $\mathrm{mol^{-1}K^{-2}}$[184]. It crystallises in a tetragonal spacegroup $P4/nmm$, with a quasi-2D structure that consists of alternating CeSb-Au and CeSb-Sb planes stacked along the c-axis. The quasi-2D nature of the material is evident in the strongly anisotropic magnetic susceptibility (easy axis along c) and anisotropic resistivity for currents in/out of the plane, ρ_{ab}/ρ_c[185]. A shoulder in the both $\rho_{ab}(T)$ and $\rho_c(T)$ indicates a Kondo temperature of $\sim$14 K [185, 11]. At a lower temperature the system orders antiferromagnetically with $T_{\mathrm{N}} \sim 6.5$ K (the actual transition temperature is sensitive to the Au occupancy) [184].

The magnetic order was thought likely to be itinerant in nature, condensing from a Fermi liquid in which the Ce $4f$ moments are incorporated into the Fermi volume. Heat capacity measurements show that above T_{N} there is good entropy balance with a Fermi-liquid (i.e. in the absence of magnetic order, $C \propto T$)[11] and for $T < T_{\mathrm{N}}$ the resistivity shows a T^2 dependence expected for a Fermi liquid [10].

Initial interest in $\mathrm{CeAuSb_2}$ was motivated by the possibility of magnetic field tuned quantum criticality, which is a rare phenomenon which to date has only been seen in two other stoichiometric Ce-based compounds $\mathrm{CeCoIn_5}$ [186] and $\mathrm{CeIrIn_5}$[187]). The paramagnetic phase of $\mathrm{CeAuSb_2}$ exhibits a non-Fermi-liquid temperature dependence of the resistivity $\rho_{ab}(T) \propto T^{\alpha}$ where $\alpha < 1$ [10, 188]. A magnetic field applied along the c-axis (easy axis) suppresses T_{N} to an end-point at about $B_{\mathrm{c}} = 5.4$ T where antiferromagnetic order terminates. However the transition at T_{N} is weakly first-order at zero field[184], and remains first-order at B_{c} down to the lowest temperature measured (22 mK)[10].

There is some evidence of quantum critical fluctuations near B_{c} at higher temperature: the coefficient of the T^2 term in the resistivity ρ_{ab} diverges and the heat capacity shows a logarithmic temperature dependence above 3 K (albeit over a relatively small temperature range $T < T_{\mathrm{K}}$[10]). But it is apparent that a magnetic field cannot tune the system to a quantum critical point. However, it does have a profound impact on the magnetic order.

8.3 Field-induced SDW order in $\mathrm{CeAuSb_2}$

Recent neutron diffraction measurements by Marcus *et al.*[154] have discovered that at zero magnetic field the antiferromagnetic order is a single-q spin-density-wave (A-phase) with two C_2 symmetric domains with incommensurate wavevectors $\boldsymbol{q}_{1/2} = (\delta, \pm\delta, 0.5)$, where $\delta = 0.136$, and an ordered-moment polarised along the c-axis (where a/b are along the in-plane Ce-Ce bond). The application of a magnetic field along c for $T < T_{\mathrm{N}}$ results in the appearance of second-order harmonics at $2q_{1/2}$ and eventually a first-order metamagnetic transition at ≈ 2.8 T into a new phase with additional Fourier components with wavevector $q_1 \pm q_2$ - i.e. at $(2\delta, 0, 0)$ and $(0, 2\delta, 0)$ (shown in Fig.8.1). Hereafter the field-induced phase will be referred to as the A$'$ phase due to the continued presence of the $q_{1/2}$ Fourier components associated with the zero field A-phase [2].

The neutron scattering data for the A-phase are largely consistent with the itinerant SDW scenario, with the absence of a third-order harmonic which is incompatible with the square-wave/local moment model. Indeed, a DFT calculation has identified Fermi surface nesting consistent with the experimentally determined wavevectors of the A phase, $q_{1/2}$[190]. However, the critical exponent of the ordered moment in both the A and A$'$ phase is inconsistent with the mean-field BCS form expected for a SDW. Additionally, the magnitude of the ordered moment in the A phase at zero field is in good agreement with the saturated bulk moment at high field, which can be interpreted as local moment-like behaviour. Marcus *et al.* also report that the inverse susceptibility at low temperature (10 K$< T <$ 80 K) is consistent with a Weiss temperature of -6.6 K that is similar to the observed T_{N} [3]. They suggest that the sum of the bulk and staggered moments (i.e. the maximum moment on a Ce site) for all fields could be set by the effective moment of the $\mathrm{Ce^{3+}}$ ion.

The coupling of components $q_1 \pm q_2$ in the A$'$ phase is not possible for domains of C_2 order and indicates the restoration of tetragonal symmetry. In an itinerant system this would typically imply a transition from single-q to double-q checkered-type order (shown in Fig.8.2), as observed in the iron pnictides [191, 192, 193]. However, Marcus *et al.* propose an alternative structure comprising domains of a C_2 symmetric woven order which produces a maximum moment on the Ce site that agrees with the effective moment (see Fig.8.2). In the woven structure the Fourier components corresponding to $q_1 + q_2$

---

[2] It should be noted that in some of the literature[178, 189] the field-induced phase is referred to as the B-phase.

[3] The observed effective moment over the same temperature range is 1.65 μ_B/Ce. The effective moment will differ from the free ion moment of $\mathrm{Ce^{3+}}$ (nominally 2.54 μ_B/Ce) due to crystalline electric field effects and Kondo screening. The latter being temperature dependent, which may explain why a higher effective moment of 2.25 μ_B/Ce is reported in[10].

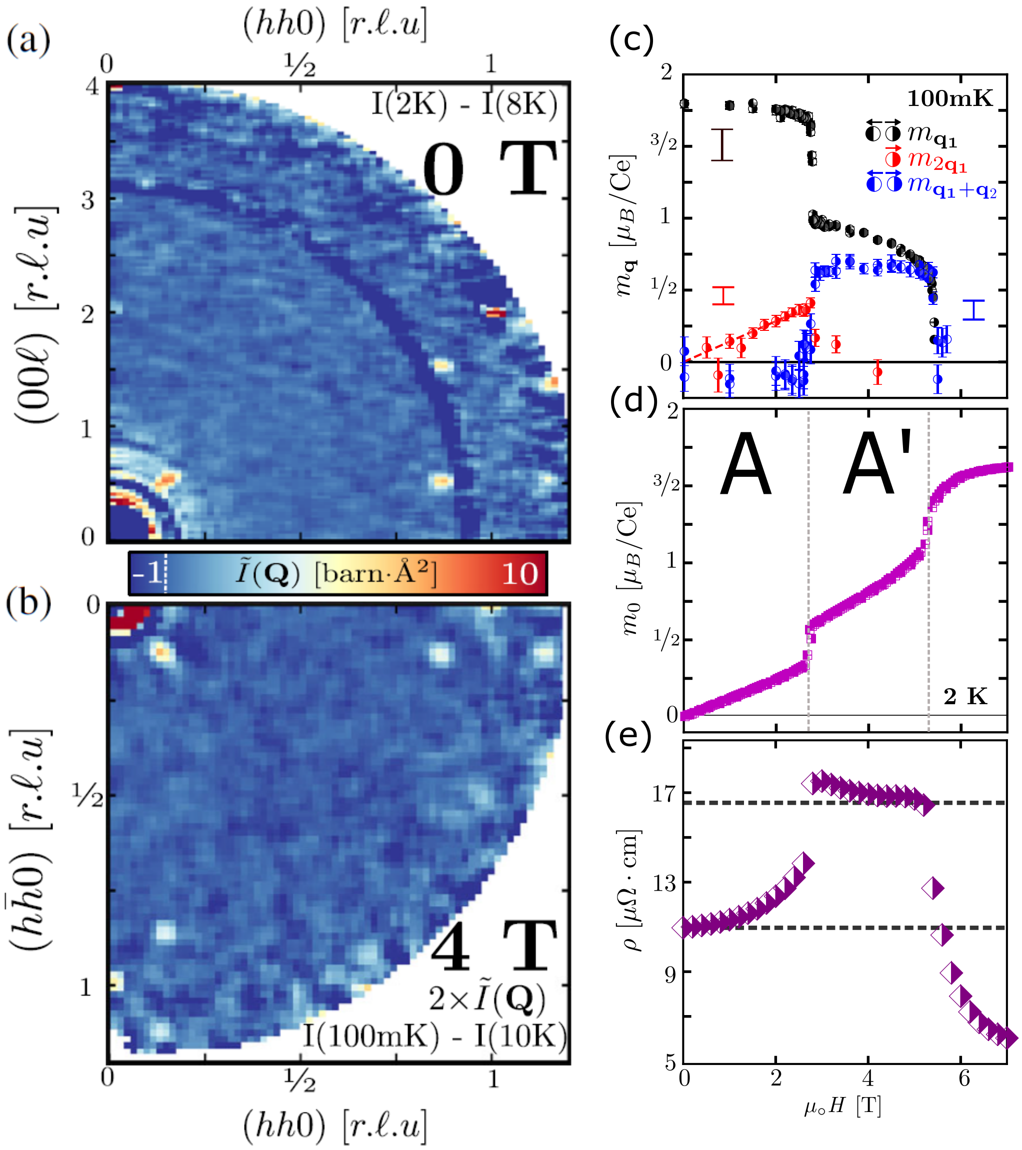

Figure 8.1: (a-b) Neutron diffraction data at two fields (0 T and 4 T) that exhibit Bragg peaks in the A and A′ phase respectively. (c) Intensity of Fourier components at three wavevectors as a function of magnetic field (see main text). (d-e) Bulk magnetisation and resistivity as a function of magnetic field at 2 K with the phase boundaries indicated by dashed grey line. Figures taken from [154].

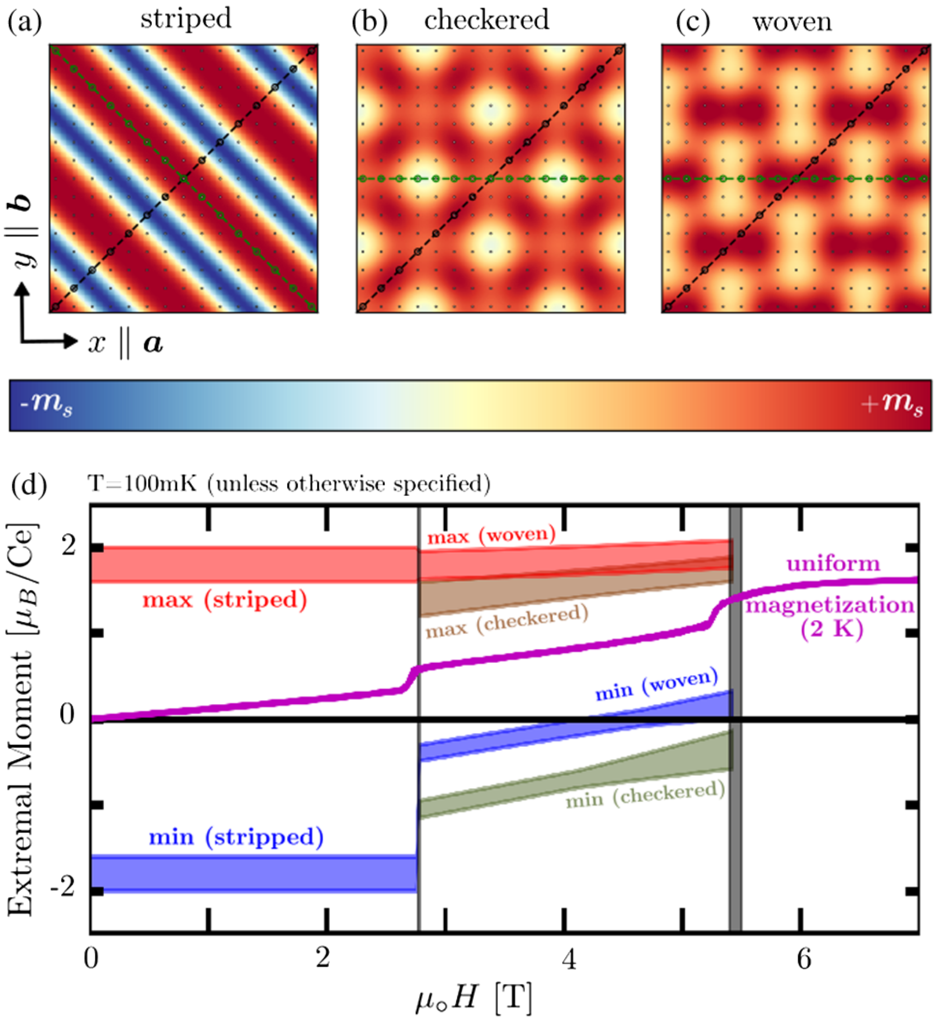

Figure 8.2: (a-c) Real space schematic of stripe, checkerboard and woven structures respectively (green and black lines refer to other figures in [154] which are not relevant). (d) Measured bulk moment and predicted staggered moment per Ce as a function of magnetic field for the checkered and woven structures. Figures taken from [154].

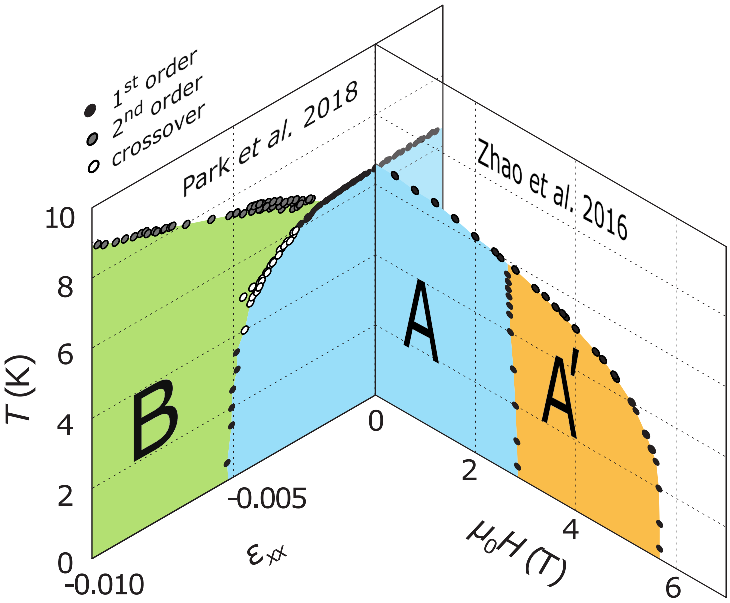

Figure 8.3: Phase diagram from transport measurements in [178, 189] for a magnetic field applied along the c-axis and a compressive stress along ⟨100⟩, ϵ_{xx}. Note that the magnetic field-temperature phase diagram has also been measured in [11], where the transition at T_N was erroneously labelled as continuous.

and $q_1 - q_2$ oscillate out of phase, which in combination with the $q_{1/2}$ Fourier components produces lobes of spin-density elongated along the a/b-axis. It should be noted that on the basis of the diffraction data alone the checkered and woven structures could not be discriminated.

8.4 Uniaxial stress tuned SDW order in $CeAuSb_2$

Uniaxial stress is becoming an increasingly popular tool for studying intertwined and competing orders that are a ubiquitous theme in condensed matter physics. Density-wave modulations in particular are often very sensitive to symmetry breaking uniaxial strains, which can favour different components and reveal the underlying symmetry of the order (for example in the SDW phases in $Sr_3Ru_2O_7$[12]) and reveal competing instabilities (for example between CDW order and superconductivity in $YBa_2Cu_3O_{6.67}$ [194]).

The magnetic order in $CeAuSb_2$ (at least in zero field) breaks tetragonal symmetry and therefore can be expected to couple to C_2 fields such as uniaxial stress. Park *et al.* [178, 189] have shown that the SDW order in $CeAuSb_2$ is highly perturbable to uniaxial stress along specific high-symmetry directions, but not along others[178, 189] [4].

---

[4] The data in references [178, 189] are presented as a function of strain, ε, which along the axis of a

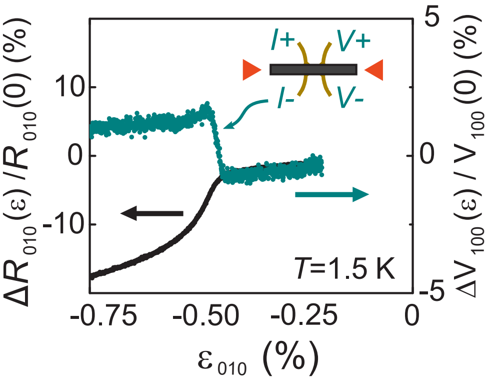

Figure 8.4: Resistance for a current applied parallel (black) and perpendicular (green) to the applied compression along the long axis of the sample as indicated in the schematic, taken from [178]. The direction of the compressive stress has been changed to be along [010] to match the convention used here.

Uniaxial stress along ⟨110⟩, the principal axis of the A-phase order, detwins the crystal, producing hysteresis and a small cusp like-feature in T_N centered on zero stress. The observed hysteresis combined with the fact the magnetic structure was refined on the basis of two C_2 domains of single-q order suggests the phase does spontaneously break rotational symmetry (unlike the SDW-A & B phases in $Sr_3Ru_2O_7$) [5]. Despite this, T_N is remarkably insensitive to ⟨110⟩ stress, changing by only 0.1 K for a compressive strain, $\varepsilon_{\langle 110 \rangle} = -0.6\%$.

Compressive stress along ⟨100⟩ at low temperature drives the system through a first-order transition at $\varepsilon_{\langle 100 \rangle} = -0.51\%$ into a very different ordered phase (B-phase in Fig.8.3), beyond which T_N becomes continuous and increases with compressive stress. In contrast, the transition into the A-phase at T_N only exhibits a weak suppression with ⟨100⟩ . The extrapolation of T_N in the B-phase to zero stress yields a transition temperature that is ≈ 90% of the A-phase T_N, indicating that the two phases are nearly degenerate at ambient pressure.

The B-phase is associated with an enhanced resistivity perpendicular to the axis of compression, as shown in Fig.8.4. This is typically a signature of an inbalance in the occupation of single-q SDW order as seen in $Sr_3Ru_2O_7$ [1] and in Cr[95] - which

---

compressive stress is negative.

[5] In isolation, the observation of hysteresis is not conclusive of rotational symmetry breaking. As discussed there are cross-terms in the free energy that couple the two components of the SDW order with a sign that determines whether single of multi-q order is favoured. These terms can compete with, for example terms which couple the SDW components to strain. Strain can then drive the system from multi-q into single-q order, but at that point the system is no longer tetragonal. Even in the absence of strain there would be a finite orthorhombic distortion due to coupling of the SDW moment to the lattice. This distortion can produce hysteresis. For example the SDW order in field-cooled chromium remains single-q when the field is removed for a similar reason.

both exhibit an enhanced resistivity for a current parallel to the SDW wavevector of the preferred domain (in general it depends on the orientation of the Fermi velocity of the nested sheets with respect to the wavevector).

The appearance of the B-phase coincides with the transition at T_N becoming continuous. Park *et al.*[178] have argued that the transition into the A-phase at T_N is driven first-order by competing fluctuations as the condensation of order with q_1 prevents order along q_2 in the same part of the sample[178]. The transition at T_N in the B-phase would then only be continuous if the order is coupled to $\langle 100\rangle$ stress in a way that selects a preferred orientation - which is likely to be one of [100] or [010]. Such behaviour has been observed in the antiferromagnetic transition of MnO, which becomes continuous under uniaxial stress[195]. Together the evidence suggests the B-phase order has a principal axis along $\langle 100\rangle$ (i.e. rotated by 45° with respect to the A-phase which is modulated along $\langle 110\rangle$).

However, the authors of [178] note that the $\langle 110\rangle$ stress did not restore a continuous transition at T_N in the A-phase by selecting between order with [110] and $[1\bar{1}0]$ components. They suggest that the transition might become continuous at larger stresses than were measured. The transport data suggest that the A-phase is robust to both $\langle 100\rangle$ and $\langle 110\rangle$ stress, but that there is separate and competing order parameter responsible in the B-phase, that couples only to $\langle 100\rangle$ stress.

Returning to the symmetry of the magnetic field-induced A′ phase, there is no observed hysteresis in the resistivity around zero stress applied along $\langle 110\rangle$ or $\langle 100\rangle$ which would indicate the A′ phase is tetragonal[189] - favouring the checkered magnetic structure.

8.5 Motivation

In the present experiment we performed neutron diffraction measurements with in-situ uniaxial stress to test the hypothesis of Park *et al.* - that $\langle 100\rangle$ stress induces single-q order modulated along $\langle 100\rangle$ with a preferred orientation selected by the axis of the stress. If this proposal was true, it would provide circumstantial evidence for uniaxial stress restoring the continuous nature of a transition by lowering the point-group symmetry of the fluctuations.

If this is the case, then why does the field-induced A′ phase, which exhibits Fourier components modulated along the $\langle 100\rangle$ direction, not couple strongly to $\langle 100\rangle$ stress? An answer could lie in the presence of the q_1 and q_2 components in the A′ phase for which $\langle 100\rangle$ is a transverse field - which would not to be present in the B-phase.

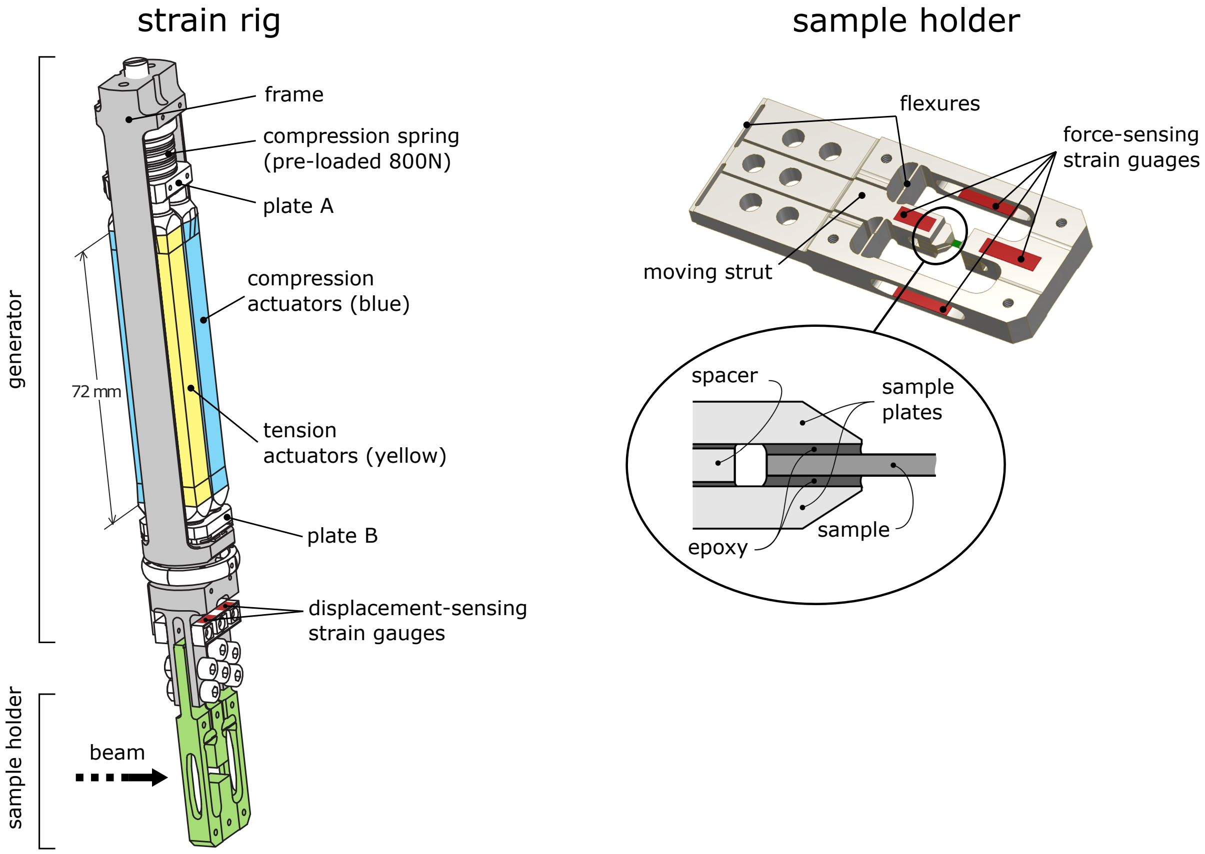

Figure 8.5: Schematic of stress rig designed by C.Hicks for in-situ tuning of compressive uniaxial stress for neutron scattering. The rig has two parts: a generator and a sample holder. The position of the strain gauges are indicated in red. (Drawings provided by C. Hicks). The drawing of the sample plates was adapted from a figure in [196]

The stress phenomenology investigated here might also have wider relevance. The field-temperature phase diagram of $CeAuSb_2$ (see Fig.8.3) has a strong similarity to those of a range of other heavy fermion compounds, including $CeNiGe_3$ [13], $CeRh_2Si_2$ [14] and $YbNiSi_3$ [15], which all exhibit an easy axis along c and transition from a zero-field magnetically ordered phase to a homogeneously-polarized state via two first-order metamagnetic transitions, through an intermediate phase with higher resistivity.

8.6 Uniaxial stress cell design

Fig.8.5 shows a schematic for a novel piezoelectric-drive uniaxial stress cell for muon spin rotation and neutron scattering designed by C. Hicks (MPI, Dresden). The cell has two parts: a generator that produces a compressive load, and a detachable sample holder that allows for quick sample changing.

The generator consists of a titanium (grade 4 alloy) frame that houses two pairs of piezoelectric actuators (in this experiment stacks of the Physik Instrumente P-887.50 and P-887.90 PICMA actuators of total length 72 mm) which will be referred to as the tension and compression actuators that are in mechanical contact with plate A(see Fig.8.5). The tension actuators are in mechanical contact with the frame via plate B and the compression actuators are connected to rods that pass through plate B that can push against a central rod connected to the central strut of the sample holder. It should be noted that that the central rod and the rods of the compression actuators are not attached, the cell cannot apply tensile loads.

When a positive voltage is applied to the compression actuators they lengthen, moving the strut downwards (away from plate A) compressing the sample. When a positive voltage is applied to the tension actuators they lengthen and move plate A upwards, decompressing the sample. At cryogenic temperatures the actuators can also withstand large negative voltages, hence the action of the two pairs of actuators can be reversed, in particular a negative voltage supplied to the tension actuators will increase the compressive load on the sample [6].

The springs between plate A and the frame keep the actuators under compressive loads (800 N in this case), to compensate for the differential thermal contraction between the actuators and the frame (the actuators lengthen dramatically as they are cooled, whereas the titanium has a small coefficient of thermal expansion) and maintain a roughly constant force that can be transmitted to the sample. It also prevents a lengthening of the compression actuators putting the tension actuators under tension (the actuators cannot withstand strong tensile loads).

The sample holder is machined from a plate of grade 5 titanium alloy [7] using wire spark erosion. The holder consists of a central strut (connected to the generator) that can move with respect to the rest of the holder. Two pairs of flexures prevent the application of transverse forces or torques to the sample. The strut and sample holder frame are bolted to the flanges of the generator. The space around the sample is kept as open as possible, with windows in the side panels of the frame. The sample is mounted between two plates with epoxy and the plates are epoxied into the two ‘claws’ of the holder (see Fig.8.5).

---

[6] At cryogenic temperatures the piezoelectric response of the actuators is considerably reduced compared with room temperature, however the actuator can also withstand larger voltages - so it is still possible to apply a relatively large stress at low temperature.

[7] Grade 5 is mechanically stronger than grade 4 titanium, however in general the latter is preferable as grade 5 titanium is a worse thermal conductor and superconducts below 3 K (as opposed to ∼0.5 K for other titanium alloys). However in this experiment, the sample was cooled in exchange gas so the

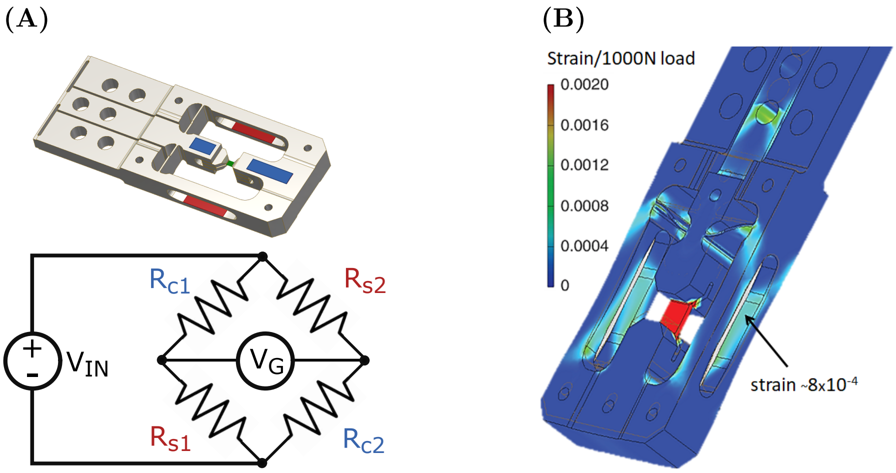

Figure 8.6: (A) Schematic of the wheatstone strain gauge bridge and the placement of the active/in-active pairs indicated on the schematic of the sample holder (for the force-sensor). (B) Finite element simulation of the strain in the sample holder for 1000 N of compressive load on the bottom bolt-hole of the central strut applied to a sample of Sr_2RuO_4. (Drawings and simulation provided by C. Hicks).

There are two strain-gauge based sensors: a displacement sensor on the flexures attached to the generator flanges that measures the displacement of plate B, and a so-called force sensor on the struts of the sample holder that measures the strain induced due to the load on the sample. Each sensor consists of a Wheatstone bridge circuit of two pairs of strain gauges (as shown in Fig.8.6A), with one pair of 'active' gauges that will respond to the change in load and a 'dummy' pair that are insensitive to the load (either due to the placement or orientation of the gauge). In this way the temperature dependence of the gauge factor and the effect of thermal contraction changes the resistance of both pairs in the same proportion. In the displacement sensor the strain gauges are measuring the deflection of the beam of the flexure so the two pairs of gauges are oriented parallel and transverse to the axis of the strain. The force sensor consists of a pair of gauges on the central strut and the side panels of the frame. When the sample compresses the side panels of the frame will stretch under tension as shown in Fig.8.6B.

8.6.1 Constraints on the sample size

The cell is designed for plate-like samples and is flexible enough to accommodate a range of sample sizes, however to achieve large strains it is necessary to optimise the aspect ratio of the sample and the thickness of the epoxy layer between the sample and plate.

---

low thermal conductivity was not an issue.

For a comprehensive explanation of the various constraints the reader is referred to the paper of Hicks *et al.* [196]. The relevant points are outlined briefly here.

The choice of exposed length, L, for a given thickness, t, is governed by two factors. The maximum ratio L/t can be estimated from the Euler formula for the buckling load on a thin beam with both ends unable to pivot. This produces the following constraint for a desired strain, ε,

$$\frac{L}{t}_{max} = \frac{\pi}{\sqrt{3\varepsilon}} \tag{8.1}$$

For a strain of $\varepsilon \approx 0.5\%$ the maximum $L/t \approx 25$ (though in practice it is recommended to stay within 60% of this limit[197]). A shorter sample may be able to withstand a higher stress before buckling, but for our experiment the strain homogeneity in the exposed length of sample is also important. Strain inhomogeneity will decay exponentially towards the mid-point of the exposed sample, with finite element simulations indicating that 5% homogeneity (relative to the value at the mid-point of the sample) is recovered after a distance $0.2w$ from the sample plate at each end[196].

The second factor is the overlap of the sample and plates required for the load to be transferred via the epoxy. When a load is applied the layers of epoxy shear such that the sample is displaced relative to the unloaded position by an amount, D, which decays exponentially along the direction parallel to the applied load, reducing by an amount $1/e$ over the distance,

$$\lambda = \sqrt{\frac{Etd}{2G}} \tag{8.2}$$

where E is the Young's modulus of the sample, d and G are the thickness and shear modulus of the epoxy [8]. Ideally the epoxied length would be of the order $\gtrsim 2\lambda$.

From Eq.8.2 it can be seen that reducing the epoxy thickness decreases the unexposed length of the sample required (which may be advantageous for smaller samples). In principle the minimum epoxy thickness, d_{min} can be determined from the shear strength of the epoxy, τ_{max}. The epoxy is under the maximum shear stress at the end of the sample plates, where $D = \varepsilon\lambda$. It can be shown that the minimum epoxy depth is then,

$$d_{min} = G\frac{\varepsilon\lambda}{\tau_{max}} \tag{8.3}$$

In practice the optimal epoxy thickness may be somewhat larger than this. Finite element

---

[8] Eq.8.2 relies on two assumptions. Firstly that the sample width w is much greater than the thickness, t, such that bonding on the sides of the sample can be ignored. Secondly that the epoxy has much lower elastic constants than the sample and plates (it is roughly an order of magnitude less[196]), such that the sample and plates to be considered as perfectly rigid (i.e. do not shear).

simulations would seem to suggest a good 'rule of thumb' for ensuring adequate strain homogeneity would be that depth of the epoxy layer should be at least $d_{min} \sim t/4$.

8.7 Experimental Details

8.7.1 Sample characterisation and preparation

Single-crystal $CeAuSb_2$ was synthesized by the group of Prof. Canfield (Ames Lab/Iowa) using a self-flux method described in [198, 199, 200]. The sample used in the neutron diffraction experiment is shown in Fig.8.7A. The antiferromagnetic transition temperature, T_N was measured in a SQUID and found to be $\approx$ 6.6 K (see Fig.8.7B), and the sample came from a batch with residual resistivity ratios of R(300K)/R(2K) $\approx$ 5. These values are comparable to those of the samples used in recent transport and heat capacity measurements[11, 178, 189].

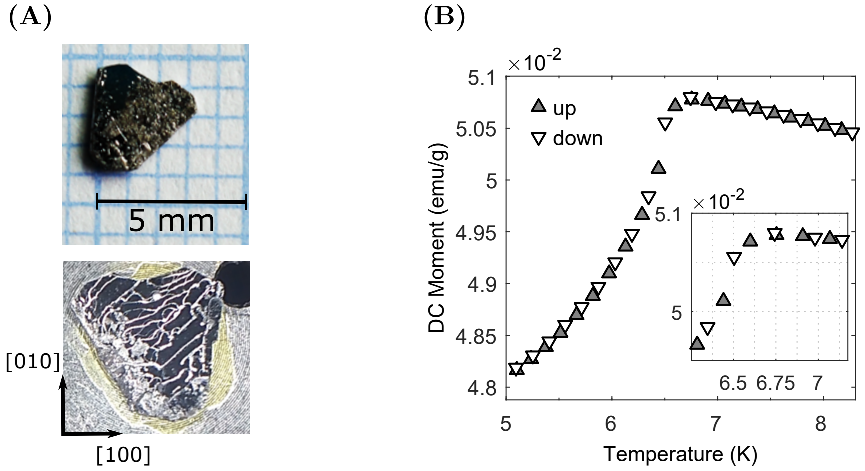

Figure 8.7: (A) Pictures of $CeAuSb_2$ sample used in diffraction experiment (DR065-B) as grown (B) DC SQUID magnetisation measurements with a field of 5 kOe in the ab-plane of the same sample for up and down temperature sweeps showing the transition at $\approx$ 6.6 K.

The $CeAuSb_2$ samples grow naturally as thin-plates of typical thickness 500 μm, with the c axis surface normal. The sample was aligned by backscattering x-ray Laue (see Fig.8.8A) such that the a and b axes were known to within 1°. The sample was cut along these directions using a commercial wire saw to produce a bar of approximate dimensions 1.3 mm × 3.1 mm in the ab-plane (the maximum length from which a bar of constant cross-section could be cut). The cross-sectional area was 0.297 mm^2. In order to apply the appropriate stress the sample was then polished on both sides with alumina paper

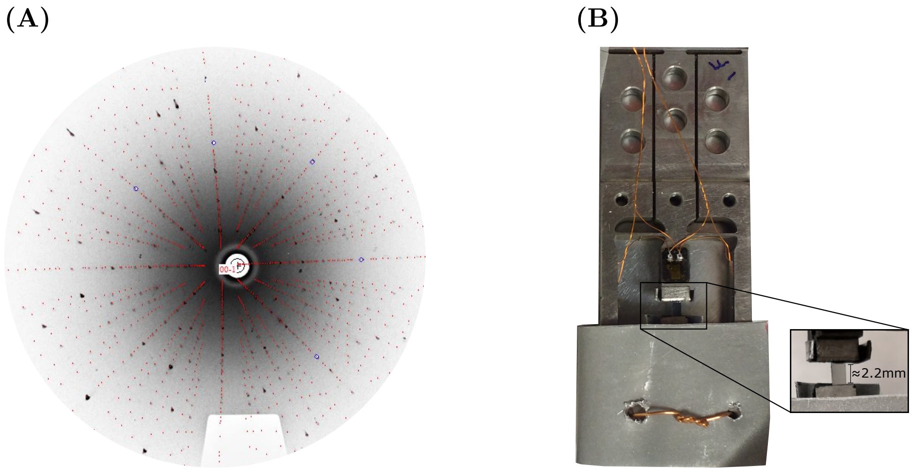

Figure 8.8: (A) Backscattering x-ray Laue picture of $CeAuSb_2$ sample before cutting with wire-saw. Refinement of orientation (red markers) performed by Orient Express software. (B) Sample holder before mounting on stress rig.

of decreasing grit size (down to 3 μm) to a final thickness of 0.21 mm (measured by an optical interferometer). The final thickness was determined by depth of features such as chips, cracks and voids in the sample which lead to points of stress concentration and premature failure.

8.7.2 Mounting the sample

The sample is held at each end between a pair of titanium sample plates. The two plates are held together at the desired separation by a spacer plate. For brevity the sample plate/spacer ensemble will be referred to as an adapter. The sample mounting procedure has three parts: the construction of the titanium adapter, the epoxying of the adapter into the sample holder and finally the epoxying of the sample ends into the adapter at each end of the sample holder. The epoxy used in this experiment was Stycast 2850FT with the catalyst 23LV, which was cured for at least 8 hours at 65°C in each step.

The sample plates and spacers were ground to the required thickness that allowed for the depth of epoxy at the sample/plate interface to be a quarter of the sample thickness, $d = t/4 \approx 50$ μm, for 20 μm of epoxy between spacer/plate interface (the mechanical strength of this interface is not critical) and 60 μm of epoxy at each plate/holder interface. Before the epoxy was applied the surfaces of the sample plates and spacer were roughened with 140 grit sandpaper. The adapters were assembled in pairs with an additional spacer of thickness $t + 2d$ (not epoxied) to act as the sample to ensure the required clearance and co-alignment of the pairs was maintained. The ensemble was cured on a hot plate between two teflon coated glass microscope slides in a vice. The adapter pairs (with sample spacer) were epoxied into the sample holder (the adapters overlapped with the end of the sample holder cavity by approximately 2 mm at each end so as to reduce the angle that the sample plane could be tilted). The thickness of the bottom epoxy layer can be ensured with pieces of wire of the appropriate diameter, however the viscosity and surface tension of the Stycast will naturally produce a layer of approximately $\sim 50\ \mu$m between two surfaces so such precautions were not necessary. After curing, the sample spacer was removed and de-gassed stycast was inserted between the sample plates. The sample was inserted into the space, with the direction of the strain along the long axis of the sample plate (along the in-plane tetragonal axis). The alignment of the sample in the cell was done under a microscope. Cadmium strips were then epoxied onto the sample plates (as shown in Fig.8.8B), extending over the sample by an amount $\approx 0.1w$ from the end of each sample plate, in order to reduce the large incoherent background from the hydrogen in the epoxy and mask the portion of the sample where the strain is expected to be very inhomogeneous.

The mounted sample had an exposed length of approximately 2.2 mm, hence a ratio $L/t \sim 11$ which is much lower than the buckling limit in Eq.8.1 for the required strains. The average length of sample overlapping the end of the sample plate (i.e. encased in epoxy) was 495 μm. Evaluating the expression in Eq.8.2 for the length-scale over which the strain decays, taking the Young's modulus of the sample to be 100 GPa (typical order of magnitude for a metal) and using an estimate of 6 GPa for the shear modulus of the Stycast at cryogenic temperature[196] [9], which yields a value of $\lambda = 295\ \mu$m (though this is likely to be an overestimate [10]) The overlap achieved is then $\sim 1.5\lambda$, which was considered a reasonable compromise in order to maximise the exposed sample length.

8.7.3 Strain gauge mounting and calibration

The force and displacement bridges used Omega SGD-1.5/120-LY41, (1.5mm grid, 120Ω resistance) strain gauges affixed with Stycast 2850FT, pressed flush to the surface with the use of teflon coated glass microscope slides. The strain gauges were connected in a wheatstone bridge circuit (an example for the force sensor is shown in Fig.8.6A) with enamelled copper wire of diameter 100 μm in twisted pairs.

---

[9] It should be noted that there is no published data for the elastic properties of Stycast 2850FT at cryogenic temperatures.

[10] The Young's modulus of $CeAuSb_2$ has not been measured, but the data presented in this chapter in combination with the published SDW phase diagram in [178, 189] would indicate that at cryogenic temperatures $CeAuSb_2$ is quite soft with a Young's modulus more comparable to that of aluminium.

The force sensor was calibrated by measuring the potential across the bridge with a lock-in amplifier as a load was applied by hanging up to 1 kg of mass from the frame at room temperature (by C. Hicks in Dresden after the beamtime). The result of the calibration is shown in Fig.8.9A where the gradient of the fit is 0.186(5) mΩ/N. However the elastic moduli of titanium increase by about 5% at cryogenic temperatures relative to the room temperature value[201], so the response of the sensor during the experiment was taken to be 0.177 mΩ/N. The temperature dependence of the gauge can be neglected due to the configuration of the Wheatstone bridge.

It should be noted that the displacement sensor does not directly measure the sample strain due to the finite spring constant of the holder. The purpose of the displacement sensor was to ensure that the displacement is proportional to the stress - i.e. that the sample deforms elastically. For example if the sample were to crack, or the epoxy to yield then the displacement measured would increase but the stress would remain constant.

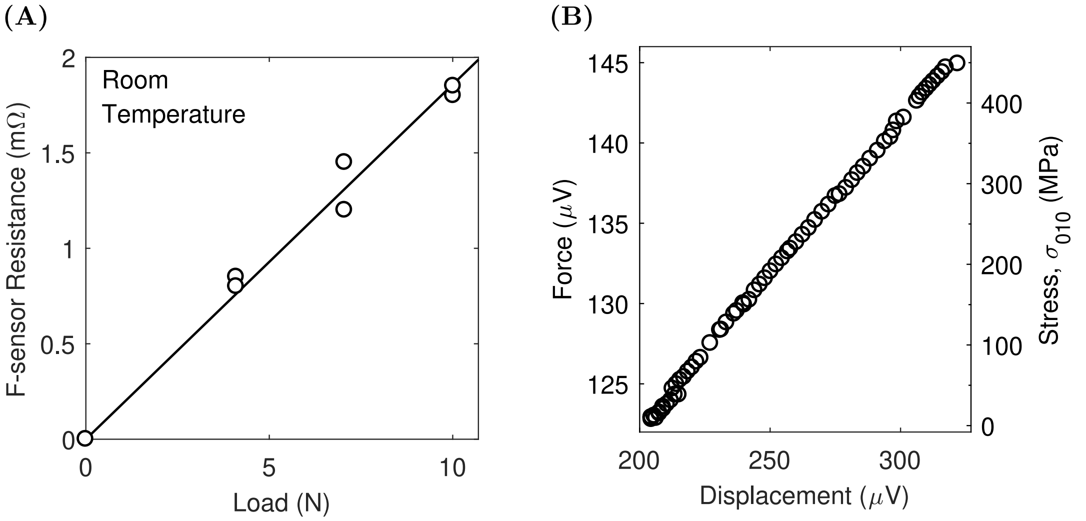

Figure 8.9: (A) Response of force sensor resistance to applied loads and linear fit for calibration applied post-experiment. (B) Response of the force and displacement sensor voltage (measured with a current of 1 mA) for readings taken during the experiment.

8.7.4 Neutron diffraction experiment

Neutron diffraction was performed on the WISH diffractometer at ISIS, UK[50]. The axis of the uniaxial stress cell was oriented vertically in a 50mm bore cryostat such that the stress was perpendicular to the scattering plane (H,0,L) - i.e. in this notation the stress was applied along the b-axis.

The voltage to the actuators was supplied by two 0-10 V DC Keithley sourcemeters (one each for the compression and tension pairs) via a 100 gain amplifier. Each strain sensor was measured with a Stanford research SR830 lock-in amplifier with a current of 1 mA [11]. Neither the power supply to the actuators nor the strain sensor measurements were computer controlled. The strain sensor voltage was recorded manually from the SR830 display when the voltage to the actuators was being changed.

The sample was cooled to base temperature (1.7 K) with $\sim$ 120 mbar of exchange gas before stress was applied. Due to differential thermal contraction of the titanium frame and the actuators, there was a possibility that there was finite load on the sample even though 0 V/0 V had been supplied to the compression/tension actuators. In order to locate the voltage at which the sample was at zero stress, a positive voltage was supplied to the tension actuators until the force and displacement sensors saturated at a constant value (i.e. the compression actuators were not in mechanical contact with the sample). The voltage to the tension actuators was then reduced until force sensor voltage started to increase, this value coincided with 0V/0V, however there appears to be some hysteresis such that when the sample was first cooled down it was under approximately 5 MPa of stress. The maximum stress achieved in the experiment was 440 MPa which corresponded to a voltage 240 V/-220 V. Over the entire voltage range the response of the force and displacement sensors was linear (as shown in Fig.8.9B).

The sample was oriented such that magnetic Bragg peaks of the SDW-A phase could be measured at the positions at $(\pm\left[1 \pm \delta_A\right], \pm\delta_A, L + 0.5)$ for $L \in [0, 1]$ simultaneously, which put the [001] axis at backscattering ($2\theta \approx 160^\circ$) where the $\Delta d/d$ resolution is best. Data were collected at select stresses at two temperatures 1.7 K (base) and 5.5 K. Only one sample orientation was measured before the sample broke.

8.8 Results

8.8.1 Measuring the orthorhombic distortion

Due to the limited detector coverage out of the scattering plane on WISH, no nuclear reflections with a component along b could be measured at the chosen sample orientation. However, the instrumental resolution was sufficient to resolve the strain along the a/c axes which expand under b-axis compression due to the Poisson ratios of the material (off-diagonal elements in the elasticity tensor).

---

[11] The strain sensor circuits had a resistance of 420 Ω and the SR830 lock-ins have an output impedance of 50 Ω therefore 470 mV was supplied to produce a current of 1 mA

Fig.8.10 shows longitudinal cuts through the (0,0,3) and (1,0,2) nuclear Bragg peaks at the stresses at which data was taken at base temperature (1.7 K), along with the fitted peak centre as a function of stress. The peak centre increases linearly with compressive stress, which is clearly evident in the raw data. At zero strain the data are well described by a Gaussian peak convoluted with a back-to-back exponential in Eq.3.73. At finite stress the (0,0,3) peak measured at backscattering (high-resolution) exhibits a shoulder at the position of the zero stress peak, therefore the data were modelled with two peaks (with the same back-to-back exponential coefficients, A/B): one at the zero-stress d-spacing with the same width as the zero stress peak and another with a peak centre and width free to vary. The residual peak at the zero stress position constitutes approximately 20% of the total area of the peaks at finite strain at all stresses, indicating that 80% of the sample is strained with a degree of homogeneity that can be modelled by a single broadened peak within instrumental resolution (indeed the Gaussian peak width does increase with stress).

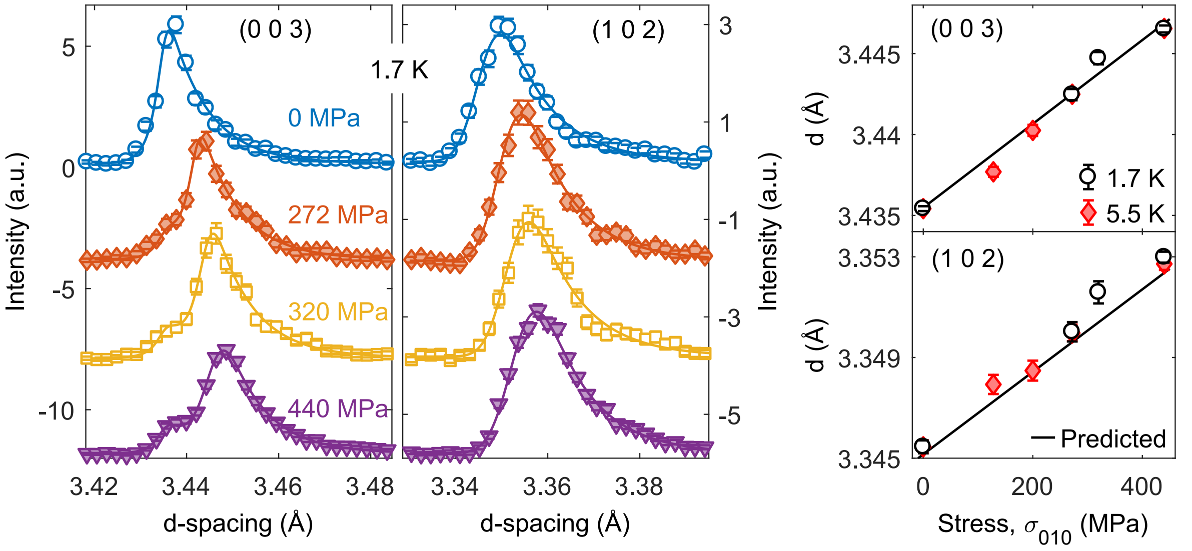

Figure 8.10: (Left) The (0,0,3) and (1,0,2) nuclear peaks as a function of d-spacing (i.e. longitudinal cuts). The peak shifts due to larger d-spacing with increasing compression along the b-axis as the *a* and *c*-axis increase due to the Poisson ratios (off-diagonal elements in the elasticity tensor). (Right) Markers show the fitted peak centre as a function of stress and the line is the prediction given the refined lattice parameters from a total of 8 peaks.

In order to determine the a/c lattice parameters as a function of stress, a total of 8 nuclear peaks in the (H,0,L) plane (6 symmetrically inequivalent peaks) at the largest d-spacing across all banks were fitted in a similar manner as above. The fitting was done in two steps, with A/B and the Gaussian peak width constrained to be the same for peaks at all strains in the same pair of banks (covering the same 2θ) in order to provide a suitable initial guess for the parameters in the second step, where all peaks were fitted independently with the only constraint that the A/B are independent of stress [12]. The lattice parameters were refined using the fitted peak centres. Fig.8.16A shows the variation between the fitted d-spacing of the peaks and the calculated d-spacing at the zero stress and the maximum stress at 1.7 K. Fig.8.16B shows the lattice parameters as a function of stress. The predicted d-spacing of the (0,0,3) and (1,0,2) peaks for the refined parameters are shown in Fig.8.10.

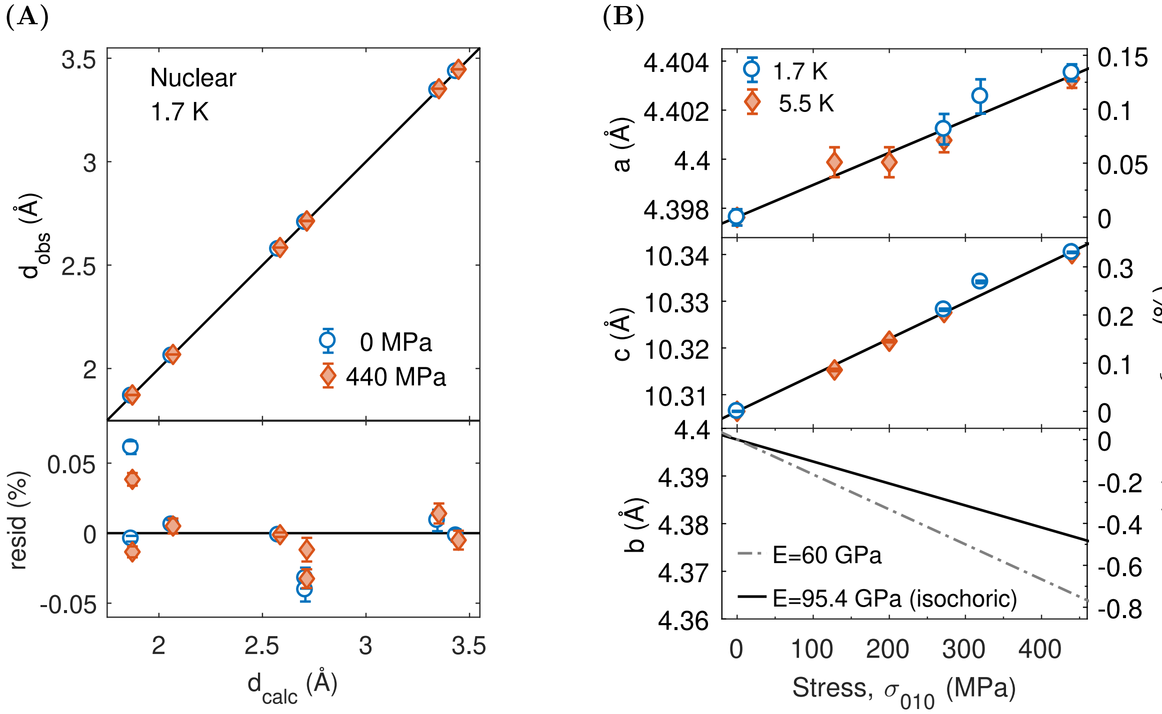

Figure 8.11: (A) Comparison of observed and calculated nuclear peak positions from refinement of a and c lattice parameters of 1.7 K data at 0 MPa and 440 MPa (maximum measured) compressive stress along b (B) Refined a and c lattice parameters at 1.7 K and 5.5 K as a function of compressive stress along b and the predicted b lattice parameter at two Young's moduli (see main text).

The increase in the a/c parameters can clearly be resolved, increasing linearly with compressive stress along the b axis, with the maximum stress of 440 MPa producing strains of roughly 0.14% and 0.33% along the a and c axes respective for both temperatures.

---

[12] In crystallographic refinement software such as FullProf and GSAS the back-to-back exponential parameters A/B and the Gaussian width are parametrised as a function of d-spacing, with coefficients that are typically refined separately for each pair of banks as the $\Delta d/d$ resolution varies with 2θ. In this case only a limited number of peaks (8) were refined and better results were achieved by fitting the peaks independently.

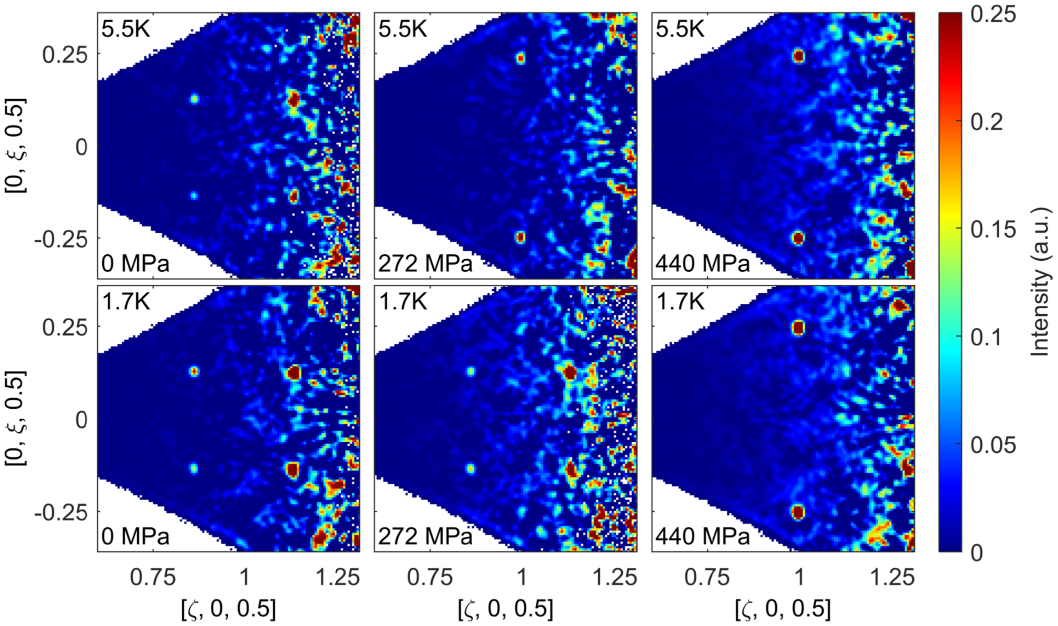

Figure 8.12: Neutron diffraction data in the (H,K,0.5) plane for three values of compressive stress along b at two temperatures (5.5K and 1.7K).

Fig.8.16B shows the b lattice parameter for two scenarios: a volume conserving lattice distortion, which corresponds to a Young's modulus $E \approx 95$ GPa, and a softer metal with $E = 60$ GPa (which is a rough estimate for CeAuSb$_2$ from comparison of our measurements with the published phase diagram in [178], as discussed in Section.8.9.1). The former is a lower bound on the applied strain, as the Poisson ratios of materials typically result in the volume decreasing under compression.

8.8.2 Discovery of stress-induced single-q SDW order

The data were transformed from angle and time-of-flight into reciprocal space by a UB matrix determined from the fitted a/c lattice parameters, with the b lattice parameter calculated under the assumption of a volume conserving distortion. Fig.8.12 shows cuts through the (H,K,0.5) plane at select stresses at the two temperatures measured. At zero stress and zero magnetic field, CeAuSb$_2$ exhibits incommensurate SDW order (A-phase), the $P4/nmm$ spacegroup gives rise to two symmetrical equivalent domains of single-q order with wavevectors $q_{1/2} = (\delta_A, \pm\delta_A, 0.5)$, producing four satellite peaks around each nuclear Bragg peak, as shown in Fig.8.12 . In Fig.8.12 it can be seen that compressive stress along the b-axis induces a new mono-domain of single-q SDW order (B-phase) with wavevector $q = (0, \delta_B, 0.5)$. The magnetisation in the new B-phase is modulated along the in-plane axis parallel to the compressive stress. Both phases (A & B) double the unit

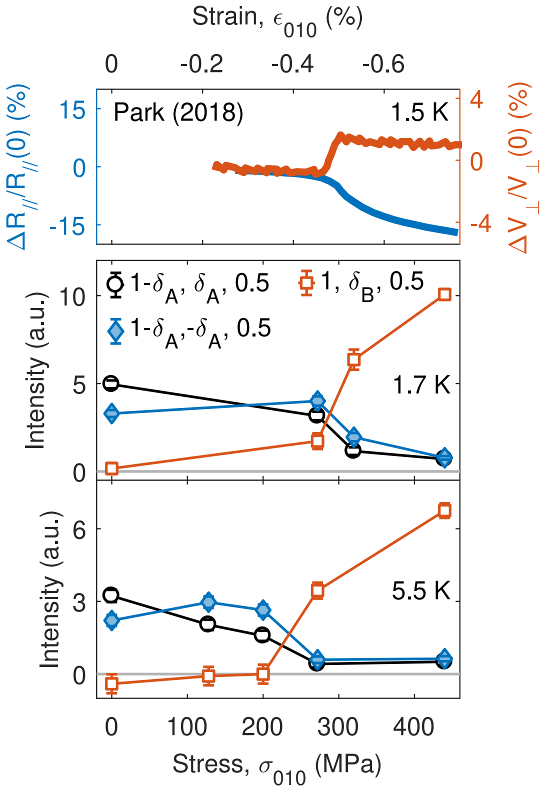

Figure 8.13: The integrated counts of SDW peaks in each phase as a function of strain. Two peaks are shown for the A-phase, $(1,0,1)+(\delta_A,\delta_A,0.5)$ and $(1,0,1)+(\delta_A,-\delta_A,0.5)$ that are due to different domains consistent with the $P4/nmm$ symmetry of the crystal structure - both respond equally to stress.

cell along the c-axis. It can be seen that the boundary between the SDW A & B phase occurs at a lower stress at 5.5 K.

Fig.8.13 shows the integrated intensity of the lowest-Q SDW peaks in the A & B phase as a function of compressive stress along the b axis at the two temperatures measured 1.7 K and 5.5 K (post subtraction of a temperature and stress independent linear background). The resistivity for a current applied parallel to the compressive strain as a function of strain at 1.5K from Park *et al.*[178] is also reproduced with the axis scaled to the stress used in this experiment by assuming a Young's modulus of 80 GPa. The origin of the discrepancy between the intensity of the symmetrically equivalent A-phase domains at both temperatures is not clear - the discrepancy is present for all satellite peaks measured. However, both domains evolve similarly under compression: the onset of the SDW-B phase peak intensity is correlated with the reduction in SDW-A peak intensity, which plateaus at a low value slightly above the background at a stress of $\lesssim$ 272 MPa and $\gtrsim$ 320 MPa at 5.5 K and 1.7 K respectively. The residual SDW-A peak intensity at

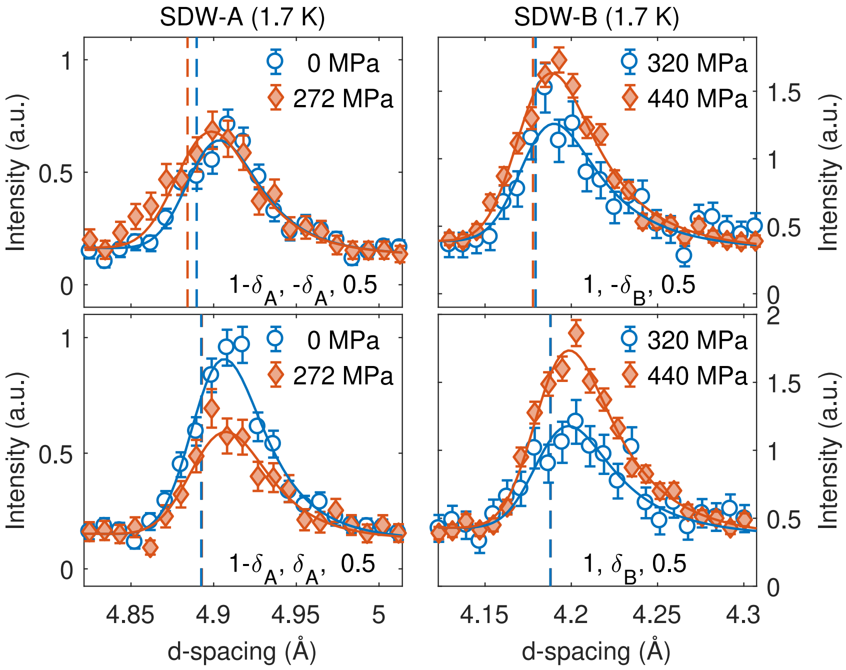

Figure 8.14: Longitudinal cuts of data for the magnetic Bragg peaks in the A-phase (left) and B-phase (right) at the minimum and maximum stress at which data were collected in each phase. The fitted centre is indicated by dashed lines.

the largest stress measured is roughly 20% of the average zero stress intensity at both temperatures, which is consistent with the volume fraction of the sample under stress determined from the fits to (0,0,3) peak in Fig.8.10.

8.8.3 Strain dependence of the SDW wavevector

To determine the SDW wavevector 8 and 6 magnetic Bragg peaks in the A and B phase respectively were fitted in order to extract the d-spacing of the reflections. The back-to-back exponential coefficients, α/β, and the Gaussian width were constrained to be the same for symmetrically equivalent peaks at the same 2θ above and below the equatorial plane of the detector (i.e. differing only by the sign of the component along b). In addition the parameters, α/β, were considered to be stress independent.

Fig.8.14 show the fits to symmetrically equivalent magnetic Bragg peaks in both phases, at the minimum and maximum stress for which they were measured at 1.7 K. The fit centre is indicated by a dashed line (note that the peak centre does not coincide with the maximum intensity due to the asymmetry of the moderator pulse[51]). It can be seen that the variation of the peak centre with stress is at most comparable to (and typically less than) the systematic difference between symmetrically equivalent peaks (that for example could arise from a combination of the sample placement being slightly off centre and variations of the calibrated detector position).

The d-spacing of the magnetic peak depends on the stress dependence of the lattice parameters and the modulation wavevector. From fits to the nuclear peaks, the a and c lattice parameters are known as a function of stress, but due to a lack of detector coverage out of the scattering plane the b lattice parameter cannot be measured directly at finite stress. At zero stress the system is tetragonal ($a = b$) therefore the d-spacing of the magnetic Bragg peaks can be used to determine the modulation wavevector in the A-phase. The L-component of the modulation was taken to be exactly 0.5 as these data are consistent with a commensurate modulation along the c-axis: the magnetic Bragg peaks in both phases exhibited only one peak along the L direction typically within $\lesssim 0.02$ of $L = 0.5$ [13]. A least squares fit to the d-spacing of the peaks using the measured lattice parameters yielded $\delta_A = 0.1372(4)$ for both the 1.7 K and 5.5 K data, which agrees within the errors with the value of 0.136(2) obtained by Marcus *et al.* [154]. To check for consistency, the refinement was repeated with the b lattice parameter allowed to vary freely, which found $b = 4.39(6)$ and $\delta_A = 0.1371(5)$ (average of values for both 1.7 K and 5.5 K data). The value of b is consistent with the fitted a lattice parameter, though the error is larger than the predicted change under the maximum stress applied, therefore this method cannot be used to determine the b lattice parameter at finite stress.

Fig.8.15 shows the fitted peak centre of the magnetic Bragg peaks as a function of stress for data taken at 1.7 K and 5.5 K. The grey lines indicate the expected d-spacing of the reflection at a given $\delta_{A/B}$, which increases with stress. This is because the component Q along b is relatively small for all peaks measured and therefore the d-spacing of the reflection is dominated by the response of the a and c lattice parameters, which expand due to the Poisson ratios of the material. The predicted d-spacing is shown for two scenarios: an isochoric (volume conserving) lattice distortion (which corresponds to a Young's modulus of $E = 95.4$ GPa), and a Young's modulus of $E = 47.7$ GPa (i.e. an improbably small value of half that of the isochoric case, such that the strain along b for a given stress is doubled). It can be seen that the variation in the b lattice strain cannot be resolved within the uncertainty on the fitted peak centre. The average d-spacing of the symmetrically equivalent A-phase peaks is consistent with δ_A decreasing slightly with

---

[13] This small discrepancy is due to the refinement of the UB matrix which assumes a nominal sample position that is centred with respect to the beam and the instrument. Data were not taken at a sufficient number of orientations to refine the actual sample position, which is typically displaced by an amount of the order of 1 mm from the nominal position. The systematic effect on the d-spacing (used to determine δ_A) is negligible as the total neutron flight path is many orders of magnitude larger (approximately 42 m on WISH).

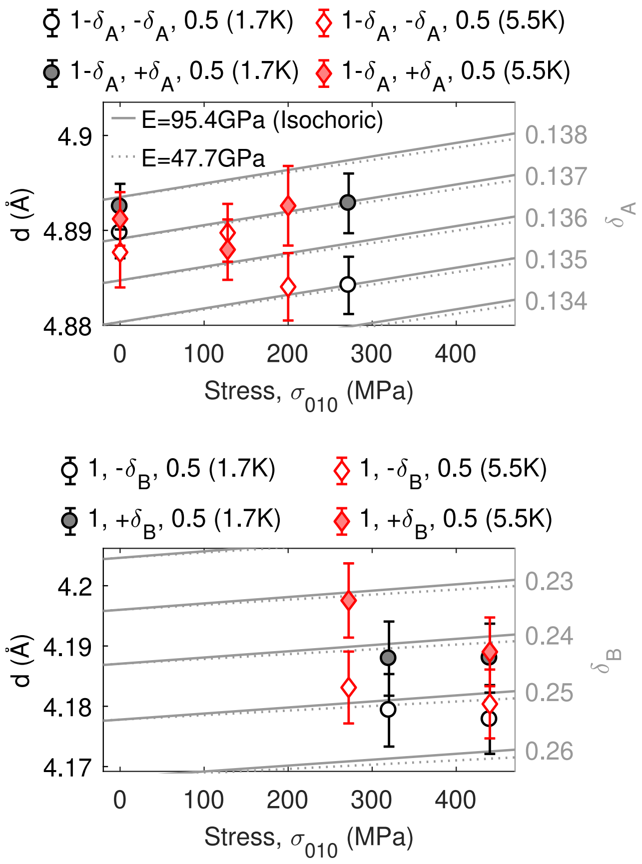

Figure 8.15: Fitted d-spacing of the lowest-Q magnetic reflections in the A-phase (top) and B-phase (bottom). Grey lines indicate the predicted d-spacing at different values of $\delta_{A/B}$ given the refined a and c for two Young's moduli (from which the b lattice parameter is calculated).

stress. The trend for δ_B is less clear.

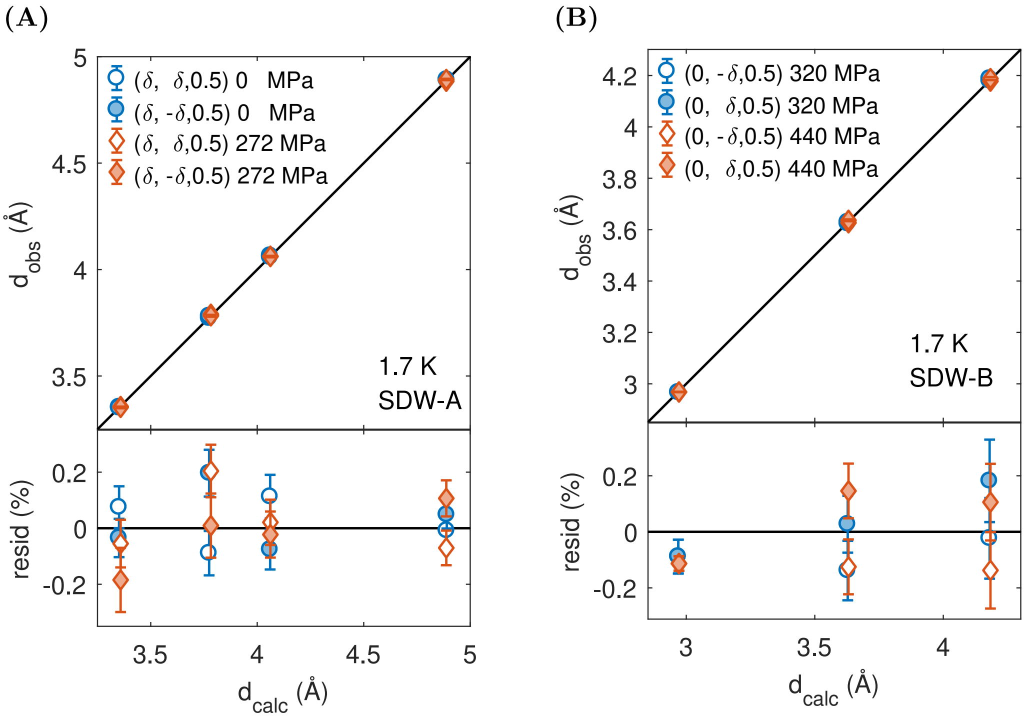

Figure 8.16: The fitted and predicted d-spacing for the magnetic reflections in the A-phase (A) and B-phase (B) at 1.7 K for the minimum and maximum stress measured in the phase. Calculated d-spacing used the fitted a and c lattice parameters, assumed a volume conserving distortion to determine b and refined the values of δ_A/B. The legend refers to the modulation vector for a set of satellite peaks.

The components of the SDW wavevector in the basal plane for the two phases, δ_A and δ_B, were refined by a least-squares fit to the fitted peak centres under the assumption of an isochoric distortion and a commensurate L-component of 0.5 (as above) Fig.8.16 shows the variation between the fitted and calculated d-spacing of the peak centres at the minimum and maximum stress for which the A and B phase were measured at 1.7 K. Note that the two lowest d-spacing reflections in the B phase, $(1, \pm\delta_B, 2.5)$, were fit with a common centre due to the low statistics.

The SDW wavevector of the A-phase at 0 MPa and the B-phase at 440 MPa are summarised in Table.8.1. As discussed the incommensurate wavevector in the A-phase ($\delta_A = 0.137$) is consistent with previous measurements at 0 MPa. The modulation in the B-phase is consistent with a commensurate value $\delta_B \approx 0.25$, which is lower than that of the field-induced A′ which orders with wavevector $(\delta_{A'}, 0, 0)$ and $(0, \delta_{A'}, 0)$ with $\delta_{A'} = 2\delta_A \approx 0.27$. Indeed the B-phase modulation also doubles the unit-cell along the c-axis.

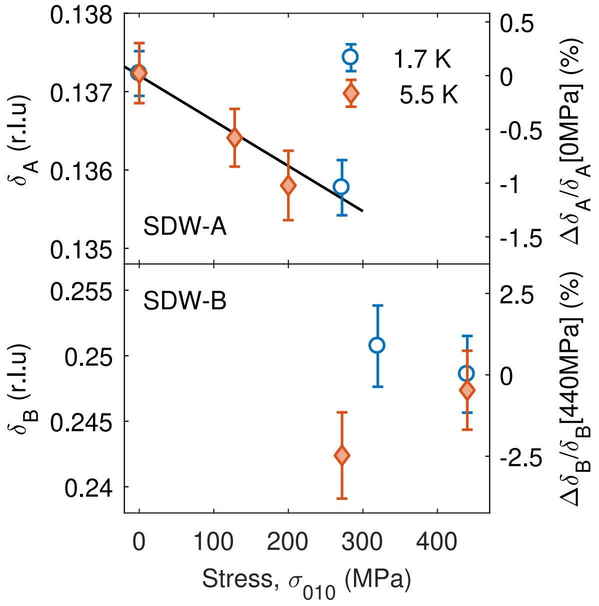

Figure 8.17: Refined value of δ_A (top) and δ_B (bottom) at two temperatures 1.7 K and 5.5 K as a function of compressive stress along b. Solid line is a linear fit.

	σ_{010} (MPa)	$\boldsymbol{q}_{\text{SDW}}$	δ (r.l.u)
SDW-A	0	$(\delta, \delta, 0.5)$	0.137(2)
SDW-B	440	$(0, \delta, 0.5)$	0.248(4)

Table 8.1: SDW wavevector in the SDW-A and SDW-B phases at zero strain and the highest compressive strain measured respectively. The wavevectors were determined with the assumption of an isochoric distortion.

Fig.8.15 shows δ_A and δ_B as a function of stress for the data at 1.7 K and 5.5 K. It can be seen that δ_A decreases by roughly 1% over the extent of the A-phase. Given the uncertainty on the refined δ_B values and the limited number of stresses measured, it is not possible to conclude that the δ_B changes with stress.

8.8.4 Structural Refinement

Data were corrected for the Lorentz factor, normalised to the total current and a vanadium standard sample to account for the incident flux and detector efficiency. Rietveld refinements of the nuclear and magnetic structures were performed using the Jana2006 software for data from a single orientation at 1.7K at two stresses 0 MPa and 440 MPa using the a/c lattice parameters from fits to the nuclear Bragg peaks, with the b lattice parameter determined with the assumption of a volume conserving lattice distortion.

The refinement returns three standard quantities (GOF, R and wR) that allow the quality of the fit to be inspected [202, 203]. The Goodness of fit, GOF, is given by

$$\mathrm{GOF} = \left[\frac{\sum_i w_i (I_{i,obs} - I_{i,calc})^2}{N_{DOF}}\right]^{1/2}, \tag{8.4}$$

where $I_{i,obs}$ and $I_{i,calc}$ are the observed and calculated intensity of the i^{th} reflection and N_{DOF} are the number of degrees of freedom. There are two common choices for the weights. Statistical weights, $w_i = 1/\sigma_i^2$, where σ_i is the error on the intensity of the i^{th} point (in which case GOF is the square-root of the reduced χ^2 value), which are commonly used in powder refinements. Unit weights ($w_i = 1$) are more commonly used in the refinement of single-crystal data to bias the fit to agree with stronger reflections [14].

Another measure of fit quality is given by the weighted R-factor, wR, defined as,

$$\mathrm{wR} = \left[\frac{\sum_i w_i (I_{i,obs} - I_{i,calc})^2}{\sum_i w_i I_{i,obs}^2}\right]^{1/2}, \tag{8.5}$$

which is a measure of the deviation normalised by the overall scale of the observed intensities. If the model used was correct and the deviations from the calculated intensities are purely due to statistical fluctuations, then for statistical weighting $w_i(I_{i,obs} - I_{i,calc})^2 \rightarrow 1$.

---

[14] Often the integrated intensity of weaker reflections is less accurate and the statistical weights are an underestimate of the actual uncertainty due to systematic effects such as the automatic background subtraction.

In which case we can define an expected R-factor,

$$\mathrm{R} = \left[\frac{N_{DOF}}{\sum_i w_i I_{i,obs}^2}\right]^{1/2}, \tag{8.6}$$

which represents the best-possible expected wR within the statistics. The ratio of the weighted and expected R-factors are related to the reduced χ^2 value,

$$\chi^2 = \left(\frac{\mathrm{wR}}{\mathrm{R}}\right)^2. \tag{8.7}$$

Here we use unit-weighting in the calculation of GOF but the R-factors are calculated with statistical weights (as is conventional) and reported as a percentage.

Nuclear structure

The results of the nuclear structure refinement are shown in Table.8.2. The zero strain data were refined from the published zero stress structure with the tetragonal spacegroup $P4/nmm$ [204]. The data at finite stress were refined with the orthorohombic spacegroup $Pmmn$ for the nuclear structure, derived from the action of the orthorhombic Γ_2^+ strain on the $P4/nmm$ spacegroup.

A total of 37 viable nuclear reflections (defined as having a residual intensity $|I - I_{calc}| < 3\sigma$, where σ is the error from Poisson statistics) were integrated in reciprocal space over a sphere of radius 0.05Å^{-1}. Parameters related to the nuclear structure were refined with the 440 MPa data which had better statistics, then fixed during the refinement of the zero stress tetragonal structure. As well as a scale factor there were two additional parameters that were refined: an isotropic atomic displacement parameter, U_{iso}, (due to thermal motion) that was constrained to the same for all atoms, and an extinction correction parameter (isotropic Becker & Coppens Type 2 model [54]). The x/y coordinates of the atomic positions are fixed by symmetry in both the tetragonal and orthorhombic spacegroups. The z-positions of the atoms that are not fixed by symmetry (as indicated in Table.8.2) are the same within the uncertainty of the refinement of both datasets. The agreement of the calculated and observed intensity of the nuclear reflections is shown in Fig.8.19. The crystal structure is shown in Fig.8.18.

Magnetic structure

In the Jana2006 software the magnetic moment on an atom is described by a Fourier series. For a structure with only a single propagation vector, $\boldsymbol{q}$, the expression for the

T = 1.7 K

	0 MPa	440 MPa
Spacegroup	$P4/nmm$	$Pmmn$
a(Å)	4.3976(3)	4.4035(3)
b(Å)		4.3772
c(Å)	10.30644(9)	10.3404(1)
Ce z	0.243(1)	0.244(2)
Au z	0.5*	0.5001(1)
Sb1 z	0*	0.0000(2)
Sb2 z	0.675(1)	0.675(2)
U_{iso}	0.002(9)	
Reflections	37	37
GOF	1.71	1.59
R	16.48	15.35
wR	16.58	14.89

* fixed in $P4/nmm$ symmetry (not refined)

Table 8.2: Lattice parameters and nuclear structure refinement results for data at 0 MPa and 440 MPa compressive stress along the b axis at 1.7 K. The a/c lattice parameters were determined from fits to nuclear Bragg peaks, the b lattice parameter assumes an isochoric distortion. Atomic positions are in fractional coordinates: Ce 2c(0,0.5,z), Au 2b(0,1,0.5), Sb1 2a(0,1,0), Sb2 2c(0,0.5,z). An isotropic thermal displacement parameter U_{iso} was constrained to be the same for all atoms and refined using the 440 MPa data which had the best statistics.

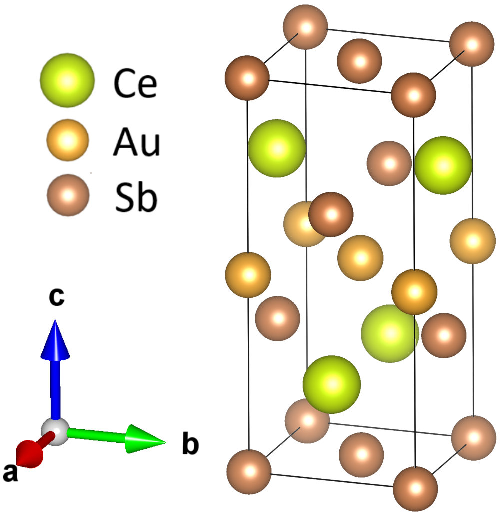

Figure 8.18: Refined crystal structure of $CeAuSb_2$ at 1.7 K and zero stress.

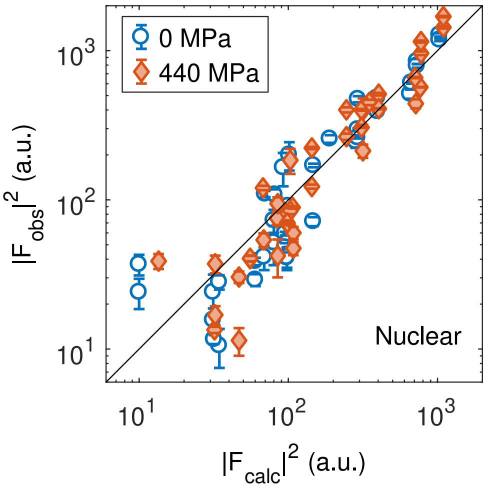

Figure 8.19: Observed and calculated intensities post refinement of the nuclear structure at two stresses $\sigma_{010} = 0$ MPa and 440 MPa at 1.7 K using Jana2006.

moment on the j^{th} site in a unit cell with position, $\boldsymbol{l}$, is given by [205],

$$\boldsymbol{m_{j,l}} = \boldsymbol{M_{c,j}} \cos(\boldsymbol{q} \cdot \boldsymbol{l} + \phi_j) + \boldsymbol{M_{s,j}} \sin(\boldsymbol{q} \cdot \boldsymbol{l} + \phi_j), \tag{8.8}$$

where $\boldsymbol{M_{c,j}}$ and $\boldsymbol{M_{s,j}}$ are vectors with real components (e.g. $\boldsymbol{M_s} = [M_s^x, M_s^y, M_s^z]$). It is these components which will be reported. [15]

The magnetic reflections were integrated over a sphere of radius 0.04Å^{-1} in reciprocal space. There were 11 and 6 viable reflections in the 0 MPa and 440 MPa data respectively (defined as having a residual intensity $|I - I_{calc}| < 1.5\sigma$) [16].

i) A-phase (0 MPa)

The magnetic structure of the SDW A-phase at zero stress has recently been published by Marcus *et al.* [154]. The magnetic structure refinement presented here is for the purpose of demonstrating that the refinement of a relatively small number of reflections collected at a single sample orientation produces a result consistent with the published structure.

There are 2 equivalent propagation vectors with respect to the tetragonal parent structure: $(\delta, \delta, 0.5)$ and $(\delta, -\delta, 0.5)$ where $\delta = 0.137$. Reflections from both domains were refined together under the assumption that the domains are equally populated. There are four irreducible representations (irreps) of the $P4/nmm$ spacegroup associated with

---

[15] This formulation includes both components $\boldsymbol{q}$ and $-\boldsymbol{q}$ - i.e. if there was more than one propagation vector there would be a summation over only the positive $\boldsymbol{q}$

[16] During initial refinements a lower tolerance on the residual intensity was used due to the risk of inaccurate integration of weak reflections - in actuality for the best-fit model all the integrated reflections were within this tolerance.

$\boldsymbol{q_{SDW}} = (\delta, \delta, 0.5)$, $\delta = 0.137$

Irrep.	Superspace group	Components	M_s^x	M_s^z	$\lvert \boldsymbol{M_s} \rvert$	GOF	R	wR
mS_1	$Cmme.1'(0b1/2)000s$	$(M^x, M^y, 0)$	-0.66(5)	0	0.98(7)	0.24	16.45	20.24
mS_3	$Cmme.1'(0b1/2)00ss$							
mS_4	$Cmme.1'(0b1/2)s0ss$	(M^x, M^y, M^z)	0.19(9)	0.79(6)	0.8(1)	0.15	10.09	11.43
mS_2	$Cmme.1'(0b1/2)s00s$	$(0, 0, M^z)$	0*	0.85(5)	0.85(5)	0.19	13.16	15.92

*M_s^x forced to zero (published magnetic structure in Marcus *et al.*[154])

Table 8.3: Results of magnetic refinement of SDW-A phase. The origin shift with respect to the parent unit cell is (0,0,0). The x, y, z directions of the Fourier components are related to the parent cell axes by the following transformation $\{(1, -1, 0), (1, 1, 0), (0, 0, 1)\}$ and are constrained by symmetry: in $Cmme.1'(0b1/2)000s/00ss$ groups $M_s^y = -M_s^x$, $M_c^x = -0.95876 M_s^x$ and $M_c^y = 0.95876 M_s^x$; in the $Cmme.1'$ (0b1/2)s0ss/s00s groups $M_s^y = M_s^x$, $M_c^x = M_c^y = 1.043 M_s^x$ and $M_c^z = M_s^z$. In all superspace groups a ferromagnetic component of the magnetisation was not allowed (i.e. $M_0^x = M_0^y = M_0^z = 0$). The structure with superspace group $Cmme.1'$ (0b1/2)s0ss/s00s was also refined with a moment constrained to be along z.

the propagation vector: mS_1 and mS_3 which describe a structure with spins in the basal plane; and mS_2 and mS_4 which describe spins aligned parallel and anti-parallel across the Au-layers in the nuclear unit cell respectively. Since the distance between Ce sites along the c-axis is approximately constant (the Ce site has a fractional coordinate $z \approx 0.25$) the diffraction data cannot distinguish between the two solutions. The associated superspace groups of the magnetic structures corresponding to the action of the above irreps on the $P4/nmm$ spacegroup of the parent structure are summarised in Table.8.3.

The results of the magnetic structure refinement of the A-phase at 0 MPa is shown in Table.8.3. The diffraction intensities are most consistent with structures produced by the mS_2/mS_4 irreps that allow the ordered moment to have a large component along the c-axis, with a small component in the ab-plane with a relatively large uncertainty. Forcing the moment to be purely along the z-direction in agreement with the structure published in [154] produces a better fit to the data than the structures corresponding to the action of the mS_1 and mS_3 irreps. The agreement of the calculated and observed intensity of the refined A-phase is shown in Fig.8.20A. The magnitude of ordered moment is 1.20(7) μ_B/Ce, which is slightly smaller than the published value of 1.8(2) μ_B/Ce[154]. Nevertheless, the data are broadly consistent with the previously published magnetic structure (moment along an easy-axis in z-direction), especially given the small number of reflections and the relatively large error associated with the integrated intensities.

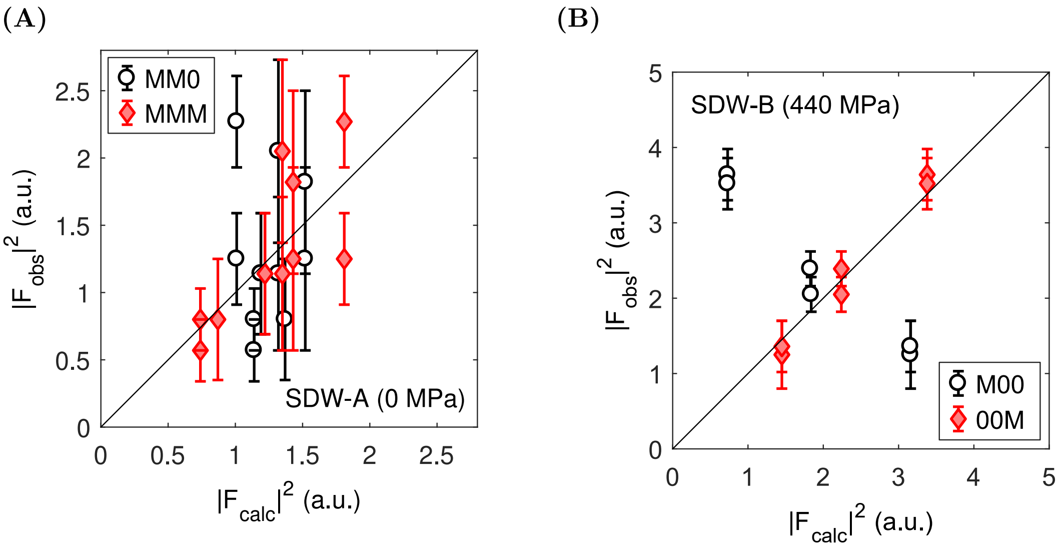

Figure 8.20: Observed intensity against predicted intensity for the refinement of the magnetic structure of the SDW-A (A) and SDW-B (B) phase for the two possible spacegroups. The legend indicates the allowed Cartesian components of the ordered moment.

ii) B-phase (440 MPa)

The following symmetry analysis was performed by taking the $P4/nmm$ space group as a parent structure (i.e. assuming only a small orthorhombic perturbation). There are 2 equivalent propagation vectors with respect to the tetragonal parent structure: $(0, \delta, 0.5)$ and $(\delta, 0, 0.5)$. The application of the orthorhombic strain along [010] selects only the component $(0, \delta, 0.5)$. As in the A-phase there are four irreps of the $P4/nmm$ spacegroup associated with the propagation vector: mU_1 and mU_3 which describe a structure with spins in the basal plane; and mU_2 and mU_4 which describe spins oriented parallel and anti-parallel across the Au-layers in the nuclear unit cell respectively.

The results of the magnetic structure refinement of the SDW-B phase at 440 MPa is shown in Table.8.4. The data are unambiguously consistent with the structures derived from the mU_2 and mU_4 irreps (which cannot be distinguished) with the Ce moments purely along the c-axis (as in the A-phase), the component of the moment in the basal plane is zero within the uncertainty. Forcing the basal plane component of the magnetisation to be exactly zero does not significantly effect the fit to the data, and produces an ordered moment of magnitude 1.15(3) μ_B/Ce (very similar in magnitude to the A-phase moment). Despite the limited number of reflections, the ratio of the integrated intensity of the measured reflections appears very sensitive to the moment direction. The agreement of the calculated and observed intensities from the refinement are shown in

$\boldsymbol{q_{SDW}} = (0, \delta, 0.5)$, $\delta = 0.248$

Irrep.	Superspace group	Components	M_s^x	M_s^y	M_s^z	$\lvert\boldsymbol{M_s}\rvert$	GOF	R	wR
mU$_1$	$Pmmn.1'(0b1/2)000s$	$(M^x, 0, 0)$	1.2(3)	0	0	1.2(3)	0.81	39.93	45.98
mU$_3$	$Pmmn.1'(0b1/2)00ss$								
mU$_4$	$Pmmn.1'(0b1/2)s0ss$	$(0, M^y, M^z)$	0	0.1(1)	0.82(3)	0.8(1)	0.08	3.76	3.86
mU$_2$	$Pmmn.1'(0b1/2)s00s$	$(0, 0, M^z)$	0	0*	0.83(2)	0.83(2)	0.08	4.16	4.74

*M_s^y forced to zero, consistent with the Ising character of moment.

Table 8.4: Results of magnetic refinement of SDW-B phase. The origin shift with respect to the parent unit cell is $(1/4, 1/4, 0)$. The x, y, z directions of the Fourier components are related to the parent cell axes by the following transformation $\{(1,0,0),(0,1,0),(0,0,1)\}$ and are constrained by symmetry: in $Pmmn.1'(0b1/2)000s/00ss$ groups $M_c^x = 0.96481 M_s^x$; in the $Pmmn.1'(0b1/2)s0ss/s00s$ groups $M_c^y = 1.0365 M_s^y$, $M_c^z = 0.96481 M_s^z$. In all superspace groups a ferromagnetic component of the magnetisation was not allowed (i.e. $M_0^x = M_0^y = M_0^z = 0$). The structure with superspace group $Pmmn.1'(0b1/2)s0ss/s00s$ was also refined with a moment constrained to be along z.

Fig.8.20B. Fig.8.21 shows the refined magnetic structure of the B-phase with superspace group $Pmmn1'(0b1/2)s0ss$ derived from the action of the mU$_2$ irrep on the $P4/nmm$ space group of parent structure, assuming an incommensurate wavevector with $\delta = 0.248$.

If the propagation vector is considered to be commensurate ($\delta = 0.25$) then the magnetic structure has an additional degree of freedom which is a choice of origin/phase - which in general will produce magnetic structures belonging to different superspace groups. There are three possible choices of origin, which produce structures with the same spacegroup in both the mU$_2$ and mU$_4$ irreps: A$_b$em2, A$_b$2$_1$/b, and A$_b$b (shown in Fig.8.22). Neutron diffraction is not sensitive to the global phase and cannot distinguish between these structures. However, an important result is that a single irrep cannot produce a structure with constant moment on the Ce sites across all layers.

8.9 Discussion

The main result of this work is the discovery by neutron diffraction of monodomain of single-q SDW order (B-phase) with commensurate wavevector $(0, 0.25, 0.5)$, induced by compressive uniaxial stress along [010]. Unlike the field-induced A' phase, the stress-induced B-phase does not exhibit any modulations along $\langle 110 \rangle$ and doubles the unit cell along the c-axis.

These data unambiguously show that the system has a separate sub-leading suscept-

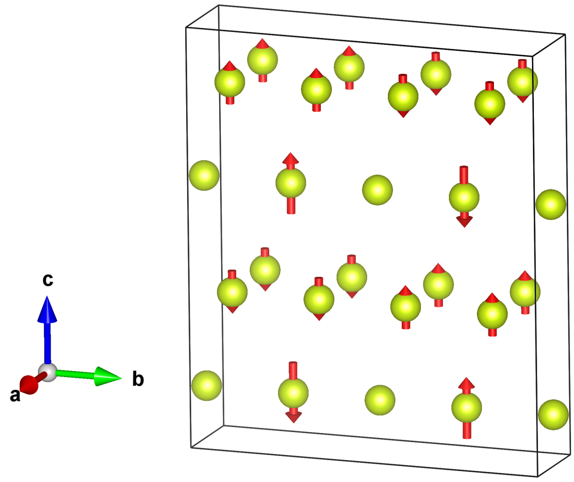

Figure 8.21: One of two equivalent magnetic structures for the strain-induced B-phase for an incommensurate propagation vector (showing the structure that results from the action of the mU_2 irrep). Only cerium atoms are shown for clarity.

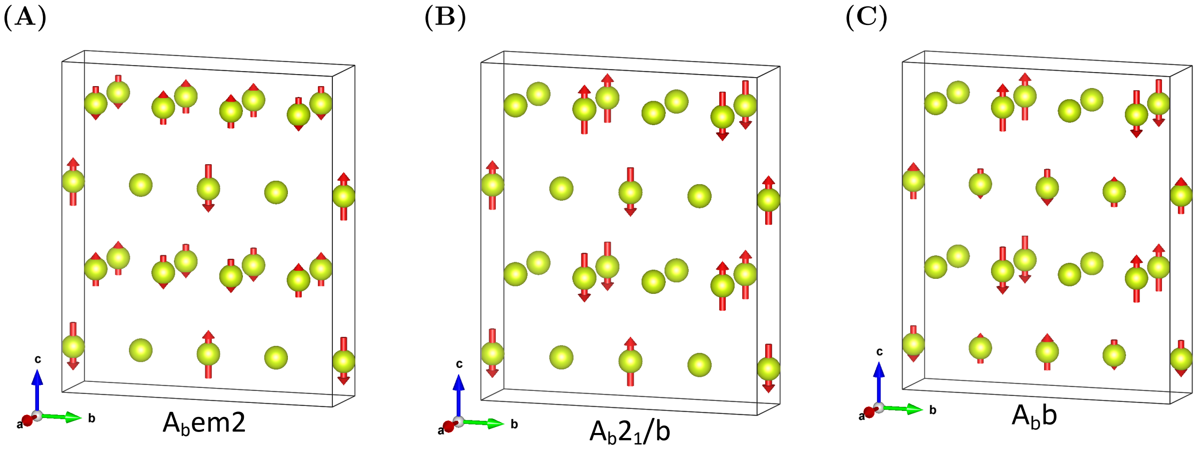

Figure 8.22: Commensurate magnetic structures for the B-phase for three choices of origin corresponding to spacegroups (A)$A_b em2$ (B) $A_b 2_1/b$ (C) $A_b b$. Only cerium atoms are shown for clarity.

ibility to ⟨100⟩ order with a preferred orientation selected by the direction of the ⟨100⟩ stress (the component of the wavevector in the basal plane is parallel to the axis of the stress). This discovery supports the hypothesis of Park *et al.*, that the ⟨100⟩ compression restores the continuous nature of the transition at T_N by lowering the point group symmetry of the fluctuations. The magnitude of the ordered moment in the A and B-phases are very similar, hinting that the two orders are nearly degenerate [17], which is consistent

---

[17] In an SDW nesting scenario the ordered moment is proportional to the gap at the Fermi-level which reduces the kinetic energy of system.

with the observation that the transition temperature of the B-phase extrapolated to zero stress is $\approx 90\%$ of the T_N of the A-phase.

8.9.1 The stress-temperature SDW phase diagram

Previous transport and heat capacity measurements have mapped out the temperature-strain-magnetic field diagram [11, 178, 189]. The neutron diffraction data presented here are qualitatively consistent with the published phase diagram. In particular we observe the onset of magnetic Bragg scattering associated with the B-phase at a lower stress at 5.5 K than 1.7 K.

Diffraction data were measured over a coarse set of stresses, such it is only possible to state that the phase boundary is between 200-272 MPa at 5.5 K and 272-320 MPa at 1.7 K. Park *et al.* found the boundary to occur at strains of $\varepsilon_{010} = -0.37\%$ and -0.51% at 5.5 K and 1.7 K respectively[178], therefore the Young's modulus for compression along the b axis is roughly in the range 50 GPa $< E <$ 70 GPa (for comparison the Young's modulus of aluminium at cryogenic temperature is 78 GPa). This indicates that $\mathrm{CeAuSb_2}$ is quite a soft metal, though it should be noted that there is a large uncertainty on this value: Park *et al.* calculated the strain as the applied displacement divided by the exposed length of the sample, then reduced the strain by 20% as an estimate for the losses due to elastic deformation of the epoxy. However, if $\mathrm{CeAuSb_2}$ has a low Young's modulus, this reduction factor may have been too large.

It is also possible to estimate the Poisson's ratios, $\nu_{100/001} = \varepsilon_{100/001}/\varepsilon_{010}$ from the fitted lattice parameters a and c. For a Young's modulus of 60 GPa the measured strain along the a and c axes correspond to $\nu_{100} \approx 0.18$ and $\nu_{001} \approx 0.45$. These values are reasonable, in particular it is highly unlikely that the ratios for a metal will be over 0.5, which from the c-axis strain provides an upper limit on the Young's modulus for the b-axis compression of 67 GPa.

The refinement of the wavevector and the structural refinement used a b lattice parameter determined under the assumption of a volume conserving lattice distortion (a well defined lower limit on the applied strain). A Young's modulus of $E \approx 60$ GPa corresponds to a very small volume reduction of $\sim 0.25\%$ under a stress of 440 MPa - which has a negligible effect on the refinements. Indeed, the uncertainty on the SDW wavevector is dominated by the uncertainty on the d-spacing of the magnetic reflections.

8.9.2 Transport signatures of SDW order

The present data shed new light on the anisotropic transport inside the B-phase. The onset of B-phase order as a function of stress at low temperature is associated with a first-order step in the resistivity perpendicular to the axis of compression[178]. We can now identify the axis of the enhanced resistivity as perpendicular to the observed wavevector in the B-phase (i.e. $\rho_{\perp} > \rho_{//}$). The B-phase exhibits only one domain, which implies the enhanced resistivity is intrinsic to the order (i.e. not due to scattering at domain walls). If the resistivity enhancement were due to the SDW gapping out carriers on the Fermi surface, this result would naively imply the Fermi velocity is perpendicular to the nesting wavevector - an unusual situation. The opposite trend is observed in $Sr_3Ru_2O_7$[88, 1] and in Cr [95] ($\rho_{//} > \rho_{\perp}$). However, this disparity might be due to the return of states at the Fermi level previously nested by the A-phase. The interpretation of the resistivity data would be greatly aided by electronic structure calculations and identifying the states involved in the B-phase nesting.

8.9.3 Evidence of itinerant antiferromagnetism

A discussed, there are two paradigms in which to consider antiferromagnetism in this compound: the localised limit and the itinerant limit in which the Ce moments are screened by the conduction electrons. These results would seem to support the itinerant description.

A-phase

These data add to the growing body of evidence that the A-phase hosts itinerant nesting driven SDW order. Previous neutron scattering measurements by Marcus *et al.*[154] were consistent with a sinusoidal (rather than square-wave) modulation of the spin-moment indicating SDW order, however the agreement between the observed magnitude of the staggered moment and the saturated bulk moment at high-field (1.65 μ_B/Ce) hinted that local-moment physics could still constrain the magnetic structure. The refinement of these data suggest the ordered moment in the A-phase may be somewhat lower than the saturated bulk moment ($\sim$ 1.15 μ_B/Ce) - however it should be noted that there were a limited number of reflections taken in one orientation and that the experimental setup (anisotropic sample shape in a strain rig) is not optimised for such measurements. Now the structure is well known, a more accurate determination of the ordered moment might be better achieved via powder diffraction, which is an efficient means of measuring a large number of reflections and can average over various systematic effects arising from the instrument (e.g. tube calibration) and from the sample (e.g. preferential domain population).

In addition we have shown the incommensurability in the A-phase, δ, decreases by roughly 1% with stress over the extent of the phase - an amount that is significantly larger than the fractional change of the a and b lattice parameters and comparable to the reported field-dependence [154]. We note other itinerant systems also exhibit a field-dependent SDW wavevector, such as $Sr_3Ru_2O_7$. It remains to be seen whether electronic structure calculation and predicted nesting [190] can reproduce the measured field and strain dependence of the wavevector.

B-phase

The refined wavevector of the B-phase is consistent within the error with a commensurate modulation, $\boldsymbol{q}_{\mathrm{SDW}} = (0, 0.25, 0.5)$. We note that this conclusion is not impacted by the systematic uncertainty on the b-axis lattice parameter. The assumption of a volume conserving distortion could overestimate the b-axis lattice parameter by $\sim 0.25\%$ for a plausible Young's modulus of 60 GPa, which is much smaller than error on the refined component of the wavevector.

A commensurate wavevector does not necessarily imply local-moment order. For example, dilute chromium alloys[206] and the iron pnictide superconductor $BaFe_2As_2$[207] exhibit a first-order incommensurate-commensurate transition that arises from slightly imperfect nesting between electron and hole-pockets, which in both of the above compounds can be tuned with doping. Unlike an incommensurate sinusoidal modulation, the free energy of a commensurate modulation depends on the phase. It might be energetically favourable to preserve a constant moment across all sites (which would hint at local moment behaviour), or conversely to have nodes of zero amplitude on specific sites (which is incompatible with local moments). This can force a modulation to 'lock-in' on a commensurate value even if the ideal nesting is slightly incommensurate[208]. Such a mechanism is believed to be behind the incommensurate-commensurate transitions of the charge-density wave in 2H-$TaSe_2$[209].

From the symmetry analysis it is not possible for a single irrep to produce a magnetic structure with a constant moment on each Ce site that is compatible with the diffraction data in the B-phase. Indeed, the possible structures shown in Fig.8.22 have a node of zero intensity that coincides with a Ce site. This suggests the antiferromagnetism is itinerant and that there is a favourable configuration of nodes that could produce a lock-in mechanism.

Given the putative nesting with a very similar wavevector observed in the incommensurate field-induced A′ phase (with a component along the b-axis of $\delta_{A'} \approx 0.27$) [18] the lock-in scenario seems very plausible. However, no nesting at this wavevector has been identified in any calculated Fermi surfaces [154, 190].

It should be noted that the possibility of local moment order cannot be ruled out by these data. The modulation in the B-phase had a large component out of the scattering plane on WISH (parallel to the axis of uniaxial compression), such that there was insufficient detector coverage to access higher-order harmonics that are characteristic of local moment order (the choice of scattering plane was constrained by the cell which applies stress vertically). Perhaps the best test of local moment order is a local probe such as Mössbauer spectroscopy, which has been used to great effect in the iron arsenides[191] - unfortunately Ce is not Mossbauer-active.

8.10 Conclusion

In recent years uniaxial stress has offered a unique insight into the coupling between electronic order, lattice symmetry and features in the electronic structure near the Fermi-level. This chapter presents the first use of a novel stress cell designed for in-situ tuning of unaixal stress in a neutron diffraction experiment, which has revealed a competing magnetic instability in $\mathrm{CeAuSb_2}$. A compressive stress along $\langle 100 \rangle$ has been shown to produce a monodomain of single-q magnetic order (B-phase) with the component of the modulation in the basal plane parallel to the axis of compression. This discovery has revealed the anisotropic transport in the B-phase to be very unusual, with the enhanced resistivity perpendicular to the wavevector of the modulation. The observation that the $\langle 100 \rangle$ produces a monodomain supports the hypothesis that the unaixial stress restores the continuous nature of the transition at T_N by selecting a preferred orientation for the fluctuations above T_N.

---

[18] Though the L-component is different, as the system is quasi-2D it is expected to exhibit only weak dispersion along the c-axis.

Chapter 9

Summary and Outlook

This thesis presents neutron scattering measurements of spin-density-waves (SDW) in two strongly correlated itinerant systems: $Sr_3Ru_2O_7$ and $CeAuSb_2$. Conclusions for each experimental chapter have been presented, here the emphasis is on the significant results and possible future directions.

The link between the supposed metamagnetic quantum criticality and SDW order in $Sr_3Ru_2O_7$ is a subject of much debate. Even in zero field the predominant fluctuations at low temperature are incommensurate rather than ferromagnetic in nature[72] and yet the neutron diffraction data in this thesis show the SDW order coincides with metamagnetism for magnetic fields applied both in and out of the bilayer plane (though no SDW order was observed at the putative QCP for a field of 7.5 T applied along the c-axis). Inelastic neutron scattering for a magnetic field applied in the basal plane show the quantum critical region hosts overdamped incommensurate spin fluctuations at the observed SDW wavevector of the high-field phase. The overdamped fluctuations exhibit slowing-down behaviour at a critical field for which the temperature dependence of the electronic heat capacity exhibits a logarithmic divergence. In order to clarify the quantum critical nature of the incommensurate spin fluctuations further inelastic measurements are required to determine whether the fluctuations at the identified critical field exhibit E/T-scaling characteristic of quantum criticality.

A general theme in this thesis has been the application of tetragonal symmetry breaking (C_2) fields in the study of SDW order. In $Sr_3Ru_2O_7$ the SDW order for a magnetic field perpendicular to the basal plane (parallel to the c-axis) preserves the tetragonal symmetry[12]. The new SDW phases for a magnetic field in the bilayer plane have shown that not only does the SDW couple to the C_2 field, but the orientation of the SDW moment with respect to the field direction can be flipped by increasing the magnitude of the field. Additionally the observed moment direction for the low-field phase, which is connected to the SDW order observed for a field along the c-axis, implies there is a further spin-flip transition as a function of field-tilt. Clearly the direction of the SDW moment with respect to the field is non-trivial function of the spin, orbital and lattice degrees of freedom. The role of spin-orbit coupling is likely to be very important, for example chromium exhibits a spin-flip transition that is believed to be driven by magnetostrictive effects. Indeed, the SDW phases in $Sr_3Ru_2O_7$ have been shown to be sensitive to uniaxial strain[12].

Uniaxial stress/strain is fast becoming a popular technique for investigating the symmetry of density wave phases - for example in x-ray scattering studies which have revealed the competition between superconductivity and charge-density wave order in the cuprates[194]. However, the in-situ application of such large uniaxial stresses in neutron scattering experiments has proven more technically challenging. Here we have presented neutron diffraction measurements of the SDW order in $CeAuSb_2$ with a novel piezo-actuated cell to apply in-situ uniaxial stress, designed by the C. Hicks at MPI, Dresden - the first experiment of its kind. The experiment was remarkably successful, with the in-situ uniaxial stress revealing a competing instability and inducing a monodomain of single-q SDW order. The data were even of sufficient quality to refine the magnetic structure of the new SDW phase. The discovery has also shed new light on the phase diagram, supporting the hypothesis that the phase boundary of the zero stress phase is driven first-order by fluctuations which do not couple to the uniaxial stress in that direction.

The successful use of the piezo actuated uniaxial stress cell paves the way for further neutron diffraction studies in a wide variety of materials - for instance geometrically frustrated magnets. For example, a recent attempt has been made to study frustration in the spin-ice compound $Ho_2Ti_2O_7$ using a standard clamp-cell design that was unable to achieve the required stress[210]. The piezo-actuated cell used in this thesis has several advantages over conventional clamp cells: they are designed to operate with small cross-section samples and therefore can achieve large stresses, in addition it benefits from a low-background and high stress-uniformity (as demonstrated by these data).

Bibliography

[1] C. Lester, S. Ramos, R. Perry, T. Croft, R. Bewley, T. Guidi, P. Manuel, D. Khalyavin, E. Forgan, and S. Hayden, Nature Materials **14**, 373 (2015).

[2] J. M. Tranquada, Spins, stripes, and superconductivity in hole-doped cuprates, in *AIP Conference Proceedings* Vol. 1550, pp. 114–187, AIP, 2013.

[3] D. C. Johnston, Advances in Physics **59**, 803 (2010).

[4] L. Landau, Exptl Theoret. Phys.(USSR) **35**, 97 (1958).

[5] N. Hussey, J. Buhot, and S. Licciardello, Reports on Progress in Physics **81**, 052501 (2018).

[6] A. J. Schofield, Contemporary Physics **40**, 95 (1999).

[7] M. Brando, D. Belitz, F. Grosche, and T. Kirkpatrick, Reviews of Modern Physics **88**, 025006.

[8] S. Saxena *et al.*, Nature **406**, 587 (2000).

[9] A. Mackenzie, J. Bruin, R. Borzi, A. Rost, and S. Grigera, Physica C: Superconductivity **481**, 207 (2012).

[10] L. Balicas, S. Nakatsuji, H. Lee, P. Schlottmann, T. P. Murphy, and Z. Fisk, Physical Review B **72**, 064422 (2005).

[11] L. Zhao, E. A. Yelland, J. A. Bruin, I. Sheikin, P. C. Canfield, V. Fritsch, H. Sakai, A. P. Mackenzie, and C. W. Hicks, Physical Review B **93**, 195124 (2016).

[12] D. O. Brodsky, M. E. Barber, J. A. N. Bruin, R. A. Borzi, S. A. Grigera, R. S. Perry, A. P. Mackenzie, and C. W. Hicks, Science Advances **3**, e1501804 (2017).

[13] E. Mun, S. L. Budko, A. Kreyssig, and P. C. Canfield, Physical Review B **82**, 054424 (2010).

[14] W. Knafo, D. Aoki, D. Vignolles, B. Vignolle, Y. Klein, C. Jaudet, A. Villaume, C. Proust, and J. Flouquet, Physical Review B **81**, 094403 (2010).

[15] S. L. Bud'ko, P. C. Canfield, M. A. Avila, and T. Takabatake, Physical Review B **75**, 094433 (2007).

[16] E. C. Stoner, Proceedings of the Royal Society of London. Series A, Mathematical and Physical Sciences **165**, 372 (1938).

[17] M. E. Barber, *Uniaxial Stress Technique and Investigations of Correlated Electron Systems* (Springer, 2018).

[18] M. Shimizu, Reports on Progress in Physics **44**, 329 (1981).

[19] K. Sandeman, G. Lonzarich, and A. Schofield, Physical Review Letters **90**, 167005 (2003).

[20] A. Boothroyd, *Principles of Neutron Scattering from Condensed Matter* (Oxford University Press, 2020).

[21] T. Izuyama, D.-J. Kim, and R. Kubo, Journal of the Physical Society of Japan **18**, 1025 (1963).

[22] G. G. Lonzarich and L. Taillefer, Journal of Physics C: Solid State Physics **18**, 4339 (1985).

[23] T. Moriya, Proceedings of the Japan Academy, Series B **82**, 1 (2006).

[24] I. I. Mazin and D. J. Singh, Physical Review Letters **82**, 4324 (1999).

[25] S. Dugdale, Physica Scripta **91**, 053009 (2016).

[26] G. Grüner, Reviews of Modern Physics **66**, 1 (1994).

[27] T. Rice and G. Scott, Physical Review Letters **35**, 120 (1975).

[28] E. Yelland, S. Yates, O. Taylor, A. Griffiths, S. Hayden, and A. Carrington, Physical Review B **72**, 184436 (2005).

[29] G. G. Lonzarich, Journal of Magnetism and Magnetic Materials **45**, 43 (1984).

[30] J. Sólyom*Fundamentals of the Physics of Solids: Volume 3-Normal, Broken-Symmetry, and Correlated Systems* Vol. 3 (Springer Science & Business Media, 2010).

[31] L.-P. Lévy, *Magnetism and superconductivity* (Springer Science & Business Media, 2013).

[32] P. Fulde, *Correlated electrons in quantum matter* (World Scientific, 2012).

[33] J. Hill, G. Helgesen, and D. Gibbs, Physical Review B **51**, 10336 (1995).

[34] D. McWhan and d. T. Rice, Physical Review Letters **19**, 846 (1967).

[35] A. Overhauser, Physical Review **128**, 1437 (1962).

[36] F. Gross, B. Chandrasekhar, D. Einzel, K. Andres, P. Hirschfeld, H. Ott, J. Beuers, Z. Fisk, and J. Smith, Zeitschrift für Physik B Condensed Matter **64**, 175 (1986).

[37] G. L. Squires, *Introduction to the Theory of Thermal Neutron Scattering*, 3 ed. (Cambridge University Press, 2012).

[38] R. Scherm, Ann. Phys **7**, 370 (1972).

[39] S. W. Lovesey, *Theory of Neutron Scattering from Condensed Matter* (Clarendon Press, 1986).

[40] A. Furrer, J. F. Mesot, and T. Strässle*Neutron scattering in condensed matter physics* Vol. 4 (World Scientific Publishing Company, 2009).

[41] I. Anderson, P. Brown, J. Carpenter, G. Lander, R. Pynn, J. Rowe, O. Schärpf, V. Sears, and B. Willis, International Tables for Crystallography (2006).

[42] V. Naish *et al.*, *Neutron diffraction of magnetic materials* (Springer Science & Business Media, 2012).

[43] L. Landau and E. Lifshitz, *Course of Theoretical Physics* (Elsevier, 2013).

[44] H. T. Stokes, D. M. Hatch, B. J. Campbell, and D. E. Tanner, Journal of Applied Crystallography **39**, 607 (2006).

[45] V. Petříček, M. Dušek, and L. Palatinus, Zeitschrift für Kristallographie-Crystalline Materials **229**, 345 (2014).

[46] J. M. Carpenter and C.-K. Loong, *Elements of Slow-Neutron Scattering: Basics, Techniques, and Applications* (Cambridge University Press, 2015).

[47] R. Cubitt and G. Fragneto, Neutron reflection: Principles and examples of applications, in *Scattering and Inverse Scattering in Pure and Applied Science*, pp. 1198–1208, Elsevier, 2002.

[48] M. T. Cooper and R. Nathans, Acta Crystallographica **23**, 357 (1967).

[49] M. Popovici, Acta Crystallographica Section A: Crystal Physics, Diffraction, Theoretical and General Crystallography **31**, 507 (1975).

[50] L. C. Chapon *et al.*, Neutron News **22**, 22 (2011).

[51] R. B. Von Dreele, J. D. Jorgensen, and C. G. Windsor, Journal of Applied Crystallography **15**, 581 (1982).

[52] S. Ikeda and J. M. Carpenter, Nuclear Instruments and Methods in Physics Research Section A: Accelerators, Spectrometers, Detectors and Associated Equipment **239**, 536 (1985).

[53] J. Peters and W. Jauch, Science Progress **85**, 297 (2002).

[54] P. J. Becker and P. Coppens, Acta Crystallographica Section A: Crystal Physics, Diffraction, Theoretical and General Crystallography **30**, 129 (1974).

[55] B. Buras and L. Gerward, Acta Crystallographica Section A: Crystal Physics, Diffraction, Theoretical and General Crystallography **31**, 372 (1975).

[56] G. McIntyre and R. Stansfield, Acta Crystallographica Section A: Foundations of Crystallography **44**, 257 (1988).

[57] B. Keimer, Emergent Phenomena in Correlated Matter (2013).

[58] E. Blackburn, Physica B: Condensed Matter **460**, 132 (2015).

[59] J. Longo, P. Raccah, and J. Goodenough, Journal of Applied Physics **39**, 1327 (1968).

[60] Y. Maeno, S. Kittaka, T. Nomura, S. Yonezawa, and K. Ishida, Journal of the Physical Society of Japan **81**, 011009 (2011).

[61] M. Braden, Y. Sidis, P. Bourges, P. Pfeuty, J. Kulda, Z. Mao, and Y. Maeno, Physical Review B **66**, 064522 (2002).

[62] K. Iida, M. Kofu, N. Katayama, J. Lee, R. Kajimoto, Y. Inamura, M. Nakamura, M. Arai, Y. Yoshida, M. Fujita, K. Yamada, and S.-H. Lee, Physical Review B **84**, 060402 (2011).

[63] S. Kunkemöller, P. Steffens, P. Link, Y. Sidis, Z. Mao, Y. Maeno, and M. Braden, Physical Review Letters **118**, 147002 (2017).

[64] Y. Maeno, T. M. Rice, and M. Sigrist, Physics Today **54**, 42 (2001).

[65] A. P. Mackenzie, T. Scaffidi, C. W. Hicks, and Y. Maeno, npj Quantum Materials **2**, 1 (2017).

[66] P. Steffens, Y. Sidis, J. Kulda, Z. Mao, Y. Maeno, I. Mazin, and M. Braden, Physical Review Letters **122**, 047004 (2019).

[67] I. Eremin, D. Manske, and K. H. Bennemann, Physical Review B **65**, 220502 (2002).

[68] I. Eremin, D. Manske, S. Ovchinnikov, and J. Annett, Annalen der Physik **13**, 149 (2004).

[69] S. Cobo, F. Ahn, I. Eremin, and A. Akbari, Physical Review B **94**, 224507 (2016).

[70] A. Rømer, D. Scherer, I. Eremin, P. Hirschfeld, and B. Andersen, Physical Review Letters **123**, 247001 (2019).

[71] H. Yaguchi, R. S. Perry, and Y. Maeno, Ferromagnetism induced by uniaxial pressure in the itinerant metamagnet sr3ru2o7, in *AIP Conference Proceedings* Vol. 850, pp. 1203–1204, American Institute of Physics, 2006.

[72] L. Capogna, E. M. Forgan, S. M. Hayden, A. Wildes, J. A. Duffy, A. P. Mackenzie, R. S. Perry, S. Ikeda, Y. Maeno, and S. P. Brown, Physical Review B **67**, 012504 (2003).

[73] S. Ramos, E. M. Forgan, C. Bowell, S. M. Hayden, A. J. Schofield, A. Wildes, E. A. Yelland, S. P. Brown, M. Laver, R. S. Perry, and Y. Maeno, Physica B: Condensed Matter **403**, 1270 (2008).

[74] J. Carlo *et al.*, Nature Materials **11**, 323 (2012).

[75] S. Kunkemöller, A. Nugroho, Y. Sidis, and M. Braden, Physical Review B **89**, 045119 (2014).

[76] S.-I. Ikeda, Y. Maeno, S. Nakatsuji, M. Kosaka, and Y. Uwatoko, Physical Review B **62**, R6089 (2000).

[77] S.-I. Ikeda, N. Shirakawa, T. Yanagisawa, Y. Yoshida, S. Koikegami, S. Koike, M. Kosaka, and Y. Uwatoko, Journal of the Physical Society of Japan **73**, 1322 (2004).

[78] S. Sachdev, Handbook of Magnetism and Advanced Magnetic Materials (2007).

[79] H. v. Löhneysen, T. Pietrus, G. Portisch, H. Schlager, A. Schröder, M. Sieck, and T. Trappmann, Physical Review Letters **72**, 3262 (1994).

[80] D. V. Efremov, A. Shtyk, A. W. Rost, C. Chamon, A. P. Mackenzie, and J. J. Betouras, Physical Review Letters **123**, 207202 (2019).

[81] A. M. Berridge, S. A. Grigera, B. D. Simons, and A. G. Green, Physical Review B **81**, 054429 (2010).

[82] R. S. Perry, L. M. Galvin, S. A. Grigera, L. Capogna, A. J. Schofield, A. P. Mackenzie, M. Chiao, S. R. Julian, S. I. Ikeda, S. Nakatsuji, Y. Maeno, and C. Pfleiderer, Physical Review Letters **86**, 2661 (2001).

[83] S. A. Grigera, R. S. Perry, A. J. Schofield, M. Chiao, S. R. Julian, G. G. Lonzarich, S. I. Ikeda, Y. Maeno, A. J. Millis, and A. P. Mackenzie, Science **294**, 329 (2001).

[84] A. M. Berridge, A. G. Green, S. A. Grigera, and B. D. Simons, Physical Review Letters **102**, 136404 (2009).

[85] G. Abdul-Jabbar *et al.*, Nature Physics **11**, 321 (2015).

[86] M. Uhlarz, C. Pfleiderer, and S. M. Hayden, Physical Review Letters **93**, 256404 (2004).

[87] R. S. Perry, K. Kitagawa, S. A. Grigera, R. A. Borzi, A. P. Mackenzie, K. Ishida, and Y. Maeno, Physical Review Letters **92**, 166602 (2004).

[88] R. A. Borzi, S. A. Grigera, J. Farrell, R. S. Perry, S. J. S. Lister, S. L. Lee, D. A. Tennant, Y. Maeno, and A. P. Mackenzie, Science **315**, 214 (2007).

[89] J. A. N. Bruin, R. A. Borzi, S. A. Grigera, A. W. Rost, R. S. Perry, and A. P. Mackenzie, Physical Review B **87**, 161106 (2013).

[90] C. Stingl, R. S. Perry, Y. Maeno, and P. Gegenwart, Physical Review Letters **107**, 026404 (2011).

[91] C. Stingl, R. S. Perry, Y. Maeno, and P. Gegenwart, physica status solidi (b) **250**, 450 (2013).

[92] S. A. Grigera, P. Gegenwart, R. A. Borzi, F. Weickert, A. J. Schofield, R. S. Perry, T. Tayama, T. Sakakibara, Y. Maeno, A. G. Green, and A. P. Mackenzie, Science **306**, 1154 (2004).

[93] C. Puetter, H. Doh, and H.-Y. Kee, Physical Review B **76**, 235112 (2007).

[94] M. H. Fischer and M. Sigrist, Physical Review B **81**, 064435 (2010).

[95] W. Muir and J. Ström-Olsen, Physical Review B **4**, 988 (1971).

[96] P. Bak and M. H. Jensen, Journal of Physics C: Solid State Physics **13**, L881.

[97] M. B. Walker, Physical Review B **22**, 1338 (1980).

[98] S. Mühlbauer, B. Binz, F. Jonietz, C. Pfleiderer, A. Rosch, A. Neubauer, R. Georgii, and P. Böni, Science **323**, 915 (2009).

[99] I. Mazin and D. J. Singh, Physical Review B **56**, 2556 (1997).

[100] C. M. Puetter, J. G. Rau, and H.-Y. Kee, Physical Review B **81**, 081105 (2010).

[101] C. Bergemann, A. P. Mackenzie, S. R. Julian, D. Forsythe, and E. Ohmichi, Advances in Physics **52**, 639 (2003).

[102] A. Tamai *et al.*, Physical Review X **9**, 021048 (2019).

[103] V. B. Zabolotnyy, D. V. Evtushinsky, A. A. Kordyuk, T. K. Kim, E. Carleschi, B. P. Doyle, R. Fittipaldi, M. Cuoco, A. Vecchione, and S. V. Borisenko, Journal of Electron Spectroscopy and Related Phenomena **191**, 48 (2013).

[104] V. Sunko *et al.*, npj Quantum Materials **4**, 1 (2019).

[105] C. W. Hicks, D. O. Brodsky, E. A. Yelland, A. S. Gibbs, J. A. N. Bruin, M. E. Barber, S. D. Edkins, K. Nishimura, S. Yonezawa, Y. Maeno, and A. P. Mackenzie, Science **344**, 283 (2014).

[106] A. Steppke *et al.*, Science **355** (2017).

[107] M. E. Barber, A. S. Gibbs, Y. Maeno, A. P. Mackenzie, and C. W. Hicks, Phys. Rev. Lett. **120**, 076602 (2018).

[108] Y.-C. Liu, F.-C. Zhang, T. M. Rice, and Q.-H. Wang, npj Quantum Materials **2**, 1 (2017).

[109] H. Shaked, J. D. Jorgensen, O. Chmaissem, S. Ikeda, and Y. Maeno, Journal of Solid State Chemistry **154**, 361 (2000).

[110] J. A. N. Bruin, *Transport studies of the itinerant metamagnet $Sr_3Ru_2O_7$ near its quantum critical point*, PhD thesis, University of St Andrews, 2012.

[111] A. Tamai, M. P. Allan, J. F. Mercure, W. Meevasana, R. Dunkel, D. H. Lu, R. S. Perry, A. P. Mackenzie, D. J. Singh, Z.-X. Shen, and F. Baumberger, Physical Review Letters **101**, 026407 (2008).

[112] J.-F. Mercure, S. Goh, E. O'Farrell, R. Perry, M. Sutherland, A. Rost, S. Grigera, R. Borzi, P. Gegenwart, and A. Mackenzie, Physical Review Letters **103**, 176401 (2009).

[113] J.-F. Mercure, A. W. Rost, E. C. T. O'Farrell, S. K. Goh, R. S. Perry, M. L. Sutherland, S. A. Grigera, R. A. Borzi, P. Gegenwart, A. S. Gibbs, and A. P. MacKenzie, Physical Review B **81**, 235103 (2010).

[114] C. Stingl, R. Perry, Y. Maeno, and P. Gegenwart, physica status solidi (b) **247**, 574 (2010).

[115] A. W. Rost, R. S. Perry, J.-F. Mercure, A. P. Mackenzie, and S. A. Grigera, Science **325**, 1360 (2009).

[116] P. Gegenwart, F. Weickert, M. Garst, R. S. Perry, and Y. Maeno, Physical Review Letters **96**, 136402 (2006).

[117] D. Sun, A. W. Rost, R. S. Perry, A. P. Mackenzie, and M. Brando, Physical Review B **97**, 115101 (2018).

[118] Y. Tokiwa, M. Mchalwat, R. Perry, and P. Gegenwart, Physical Review Letters **116**, 226402 (2016).

[119] D. V. Efremov, J. J. Betouras, and A. Chubukov, Physical Review B **77**, 220401 (2008).

[120] D. L. Maslov and A. V. Chubukov, Physical Review B **79**, 075112 (2009).

[121] G. Conduit, A. Green, and B. Simons, Physical Review Letters **103**, 207201 (2009).

[122] C. Pedder, F. Krüger, and A. Green, Physical Review B **88**, 165109 (2013).

[123] P. G. Niklowitz, M. Hirschberger, M. Lucas, P. Cermak, A. Schneidewind, E. Faulhaber, J. M. Mignot, W. J. Duncan, A. Neubauer, C. Pfleiderer, and F. M. Grosche, (2017).

[124] M. B. Stone, M. D. Lumsden, R. Jin, B. C. Sales, D. Mandrus, S. E. Nagler, and Y. Qiu, Physical Review B **73**, 174426 (2006).

[125] O. Arnold *et al.*, Nuclear Instruments and Methods in Physics Research Section A: Accelerators, Spectrometers, Detectors and Associated Equipment **764**, 156 (2014).

[126] R. Daou, C. Bergemann, and S. Julian, Physical Review Letters **96**, 026401 (2006).

[127] K. K. Kesharpu and P. D. Grigoriev, Temperature dependence of resistivity at the transition to a charge density wave state in rare-earth tritellurides, in *Journal of Physics: Conference Series* Vol. 1238, p. 012019, IOP Publishing, 2019.

[128] D. Pajerowski, C. Rotundu, J. Lynn, and R. Birgeneau, Physical Review B **87**, 134507 (2013).

[129] C. Dhital, T. Hogan, Z. Yamani, R. J. Birgeneau, W. Tian, M. Matsuda, A. Sefat, Z. Wang, and S. D. Wilson, Physical Review B **89**, 214404 (2014).

[130] W. Zhang *et al.*, Physical Review Letters **117**, 227003 (2016).

[131] Y. Feng, J. Van Wezel, J. Wang, F. Flicker, D. Silevitch, P. Littlewood, and T. Rosenbaum, Nature Physics **11**, 865 (2015).

[132] K. Huang, *Introduction to statistical physics* (CRC press, 2009).

[133] A. Rost, *Magnetothermal properties near quantum criticality in the itinerant metamagnet* $Sr_3Ru_2O_7$, PhD thesis, University of St. Andrews, 2009.

[134] S. D. Wilson, Z. Yamani, C. Rotundu, B. Freelon, E. Bourret-Courchesne, and R. Birgeneau, Physical Review B **79**, 184519 (2009).

[135] K. Kitagawa, K. Ishida, R. S. Perry, T. Tayama, T. Sakakibara, and Y. Maeno, Physical Review Letters **95**, 127001 (2005).

[136] K. Ishida, H. Mukuda, Y. Kitaoka, K. Asayama, Z. Q. Mao, Y. Mori, and Y. Maeno, Nature **396**, 658 (1998).

[137] A. Pustogow *et al.*, Nature **574**, 72 (2019).

[138] K. Ishida, M. Manago, K. Kinjo, and Y. Maeno, Journal of the Physical Society of Japan **89**, 034712 (2020).

[139] A. T. Rømer *et al.*, Physical Review B **87**, 144513 (2013).

[140] S. Hayden, G. Lonzarich, and H. Skriver, Physical Review B **33**, 4977 (1986).

[141] S. Julian, P. Teunissen, and S. Wiegers, Physical Review B **46**, 9821 (1992).

[142] L. Zhu, M. Garst, A. Rosch, and Q. Si, Physical Review Letters **91**, 066404 (2003).

[143] D. E. Moncton, D. B. McWhan, J. Eckert, G. Shirane, and W. Thomlinson, Phys. Rev. Lett. **39**, 1164 (1977).

[144] A. Alam and D. D. Johnson, Physical Review Letters **107**, 206401 (2011).

[145] N. H. van Dijk, B. Fåk, L. P. Regnault, A. Huxley, and M.-T. Fernández-Díaz, Phys. Rev. B **58**, 3186 (1998).

[146] A. Suslov, D. Dasgupta, J. Feller, B. K. Sarma, J. B. Ketterson, and D. G. Hinks, International Journal of Modern Physics B **16**, 3066 (2002).

[147] B. Shivaram, L. Holleis, V. W. Ulrich, J. Singleton, and M. Jaime, Scientific Reports **9**, 1 (2019).

[148] A. McCollam, M. Fu, and S. R. Julian, Journal of Physics: Condensed Matter **33**, 075804 (2020).

[149] J. Mydosh, P. M. Oppeneer, and P. Riseborough, Journal of Physics: Condensed Matter **32**, 143002 (2020).

[150] W. Knafo *et al.*, Nature Communications **7**, 13075 (2016).

[151] W. Knafo, D. Aoki, G. Scheerer, F. Duc, F. Bourdarot, K. Kuwahara, H. Nojiri, L.-P. Regnault, and J. Flouquet, Physica B: Condensed Matter **536**, 457 (2018).

[152] A. Pourret, A. Palacio-Morales, S. Krämer, L. Malone, M. Nardone, D. Aoki, G. Knebel, and J. Flouquet, Journal of the Physical Society of Japan **82**, 034706 (2013).

[153] M. Wartenbe, R. E. Baumbach, A. Shekhter, G. S. Boebinger, E. D. Bauer, C. C. Moya, N. Harrison, R. D. McDonald, M. B. Salamon, and M. Jaime, Physical Review B **99**, 235101 (2019).

[154] G. G. Marcus, D.-J. Kim, J. A. Tutmaher, J. A. Rodriguez-Rivera, J. O. Birk, C. Niedermeyer, H. Lee, Z. Fisk, and C. L. Broholm, Physical Review Letters **120**, 097201 (2018).

[155] S. A. Grigera, R. A. Borzi, A. P. Mackenzie, S. R. Julian, R. S. Perry, and Y. Maeno, Physical Review B **67**, 214427 (2003).

[156] W. Wu, A. McCollam, S. Grigera, R. Perry, A. Mackenzie, and S. Julian, Physical Review B **83**, 045106 (2011).

[157] R. S. Perry, T. Tayama, K. Kitagawa, T. Sakakibara, K. Ishida, and Y. Maeno, Journal of the Physical Society of Japan **74**, 1270 (2005).

[158] K. Schmalzl, W. Schmidt, S. Raymond, H. Feilbach, C. Mounier, B. Vettard, and T. Brueckel, Nuclear Instruments and Methods in Physics Research Section A: Accelerators, Spectrometers, Detectors and Associated Equipment **819**, 89 (2016).

[159] M. Boehm, A. Hiess, J. Kulda, S. Roux, and J. Saroun, Measurement Science and Technology **19**, 034024 (2008).

[160] D. Sun, W. Wu, S. A. Grigera, R. S. Perry, A. P. Mackenzie, and S. R. Julian, Physical Review B **88**, 235129 (2013).

[161] M. L. Plumer and M. B. Walker, Journal of Physics C: Solid State Physics **14**, 4689 (1981).

[162] E. Fawcett, Reviews of Modern Physics **60**, 209 (1988).

[163] W. Cowan, Journal of Physics F: Metal Physics **8**, 423 (1978).

[164] G. Shirane and W. Takei, J. Phys. Soc. Japan **17** (1962).

[165] D. Sun, *The effect of hydrostatic pressure on the nematic phases of Sr3Ru2O7*, PhD thesis, University of Toronto (Canada), 2015.

[166] C. Lester, S. Ramos, R. Perry, T. Croft, R. Bewley, T. Guidi, M. Laver, A. Heiss, A. Mackenzie, E. Forgan, and S. Hayden, Nearly singular low-frequency magnetic excitations at a metamagnetic quantum critical point, not submitted.

[167] P. Mikula, P. Lukáš, and R. Michalec, Journal of applied crystallography **20**, 428 (1987).

[168] M. Braden, P. Steffens, Y. Sidis, J. Kulda, P. Bourges, S. Hayden, N. Kikugawa, and Y. Maeno, Physical Review Letters **92**, 097402 (2004).

[169] P. Steffens, O. Friedt, Y. Sidis, P. Link, J. Kulda, K. Schmalzl, S. Nakatsuji, and M. Braden, Physical Review B **83**, 054429 (2011).

[170] C. Monney, T. Schmitt, C. Matt, J. Mesot, V. Strocov, O. Lipscombe, S. Hayden, and J. Chang, Physical Review B **93**, 075103 (2016).

[171] M. Dean *et al.*, Nature Materials **12**, 1019 (2013).

[172] T. Moriya, Physical Review Letters **24**, 1433 (1970).

[173] A. Gukasov, M. Braden, R. J. Papoular, S. Nakatsuji, and Y. Maeno, Phys. Rev. Lett. **89**, 087202 (2002).

[174] T. Moriya and T. Takimoto, Journal of the Physical Society of Japan **64**, 960 (1995).

[175] D. K. Singh, A. Thamizhavel, J. W. Lynn, S. Dhar, J. Rodriguez-Rivera, and T. Herman, Scientific Reports **1**, 117 (2011).

[176] B. Keimer, R. Birgeneau, A. Cassanho, Y. Endoh, R. Erwin, M. Kastner, and G. Shirane, Physical Review Letters **67**, 1930 (1991).

[177] A. Schröder, G. Aeppli, R. Coldea, M. Adams, O. Stockert, H. Löhneysen, E. Bucher, R. Ramazashvili, and P. Coleman, Nature **407**, 351 (2000).

[178] J. Park, H. Sakai, O. Erten, A. P. Mackenzie, and C. W. Hicks, Physical Review B **97**, 024411 (2018).

[179] P. Coleman, C. Pépin, Q. Si, and R. Ramazashvili, Journal of Physics: Condensed Matter **13**, R723 (2001).

[180] P. Coleman, Handbook of magnetism and advanced magnetic materials (2007).

[181] P. Gegenwart, Q. Si, and F. Steglich, Nature Physics **4**, 186 (2008).

[182] K. Andres, J. Graebner, and H. Ott, Physical Review Letters **35**, 1779 (1975).

[183] S. Paschen, T. Lühmann, S. Wirth, P. Gegenwart, O. Trovarelli, C. Geibel, F. Steglich, P. Coleman, and Q. Si, Nature **432**, 881 (2004).

[184] S. Seo, V. Sidorov, H. Lee, D. Jang, Z. Fisk, J. Thompson, and T. Park, Physical Review B **85**, 205145 (2012).

[185] A. Thamizhavel *et al.*, Physical Review B **68**, 054427 (2003).

[186] A. Bianchi, R. Movshovich, I. Vekhter, P. Pagliuso, and J. Sarrao, Physical Review Letters **91**, 257001 (2003).

[187] C. Capan, A. Bianchi, F. Ronning, A. Lacerda, J. Thompson, M. Hundley, P. Pagliuso, J. Sarrao, and R. Movshovich, Physical Review B **70**, 180502 (2004).

[188] K.-A. Lorenzer, A. Strydom, A. Thamizhavel, and S. Paschen, physica status solidi (b) **250**, 464 (2013).

[189] J. Park, H. Sakai, A. P. Mackenzie, and C. W. Hicks, Physical Review B **98**, 024426 (2018).

[190] G. Yumnam, Y. Chen, Y. Zhao, A. Thamizhavel, S. K. Dhar, and D. K. Singh, physica status solidi (RRL)–Rapid Research Letters **13**, 1900304 (2019).

[191] J. Allred *et al.*, Nature Physics **12**, 493 (2016).

[192] S. Avci *et al.*, Physical Review B **88**, 094510 (2013).

[193] S. Avci *et al.*, Nature Communications **5**, 1 (2014).

[194] H.-H. Kim *et al.*, Science **362**, 1040 (2018).

[195] D. Bloch, D. Hermann-Ronzaud, C. Vettier, W. Yelon, and R. Alben, Physical Review Letters **35**, 963 (1975).

[196] C. W. Hicks, M. E. Barber, S. D. Edkins, D. O. Brodsky, and A. P. Mackenzie, Review of Scientific Instruments **85**, 065003 (2014).

[197] A. I. of Steel Construction, *Steel Construction Manual*, 14 ed. (American Institute of Steel Construction, 2011).

[198] P. C. Canfield and Z. Fisk, Philosophical magazine B **65**, 1117 (1992).

[199] K. Myers, S. Bud'ko, I. Fisher, Z. Islam, H. Kleinke, A. Lacerda, and P. Canfield, Journal of Magnetism and Magnetic Materials **205**, 27 (1999).

[200] P. C. Canfield and I. R. Fisher, Journal of Crystal Growth **225**, 155 (2001).

[201] F. R. Schwartzberg, S. Osgood, and R. Keys, *Cryogenic Materials Data Handbook* (US Department of Commerce, 1963).

[202] J. Henn, Crystallography Reviews **25**, 83 (2019).

[203] B. H. Toby, Powder diffraction **21**, 67 (2006).

[204] O. Sologub, K. Hiebl, P. Rogl, H. Noël, and O. Bodak, Journal of alloys and compounds **210**, 153 (1994).

[205] J. Rodríguez-Carvajal and J. Villain, Comptes Rendus Physique **20**, 770 (2019).

[206] E. Fawcett, H. Alberts, V. Y. Galkin, D. Noakes, and J. Yakhmi, Reviews of modern physics **66**, 25 (1994).

[207] D. Pratt *et al.*, Physical Review Letters **106**, 257001 (2011).

[208] P. Lee, T. Rice, and P. Anderson, Solid State Communications **88**, 1001 (1993).

[209] R. Fleming, D. Moncton, J. Axe, and G. Brown, Physical Review B **30**, 1877 (1984).

[210] R. Edberg *et al.*, arXiv preprint arXiv:2006.02756 (2020).

List of Figures

List of Tables